2013

A study of the mechanical properties and wear behaviour of the oxide layer formed on high speed steel work rolls

Wan Fathul Hakim Zamri
University of Wollongong

Recommended Citation

Zamri, Wan Fathul Hakim, A study of the mechanical properties and wear behaviour of the oxide layer formed on high speed steel work rolls, Doctor of Philosophy thesis, School of Mechanical, Materials and Mechatronic Engineering, University of Wollongong, 2013. http://ro.uow.edu.au/theses/3978

A study of the mechanical properties and wear behaviour of the oxide layer formed on high speed steel work rolls

A thesis submitted in fulfilment of the requirements for the
award of the degree of

Doctor of Philosophy

from

UNIVERSITY OF WOLLONGONG

by

WAN FATHUL HAKIM W. ZAMRI

School of Mechanical, Materials and Mechatronics Engineering
Faculty of Engineering

2013

Declaration

I, Wan Fathul Hakim W Zamri, declare that this thesis, submitted in fulfilment of the requirements for the award of Doctor of Philosophy, in the School of Mechanical, Materials and Mechatronic Engineering (MMM), University of Wollongong, is wholly my own work unless otherwise referenced or acknowledged. The document has not been submitted for qualifications at any other academic institution.

Wan Fathul Hakim W. Zamri
August 2013

To my loving mum and dad

Acknowledgements

First and foremost, I would like to express my heartfelt gratitude to my principal supervisor, Dr Buyung Kosasih, for his invaluable guidance, intellectual support, scholarly insight, and genuine encouragement during my study at the University of Wollongong.

My sincere appreciation is also extended to my co-supervisor, Prof Kiet Tieu, for his invaluable assistance, support, and guidance in supervising my thesis. My special thanks go to Dr. Hongtao for his assistance and critical advice in relation to the finite element model and the uses of High Performance Computing and cluster programs. Nor must I forget Dr. Qiang Zhu, an expert on nanoindentation, for his assistance and invaluable advice.

I would like to convey my gratitude to the Government of Malaysia, especially the Ministry of Higher Education and *Universiti Kebangsaan Malaysia*, for providing me with a scholarship to carry out my doctoral study at the University of Wollongong. I am also grateful to the University of Wollongong for providing this HDR scholarship.

Many thanks to all the friends at the Engineering Faculty, especially Guanyu, Laia, Ahmad, and Sue for always being present and making me feel special. Special thanks should also go to my best friends Faiz Md Din, Fandy, Jad and Fainida for providing the support and friendship that I needed.

Most importantly I would like to thank my beloved parents Nor Aziah and W. Zamri, and my family members, especially akak Nana, Saufi and Mimi for their prayers, moral support, and encouragement during my study. Thanks for always being there for me.

List of publications during the PhD course

1. **Zamri, W. F. H.,**Kosasih, P. B., Tieu, A. K., Zhu, Q., & Zhu, H. (2012). Variations in the microstructure and mechanical properties of the oxide layer on high speed steel hot rolling work rolls. *Journal of Materials Processing Technology*.
2. **Zamri, W. F. H**., Kosasih, P. B., Tieu, A. K., & Zhu, H. (2012). Finite element modelling of the nanoindentation of layers of porous oxide on high speed steel. *15TH International Conference on Advances in Materials & Processing Technologies*, 23-26 September 2012, Wollongong, Australia.
3. **Zamri, W. F. H.,** Kosasih, P. B., Tieu, A. K., Zhu, Q., & Zhu, H (2013). Finite element modelling of the nanoindentation of layers of porous oxide on high speed steel. *Journal of Steel Research International* (accepted)

Abstract

This research is part of a larger study conducted to understand the wear of hot rolling rolls. A significant cost of hot rolling is associated with the consumption of rolls; hence a comprehensive understanding of how the roll material wears is important. As the surfaces of rolls are covered by an oxide layer it is important that the mechanical and tribological properties of these oxides be known. The mechanical properties of the oxide layer are an important aspect that leads to a better prediction of its behaviour during hot rolling operations. Due to the complex nature of the phenomena that occur in, and the practical difficulty of accessing the hot strip and work roll interface, computer based simulations coupled with experimental study are needed to understand and predict the wear of the oxide layers.

A combined FE simulation and nanoindentation experiments approach was developed and used to characterise the mechanical properties of the oxide scale formed on the HSS sample. The main procedure consisted of two approaches: first, a nanoindentation experiment was carried out to determine the load-displacement curve, and second, the load-displacement curve was validated against the simulation based curve. In this thesis, nanoindentations were performed on the cross section of the oxide layers. The experiments clearly revealed the variation of mechanical properties in the inner and outer sub-layer. The XRD pattern and SEM-EDS analysis of the oxide layer sample indicated that these layers consist of two sub-layers, namely Fe_2O_3 and $(Fe,Cr)_3O_4$ in the outer and inner sub-layers respectively. The result of the load-displacement curves indicated that the outer sub-layer of Fe_2O_3 is generally harder, as demonstrated by the smaller penetration depths on the outer sub-layer compared to the inner sub-layer. It was hypothesized that the mechanical properties of the outer sub-layer were significantly influenced by the hard grains and small pores.

From the FE simulations, the output load-displacement curves were obtained. The simulated load-displacement curves were then analysed in terms of the unloading slope (dP/dh) and the maximum load (P_{max}) and compared with the experimental curves. Each simulation was refined iteratively until the values of the mechanical properties used in the simulation yielded an average unloading slope and maximum load difference with the experiments of less than 1 percent.

FE simulations were carried out to simulate the load-displacement curves of the nanoindentation experiments to give the properties of the oxide layer. In this application the use of a nanoindentation experiment alone to measure the properties was hindered by the unknown value of the Poisson's ratio and porosity effect of the sample. In a porous media, the load displacement relationship depends on the porosity and grain sizes, which are largely heterogeneous. To account for the porosity effect, the finite element model adopted Gurson's model of plasticity for porous material. The mechanical properties of the oxide sub-layers were determined from the FE simulations input parameters e.g. elastic modulus, *E*, yield strength, σ_y, Poisson's ratio, υ and pore fraction, f, which could not be measured directly from the nanoindentation experiments. It was found that the outer sub-layer has a higher *E* of around 200-240 GPa compared to the inner sub-layer's *E* of 90-220 GPa. The large variation of *E* in the inner sub-layer was probably due to the influence of voids and a non-uniform porosity of the sub-layer. The smaller size grains of the inner sub-layer increased the sensitivity of the indentations to variations in porosity. The *E* and *H* for the 20 mN load tests are lower than for the 5 mN load. This phenomenon was probably caused by the hardening which arises from the interaction between geometrically necessary dislocations (GNDs) and grain boundaries.

To understand how the oxide layer deforms when scratched by asperity, a three-dimensional (3D) finite element (FE) simulation was carried out to investigate an indenter scratching on the oxide layers/high speed steel substrate system. Both ductile and brittle failure models were used to study the deformation and failure modes of the oxide layer. The coefficient of friction increased in an approximately linear function with the depth of the scratch. The oxide layer formed on HSS can be considered as ductile rather than brittle material based on the better agreement between the FE simulations and the scratch experiments when the ductile model was used. In fact the nanoindentation results on the oxide scales showing cracking free deformation, which further corroborated a ductile behaviour of the oxide layers.

An investigation on the deformation of the oxide layers and indenter-carbide particle interactions during a scratch test was also carried out using a three-dimensional finite element method. The interaction between the indenter and the carbide particle reinforcements were investigated after three different possible scenarios: particle on an oxide free surface, particle on an oxide-substrate interface, and particle in the substrate. The results showed that the magnitude and distribution of stresses/strains in the oxide layer and interaction of the particle with the tip are the main reason for the particle de-bonding during scratching. The von Mises stress at room temperature was significantly higher than at high temperature. This situation was probably due to the difference between the mechanical properties such as elastic modulus and yield strength of the oxide layer in both cases.

In summary, this thesis has presented 6 major contributions to the study of oxide layers formed on high speed steel hot rolling material, namely:(i) the development of combined FE simulations and nanoindentation experiments to study the mechanical properties of the oxide layer, (ii) finding the variation in the oxide layer morphology, (iii) finding the significant relationship between the mechanical properties of the oxide layer and the nanoindentation parameters, (iv) development of FE simulation to predict the oxide layer wear, (v) suggestion on how and when to treat the oxide layer as brittle and as ductile material, and (vi) development of an FE model of oxide layer deformation and wear with carbide inclusion.

List of Tables

List of Figures

List of Content

Chapter 7 FE study of the effect of carbide particles on the behaviour of the oxide layer

Chapter 1

Introduction

High speed steel (HSS) is the most common work roll material used in the early to the last finishing stands in modern hot rolling mill due to its excellent mechanical properties such as high hardness and strong wear resistance at high temperature (Hwang *et al.,* 1998; Kim *et al.,* 2003; Hanlon and Rainforth, 2003). HSS rolls which are three times better in terms of performance have replaced high chromium (HiCr) rolls (De Carvalho *et al.,* 2002). High speed steel rolls are used because they improve the quality of the strip surface by up to 20% and increase rolling mill productivity. The superior characteristics of HSS roll materials are influenced by a carbon content ranging from 1.5 to 2%wt and some alloying elements such as V, W, Cr, Ni, and Mo (Rodenburg and Rainforth, 2007; Kang *et al.,* 2001). The microstructure of HSS contains primary MC and M_6C carbides (10-20%) dispersed in martensite matrix and fine secondary carbide formed by the high concentration of strong carbide forming elements lead to a precipitation hardening of the matrix. Because these carbides are harder than the matrix, they directly influence the mechanical strength and high wear resistance of HSS rolls material (El-Rakayby and Mills, 1986; Park *et al.,* 1999; Badisch and Mitterer, 2003).

In hot rolling the surface of the roll is heated to approximately 700°C while in contact with the hot strip for short periods (10^{-2}-10^{-3}s). It is subsequently cooled by water to around 50°C during the same cycle (Kato *et al*., 1992; Spuzic *et al.,* 1994). Because of this cyclic thermal working environment, hot rolls are prone to thermal fatigue and oxidation causing the surface of the roll to deteriorate (Vergne *et al.,* 2001; Li *et al.,* 2001; Dai *et al.,* 2007).

This degradation process involves mechanisms such as two-body abrasion, oxidation, and thermal fatigue. Abrasion is the dominant component in a total wear process dominated by oxide layers breaking off between the work roll and steel strip (Ginzburg, 1989; Kato, 1997). These particles may roll/slide and are expected to be a dominant roll wear mode. Meanwhile, the high surface temperature of the work rolls and the high humidity conditions accelerates the growth of the oxide layer on the surface of the rolls and can degrade the surface. The degraded surface directly affects the surface quality of the processed strip. However, from a tribological perspective the magnetite Fe_3O_4 and wustite FeO oxide layer can be viewed as a protective layer which influences the wear and friction in the strip/roll contact and can be beneficial in the application of the work roll in hot strip mills (Molinari *et al*., 2000). On the contrary, the rhombohedral hematite α-Fe_2O_3, a hard material at room temperature, is known to be abrasive and tends to increase friction and wear.

One of the significant operating cost components of modern hot rolling mill is related to work rolls because they are expensive and a large stock must be kept in store to ensure that the mills can operate continually. Therefore, a study of the mechanical properties and failure of the oxide layer formed on high speed steel roll material is very important.

Firstly, the mechanical properties of the oxide layer can lead to a better prediction of the behaviour of the scale layer during hot rolling because as the wear of the substrate material depends on the wear resistance of the oxide layers, it is essential that the mechanical properties of these layers be known accurately in the roll wear analysis. However, unlike strip oxidation, the oxidation of work rolls and the oxide has received little attention.

Secondly, the material properties of the oxide layer can be used by other researchers in their simulation to provide realistic description of the strip-oxide-oxide-work roll system in an industrial application. The mechanical properties of the oxide layers formed on high speed steel roll material are poorly understood. It is difficult to quantify the porosity of these layers in a realistic laboratory experiment so a computer based model is needed to analyse the result so that the properties of the oxide layer can be extracted for use in industrial application.

Thirdly, considerable amount of computer based modelling work has been carried out to study the failure of the oxide layer on strip surface, but not much has reported on the oxide scale on the work roll. Oxidation of the strip has been investigated over many years with different types and structures of oxide

(Krzyzanowski and Rainforth, 2010; Graf and Kawalla, 2012), but the deformation mechanism and wear of the oxide layer work roll are still not understood very well.

Fourthly, since carbide influences wear resistance, it is important to understand the behaviour of a carbide particle. According to the author's knowledge, no computational study to date has investigated the behaviour of the carbide particles of high speed-steel-based material. In this thesis the effect of carbide has been studied by scratch simulations. Currently, and to the best of the author's knowledge, there is no work that has specifically studied the behaviour of the oxide layer formed on high speed steel work roll. Due to the complex nature of the phenomena that occur in and the accessibility of the hot strip and work roll interface, computer based simulations coupled with experimental study are needed to understand and predict the wear of the oxide layers.

The aims of this research are the following:

(i) to develop a methodology to obtain the comprehensive mechanical properties of oxide layers such as the elastic modulus (*E*), yield stress, and Poisson's ratio and porosity. A combination of nanoindentation experiments and FE simulation method has been developed.

(ii) study the mechanical properties of the oxide layer formed on the surface of high speed steel rolls. The mechanical properties of the inner and outer oxide layer on samples prepared in the laboratory were obtained and studied in detail using the combined nanoindentation experiments and FE simulations.

(iii) to understand the wear process of oxide layers. Two-body scratch experiments and FE simulations were carried out, and predictions of the wear rate of the oxide layers based on the results have been made. Consideration of the abrasive wear of the oxide layer actually represents the behaviour of abrasive wear phenomena of work roll in practice. Abrasive wear along with other wear mechanisms such as thermal and mechanical fatigue causes materials to progressively degrade. Although this study only considered one part of the wear mechanisms, the knowledge of this dominant wear mode should enhance the understanding of how the oxide layers affect the wear rate of the work roll, and the resulting strip profile.

(iv) to understand the effect of the presence of carbide in the substrate on the deformation and wear of the oxide layer. FE simulations of scratch processes were also carried out to achieve this objective.

By the end of this thesis there are still many questions that need to be answered regarding hot roll wear. Despite of this, this research has contributed important knowledge towards understanding and prediction of the wear of hot rolling work rolls. Understanding the lubrication mechanisms of the oxide layer and their role in the rolling process allows hot rolling industry to predict the wear rate and estimate progressive wear during hot rolling. This research has also contributed towards better understanding of the control of roll damage and its life cycle, which consequently allows for reduction of the running cost of the mill. In summary, the main contributions of this thesis are:-

(i) the development of combined FE simulations and nanoindentation experiments to study the mechanical properties of the oxide layer

(ii) finding the variations in the oxide layer morphology

(iii) finding the significant relationship between the mechanical properties of the oxide layer and the nanoindentation parameters

(iv) development of FE simulation to predict the oxide layer wear

(v) suggestion on how and when to treat the oxide layer as brittle and as ductile material

(vi) development of an FE model of oxide layer deformation and wear with carbide inclusion

In this chapter the background of work rolls in the hot rolling mill is introduced, the aims of this thesis are given, and its importance is discussed.

Chapter two reviews previous researches relevant to this study. They include (i) fundamentals of work roll wear and oxides layers formed on work rolls. (ii) Review of nanoindentation and scratch experiments modellings are also presented.

Chapter three introduces the experimental instruments and analytical methodology used.

Chapter four describes the nanoindentation experiments performed on the oxide layer on HSS material, and the finite element simulation model of the nanoindentation of oxide layers to determine their mechanical properties. The results of these simulations were compared and validated with experiments.

Chapter five analyses the mechanical properties of the oxide layer for both experimental and FEM simulation for two cases of load, 5 mN and 20 mN. They include the mechanical properties of the oxide sub-layers for the inner and outer layers. The correlation between the mechanical properties and nanoindentation parameters is also presented.

Chapter six studies the wear behaviour of the oxide scale formed on a HSS by an asperity using the ductile and brittle failure models.

Chapter seven investigates the behaviour of a carbide particle during scratch process using FE model.

Chapter eight presents conclusions and recommendations for further work.

Chapter 2

Review of work roll wear and oxide layers formation and modelling

Wear on a hot rolling roll is a progressive process that can lead to unexpected roll failure or product defects (John *et al.*, 2006). At high rolling temperatures up to 500-650°C (Garza-Montes-de-Oca *et al*., 2011) and rolling pressures up to 100-300 MPa (Magnee *et al*., 1980; Ohnuki *et al*., 1984), worn rolls not only affect the quality of the strip, but also the productivity of the mill. However, most research on hot rolling seems to focus on the strips rather than the work rolls. The strip is often considered to be the most important outcome in a rolling campaign, but the fact that its quality is strongly influenced by the work roll suggests that research of hot roll wear is as crucial as that for hot rolled strip. For example, the quality of the strip is known to relate to the geometry and surface roughness of the work roll (De Carvalho *et al*., 2002). Moreover, rolling productivity is related to the duration that the work rolls can operate without replacing the worn rolls. This chapter reviews existing studies on work roll wear in section 2.1, oxide layers on the hot roll surface in section 2.2, and the FE modelling of oxide layers in section 2.3.

2.1 Work roll wear

Many investigations have been carried out to understand the factors and their interaction that contribute to work roll wear. Spuzic *et al*. (1994) summarised several factors that affect roll wear, including roll geometry, lubrication and the cooling media, stress state in the roll, roll material properties, rolling pressure, sliding velocity and distance, friction, oxide films, hot steel material and temperatures (Figure 2.1). They discussed the effects of temperature on the wear of roll materials via the influence of oxide. In the 400-600°C range, hematite (Fe_2O_3) and magnetite (Fe_3O_4) oxides increase abrasive wear while within the 600-900°C range formation of wustite (FeO) influences the lubricating effect. In addition, it has been found that the mechanical properties of work roll material have a significant influence on the removal of material from the work roll. These properties of work roll material are significantly affected by microstructures and chemical compositions, especially the carbon C content, and the quantity and distribution of the carbides (M_xC_y). Guo (1998) reported many factors such as chemistry, materials, mechanical load, and thermal physics contribute to roll wear.

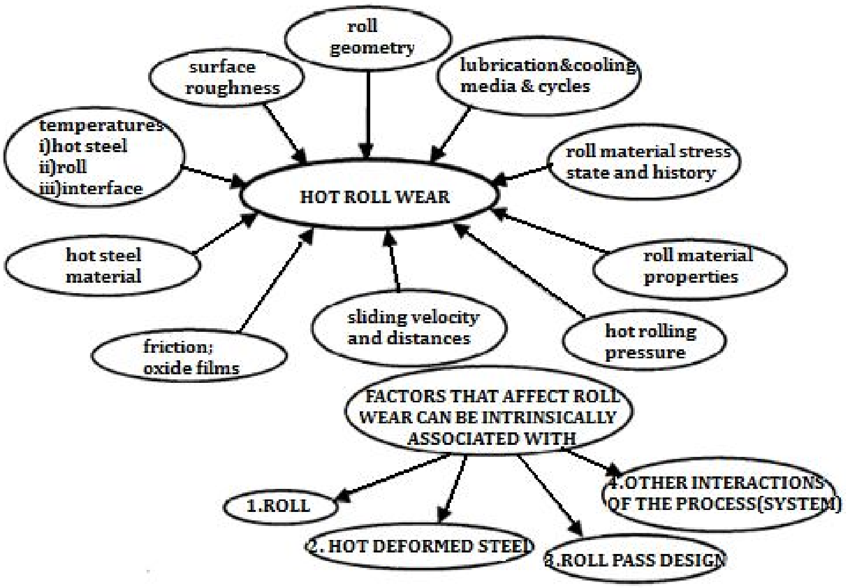

Figure 2.1: Factors influencing hot roll wear (Spuzic *et al*., 1994).

John *et al*. (2006) studied the correlation between the roll wear of hot strip mills with the shape theories and developed a wear model for the finishing stands to predict progressive roll wear during rolling. The model is based on experimental measurements of the roll force and changes in the shape of the work roll. Changes in roll shape can be calculated from the integration of roll force model. Wang *et al*. (2007) calculated the profile of a work roll using a contour prediction model (Figure 2.2) by considering three parts, namely: the initial, thermal, and wear contours. The initial work roll contour is designed by the operators and provides effects on the strip crown magnitude during the initial phase of rolling campaign. The roll thermal contour is a result of thermal expansion during hot rolling. Work roll wear effect is a major reason for the variation of the roll contour during rolling. The difference between the hot and cold roll measurements will show the thermal effect and the difference between the original first measurement and final cold measurement will provide the roll wear. Abbasapour and Saboonchi (2008) developed a computer model of transient roll temperatures and its effect on work roll thermal crown profile.

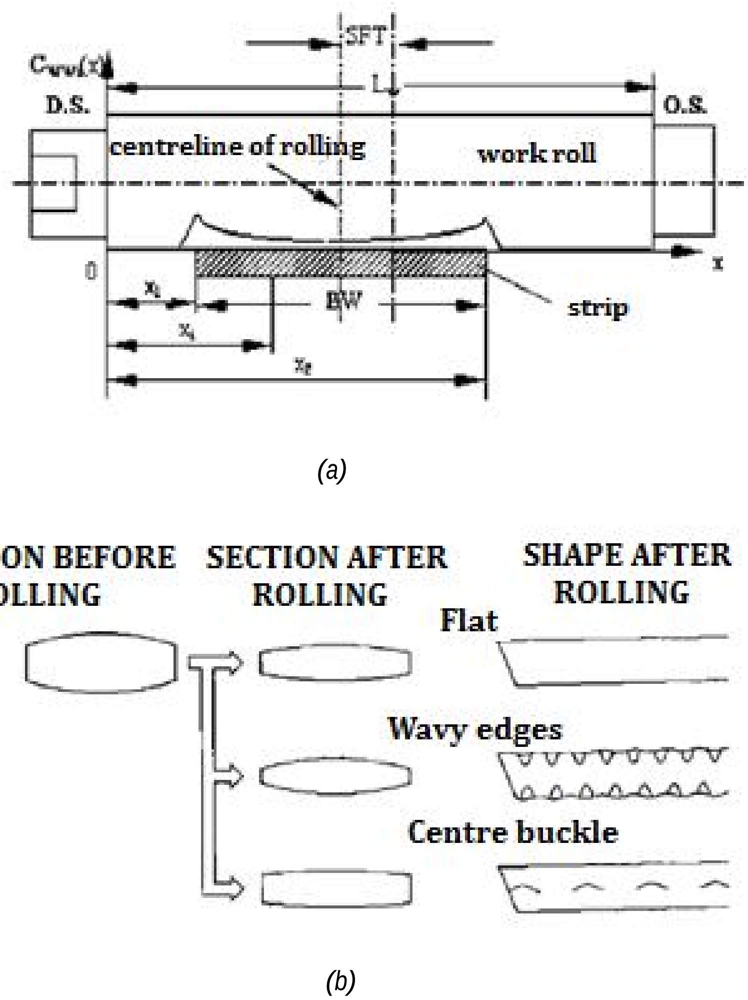

Figure 2.2: Contour prediction model (a) wear contour calculation model of work roll (b) shape of roll after rolling (Wang *et al*., 2007).

Many researches have been conducted to investigate the mechanisms of hot roll wear during the rolling process. Colas *et al.* (1999) characterised the oxidation of high chromium work rolls by electron back scattered diffraction (EBSD). Garza-Montes-de-Oca and Rainforth (2009) studied the wear mechanism experienced by high speed steel (HSS) work roll under different environmental conditions.

According to Garza-Montes-de-Oca and Rainforth (2009), the high wear rates under dry sliding conditions are associated with oxidation and plastic deformation (*e.g.* ploughing and abrasion). These results suggest that the combined wear mechanism of oxidation and abrasion of HSS rolls affect the characteristics and the wear behaviour of HSS work rolls during rolling process. The review clearly identified the need for research that focuses on a combination of abrasive factors and oxidation.

Table: 2.1: Current work roll wear research emphases.

Author	*Roll Wear Research*
John *et al*. (2006); Wang *et al.* (2007); Abbasapour and Saboonchi (2008).	Based on the profiles or the contour of work rolls
Colas *et al*. (1999); Garza-Montes-de-Oca and Rainforth (2009); Molinari *et al*. (2000); Zhu *et al*. (2010).	Based on the wear mechanism

Despite there being numerous studies, most of them focussed on the oxidation mechanism only. For example, Molinari *et al*. (2000) studied the oxidation mechanisms of high speed steels and their correlation with the particular microstructure and chemical composition. They showed that oxide scale grows non-uniformly from the carbide-matrix interface and only involves the matrix. The high oxidation resistance characteristics of carbides have made it more difficult for oxide to form on the carbides. Zhu *et al*. (2010) comprehensively studied the oxidation in high speed steel roll material by in-situ investigations. Oxidation was observed to occur in three stages that began at the carbides/matrix interface, followed by in the carbides, and then by continuous growth over the whole surface. As the current published research is mainly concerned with the behaviour of oxidation, less attention was paid to the abrasive factor. Abrasion represents the scratching of asperities of strip oxide layers against the oxide layers of the work rolls.

The summary of the research focusing on roll wear is shown in Table 2.1. In this review an attempt was made to understand the potential research related to the wear of the work roll. However, the published work provided very little information on the wear mechanism and behaviour of the oxide layer with ploughing or abrasion contact and interaction of carbides particles in high speed steel. In addition, there is a lack of knowledge on the mechanical properties and variation in the morphology of oxide layers on HSS work roll that contributes to work roll wear. The ability to understand all the potential mechanisms and their contribution to the rolling process is important for the prediction of the wear rate. According to Colas *et al*. (1999), in most cases the rolls are replaced because of surface deterioration and worn profile rather than because of changes in shape due to thermal expansion. For that reason, a study of the mechanical properties, microstructures, and wear mechanism of the oxide layer is an important area to be investigated. The wear modes for work rolls and each potential mechanism is discussed in 2.1.1 while the specific modes or wear mechanisms of high speed steel work rolls based on the previous studies is explained in 2.1.2.

2.1.1 Roll wears modes and mechanisms

In hot strip mills the work rolls operate in severe conditions and experience a number of degradation mechanisms. It has been reported that the rate of roll wear increases after a specific amount of rolled steel has been produced. Referring to some published papers, the wear process is an interaction of different factors that affect the roll wear modes.

Table: 2.2: The general modes or wear mechanisms of work rolls.

Author	*Type of mills*	*Roll Wear Modes*
Nakagawa *et al.* (1982); Lundberg (1993).	High chromium iron roll	Thermal, mechanical fatigues and abrasion
Colas *et al*. (1999)	High-speed-steel rolls	Consider oxidation as one of the mechanisms besides thermal and mechanical fatigue
Boccalini and Sinatora (2002); Garza-Montes-de-Oca and Rainforth (2009)	High-speed-steel rolls	At least abrasion, oxidation and thermal fatigue

Apparently there are controversial reports on the roll wear modes. Classical research by Nakagawa *et al.* (1982) and Lundberg (1993) argues that thermal and mechanical fatigues, as well as abrasion by hard iron oxides, are the most significant degrading contributors of the surface of work rolls. On the other hand, Colas *et al*. (1999) indicated that oxidation might be one of the mechanisms responsible for wear damage without abrasion. A comprehensive study of the degradation of work rolls in early finishing mills was carried by Boccalini and Sinatora (2002); Garza-Montes-de-Oca and Rainforth (2009). They summarised the potential mechanisms involving at least abrasion, oxidation, and thermal fatigue. Table 2.2 summarises the general modes or wear mechanisms of work rolls.

Figure 2.3 illustrates a general set of mechanical wear processes that are related to work rolls grouped under three general headings. These mechanisms have the capability of removing material from the surface. The description of each wear mechanism such as abrasion, thermal fatigue, and oxidation is explained below.

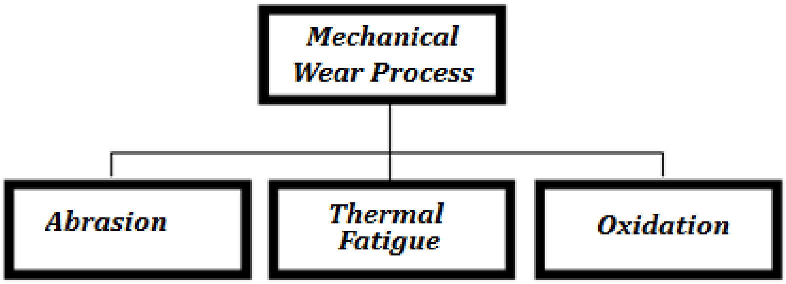

Figure 2.3: Mechanical wear processes of work roll.

Abrasion is a dominant component of the total wear process (Ginzburg, 1989). Abrasion can be conceptually divided into two-body or three-body wear. Three-body wear is determined by the additional effect of oxide scales that have been broken off and become trapped between the roll and steel strip. These particles may roll/slide rather than simply abrade and are expected to be an important mode of roll wear. But from the point of view of modelling, it is easier to consider two-body abrasion which can be further sub-classified into three main categories, ploughing, wedge formation and cutting (Kato, 1997).

Thermal fatigue is one of the factors influencing the wear of work rolls in the finishing stands of hot strip mills. This damage is due to the sudden changes of surface temperatures caused by alternating contact between the work rolls with the hot strip and the cooling water in each rotation. The difference in temperatures (100-650°C) can produce compressive surface stress during heating (within the roll gap) and tensile during cooling (outside the roll gap). As a consequence, the work rolls are prone to thermal cracks or spalling of the roll surface segments (Mercado-Solis *et al.*, 2007).

Oxidational wear was identified by Fink (1930). According to Quinn (1983), there are two possible mechanisms of wear particle formation contributing to oxidational wear. First, the bulk of the oxidation occurs when the metal is exposed and it then shears in contact at the oxide-metal interface. Second, an equal amount of oxidation occurs at each contact until a critical thickness is reached, beyond which shearing occurs at the oxide-metal interface.

2.1.2 Wear modes and mechanism of a high speed steel (HSS) work roll

A number of papers (Pellizzari *et al.,* 2005, 2009; Garza-Montes-de-Oca and Rainforth, 2009; Joos *et al*., 2007) explored the wear mechanism of high speed steel work roll and discussed different modes of failure.

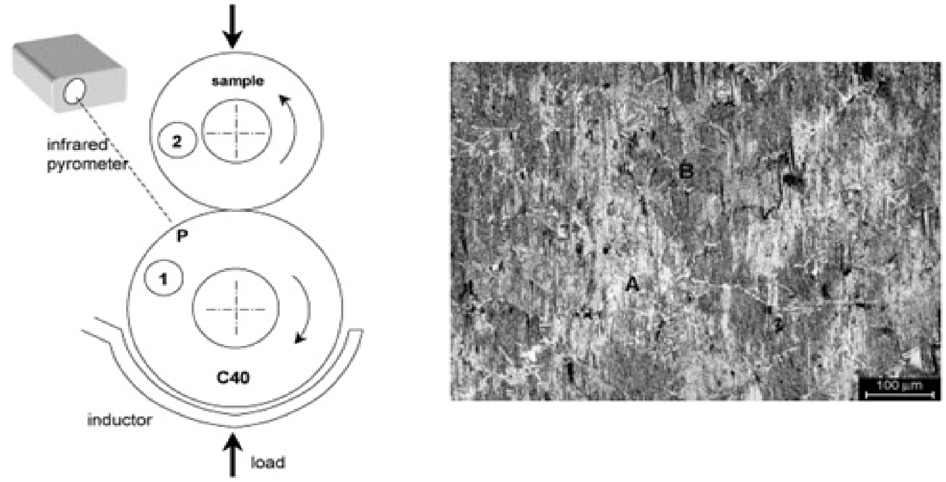

(a) (b)

Figure 2.4: (a) Configuration of hot wear test (b) The worn surface of HSS work roll (Pellizzari *et al.,* 2005).

Pellizzari *et al.* (2005) studied the wear behaviour of several HSS grades by means of rolling/sliding hot wear experiment at 700°C with an Amsler tribometer (Figure 2.4). Figure 2.4(a) shows the configuration of dry rolling-sliding hot wear tests where the disc sample was allowed to rotate against a counterpart in C40 plain carbon steel. The typical topography of the worn surface at the end of a wear test is shown in Figure 2.4(b). Two distinct regions can be distinguished. Region A which the material is practically not oxidised shows the same bright colour of the surface before the test. Clear abrasion scratches are evident, produced by the hard iron oxide scale covering the C40 counterpart material induction heated at 700 °C. Region B which the material covered by oxide shows the abrasion scratches are less deep and the surface smoother. They reported that the main wear mechanism was governed by a combination of abrasion and oxidation. The wear mechanisms were confirmed by the SEM-EDX analysis, SEM observation, and a light optical micrographic analysis on the typical topography of the worn surface at the end of a wear test.

Pelizzari *et al.* (2009) studied the wear mechanism of HSS by considering the homogeneity of wear across the roll track where higher consumption occurs at the centre because of the higher temperature (Figure 2.5). It is claimed that the wear mechanism of rolling/sliding contact HSS against plain carbon steel is given by an abrasion, oxidation, and adhesion, although abrasion is the dominant wear mechanism. This conclusion was based on observation of the roll track. It has been reported that the region (A) close to edges (Figure 2.5) is poorly oxidised compared to the inner region (B) of the track and more deeply abraded. These observations also suggest that abrasion is the dominant wear mechanism in both the external region of the wear track and in the central part of specimen.

This finding indicated that during the early stage of the experiment, the abrasion of HSS roll materials is caused by the hard oxide scale developed on the hot carbon steel strip. Abrasion is then enhanced by the removal of hard particles from the roll. XRD analysis in this study provided evidence for the above explanation where Cr-rich oxide spinel was detected in the outer layer of the glazes. In addition, the breakdown of such layers due to mechanical stresses further aids the ploughing of oxide asperities.

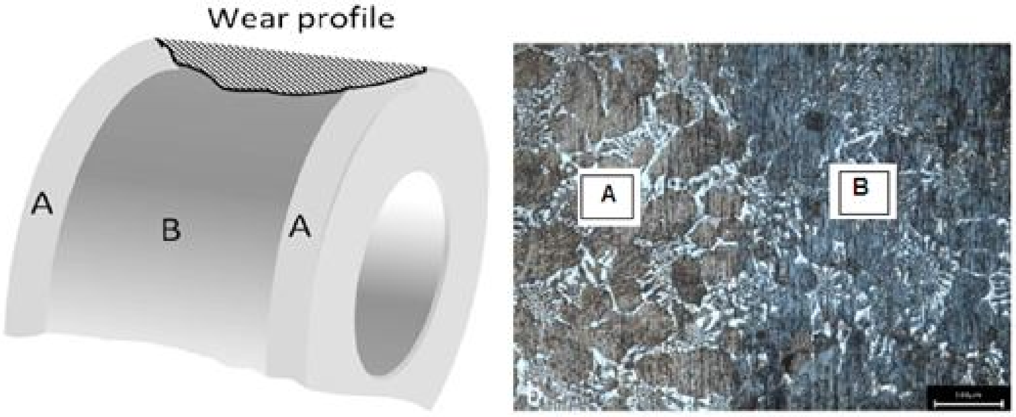

(a) (b)

Figure 2.5: Schematic of the worn surface of the disc and micrographic detail of the transition zone between A (close to edges) and B (inner region) (Pellizzari *et al*., 2009).

In another study, Garza-Montes-de-Oca and Rainforth (2009) investigated the wear mechanism of a work roll grade HSS roll under different environmental conditions and proposed two types of wear mechanisms. For the dry condition, the wear is a mixture of oxidation and plastic deformation (metallic ploughing) while for a wet condition, the main wear mechanism is essentially oxidation at all temperatures. The declaration of wear mechanisms for both tests was based on several measurements and observations. Garza-Montes-de-Oca and Rainforth (2009) claimed the wear mechanism of dry conditions based on the following reasons. First, the level of oxidation of the surface increases during the test, and second, the oxide is mechanically mixed into the metal surface (Figure 2.6) thus indicating a high degree of plastic deformation. Third, the resulting XRD diffraction showed that the proportion of metal in wear debris increased significantly with temperature. On the other hand, the wear mechanism of a wet test was identified as oxidation from the wear debris where the surface was almost entirely covered with oxide.

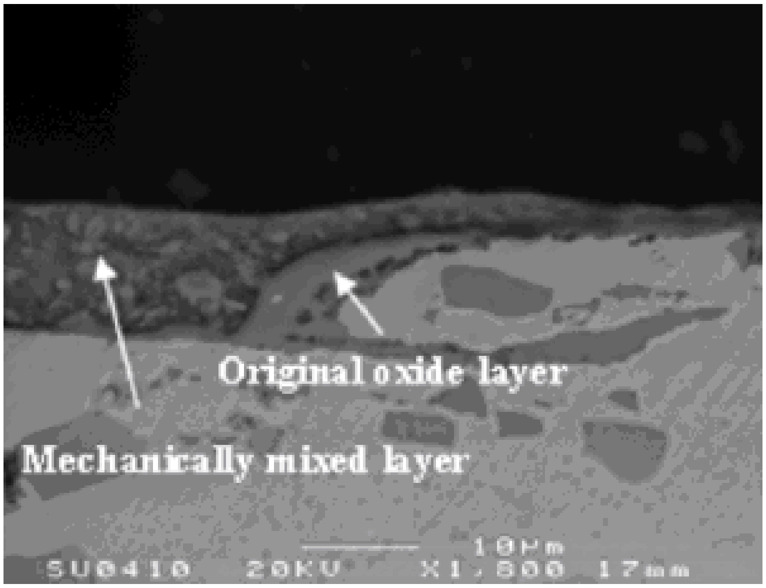

Figure 2.6: SEM cross section for the surface tested under dry conditions (Garza-Montes-de-Oca and Rainforth, 2009).

Table: 2.3: The wear mechanisms of HSS work rolls.

Authors	Mechanism of HSS work roll	Justification
Pellizzari *et al.* (2005)	combination of abrasion and oxidation	Based on typical topography of the worn surface (abrasion) and SEM observations of oxide (oxidation)
Pellizzari *et al.* (2009)	abrasion, triboxidation and adhesion. However, abrasion is a dominant mechanism.	Based on observation on the roll track and XRD analysis`
Garza-Montes-de-Oca and Rainforth (2009)	i) Dry condition : A mixture of oxidational and plastic deformation ii) Wet condition: Oxidation	Based on level of oxidation of the surface; oxide is mechanically mixed into metal surface and XRD diffraction
Joos *et al*. (2007)	abrasion	Based on the formation of oxide debris, SEM observations and the coefficient of friction

Joos *et al*. (2007) assessed the influence of the oxide layer on wear damage and found that the wear mechanism at 20^{o}C and 650^{o}C is abrasion. The type of mechanism considered in this study is based on the formation of oxide debris, SEM observations, and the coefficient of friction. The wear scar of a HSS pin for both temperatures is shown in Figure 2.7. The wear track for 20^{o}C was covered by agglomerated debris (Figure 2.7a) and the surface for 650^{o}C was partially covered by oxide strips and compacted debris (Figure 2.7b). Joos *et al*. (2007) suggested that the coefficient of friction for a disc temperature 650^{o}C is lower than 20^{o}C because the disc oxide layer acts as a solid lubricant.

The summary of modes and wear mechanism of HSS work rolls is shown in Table 2.3. In this review an attempt was made to understand the wear mechanism of a HSS work roll. Based on this summary, it can be concluded that abrasion is an important mechanism influencing the wear of HSS work rolls. All the examples that were chosen here are from the literature and the materials discussed are mainly HSS. Because of its wide usage, this study focused on the characteristics, mechanical properties, and abrasive contact of the oxide layer formed on HSS work rolls.

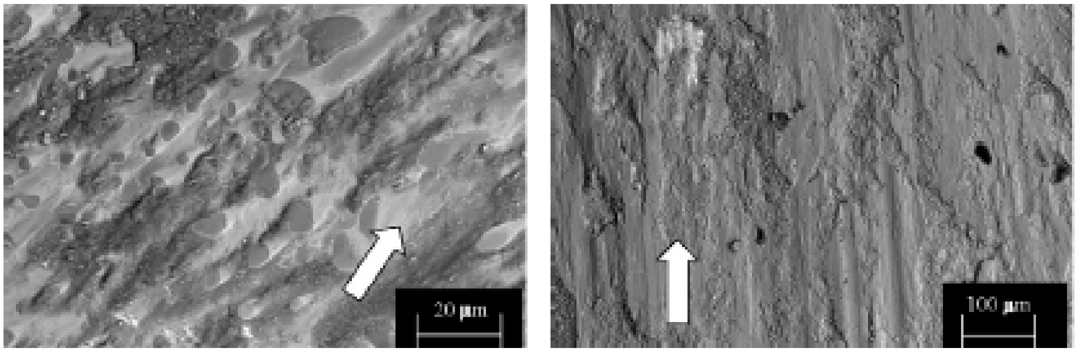

(a) (b)

Figure 2.7: Wear scar for HSS pin for disc temperature of 20^{o}C (a) and 650^{o}C (b) (Joos *et al*., 2007).

2.1.3 High speed steel (HSS) material of work roll

Work roll materials continuously evolve with the improvements of the existing material and the development of new materials. The work rolls for finishing stands of hot strip mills are crucial because they are responsible for strip reduction and strip quality. It has been reported that the development of early finishing stands work rolls evolved rapidly in the early 1980s (Boccalini and Sinatora, 2002). In the early development of work rolls the cast iron outer shells were used in all stands. This material has gradually been replaced by cast steels known as Adamite. In order to enhance performance in terms of hardenability and mechanical resistance, these alloys have been replaced again by high chromium iron rolls containing 2.5 to 3 %C and 14 to 18 %Cr. Currently, high speed steel rolls are the most popular material. Based on the preliminary results in Japan and United States (De Carvalho *et al*., 2002), the performance of high speed steel rolls is estimated to be around three times better than high chromium rolls.

High speed steel could be considered as a composite material that contains primary carbides, secondary carbides, and a matrix. According to Badisch and Mitterer (2003), the large primary carbides (1 to 10 μm in diameter) are mainly MC and M_6C-types which are harder than the matrix. Because the carbides are very hard, when they are dispersed in the martensitic matrix they can improve the wear resistance. The fine secondary carbides (< 100 nm in diameter) facilitate precipitation hardening of the matrix.

High speed steel has inherently high mechanical resistance at the working temperature and high wear resistance (Park *et al.,* 1999). The excellent characteristics of these steel are influenced by the high carbon content (1.5-2 wt%), the existence of alloying element such as V, Mo ,W, Nb and Cr and the significant presence of primary carbides. It has been reported in the literature that these carbides contribute to the mechanical strength, the load bearing capacity and the wear resistance, but they also decrease ductility and promote failures since they promote a favourable propagation path for mechanical and thermal fatigue cracks (Molinari *et al*., 2000).

2.1.4 Tests to simulate roll wear phenomena

The tests for roll wear have been simplified for laboratory based tests. As has been reported in the literature, several laboratory tests were conducted which represent real work rolls in industry. The results of the performance, behaviour, and conditions in these tests should reflect the real service life of actual rolls, but it is difficult to achieve. The roll is in contact with the hot strip for a short time and then quenched by cooling water. However the tests can provide qualitative information about the roll materials or the behaviour of the oxide layers. This test is frequently conducted when the surface of the roll makes contact with a counter surface under defined conditions (temperature, pressure, time, speed). In this situation, the contact might be sliding or rolling with or without abrasion, and one material can be tested in contact with identical, similar, or dissimilar materials. In most cases a measurement of the loss of sample weight per unit of surface area of the sample is carried out in a typical wear test.

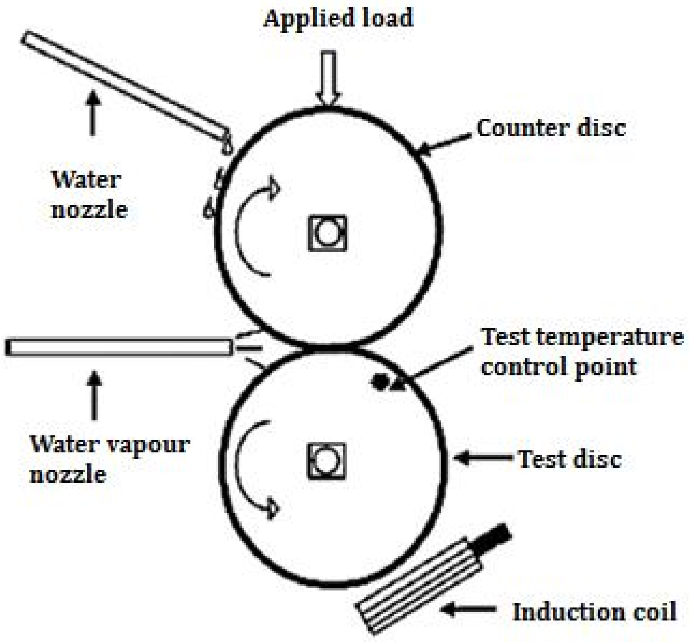

Figure 2.8: Schematic representation of two disc wear (Garza-Montes-de-Oca and Rainforth 2009).

A significant number of authors performed a two-disc wear test (Figure 2.8) to simulate roll wear at high temperatures because this type of apparatus enables three fundamental aspects in the investigation of roll wear to be separated, mainly load, slip, and temperature (Spuzic *et al*., 1994). As previously summarized in a review (Spuzic *et al.,* 1994), one advantage of this two-disc method is the ability to simulate cyclic wear involving long sliding distances. However, Spuzic *et al.* (1994)

reported two main disadvantages: (i) the stress state in the roll material is only a rough approximation to real conditions, and (ii) the ratio of elastic to plastic deformation of the counter body is much higher than in a real situation.

Matsuda *et al*. (1991) and Goto and Mase (1991) carried out wear experiments using a block-on-ring tester (Figure 2.9) as well as the two disc method (Figure 2.8). In other studies some authors identified the primary wear resistance of roll materials by using small, laboratory scale hot rolling mills. It has been reported that an experimental mill is able to give the closest approximation to actual industrial conditions, but unfortunately these tests are much more expensive than other tests.

Spuzic *et al.* (1994) indicated that the two-disc testing device and the scratch tester can be considered as two extremes in the experimental approach based on their capability and performance. Although the two-disc test has its own disadvantages, this test is a comprehensive method that allows focusing on simulating the real situation as closely as possible. Meanwhile, the scratch test enables particular wear mechanisms to be identified and wear factors to be isolated.

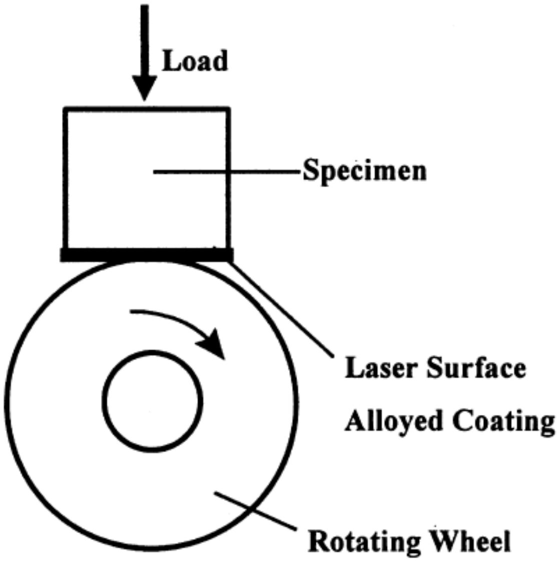

Figure 2.9: Schematic representation of block-on ring test (Jiang *et al*., 2000).

The purpose of this review is to provide some points of view on the reason why the modelling and experiments of scratch of an asperity against oxide layer was carried out to study the behaviour of oxide layer formed on high speed steel work rolls. Since the dominant mode of wear for work roll is abrasion, Berns *et al*. (1991) described the scratch test as one approach to study this mechanism because it can isolate one mechanism from others. In addition this test was considered to be a scientific method to assess abrasive wear. Moreover, the scratch tests allow abrasion to be studied without the super-imposition of other major wear mechanisms such as surface fatigue or adhesion (Spuzic *et al.,* 1994). In fact, modelling the scratch test means that the sliding wear may be studied, where many complex mechanisms such as abrasive wear, adhesive wear, delamination wear, and oxidational wear and so on may be involved.

2.2. Oxide layers formed on hot rolling work rolls surfaces

2.2.1 Composition of the oxide scale

Oxide scale on pure iron typical of oxide scale on strip has been studied well. Birks *et al.* (2006) found that oxide scales formed on the pure iron consist of three sub-layers mainly Wustite (FeO), Magnetite (Fe_3O_4) and Hematite (Fe_2O_3). According to their work, wustite is the inner sub-layer, magnetite is the middle layer, and hematite is the outer sub-layer. This finding also suggests the ratio of wustite : magnetite : hematite is around 95 : 4 : 1 for oxidation in air at a temperature range between 700-1250^{o}C. Many have confirmed these three sub-layers oxide structure but the ratio remains a subject for discussion. Vergne *et al*. (2006) determined the morphology of oxide layers that formed on a cast iron pin after pre-oxidation and contact with a warm low carbon steel (AISI 1018 steel) disc. This observation clearly explains the distinct sub-layers on both the pin and the disc (Figure 2.10).

However, published works give very little information about the oxide layer on high speed steel and no study has been done on the mechanical properties of the oxide layers formed on a HSS surface. Most of the reported studies concentrated on the morphologies and microstructures of these layers but not the mechanical properties and wear behaviour. Below are some reviews of the studies on the morphologies and microstructures of oxide layers formed on HSS surfaces. Colas *et al*. (1999) indicated that the oxide layer of work rolls probably consists of magnetite and hematite, an observation based on an X-ray diffraction analysis of the debris (Figure 2.11).

Molinari *et al*. (2000) found that the oxide scale of high speed steels (HSS) at 700°C consists of three layers and the SEM result for this research is shown in Figure 2.12.

1. a thin α-hematite (α-Fe_2O_3) outer layer
2. a thick and porous γ-hematite (γ-Fe_2O_3) intermediate layer
3. the inner M_3O_4M spinel (M = Fe, Cr, V) produced by internal oxidation.

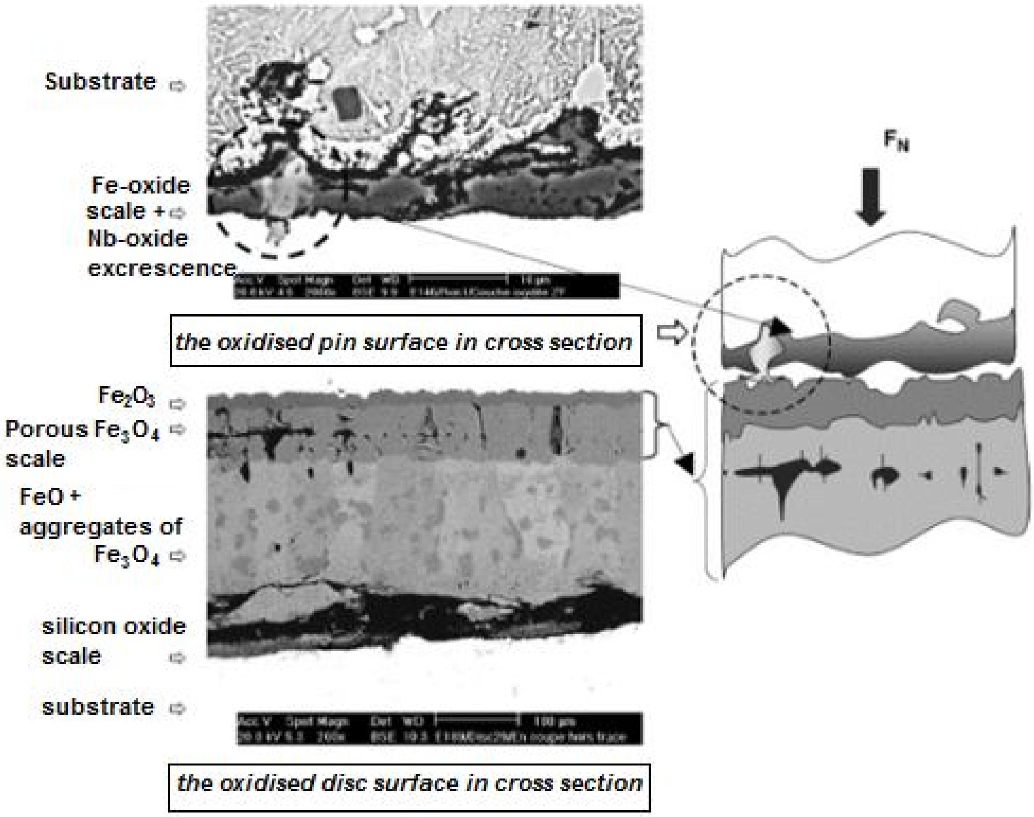

Figure 2.10: SEM observation of oxide layers on cast iron pin and low carbon steel disc (Vergne *et al*., 2006).

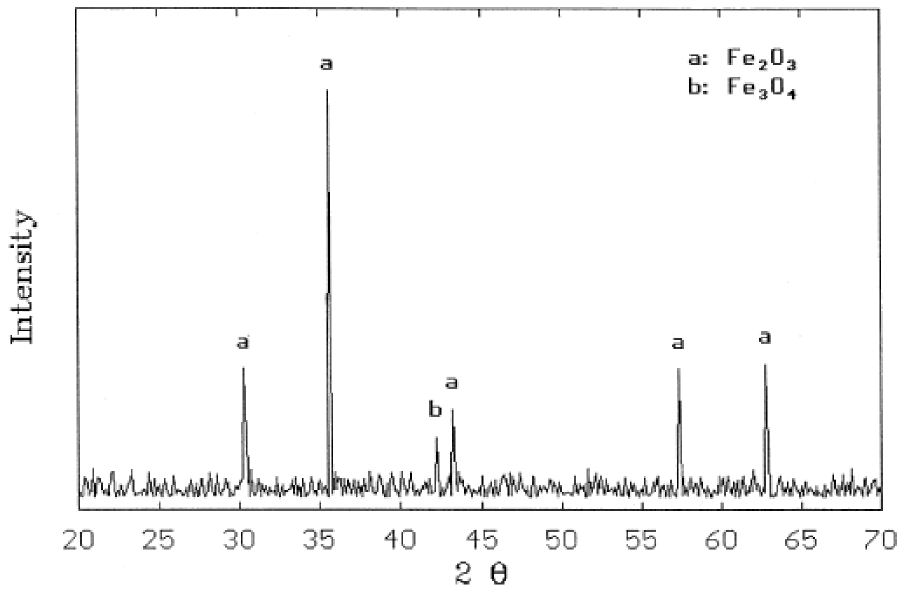

Figure 2.11: X–ray diffraction of the oxide layer taken from high speed steel work roll (Colas *et al*., 1999).

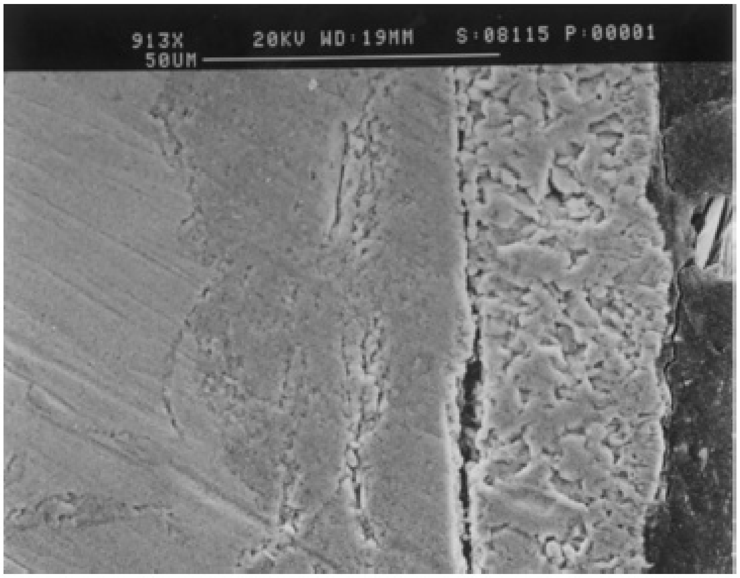

Figure 2.12: Oxide scale on high speed steels oxidised at 700^{o}C (Molinari *et al*., 2000).

Garza-Montes-de-Oca and Rainforth (2009) reported that there is a difference in the wear debris of a high speed steel (HSS) disc between a dry test and a wet test for a rolling and sliding disc on disc. They suggested hematite (Fe_2O_3) is the only iron oxide phase detected in the dry test while a mixture of spinel (M_3O_4 where M =

Fe and Cr) and hematite (Fe_2O_3) was found in the wet analysis. The work also described the presence of three oxides based on the examination of cross section of the worn surfaces of a dry test which showed surface islands comprising agglomerated oxide debris, oxide mechanically mixed with the metal surface, and fissures of oxide that penetrated from the surface into the material.

Zhu *et al*. (2010) reported that the main phases of oxide scale on high speed steel are hematite (Fe_2O_3) and magnetite (Fe_3O_4). In this study they determined the thickness of the oxide layers by SEM, FIB/TEM, and found the oxide layer to be less than 6 µm thick and only 500-600 nm after oxidation at $T(^oC) = 700^oC$ and $T(^oC) = 550^oC$ respectively for 30 min in dry air.

Based on previous literature, knowledge of the various phases of these oxide layers will help in studying the complex mechanical properties of the oxide layers.

2.2.2 Role of oxide layer in the work roll– strip interface friction and wear

A number of papers have reported the tribological behaviour of the oxide layer on roll surfaces, but there are conflicting suggestions on the exact role the oxide layers play, either against wear or vice versa. Kato *et al*. (1992) reported that the formation of a dark oxide layer on the surface of high chromium iron work rolls played an important role protecting the roll against wear, while Erickson and Hogmark (1993) pointed out that the wear of work rolls corresponds to adhesion and the strength of the oxide scales on the surface. Spuzic *et al*. (1994) identified the role of the oxide layer on a cast steel work roll based on the type of oxide scale, and reported that hematite (Fe_2O_3) and magnetite (Fe_3O_4) can lead to increased abrasive wear while the progressive formation of wustite (FeO) reduces friction and wear by acting as lubricant. Rodenburgh and Rainforth (2007) proposed that the exact role of the oxide depends on the thickness of oxide layer relative to the size of the carbides within the substrate.

Zhu *et al*. (2010), Molinari *et al*. (2000) and Colas *et al*. (1999) clarified the role of oxide layers based on their characteristics. Compact, ductile, and adherent oxide layers help to reduce the coefficient of friction between the roll and the hot strip, which helps to reduce wear on the rolls. As a result, the quality of the rolled product would be improved. In addition, this kind of layer also reduces the transfer of heat from the hot strip to the roll surface. On the other hand, a hard and brittle oxide scale may increase the wear of rolls due to a tendency for abrasive materials to develop between the rolls and the strip. The existence of these abrasive materials may also contribute to higher coefficients of friction, and a higher rolling force and consumption of power.

There are also controversial reports related to the coefficient of friction of oxides layers on high speed steels at different test temperatures. Joos *et al*. (2007) argued that the coefficient of friction decreases with disc temperatures, a trend which they claimed is due to the matrix and carbides at 20°C of HSS pins not being oxidised and by considering the carbides to be large asperities while the rubbing surface consisted of sintered oxides at 650°C and sintered and glazed oxides at 950°C respectively (Figure 2.13). In this configuration the pin represents the tool and the disc represents the rolled material. Similar observations were reported by Earles and Hayler (1972) and Stott (1998) where the formation of oxides on the surface of metals subjected to sliding can generally be expected to reduce the coefficient of friction. They attributed this phenomenon to the oxide acting as solid lubricant, and the interfacial strength between the oxide and another oxide being lower than between a metal and metal because the adhesive forces are lower.

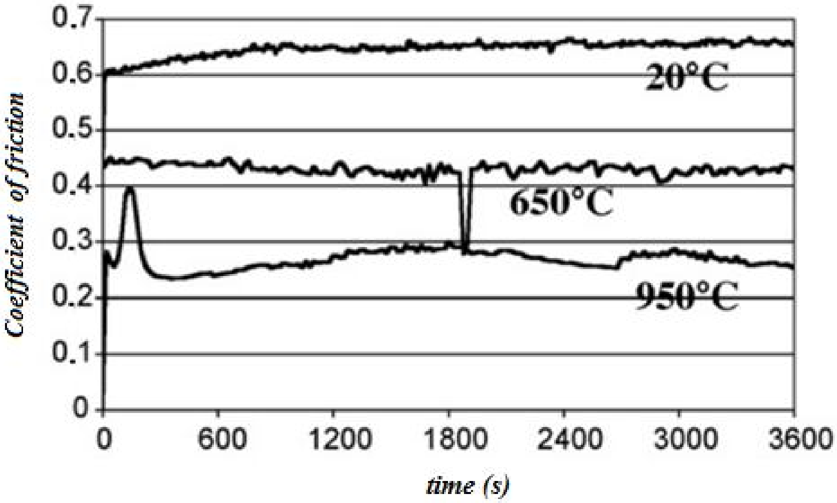

Figure 2.13: The coefficient of friction curves of HSS by Joos *et al*. (2007).

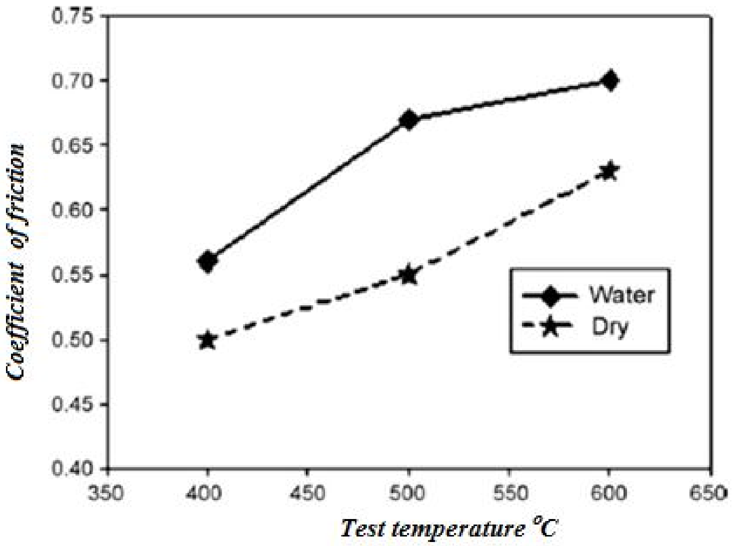

Figure 2.14: The coefficient of friction of HSS roll for dry and wet conditions (Garza-Montes-de-Oca and Rainforth, 2009).

Garza-Montes-de-Oca and Rainforth (2009) found that the coefficient of friction of a HSS roll increases in an approximately linear function with temperatures in both dry and wet conditions (Figure 2.14). In this case the wear of the high speed steel was determined using a high temperature Cameron-Plint multi-purpose wear rig in a rolling disc on disc configuration. They suggested that the formation of oxide on the surface increases with the temperature, and that greater friction is caused by the components ploughing together. This explanation is also related to the coefficient of friction where friction consists of adhesion, $F_{adhesion}$, and ploughing, $F_{ploughing}$. The coefficient of friction increases with $F_{ploughing}$.

2.2.3 Development of an oxide layer on high speed steels

Formation of oxide layer on work rolls during hot rolling occurs due to thermal cycling. Heat transfers for short periods (10^{-2}–10^{-3}s) from the hot strip to the rolled surface raise the surface temperature of the rolls up to 700°C and cooled to around 50°C in an extremely humid atmosphere, causes a build-up of oxide layer (Kato *et al*., 1992).

There are a numbers of reports on the initial formation and growth of oxide scales on the carbides and matrix in HSS materials, although some conflicting opinions seem to exist in literature. Molinari *et al*. (2000) found that oxidation initially nucleates at the matrix-carbide, propagates to the matrix and eventually covers the whole surface, leading to an uneven oxide layer. The Cr carbides have been reported to have a negative effect on oxidation.

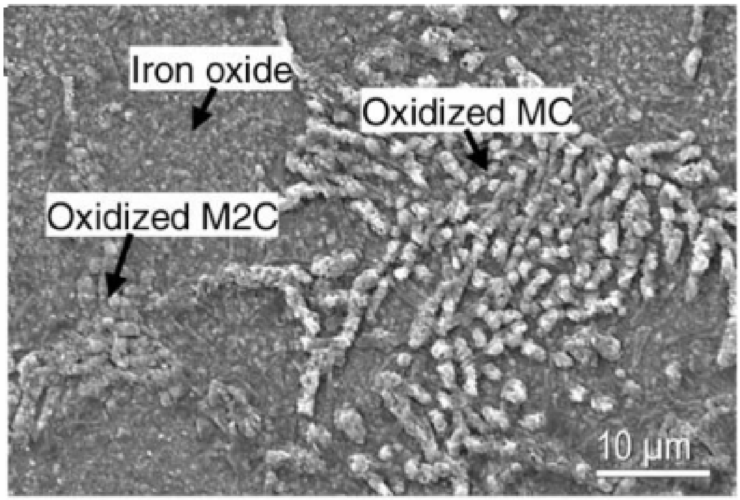

Figure 2.15: Surface morphologies of the samples after oxidation at 600°C (Zhu *et al.,* 2010).

On the other hand, Kim *et al*. (2003) argued that all carbides oxidise faster than the matrix and oxides grow thicker over the oxidised surface of the matrix. To specifically clarify the relationship between oxidation and types of carbides, Molinari *et al.* (2005) carried out experiments to show that different types of carbides have different oxidation. They found that V-rich MC carbides and the matrix oxidised faster, Mo-rich M_2C carbides oxidise at a medium rate, and Cr-rich M_7C_3 carbides oxidise quite slowly. Zhu *et al*. (2010) comprehensively investigated the oxidation and formation of oxide layers on carbides and matrix in HSS material using in-situ techniques (Figure 2.15). The result confirmed the same trend as Molinari *et al.* (2005) in terms of the magnitude of carbide oxidization for different types of carbides.

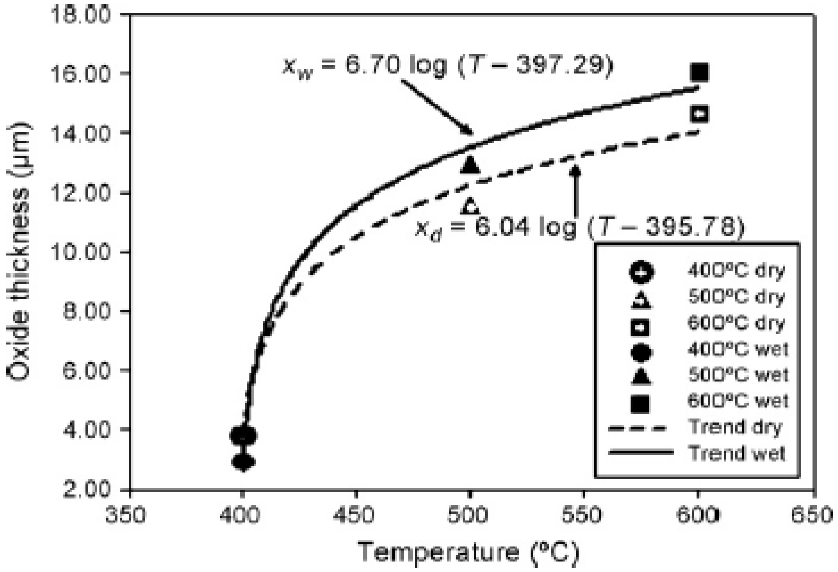

Figure 2.16: Oxide thickness as a function of test temperature (Garza-Montes-de-Oca and Rainforth 2009).

Several researches on the oxidation kinetics of oxide layers on high speed steels (HSS) have been conducted. For instance Zhu *et al*. (2010) reported that oxidations begin at the carbides/ matrix interface and then spread rapidly over the carbides and continue to grow over the whole surface. Molinari *et al*. (2000) summarised three important steps in the growth of the oxide layers. The first step is the formation of thin outer sub-layer α-hematite. The growth of this sub-layer is attributed to the out-diffusion of oxygen ions. The second step is the development of an internal M_3O_4 spinel in the inner sub-layer which is attributed to in-diffusion of oxygen ions. In the final step γ-hematite is created at the interface between the α-hematite and M_3O_4 spinel.

Garza-Montes-de-Oca *et al. (*2011) reported that the level of oxidation of the surface increased with the disc temperature. This situation is explained in Figure 2.16 where the oxide thickness increases with temperature in algorithmic relationship; with the thickness of oxide in the wet tests being marginally greater than in dry test.

2.2.4 Porosity of oxide layer

For development of oxide layer on high speed steel the layer formed consists of porous structures, indicating the growth of incompact layer on the substrate. It has been reported by Molinari *et al*. (2000) that a thick and porous γ-hematite (γ-Fe_2O_3) intermediate oxide layer exists on high speed steels (HSS), but the porosity value of the oxide layer on high speed steel remains unexplored. In a different investigation, Higginson *et al*. (2002) identified the scale porosity of steel alloy substrates. Their result describes the porosity changes of oxide scales on alloy substrates with temperature. These findings identified two types alloys with a different composition when the porosity of the scale was reduced from 10.06 to 1.35% and 7.02 to 6.49% respectively by increasing the temperature. In contrast, the porosity of the scale of another alloy increased from 20.71 to 29.38% due to higher temperature.

The porosity of the oxide layer is affected quite significantly by the cooling rate. Echsler *et al*. (2003) suggested that rapid cooling rate leads to larger pores and cracks. This explains the effect of the cooling rate where rapid rates might initiate cracks in the entire oxide while the cracks that formed after slow cooling tend to occur near the substrate interface.

2.2.5 Mechanical properties of the oxide layer

Knowledge of the mechanical properties is useful for the design engineer to ensure that the equipment can maintain its serviceability for a certain period of time. Data from bulk materials are typically used instead of the thin layers. As has been reported in several papers, the properties of bulk material are different from a thin layer because they behave differently (Nicholls and Hall, 1994). To date, there are only a limited number of papers that studied the mechanical properties of a thin oxide layer.

Xia *et al.* (2006) investigated the mechanical properties of an oxide layer formed by thermal oxidation on γ-TiAl based alloy using nanoindentation and nano-scratch tests. The nanoindentation tests with a maximum load of 20 mN (Figure 2.17) were carried out on the top TiO_2 layer, the inner α-Al_2O_3-rich sub-layer, the diffusion zone, and the substrate. It was found there was a variation of mechanical properties across the oxide layer which may be attributed to the different structures in the sub-layers. Hosemann *et al.* (2008) investigated the mechanical properties of the oxide layers that formed on ferritic/martensitic steels using nanoindentation tests. The elastic modulus and hardness of the oxide layers on the surface of the sample were found to be lower than in its dense bulk form. The lower values may be attributed to the higher porosity of the oxide layer than in its dense form but they did not quantify the porosity. Based on the SEM image of the cross sections of the layer, Hosemann *et al.* (2008) confirmed that the inner oxide sub-layer has a lower elastic modulus and hardness which can be explained by the inner sub-layer being more porous than the outer sub-layer.

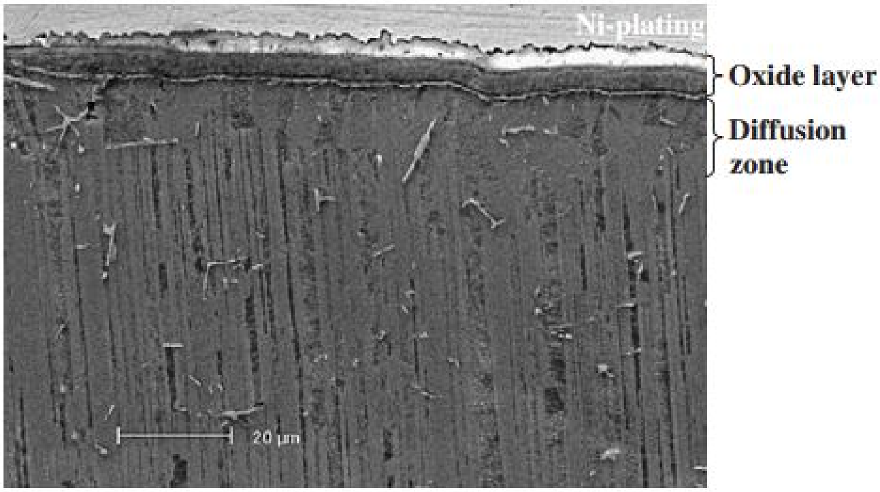

Figure 2.17: A typical microstructure of the thermal oxidation treated titanium aluminide. The surface layers consist of TiO_2 and α-Al_2O_3 (Xia *et al.*, 2006).

Although the oxide layer plays a significant role in the tribological performance of a work roll in hot rolling, the published works give very little information on the mechanical properties of oxide layers formed on HSS surface. Nicholls and Hall (1994) determined the hardness and elastic modulus of bulk oxides Al_2O_3 and Cr_2O_3 and compared them with other oxides such as FeO, Fe_2O_3 and Fe_3O_4. As their techniques can only access the oxide layer from the free surface, the depth-dependent mechanical properties of the oxide layer remains unexplored. One objective of this thesis was to study the mechanical properties of various oxide layers on a HSS work roll that lead to work roll wear. The mechanical properties of the oxide layers contribute to an understanding of the work roll and wear/removal process of oxide layer during hot rolling operations.

2.2.6 Behaviour of oxide layers in the rolling process

An explanation of the behaviour of oxide layers has rarely been reported because it is difficult to make direct observations in the laboratory and it is even more difficult under industrial working conditions. In hot strip mills most of the research focused on modelling the behaviour of the oxide layer on the strip rather than on the work roll. Tang (2006), Krzyzanowski and Beynon (2006), Krzyzanowski and Rainforth (2010), did a considerable amount of research on modelling the behaviour of the oxide layer on steel strip. Years of research in this area has enabled finite element (FE) models to simulate a range of events that affect hot rolled products. Hence, in this thesis a range of experimental techniques were developed to understand the mechanical properties, microstructures, and behaviour of oxide scales on a work roll. The finite element analysis of the indentation and scratch process of the oxide layer complements the experimental results.

2.2.7 Failure of oxide scale: brittle and ductile

Some conflicting opinions still exist in literature regarding the failure of the oxide layer. This is due to the difficulty of differentiating the behaviour of oxide scale according to their characteristics of failure. By studying the oxidation and the behaviour of the scale grown in ultra-low carbon steel during deformation, Suarez *et al*. (2009) concluded that thin layers exhibit plastic behaviour when deformed at temperatures above 900^{o}C and brittle behaviour at temperatures below 700^{o}C; mixed behaviour is observed between this temperature range, as the scale was found to resist limited amounts of deformation (Figure 2.18).

A similar point was made by Suarez *et al*. (2011) who studied the deformation of the oxide layer grown in ultra-low carbon steel by means of electron backscattered diffraction (EBSD) analyses. They found that the oxide layer could resist deformation without breaking when the specimens were deformed at or above 950°C, but the integrity of the layer was compromised when the material was deformed below 800°C. In EBSD analyses of the specimens deformed at 650°C, Suarez *et al*. (2011) found that the oxide layer exhibited brittle behaviour and penetrated into the steel substrate.

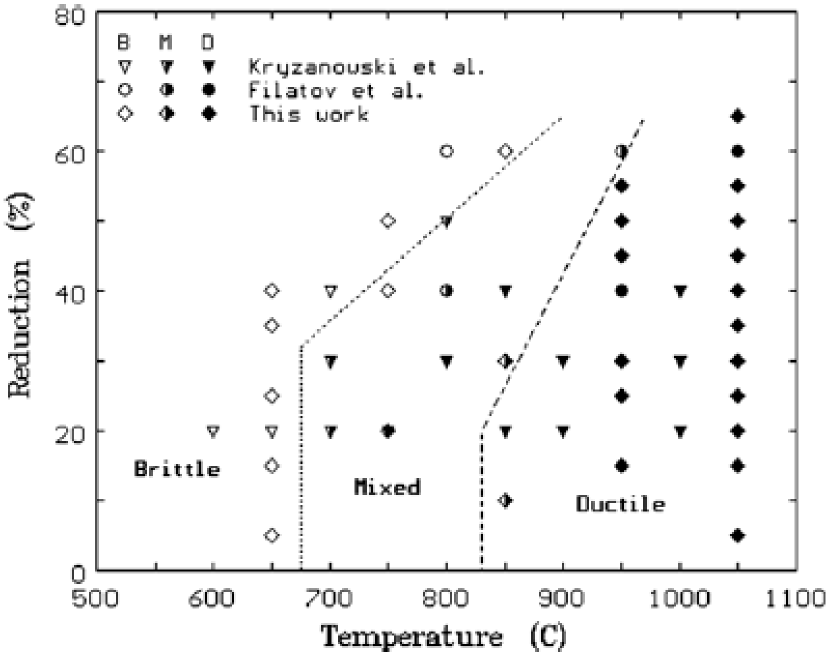

Figure 2.18: The behaviour of the oxide crust by Suarez *et al*. (2009).

The above conclusions made by Suarez *et al*. (2011) were based on the wustite characteristics grown in ultra-low carbon steel. This steel was covered entirely by wustite for a period of time at 1050°C in an experimental chamber. Wustite exhibits high ductility when deformed in plane strain compression at temperatures above 950°C but it becomes fragile and penetrates (brittle characteristics) into the steel substrate when deformed below 700°C. Figures 2.19 to 2.21 show the strong dependence on temperature. It can be seen in Figure 2.19 that oxide layer can be deformed to very high extend at 1050°C, but the layer can only sustain small amounts of deformation when the compression tests were conducted at 650°C (Figure 2.21). Figure 2.20 can be classified as in between brittle and ductile behaviour since the scale sustained a limited amount of deformation before cracking at 850°C. However, the characteristics of the oxide layer based only on optical microscopy observations can be argued due to the inconsistent behaviour. For example, at the tested temperatures of 1050°C (Figure 2.19c), the oxide layers were reported as ductile due to the influence of temperature, but from the image of Figure 2.19c, the layer seems to behave like brittle material at 23% reduction because cracking occurred on this layer. At 65% reduction (Figure 2.19d) the oxide layer changed back to ductile. Based on these results the behaviour of the oxide scale remains questionable and should be explored.

Meanwhile, Krzyzanowski and Rainforth (2010) reported that the oxides grown in low carbon steel can show brittle failure at temperatures below 800°C and signs of ductile failure at higher temperatures. In addition, at high strain rates this failure can become brittle in spite of high temperatures.

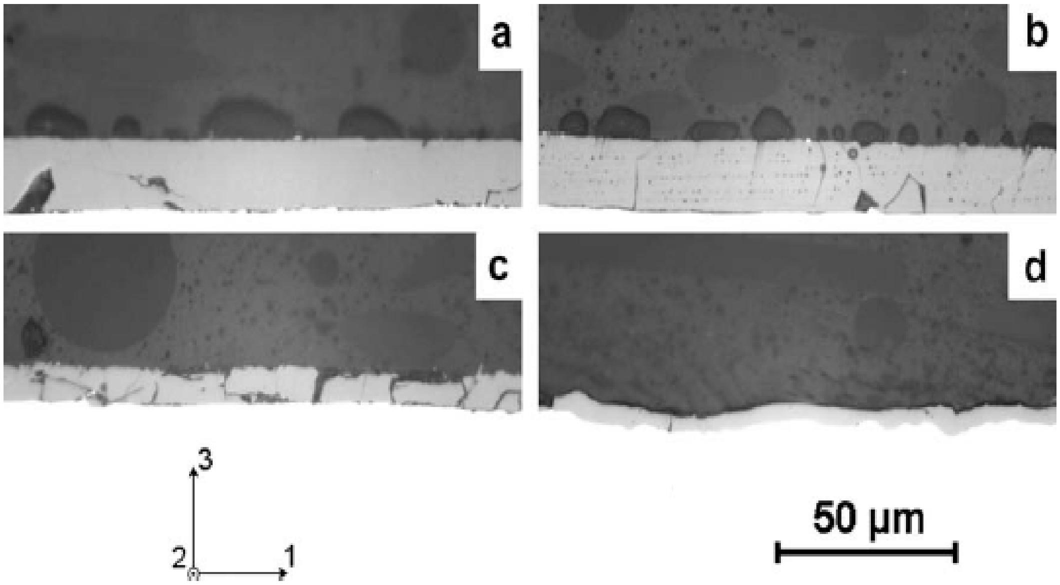

Figure 2.19 The images of crust at tested temperature 1050°C and compression direction (3) is indicated. The types of samples are: (a) undeformed sample; (b) samples tested to reduction of height 4%, (c) 23% and (d) 65% (Suarez *et al*., 2011).

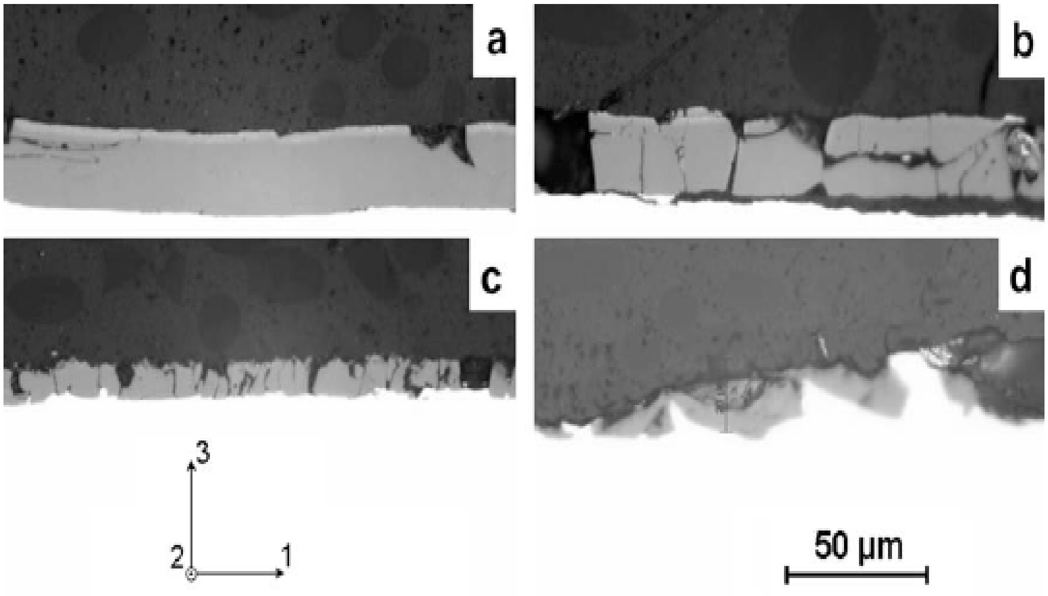

Figure 2.20 The images of crust at tested temperature 850°C and compression direction (3) is indicated. The types of samples are: (a) undeformed sample; (b) samples tested to reduction of height 7%, (c) 27% and (d) 63% (Suarez *et al*., 2011).

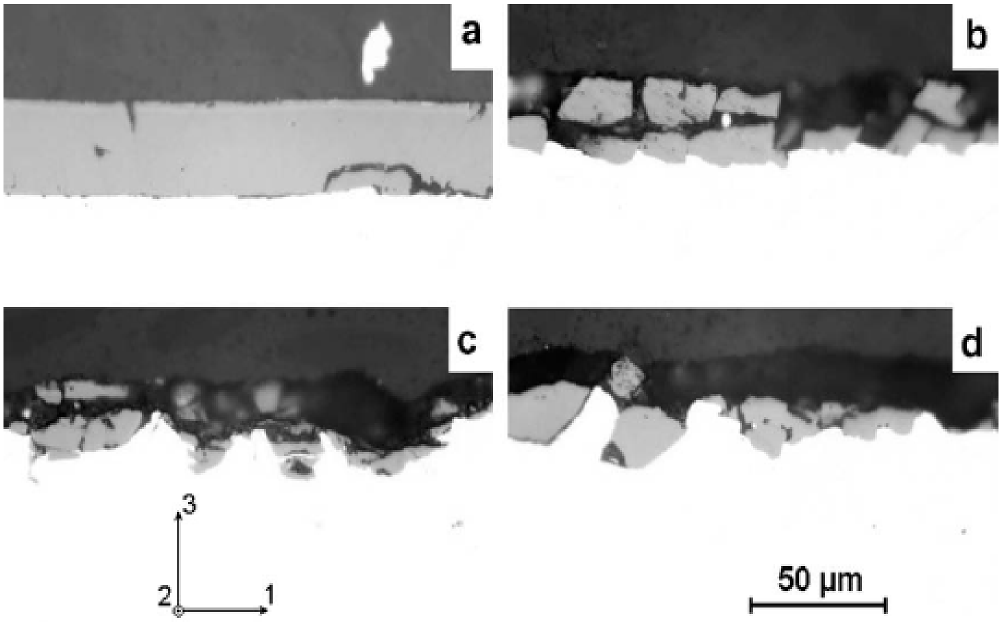

Figure 2.21 The images of crust at tested temperature 650°C and compression direction (3) is indicated. The types of samples are: (a) undeformed sample; (b) samples tested to reduction of height 23%, (c) 25% and (d) 35% (Suarez *et al*., 2011).

In another study Garza-Montes-de-Oca *et al.* (2011) investigated the behaviour of an oxide scale grown on the surface of high-speed steel (HSS) subjected to thermal cycling. In this finding Garza-Montes-de-Oca *et al.* (2011) reported the related failure mechanism of the HSS oxide for the testing temperatures of 615^{o}C or 550^{o}C. Under these conditions, spallation of the hematite layer (Figure 2.22) was common and must be considered as an important mechanism that controls friction and the wear properties of work rolls in hot strip mills.

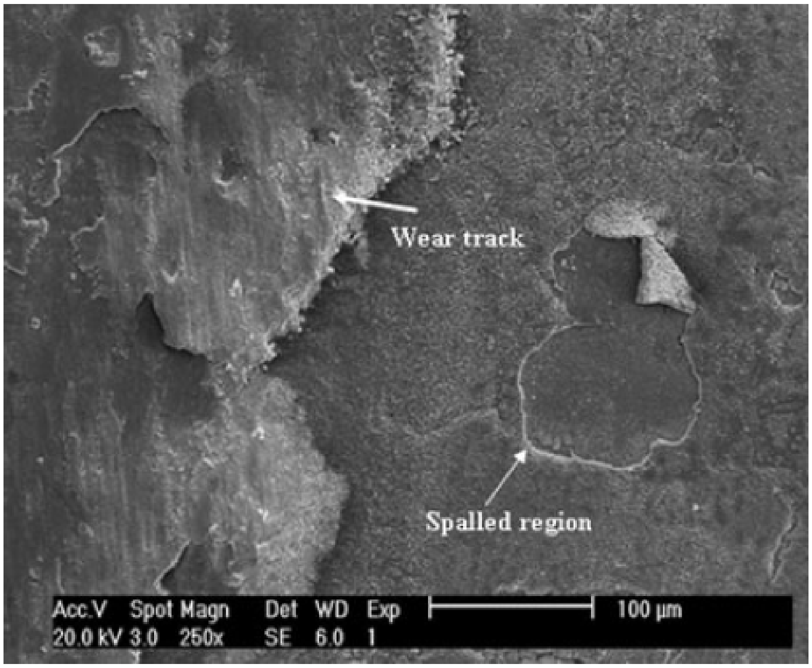

Figure 2.22: Spallation of hematite layer (Garza-Montes-de-Oca *et al.*, 2011).

Garza-Montes-de-Oca *et al.* (2011) detected oxide spallation at the outer hematite layer with the formation of lumps that detached this phase from the inner Fe_3O_4 layer. This mechanism was described as buckling. Buckling is associated with the development of compressive thermal stresses acting on fairly plastic oxide layer during the cooling stage of the steel that favoured the preferential spallation of hematite. In contrast, a different failure mechanism was observed in the magnetite layer, as indicated by the formation of cracks on the surface in this phase. This mechanism is wedging, which is typical in brittle oxide layers that exhibit a strong adhesion to substrate subjected to tensile stresses. It is highly possible that tensile stresses were imposed to this layer as result of the rapid heating of the test specimen given its small size in addition to the growth stresses present as result of the formation of this phase.

Based on Garza-Montes-de-Oca *et al.* (2011) findings, it seems that there are two failure modes of oxide layer on HSS which depend on the types of oxide layers. A clear evidence of the distinctive failure mode of the outer and inner oxide is revealed based on the typical failure zones in the samples. The existence of the compressive stress and plasticity of the outer hematite layer is presented in Figure 2.23a where forms of lumps remained adhered to the sample. According to this author, it is highly possible that the type of this condition are achieved by two mechanisms: (1) compressive thermal stresses imposed to the steel samples during the cooling stage (2) ductility of hematite could have been increased by the presence of water vapour in the atmosphere inside the chamber. In contrast, a different failure mechanism was observed in the magnetite layer, expressed by the formation of surface cracks with brittle characteristics (Figure 2.23b).

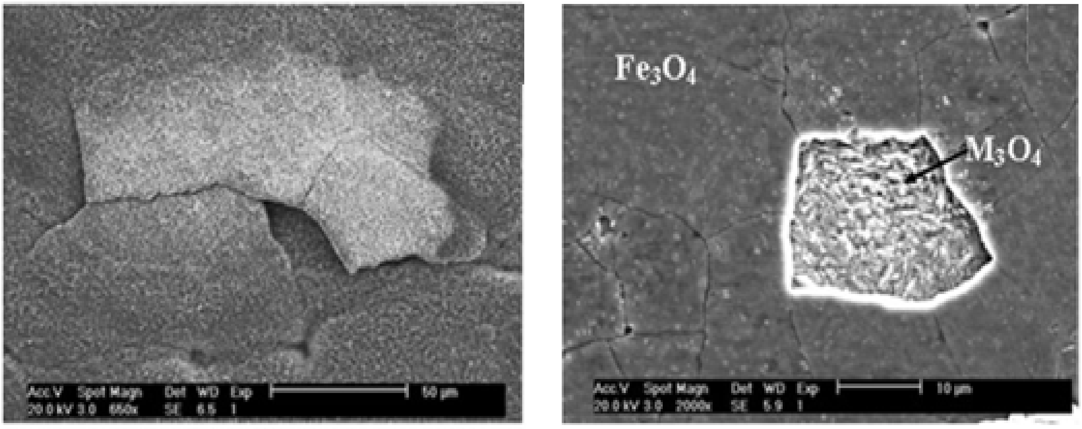

(a) (b)

Figure 2.23: Typical failure mode observed for the (a) Fe_2O_3 layer (b) Fe_3O_4 (Garza-Montes-de-Oca *et al.*, 2011).

In this review an attempt has been made to understand the behaviour of the oxide layer from previous studies. There are numerous reports that explained the behaviour of the oxide layer in low carbon steel but there is still a limited number on the oxide layers formed on high speed steel (HSS). In fact, there is no clear consensus on whether the behaviour and characteristics of the oxide layer are either brittle or ductile. Classifying the oxide layer using the images of cracking as an indicator to categorize them as either ductile or brittle is a subjective benchmark.

The purposes of this review is to provide some basis for why both the ductile and brittle models were chosen to investigate the scratch behaviour of the oxide layer on HSS work rolls in this thesis. A summary of the characteristics of the oxide layer is given in Table 2.4.

Table 2.4: A summary of oxide layers behaviours.

Oxide scale on the following substrate	***Type of behaviour***	***Type of Test***
Ultra low carbon steel (Suarez *et al*., 2009)	+a plastic behaviour: T > 900^{o}C +a brittle behaviour; T< 700^{o}C; +a mixed behaviour; 700^{o}C < T < 900^{o}C	Deformation test by a chamber
Ultra low carbon steel (Suarez *et al*., 2011)	+ a brittle behaviour; at 650^{o}C + a ductile behaviour at T > 950^{o}C	Deformation test by a chamber
Low carbon steel (Krzyzanowski and Rainforth, 2010)	+brittle failure; T < 800^{o}C +ductile failure; at higher temperature (T)	
High speed steel (Garza-Montes-de-Oca and Rainforth *et al.,* 2011)	+ Failure mechanism is buckling for outer hematite layer (a fairly plastic oxide scale) + Failure mechanism is wedging for inner magnetite layer (brittle oxide layer)	Thermal cycling test. The oxide layer was subjected to the action of thermal stresses generated during either cooling or heating stages.

2.2.8 Wear of high speed steel (HSS) work roll

Some reports on the wear rate of a high speed steel of work roll define the wear rate by the following equation:

$$K = \frac{V}{SL} \qquad (2.1)$$

where K is the specific wear rate (or dimensional wear coefficient) in units of mm^3/Nm, V is the volume of material removed in mm^3, S the applied load in N and L the sliding distance in m. The calculation of the wear rate of a work roll can be used to define its failure, and since the oxide layer formed on the high speed steel work roll, it is clear that the oxide contributes to the wear rate based on the formation of debris and the wear scar on the surfaces.

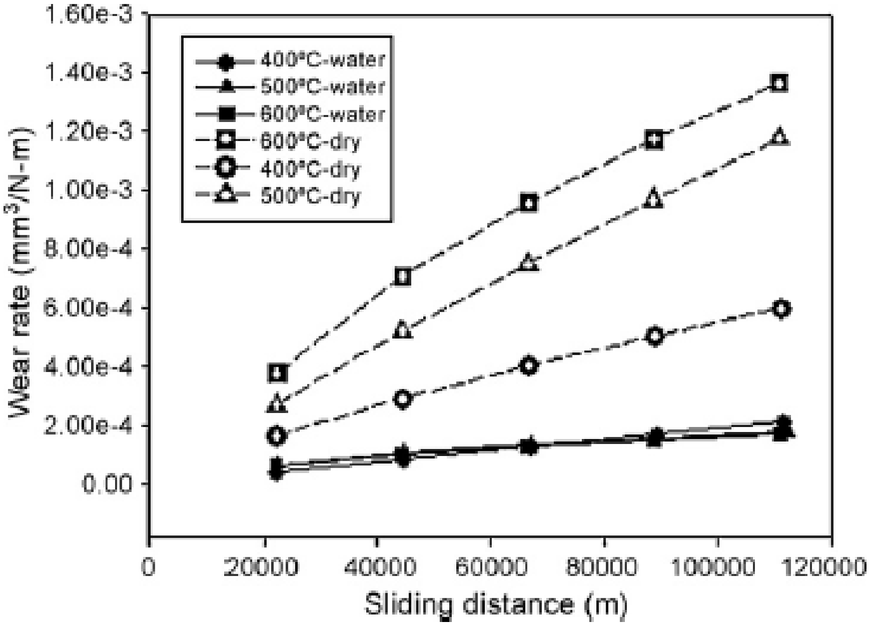

Figure 2.24: Wear coefficient calculated for all temperatures and both experimental condition (Garza-Montes-de-Oca and Rainforth, 2009).

Garza-Montes-de-Oca and Rainforth (2009) studied the wear rate of high speed steel using a high temperature multi-purpose rig in a rolling/sliding disc on disc (Figure 2.24) experiment. This work describes the wear coefficient K as a function of the sliding distance for both wet and dry conditions at temperatures from 400-600°C. The highest wear rates occurred in tests in dry condition at 600°C, which indicated that wear rates in dry tests are significantly affected by temperatures while those in wet tests are not. Pellizzari *et al.* (2009) also concluded that wear is not the simple summation of individual mechanisms, but rather a "rate process" where the total wear rate may be defined as a combination of converting irons, and the mechanism of abrasion and adhesion.

2.2.9 The role of carbide particles

Most of recent work on the oxidational wear has been conducted using alloys and mainly low alloy steel. More complex microstructures of a metallic matrix with carbide particles have not been investigated very much, and the role of the particles in the oxidational wear mechanism has not been discussed comprehensively.

Vardavoulias (1994) and Rodenburg and Rainforth (2007) reported that carbide particles existing in the matrix play a significant role in the wear behaviour. According to Vardavoulias (1994), the HSS matrix protection depends not only on the thickness of the oxide, but also on the mean particle size (*d*). When the particles are entirely embedded in the oxide layer, it can be removed together with the oxide when the oxide layer breaks up as deformed debris. As a result, the particles cannot protect the metallic matrix and thus positively influence the wear behaviour (Figure 2.25a). Meanwhile, when the particles are several times larger than the thickness of the oxide layer, a small amount of particles may be removed with the oxide, while most of them remain in the substrate (Figure 2.25b). Accordingly, the counterbody will slide on this particle and may contribute to wear.

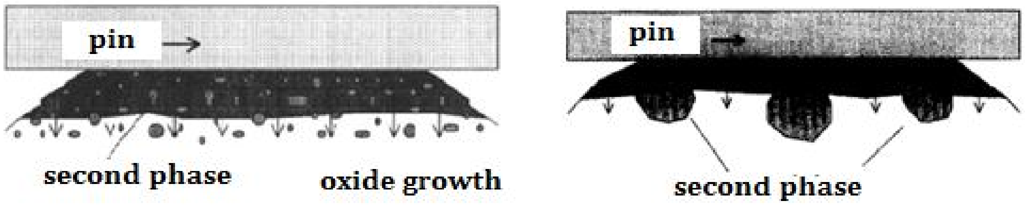

(a) (b)

Figure 2.25: The possibility of particle position (a) in the oxide layer (b) in both oxide layer and substrate (Vardavoulias, 1994).

Vardavoulias (1994) provided an explanation for most experimental results, but this theory is qualitative and is not supported with any numerical foundation to explain the exact behaviour of the particles. Therefore, Chapter 7 will explain the behaviour of the carbide particles using the finite element method in order to investigate the role of carbides in the oxidation wear mechanism that contributes to wear of the work roll. According to the author’s knowledge, none of studies to date have computationally investigated the behaviour of the carbide particles of high speed-steel-based material.

2.3 Modelling the oxide layer

There is limited information from existing literatures regarding the modelling of oxide scale formed on the work rolls. Krzyzanowski and Rainforth (2010) conducted a comprehensive study on the oxide scale formed on the strip. In this study a continuous oxide layer was introduced onto the top and bottom surfaces of the strip (Figure 2.26). The results of this modelling showed that after a rolling pass the oxide scale had deformed, fragmentized, and partly spalled from the surface of the metal.

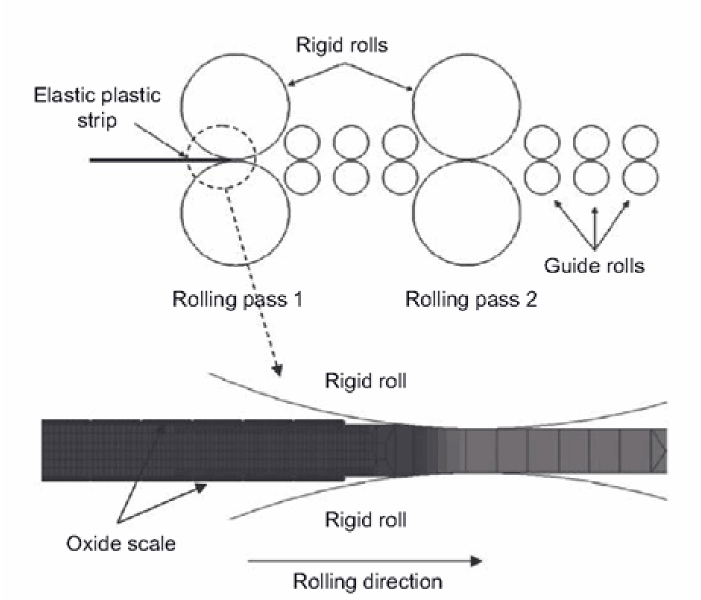

Figure 2.26: Schematic representation of a multi-pass hot rolling model by Krzyzanowski and Rainforth (2010).

According to Krzyzanowski and Rainforth (2010), the morphology of the oxide layer is complicated because it consists of different sub-layers of oxide, voids, roughness at the interfaces, and a proportion of each layer is at different temperatures, oxidation times and has a different composition of the steel. The model of oxide scale on strip steel by Krzyzanowski and Rainforth (2010) consisted of three sub-layers, each having different mechanical properties (Figure 2.27).

However, Krzyzanowski and Rainforth (2010) did not apply an oxide layer on the work roll in their model because they focused only on the strip. A small part of the studies contributed to the scale on the work roll. They suggested that the scale on the work roll acts as an additional thermal barrier between the roll and the strip, affecting the failure of the strip scale within the roll gap (Figure 2.28). Krzyzanowski and Rainforth (2010) also investigated the temperature history at different points across the strip/work roll interface. As seen in Figure 2.29, the temperature of the oxide scale on the work roll at point 2 was around 550-600°C and at point 1 around 300°C.

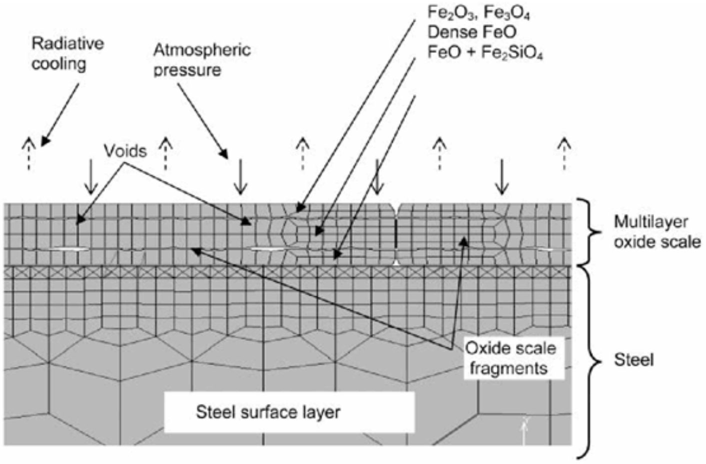

Figure 2.27: Schematic representation of the multi-layer oxide scale model (Krzyzanowski and Rainforth, 2010).

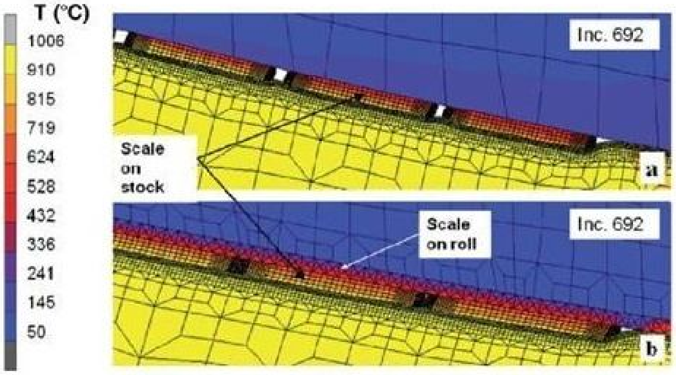

Figure 2.28: Differences in crack opening within the roll gap predicted for (a) not oxidised (b) oxidised roll (Krzyzanowski and Rainforth, 2010).

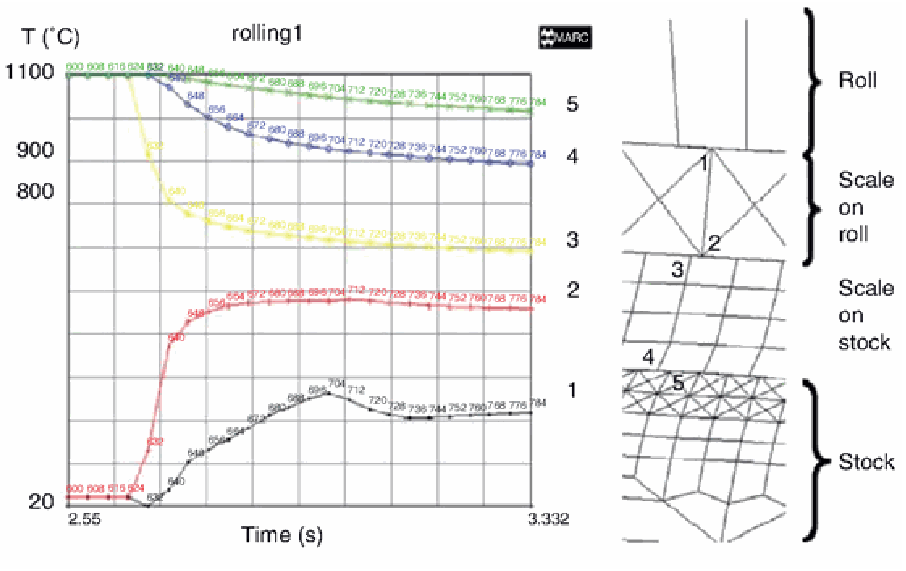

Figure 2.29: Temperature history predicted in different points (Krzyzanowski and Rainforth, 2010).

In summary, the information on the modelling approach of oxide scales on a work roll from literature is too limited. Therefore, the main aim of the modelling was to develop a finite element model with data that reflects properties that are more specific for a particular oxide scale under investigation. Many models describing the properties and behaviour of oxide scale on stock (strip) are available (Tang, 2006; Krzyzanowski and Rainforth, 2010) but only a limited number of researches concentrate on the oxide layer on the work roll. In fact, the research that studied the modelling of oxide scale on strip considered the work roll as having no oxide layer for simplification. Hence, a range of techniques have been developed, each providing a partial insight.

2.3.1 Thickness of the oxide layer

It has been shown that there are differences in the thickness and structures of oxide scales between a carbon steel strip and a high speed steel (HSS) work roll. In fact, according to Krzyzanowski and Beynon (2006) low carbon steel strip itself has been found to have different thicknesses and microstructures due to different crack width, crack spacing, and the extent of fresh steel flowing through the gaps during hot rolling, as a function of temperature and rolling reduction.

In hot strip investigations, Krzyzanowski and Beynon (2006) and Krzyzanowski and Rainforth (2010) assumed the oxide layer as made up of scale fragments that have a thickness of around 10-100 µm. The oxide layers were modelled using a meso-model instead of a macro-model because the layer was very thin. This approach reduced the model of the oxide layer to a small segment at the stock roll interfaces in order to link 'macro' and 'meso-scales' (Figure 2.30).

Krzyzanowski and Rainforth (2010) also proposed a combined discrete/finite element approach to overcome the prediction of physical phenomena during high temperature metal processing. This combined method has the potential to simulate multi-scale and multi-phase phenomena that led to precise modelling. The latest discrete element method 3D model of the scale proposed by Krzyzanowski and Rainforth (2010) is shown in Figure 2.31. This latest approach can account for a generation of abrasive particles and delamination of the oxide layer. The difficulty is to accurately determine the bonding strength of the particles.

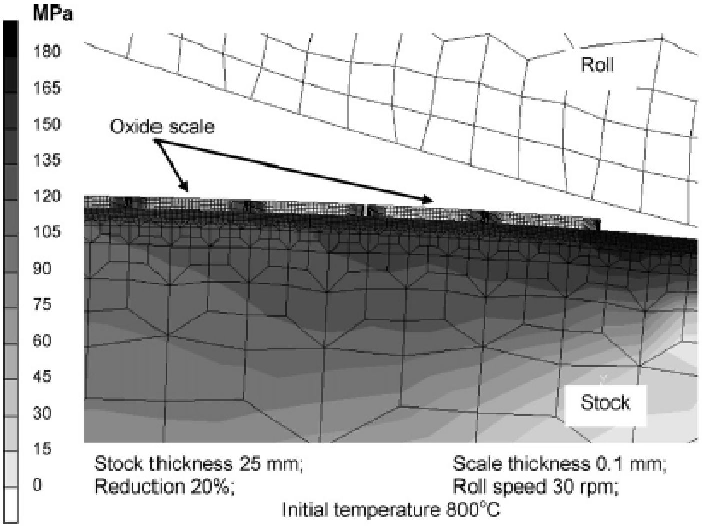

Figure 2.30: Hot strip rolling model by Krzyzanowski and Beynon (2006).

Torres and Colas (2000) investigated the growth of the oxide layer on a carbon steel strip with temperatures and found that the thickness at 1150°C was less than 7 µm. The oxide layer trend is shown in Figure 2.32 and the oxide consists of three layers, namely hematite, magnetite, and wustite.

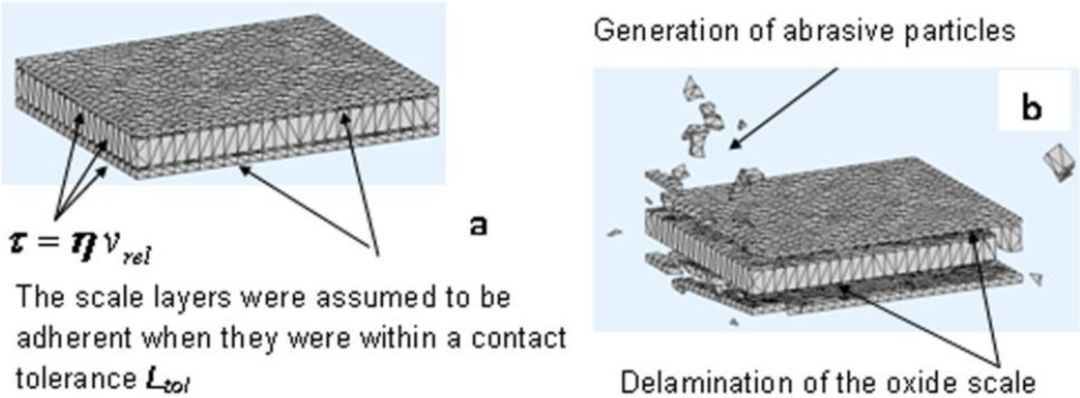

Figure 2.31: Discrete element three-dimensional model of oxide scale (Krzyzanowski and Rainforth, 2010).

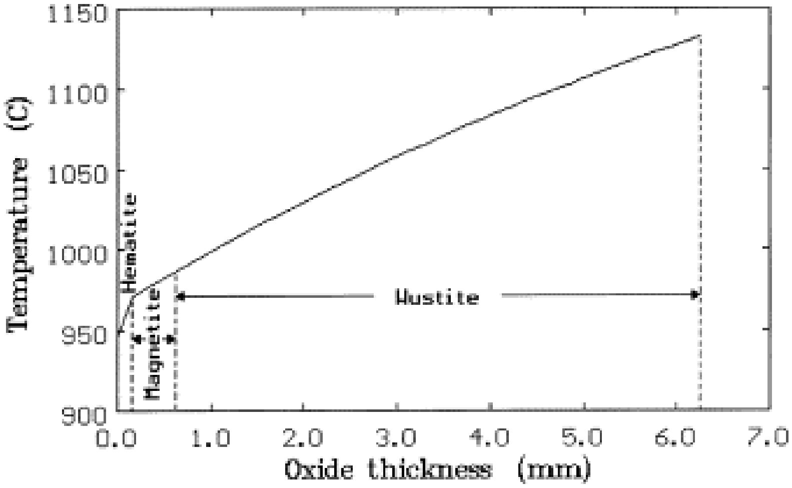

Figure 2.32: Temperature profile within the oxide layer of the 254 mm thick strip of carbon steel (Torres and Colas 2000).

In this review an attempt was made to understand the structures and the thickness of the oxide layer used in the existing modelling studies. The purpose of this review is to provide some points of view on the range of oxide thickness and structure of the layers formed on work rolls. According to Schroeder (2004), the roll surface temperature in rolling gap does not normally exceed 700^{o}C, thus, it can be concluded that the oxide thickness on the work roll is relatively smaller than the strip. According to Zhu *et al.* (2011), the maximum thickness of the oxide layer is approximately 2.3 μm based on the TEM bright field image of the cross section of the oxide layer at 650°C for 30 min in dry air. Based on this finding, modelling the behaviour of the oxide scale of a work roll can be performed by assuming it is less than 4 μm thick.

2.3.2 Finite Element modelling of nanoindentation of oxide layer

Nanoindentation is a technique to evaluate mechanical properties such as the hardness and elastic modulus from the load-displacement curve and the contact area function. This technique is a promising method for mechanical testing in shallow indentations less than 100 nm deep (Doernex and Nix, 1986; Oliver and Pharr, 1992). The elastic modulus and hardness of the coating and substrate can be evaluated by the load-penetration depth curve. According to Doerner and Nix (1986) and Oliver and Pharr (1992), the elastic modulus is obtained from the following equation:-

$$E_r = \frac{\sqrt{\pi}(\frac{dP}{dh})_{unload}}{2\sqrt{A}} = \frac{\sqrt{\pi}}{2}\left(\frac{S}{\sqrt{A}}\right) \qquad (2.2)$$

where *P* is indentation load; *h* is penetration depth; *S* is the experimentally measured stiffness of the upper portion of the unloading curve; *A* is the contact area, and E_r is the reduced modulus. Furthermore, the reduced modulus is defined by

$$\frac{1}{E_r} = \frac{1-v_i^2}{E_i} - \frac{1-v^2}{E} \qquad (2.3)$$

where *E* and v are the elastic modulus and Poisson’s ratio for the material to be measured, and E_i and v_i are the properties for the indenter. The depth of actual contact, h_c between indenter and the material is calculated by:-

$$h_c = h_{max} - \varepsilon\frac{(P_{max})}{S} \qquad (2.4)$$

where ε is a geometrical constant and is 0.75 for a Berkovich indenter. The ideal indenter area is a function of h_c and defined is given as:

$$A = C_o h_c^2 \tag{2.5}$$

where C_o is a fixed constant and is 24.50 for Berkovich indenter. The hardness is readily obtained by:

$$H = \frac{P_{max}}{A} \tag{2.6}$$

The measurement of hardness and modulus of films at the macro and nano scale in nanoindentation experiment has been widely reported. Rao and Reddy (2009) investigated the loading and unloading characteristics of bulk materials and thin films by extracting the load-displacement data. Bai *et al.* (2000) investigated the effect of internal stress by observing the sink-in and pile-up effects using FEM. The hardness and elastic modulus were determined in the simulation through the loading and unloading stage (Figure 2.33).

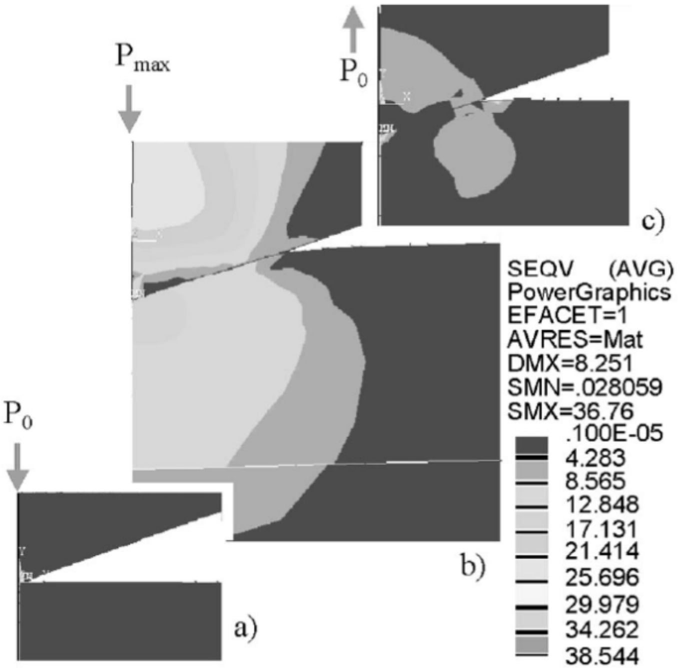

Figure 2.33: Typical von Mises distribution contour; (a) before loading, (b) during loading, (c) after unloading (Bai *et al*., 2000).

However, the number of investigations on the hardness and modulus of the oxide layer on substrate using nanoindentation is limited. Xia *et al.* (2006) investigated the mechanical properties of the oxide layer on aluminide surface after a γ-based titanium aluminide had undergone a series of thermal oxidation processes. The characteristic of the load-displacement curve indicated variations in the mechanical properties for different sub-layers (Figure 2.34). There was a large reduction in the depth of penetration and an increase in the contact stiffness when the indentation position was moved from the TiO_2 layer to the Al_2O_3-rich layer, thus indicating that the Al_2O_3-rich layer has higher hardness and higher elastic modulus than the TiO_2. Both the oxide layer and the diffusion zone have much higher resistance to the penetration than the substrate.

The elastic-plastic behaviour of films during the nanoindentation process has also been explained by Bai *et al.* (2000) by considering the elastic, elastic-plastic, and residual impression conditions. A schematic illustration of the elastic plastic behaviour is shown in Figure 2.35. When a small load was applied elastic regime occurred in the material, as shown (Figure 2.35a). As load became higher, plastic deformation occurred and there was a residual impression in the surface of the specimen (Figure 2.35b). When the load was removed from the indenter (Figure 2.35c) the material does not regain its original shape due to plastic deformation.

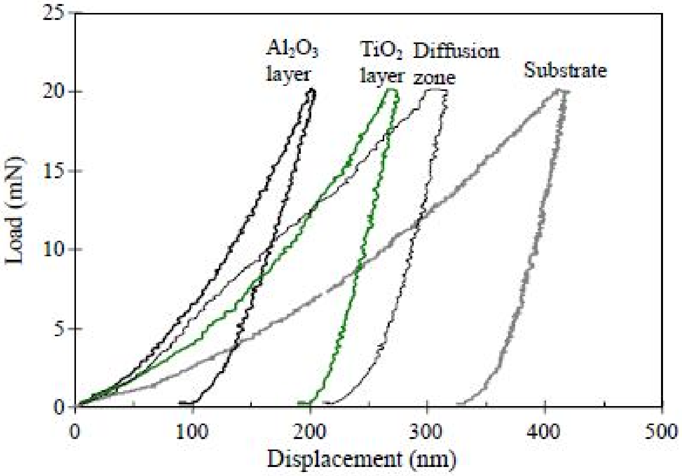

Figure 2.34: Nanoindentation load vs. displacement curves on the substrate of a based TiAl (Xia *et al*., 2006).

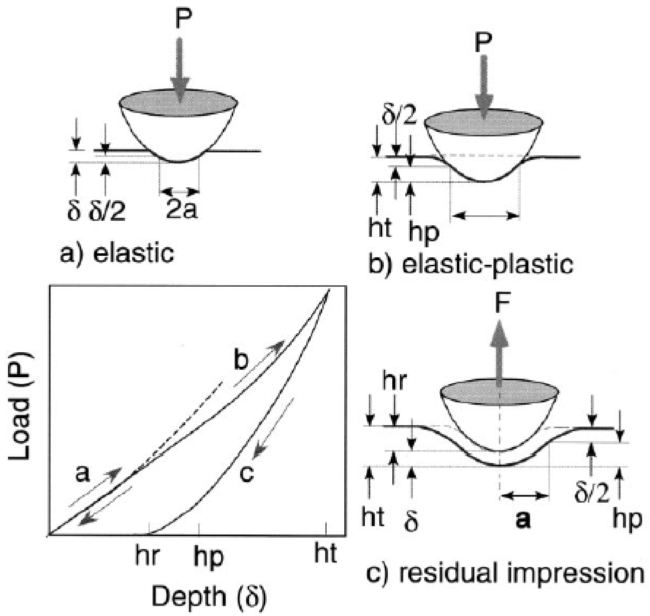

Figure 2.35: A schematic illustration of elastic-plastic behaviour of films during nanoindentation (a) elastic regime, (b) plastic deformation above a critical load on loading, (c) elastic behaviour (Bai *et al*., 2000).

2.3.3 Finite Element modelling for a scratch test

The scratch test is commonly used to measure the surface mechanical properties such as hardness, abrasion and wear resistance, coating-substrate adhesion properties, and friction. A large number of studies have been carried out to better understand the scratch behaviour. When analysing scratch tests that lead to damage, various morphologies and wear mechanisms corresponding to abrasion are apparent. The abrasive wear mode can be expressed as a combination of cutting, ploughing, and wedge formation processes, but a mechanical analysis of the scratch is not straightforward because of the interaction between various parameters of the test. Moreover the experimental analysis cannot give sufficient information on the local behaviour e.g. strain hardening, residual stress, etc. Apart from that, it is difficult to numerically and experimentally identify the distribution of stress inside the oxide layer and the interface between the oxide layer and substrate because of the complicated loading conditions. In fact, according to Li *et al*. (2006), there is no adequate theoretical model to predict the stress generated by a moving indenter. They reported that these phenomena can only be solved numerically because every attempt to explain this phenomenon by theoretical modelling has been unsuccessful due to its inability to handle non-linearity.

Bucaille *et al*. (2001) studied the effect of rheology by modelling the scratch process using the three dimensional (3D) finite element (FE) software (Forge3). A rheological factor was defined as the function of E/σ_o, where σ_o is the yield strength of the material and E is the Young's modulus. They reported that small rheological factor causes a sinking in profile under the scratch load and elastic recovery behind the moving indenter, while the larger factor leads to plastic deformations at the front and a lateral pile-up. In another study Ben-Tkaya *et al*. (2007) showed the effect of rheology and the attack angles on the wear mechanism. They proposed two models with and without damage to investigate the effect of the attack angle and found there is a transition of wear mechanism from ploughing to cutting which corresponds to the attack angle. In fact, a correlation between the wear mechanism and coefficient of friction was also identified, and the summarised result is shown in Figure 2.36.

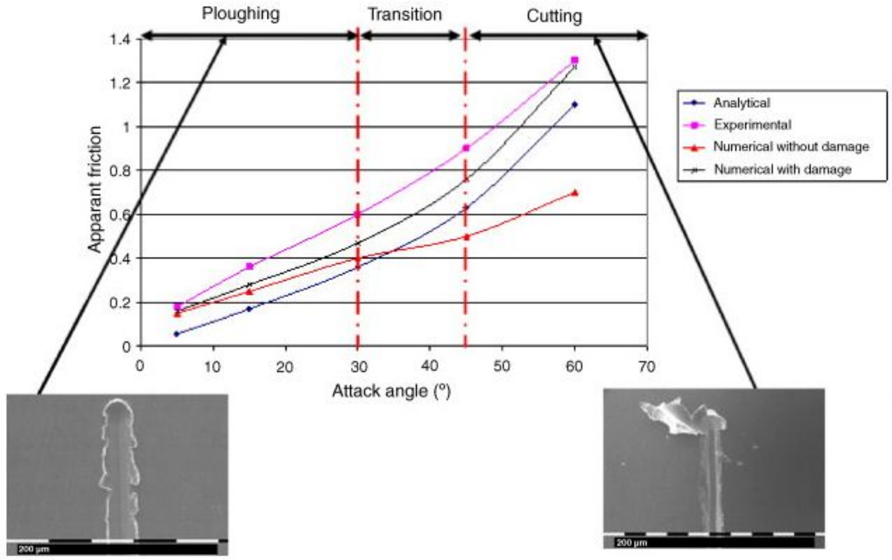

Figure 2.36: Correlation between coefficient of friction and wear mechanism for different attack angle (Ben-Tkaya *et al*., 2007).

More recently, the scratch test has been used to extend its capability to predict the wear rate of material. Fang *et al*. (2004; 2005) used ridge curves on both sides of scratch grooves to determine material removed. Then the Monte Carlo method was applied to simulate plastic deformation wear rate in two and three body abrasion.

The approach proposed by Fang *et al*. (2004) showed a good agreement with the experimental results for ductile materials such as steels.

Da Silva and De Mello (2009) proposed a new methodology for simulating abrasive wear using parallel scratches. They developed special method using superimposition technique of parallel scratches to produce a surface with similar reference surface in terms of morphology and topography. They developed a database using a single scratch to identify the relationship between normal load, degree of superimposition, and average depth. Then, based on this relationship, they directly identified the normal load for each depth location of the reference surface which led to reproduction of abrasive surface wear by simulation.

2.4 Abrasive wear model

2.4.1 Abrasive wear model of material with carbide particles

It is important to understand the influence that the formation of an oxide layer on high speed steel (HSS) work roll has on wear in order to determine the superficial damage and as a consequence, to reduce the running cost of a mill. High speed steel (HSS) could be considered as a composite material which contains a combination of primary and secondary carbides distributed in the martensitic matrix. Badisch and Mitterer (2003) reported the diameter of large primary carbides, mainly MC and M_6C-types, of around 1 to 10 µm while the small secondary carbides are less than 100 nm in diameter. Therefore, in order to understand the wear behaviour of oxide layers on high speed steel, the interaction of these carbide particles should be taken into account.

Several reports can be found in the literature describing the modelling based studies related to machining the metal matrix composite (MMC) where the matrix metal is reinforced with silicon carbides particles for cutting and machining applications. This thesis extends this approach to the rolling application by simulating the scratch behaviour of oxide scale on high speed steel (HSS) that contains the matrix of steel oxides and carbides particles.

The review of literature on modelling in machining reveals that the metal matrix composite (MMC) was used extensively where reinforcement particles were introduced into the matrix. Pramanik *et al*. (2007) developed an FE model to investigate the behaviour of metal matrix composite during orthogonal cutting, while Shetty *et al*. (2008) investigated the fundamental aspects of machining metal matrix composites involving the chip formation mechanism experimentally and analytically. It was reported by Pramanik *et al*. (2007) that the particles were 20% by volume and were assumed to be perfectly bonded with the matrix. In the work reported by Shetty *et al*. (2008), the interface nodes of the matrix and reinforcements were tied together. The 2D finite element model of MMC during machining by Pramanik *et al*. (2007) is shown in Figure 2.37. Based on this model, tool-particle interaction during machining was analysed and the high tool wear that occurred when machining MMCs was due to the sliding of debonded particles.

In another study, Lee *et al*. (2002) used a simple physical model for the abrasive wear of composite material to explore the removal of the reinforcement. The failures of reinforcement typically occurred at the matrix/reinforcement interface or in the reinforcement itself. They carried out a model analysis for three primary abrasive mechanisms, namely ploughing, cracking at the interface or in the reinforcement, and particle removal.

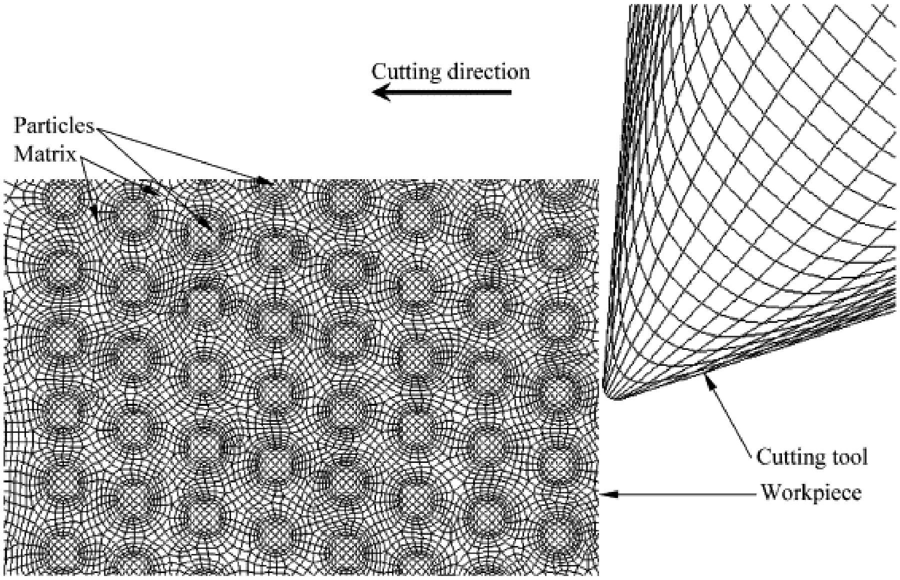

Figure 2.37: Finite element model set up representation of the workpiece and tool by Pramanik *et al*. (2007).

2.4.2 Abrasive wear model for work roll material

The aim of this investigation was to identify the abrasive wear of work roll material rather than strip material. The abrasive wear model of the oxide layer on high speed steel (HSS) is expected to be different from strip materials. Numerous reports can be found in the literature describing the experimental studies related to the hot rolling of high speed steels, but analytical and numerical investigations are limited. In fact, based on the author's knowledge, there are no studies that describe the behaviour of the oxide layer on high speed steel of work roll with a modelling approach.

With regards to the abrasive wear of the layer on high speed substrate, Panich and Sun (2006) developed a three-dimensional finite element (FE) model to simulate the scratch process of TiB_2 coatings on high speed steel (HSS) substrate (Figure 2.38). This was achieved by introducing a hard coating TiB_2 on a substrate scratched by a rigid conical indenter. They identified von Mises stress contours and plastic deformation behaviour during scratch process.

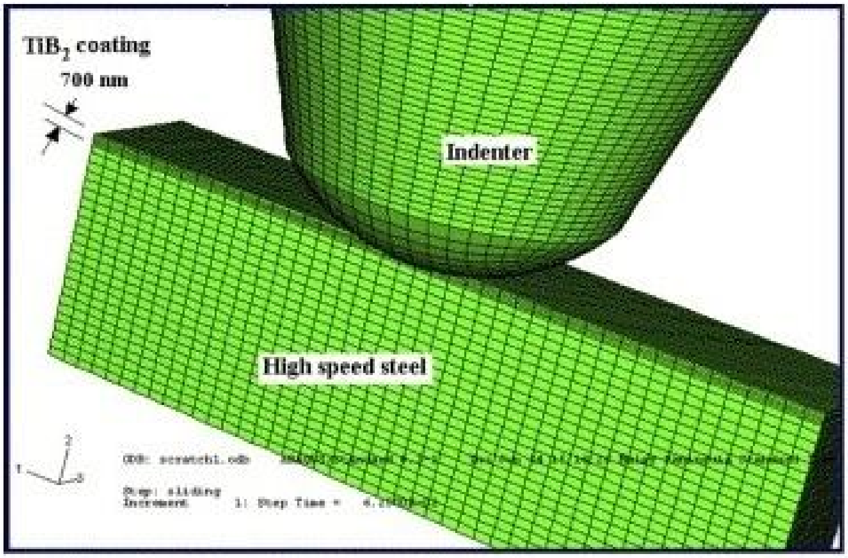

Figure 2.38: Finite element model set up of scratch process by Panich and Sun (2006).

However, this model is an oversimplified version of the real case because it was simulated by a model with a step-wise process and frictionless interface. Indeed this does not introduce a realistic high speed steel substrate that consists of carbide particles, so the results may only be compared qualitatively by experiments. Hence, a detailed finite element model was developed to simulate the behaviour of oxide layers and particles during a scratch test. To understand the behaviour of the material during the scratch test, a trace of the strip was examined under an optical microscope and the normal and tangential force and the coefficient of friction were measured. The objectives of the simulation were to upgrade the finite element model with data reflecting properties that were more specific for the particular oxide scale, and to improve the model of high speed steel substrate by including carbide particles in the matrix.

2.5 Summary

In this review an attempt has been made to understand the whole potential research related to work rolls. However, published works contain very little information on the mechanical characteristics and microstructure of the oxide layers, as well as their behaviour in ploughing or abrasion contact, and the interaction of carbide particles with the oxide layers in high speed steel rolls. Understanding the behaviour of the oxide layer by abrasion is important because it is the dominant mechanism in the wear of hot work rolls. Moreover, there is a lack of knowledge about the mechanical properties and morphology of oxide layers on HSS work roll that contribute to work roll wear. It is important to understand the mechanical characteristics and potential mechanisms that contribute to roll wear. Thus, the mechanical properties and microstructures of various oxide layers on HSS work rolls are explored in detail in Chapters 3-5. The stress and deformation study of oxide layer using the ductile and brittle damage model is presented in Chapters 6-7.

Chapter 3

Experimental instruments and analytical methodology

This chapter presents detailed description of the experimental instruments and analytical methodology used in the current study.

3.1 Oxidation treatment

3.1.1 High Speed Steel (HSS) samples

To investigate the mechanical properties and characteristics of oxide layers formed on high speeds steel, oxide layers were generated by subjecting the HSS samples to oxidation treatment. It is important that the laboratory generated oxide layers have thicknesses and sub-layers with structure similar to that in real hot rolling practices because these characteristics of oxide could affect the wear rate of the work rolls.

Because the oxide formed on metallic surfaces depends on the composition of the substrate, the HSS used in this thesis was chosen to be typical HSS work roll material with the typical nominal composition as given in Table 3.1. Therefore, the composition of the high speed steel samples represents the typical compositions of HSS work rolls in practice.

Table 3.1: Chemical composition of the high speed steel samples (in *wt* %) analysed by X-ray fluorescence spectroscopy.

Element	***C***	***Mo***	***W***	***V***	***Cr***	***Mn***	***Ni***	***Si***	***P***	***S***
Composition (wt%)	1.96	4.47	3.40	4.00	4.85	1.26	0.78	0.99	0.028	0.034

Before the oxidation treatment, the HSS samples were cut into 2.7×2.7×2 mm^3 cuboid specimens and their surfaces were then polished and finished with 1 μm diamond paste. After oxidation the samples were cut into sections and the surfaces were polished with 1 μm diamond paste to produce a high surface finish. It was important that when the samples were cut into sections that the layers were not damaged and their properties were not modified by residual stresses induced by the surface processing.

3.1.2 Oxide growing instrument

The oxide layers generations were conducted in a high temperature microscope (HTM) with a CCD camera, unlike traditionally, where oxide generations were done in Thermo-gravimetric Analysis (TGA) and Gleeble thermal mechanical simulators. These traditional techniques do not allow for direct observation of the oxidation process, but the present set-up allows the oxide growth processes to be continuously recorded. This enabled the growth of the oxides to be observed and any non-uniform growth that was detected on the samples to be replaced.

Figure 3.1 shows a schematic of the transverse cross section of the high temperature furnace. One end of the gas entry tube supplying the oxidising gas is positioned above and adjacent to the sample. The oxidation tests were carried out at 700^oC for 120 min in a 12.5% H_2O humid atmosphere. The procedure was similar to that described in the experiments by Zhu *et al*. (2010):

(1) The samples were heated to 700^oC under a high argon atmosphere (Ar, 99.9999% pure) at a rate of 1.7^oCS^{-1} and held for 5 min to allow the system to reach thermal equilibrium.

(2) The argon flow was then switched off concurrently with the introduction of oxidising gas and the samples were then oxidised.

(3) The gas flow was switched back to pure argon to prevent further oxidation and the samples were allowed to cool to room temperature.

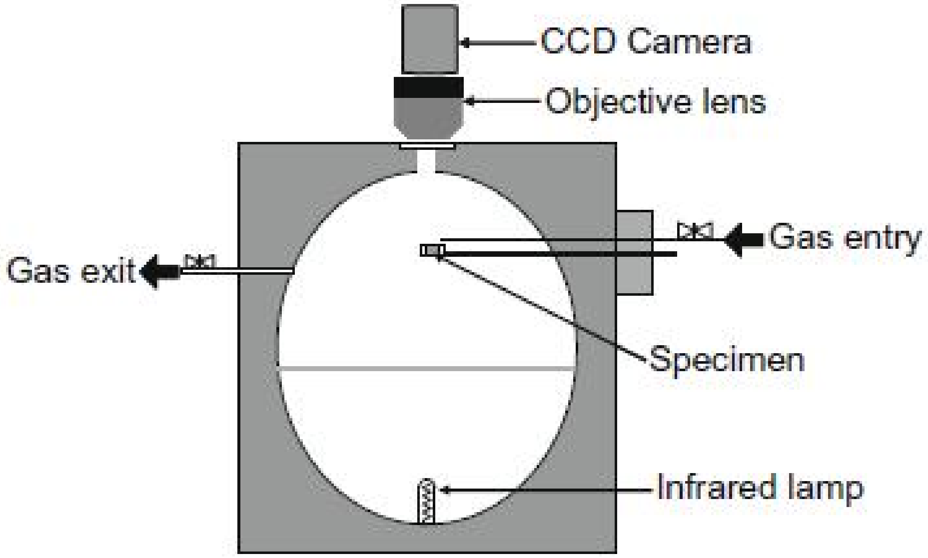

Figure 3.1: Schematic illustration of the high temperature furnace chamber (Zhu *et al.*, 2010).

3.2 Nanoindentation

3.2.1 IBIS/UMIS nanoindentation system

The nanoindentation system used was the IBIS/UMIS nanoindentation system developed in 1984 by the CSIRO Division of Applied Physics in Sydney, Australia. The system can perform nanoindentation experiments over a wide load range from 0.1 mN up to 500 mN and also record the load and displacement concurrently. Load against depth curves with a resolution of 75 nN in load and 0.05 nm in depth can be achieved by the system. Figure 3.2 shows a photo of the IBIS/UMIS nanoindentation system in the tribology laboratory at the University of Wollongong, Australia.

Nanoindentations were carried out using a Berkovich diamond indenter. The force and displacement were recorded as the tip of the indenter was pressed into the surface of the material with a prescribed loading profile. The hardness and reduced elastic modulus of the oxide scale was calculated from the measured load-displacement curves. The indentation instrument was set in a square root load control mode where the load was gradually increased until it reached the specified maximum load, and then it was reduced. Typically, 2% of the unloading data were used to calculate the unloading slope (*dP/dh*) used in the modulus analysis.

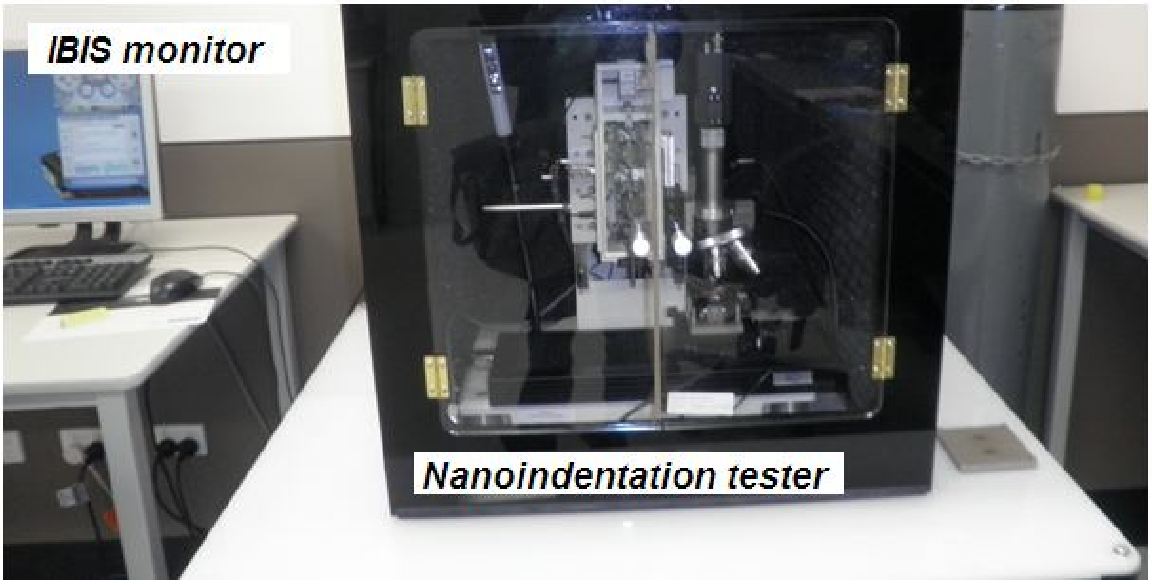

Figure 3.2: IBIS nanoindentation system.

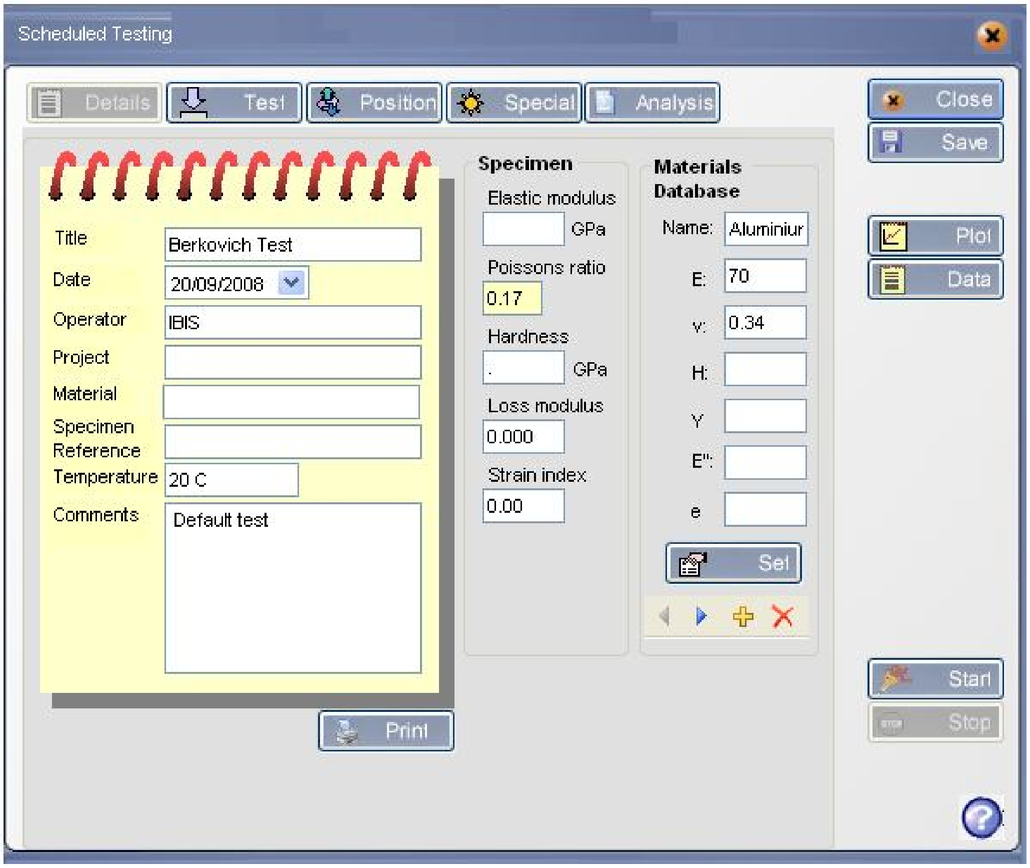

Title Berkovich Test
Date 20/09/2008
Operator IBIS
Project
Material
Specimen Reference
Temperature 20 C
Comments Default test

Specimen
Elastic modulus GPa
Poissons ratio 0.17
Hardness GPa
Loss modulus 0.000
Strain index 0.00

Materials Database
Name: Aluminiur
E: 70
v: 0.34
H:
Y
E'':
e

Figure 3.3: IBIS Interface for details of tip and sample parameter.

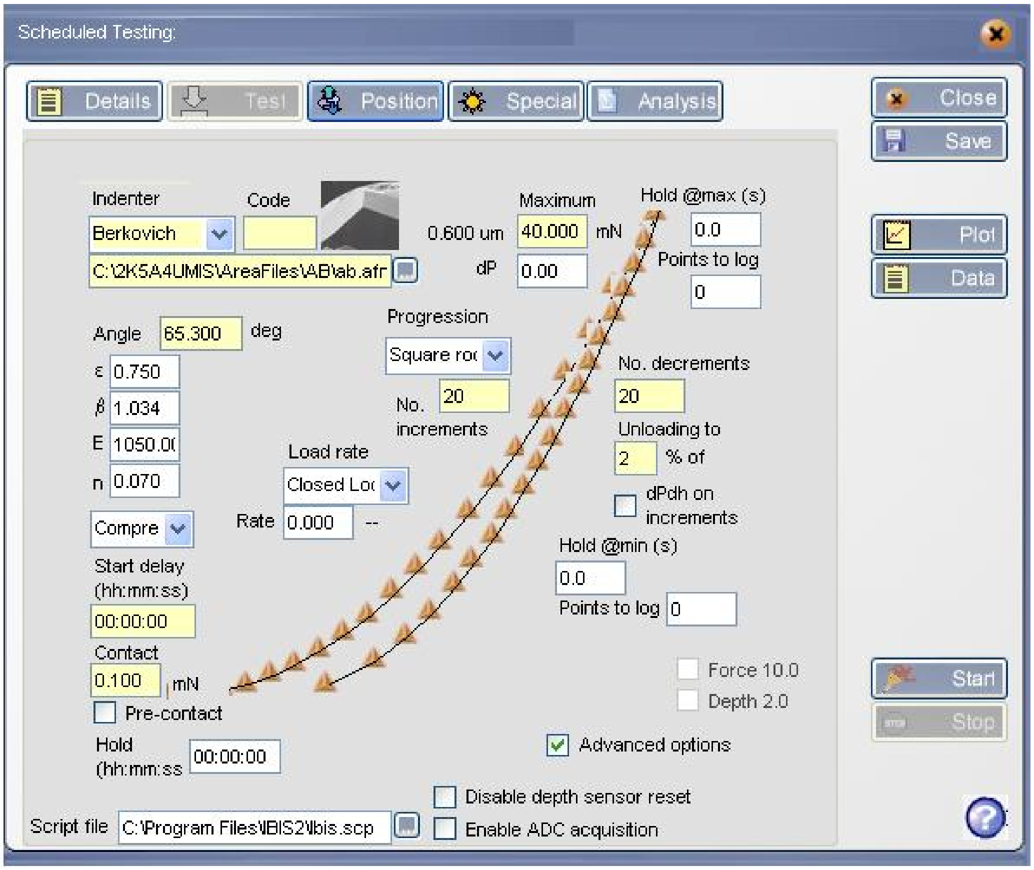

Indenter: Berkovich
Code:
C:\2K5A4UMIS\AreaFiles\AB\ab.afr
0.600 um
Maximum: 40.000 mN
dP: 0.00
Hold @max (s): 0.0
Points to log: 0
Angle: 65.300 deg
ε: 0.750
β: 1.034
E: 1050.0(
n: 0.070
Compre
Progression: Square roo
No. increments: 20
Load rate: Closed Loo
Rate: 0.000 --
Start delay (hh:mm:ss): 00:00:00
Contact: 0.100 mN
☐ Pre-contact
Hold (hh:mm:ss: 00:00:00
No. decrements: 20
Unloading to: 2 % of
☐ dPdh on increments
Hold @min (s): 0.0
Points to log: 0
☐ Force 10.0
☐ Depth 2.0
☑ Advanced options
☐ Disable depth sensor reset
☐ Enable ADC acquisition
Script file: C:\Program Files\IBIS2\Ibis.scp

Figure 3.4: IBIS interface for test parameters.

The IBIS interface in Figure 3.3 shows how the user input nanoindentation parameters such as Poisson's ratio, temperature, and the properties of the specimen, etc. The test parameters dialog interface is shown in Figure 3.4. Some experimental parameters such as type of indenter, maximum load, contact load, start delay time, number of increments during loading and number of decrements during unloading had to be inserted into the parameters dialog. Once the required parameters have been entered in the IBIS program, the nanoindentation experiments are ready to commence.

3.2.2 Nanoindentation experiments

All the experiments were performed at room temperature between 25-28^{o}C. As these tests are sensitive to mechanical vibration and thermal expansion from temperature changes, several considerations have been taken. For example, nanoindentation system is placed on air tables which can isolate the system from the external vibration and time delay in the process of indentation for the system to reach steady state. Another effort to minimize the effect of vibration was to carry out experiments during the quiet time in the building which was normally over the weekend or late at night. The delayed experiments procedure was used to minimize the effect of thermal drift during experiments that can affect the displacement measurements.

3.3 Analytical methodology

3.3.1 Scanning electron microscopy (SEM)

The microstructures of the oxide layers were examined by X-ray diffraction (XRD) using a GBC MMA diffractometer with monochrometed Cu-$K\alpha$ radiation, and a JEOL JSM 6490 scanning electron microscope (SEM) equipped with energy-dispersive X-ray analysis (EDX). Microstructures analyses were necessary to identify the structure and phase composition of each sub-layer. Besides microstructure characterization, the microscopy techniques were also used to analyse the indentation impressions e.g. detection of precise indents locations within the sub-layers.

3.3.2 Atomic force microscopy (AFM)

While sample morphologies can be examined by SEMs, the topographical details, such as the indentation impressions at different locations and sizes of the indents, were obtained with the Nanoscope IIIA atomic force microscope (AFM) which is attached to the UMIS nanoindentation unit. Scannings of the surfaces were performed in non-contact or tapping mode. The nanoprobe cantilevers were made of silicon nitride (Si_3N_4) with a spring constant of 0.06 Nm^{-1}.

3.3.3 Transmission electron microscopy (TEM)

To observe the grains and to estimate the fractional area of the pores, oxide layers examinations were carried out in a Phillips CM200 field emission gun transmission electron microscope (FEGTEM). There are two steps for preparing the samples in these works. Prior to cutting, a typical feature had to be chosen using the electron beam and a selected surface had to be deposited using a protective Pt film to protect the oxide scale. For a TEM examination, ion beam was used to cut-off the cross-section. The detailed regarding the procedure was explained by Zhu *et al.* (2011).

Chapter 4

Development of the combined FE simulations and nanoindentation experiments for characterising oxide layers

The importance of the mechanical properties of oxide layer on high speed steels cannot be overstated because these oxide layers can be viewed as protective layers which influence the wear and friction in the strip/roll contact and can be beneficial for the work roll in hot strip mills. As the wear of the bulk material depends on the wear resistance of the oxide layers, it is important in the analyses of the roll wear that their mechanical properties be known accurately. However, accurately measuring the mechanical properties of the oxide layers is difficult and complicated because of the unknown effect of internal porosity. Despite of the significant role that oxide layers play in the tribological performance of a work roll in hot rolling, to the best of the author’s knowledge, no studies have been conducted on the mechanical properties of oxide layers formed on HSS surface.

In this thesis a combination of FE simulations and nanoindentation experiments was applied, and the experimental load – displacement curves were correlated with the FE based nanoindentation simulations. In this chapter it is shown that with this combined approach the effect of the porosity of the oxide layer can be accounted for in the mechanical properties of the oxide layers.

4.1 Overview of the combined approach

The main objective of the Finite Element (FE) simulations is to generate load-displacement curves that agree closely with the measured curves. The FE simulations were carried out in the ANSYS general purpose FE code which has the capability of defining the yield criterion, the flow rule, and the hardening rule governing the plastic behaviour of the material. The FE code has become the main technique for predicting and simulating the physical behaviour of complex engineering systems. The parameters required in the FE model can be found in *Appendix*.

The plasticity of ductile porous materials was modelled using the Gurson model (1975) which describes the plastic behaviour of porous ductile materials with dilute void concentrations i.e. with porosity levels of less than 30%. In this model the matrix material is taken to be a continuum and the effect of the voids is averaged through the elastic perfectly plastic material. The voids appear indirectly in the Gurson model through the pore volume fraction *f* on the global flow behaviour.

The capability of a nanoindentation experiment as the sole technique to measure the properties of the oxide layer is restricted because the Poisson’s ratio of the porous layers is generally unknown. When the Poisson’s ratio is unknown it is common to assume 0.3 for metal and 0.2 for ceramic material, but this approach cannot be used for porous material where Poisson’s ratio also depends on porosity (Boccaccini and Boccaccini, 1997). To overcome this problem a combined nanoindentation simulation and experimental approach was developed.

The flow chart of the combined nanoindentation simulations and experimental approach is shown in Figure 4.1. The main procedure consists of two parallel processes where: firstly, the nanoindentation experiments are carried out to establish the load-displacement curves, and second, the load-displacement curves are validated and compared with the FE simulations that were generated. There are 4 main phases in the simulation process; in phase one, input parameters such as the elastic modulus, yield strength, Poisson’s ratio, and porosity are defined, and from which the simulation output load-displacement curve which provides the unloading slope (dP/dh) and the maximum load (P_{max}) is obtained.

At the end of this phase each load-displacement curve was analysed and compared with the experimental curves. The simulated curves are then refined iteratively with the renewed input values and the mechanical properties are updated i.e. failed input parameters are removed from the process and new parameters are inserted as “new mechanical properties” of the oxide layer. As Figure 4.1 shows, the cycle is repeated until the simulation based load-displacement curve match the experimental one within a specified tolerance. The values of the mechanical properties are selected in such a way that the difference between the average unloading slope and maximum load are less than 1 percent between the experimental measurements and the FE simulation.

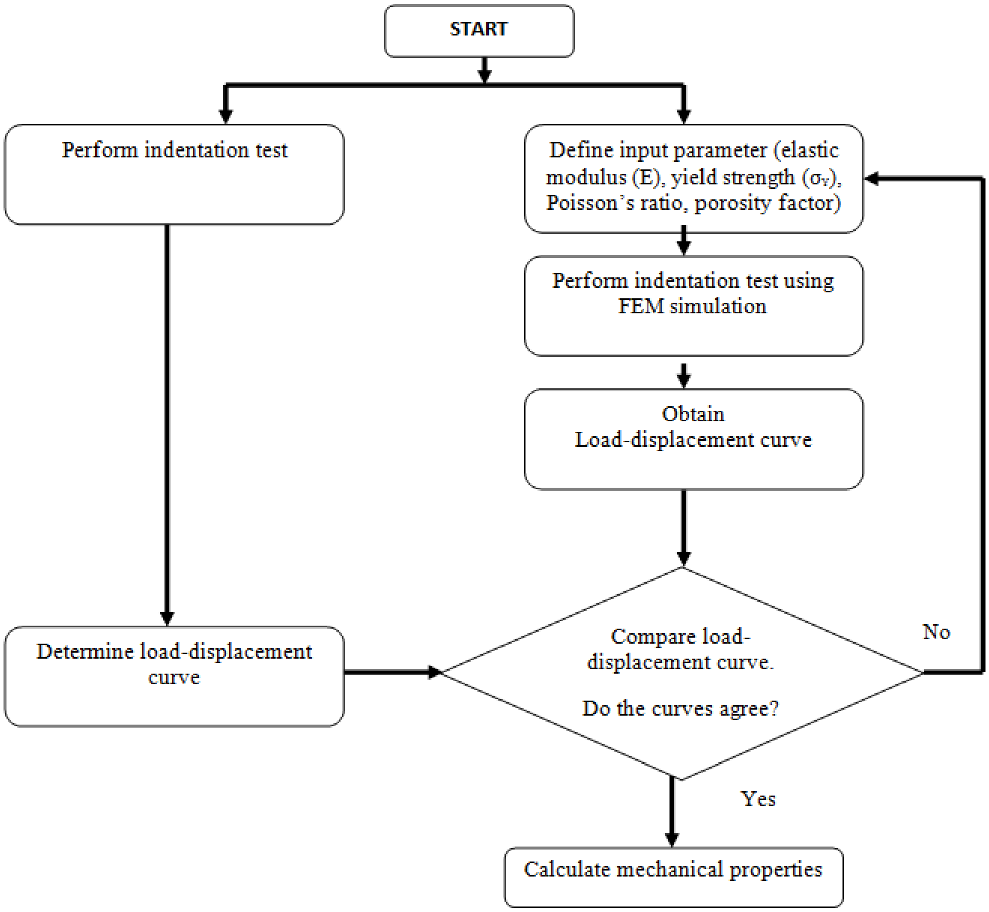

Figure 4.1: The combined nanoindentation measurements and FE simulation approach.

4.1.1 Experimental methods

Samples of the oxide layers were prepared by isothermal oxidation in a circulating air furnace heated to 700°C for 120 min, as described in Chapter 3. Layers of oxide grew to a few micrometers in thickness through the process of diffusion. After cooling the oxidised samples were hot mounted in DuroFast resin at 150°C and under 20 MPa. The samples were then ground with SiC paper, polished, and finished with a 1 μm diamond suspension. Zhu *et al.* (2010; 2011) found that at the 700°C the microstructures of the oxides are not much different from those between 550-650°C, except for the thickness.

It was necessary to allow the samples to cool slowly to ensure that no cracks occurred in the oxide layer. In this work the samples were cooled to room temperature at a rate of 1.7°Cs^{-1}. Echsler *et al.* (2003) showed the effect of the cooling rate on the porosity of oxide scale, where rapid cooling can lead to larger pores and cracking of the layer. With rapid cooling, cracks can occur in the entire oxide whereas during slow cooling the cracks tend to occur near the interface of the substrate oxide.

All nanoindentations were performed on the cross sectioned surface of the layer, in a controlled loading mode, up to a maximum load (P_{max}) of 5 mN and 20 mN. Following the nanoindentation experiments, samples were characterised by atomic force microscope (AFM), scanning electron microscope (SEM), and transmission electron microscope (TEM).

4. 2 Results

4.2.1 Identification of the oxide layers

A column of 11 indentation locations was chosen across the oxide layer, from the outer sub-layer to the inner sub-layer (Figure 4.2). Each indent was analysed using a scanning electron microscope (SEM) and their locations were carefully identified to determine whether they were in the epoxy, in the outer sub-layer, in the inner sub-layer, or in the substrate. The approximate locations of the indentation points are shown in Figure 4.2a. Figure 4.2b shows the atomic force microscope (AFM) image of the nanoindentation impressions at different locations, i.e., in the substrate and in the inner sub-layer. A dense outer sub-layer and a more porous inner sub-layer can be seen in Figure 4.2c.

A TEM examination was carried out on the cross sections in which the samples were prepared, using a focused ion beam (FIB) microscope. Before the specimens were cut at the cross section by the ion beam, an electron beam was used to choose a typical feature and a protective film was deposited to cover the oxide scale (Zhu *et al.,* 2011). Based on the TEM images, the porosity of the inner and outer sub-layers were estimated from the fractional area of the pores (Figure 4.3). The porosity of the outer sub-layer was approximately 2% while the inner sub-layer was around 8%.

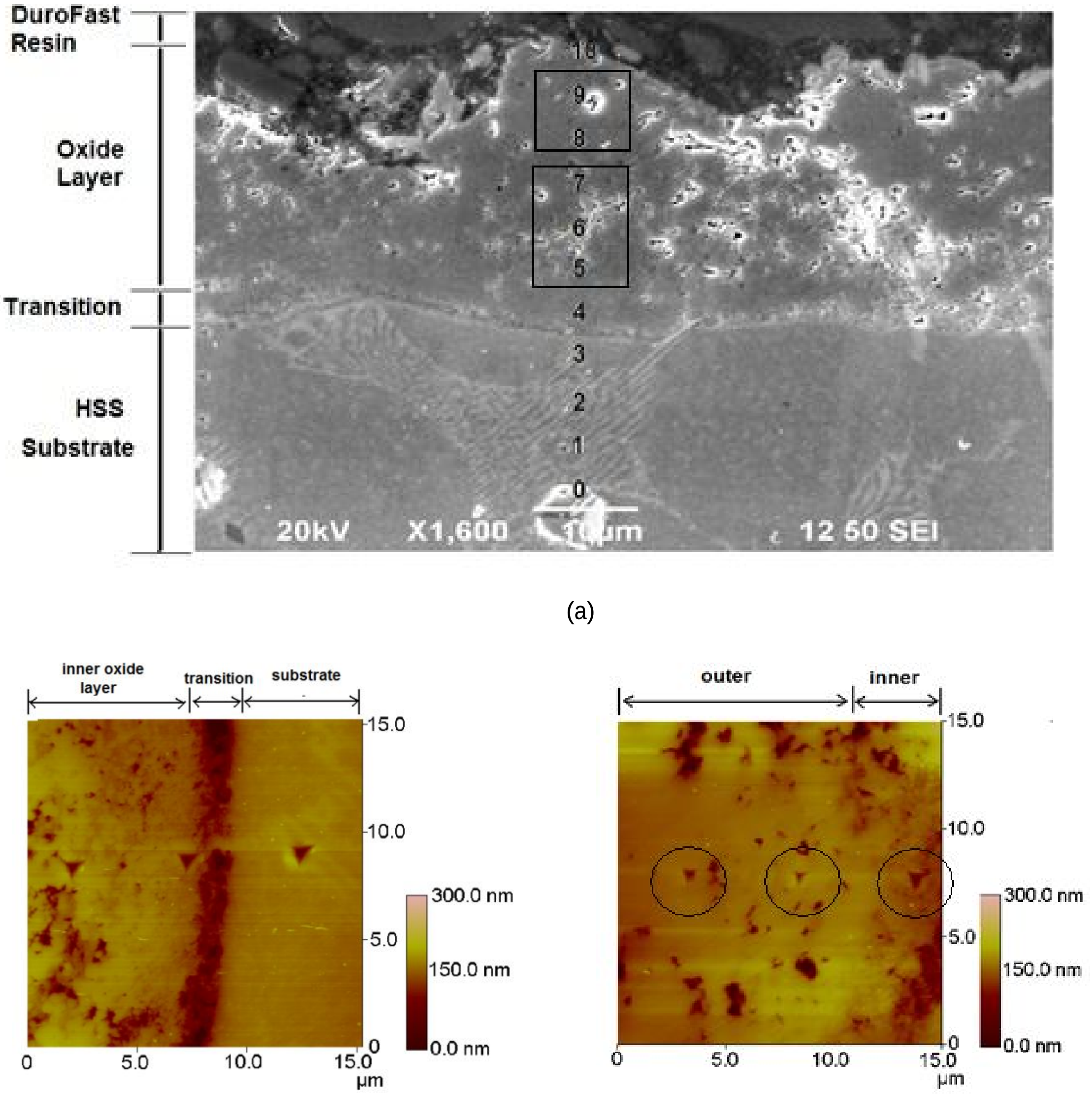

(a)

(b)

(c)

Figure 4.2: (a) SEM image showing distribution of the indentation locations in the oxide layers. An AFM analysis of the indents: (b) from the substrate to the inner sub-layer and (c) from the inner to the outer sub-layer.

Vergne *et al.* (2006) showed that multi-layered oxide consists of different types of oxide where the outer sub-layer is mainly composed of Fe_2O_3 and the inner sub-layer is Fe_2O_3 + Fe_3O_4. In this work the XRD pattern and SEM-EDS analysis indicated there are two types of oxide layers formed on the HSS surface, namely Fe_2O_3 and $(Fe,Cr)_3O_4$ in the outer and inner sub-layers respectively. Figure 4.4 and 4.5 shows XRD pattern and EDS spectrum of the oxide layer. The reflections of iron substrate that are present in Figure 4.4 indicate that the thickness of the oxide layer was smaller than the depth of X-ray diffraction. According to Zhu *et al.* (2010), the XRD patterns of the oxidised samples at lower temperatures were not apparent because the oxide layer was too thin to be detected by the X-ray diffraction. The detailed XRD and SEM analyses of these oxide layers were similar to that reported by Zhu *et al.* (2010; 2011).

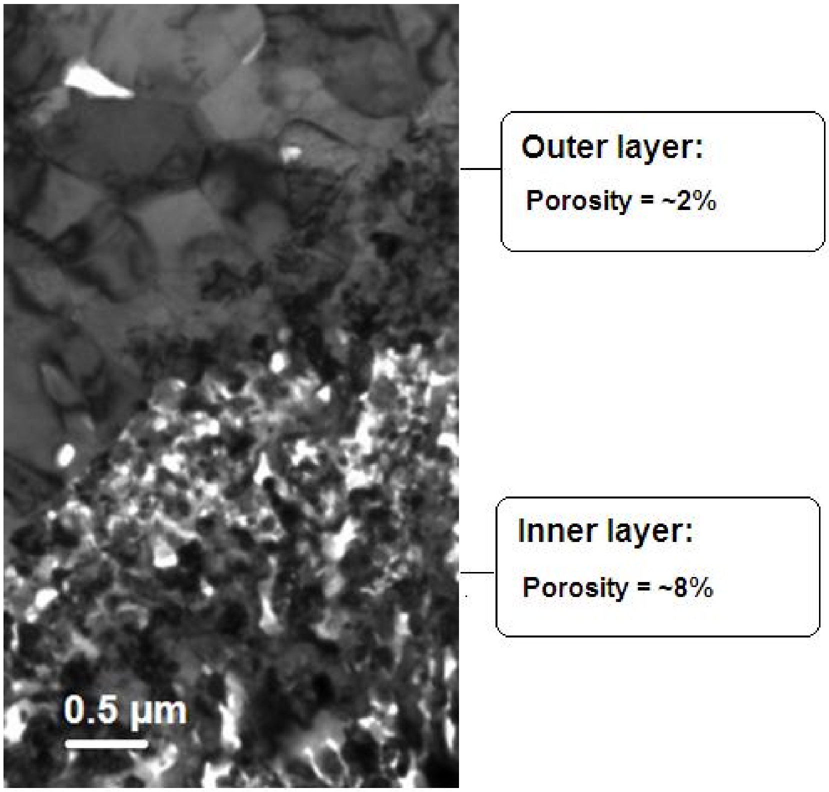

Figure 4.3: Measurement of the porosity levels, based on TEM analysis.

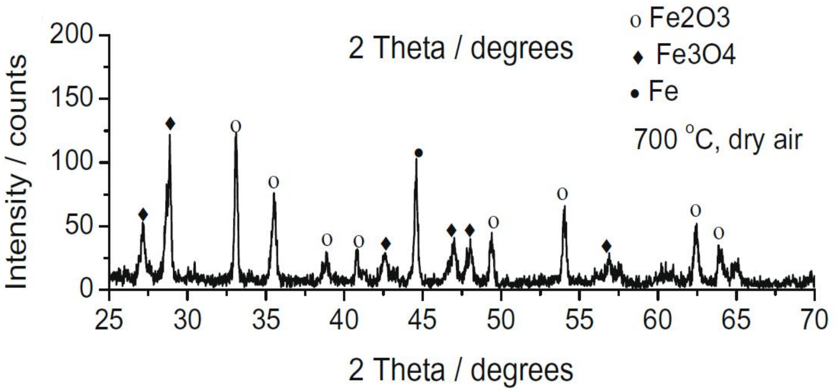

Figure 4.4: XRD patterns of oxidised sample at 700°C.

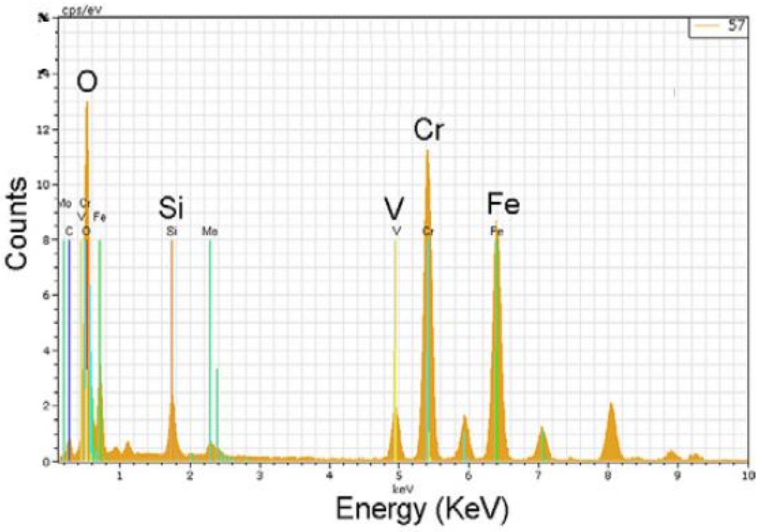

Figure 4.5: An EDS spectra of a selected area on the oxide scale.

4.2.2 Load-displacement curves

The two sub-layers identified in Table 4.1 can also be inferred from the maximum displacements of the load-displacement curves, as shown in Figure 4.6. The load displacement curves are based on the maximum 5 mN load nanoindentation experiments across the thickness of the oxide layer. The difference in the maximum depth of penetration between these two sub-layers is significant in that two distinct sub-layers can clearly be identified. The load-displacement curves of the inner sub-layer indentations at points 5, 6, and 7 show a deeper maximum depth (>130 nm) than the outer sub-layer (~110 nm) at points 8 and 9. These different depths of penetration indicate that the outer sub-layer which is mainly Fe_2O_3, is harder than the inner sub-layer.

Table 4.1: Identification of the oxide sub-layer based on the indentation depth with P_{max}= 5 mN.

Point	Max. displacement (μm)	Indent location	Estimation of oxide layer type
10	0.138	Epoxy	
9	0.118	Outer oxide sub-layer	Fe_2O_3
8	0.114	Outer oxide sub-layer	Fe_2O_3
7	0.147	Inner oxide sub-layer	$Fe_3O_4 + Cr_3O_4$
6	0.149	Inner oxide sub-layer	$Fe_3O_4 + Cr_3O_4$
5	0.157	Inner oxide sub-layer	$Fe_3O_4 + Cr_3O_4$
4	0.154	Transition	-
3	0.128	HSS	-
2	0.152	HSS	-

Apart from the maximum displacement, an identification of the sub-layers can also be inferred from the sizes of the indents where the indents in the inner sub-layer are larger than in the outer sub-layer. At a maximum load of 5 mN the indents in the inner sub-layer are approximately 1.25 μm (Figure 4.7a) rather than 0.7 μm (Figure 4.7b) in the outer sub-layer.

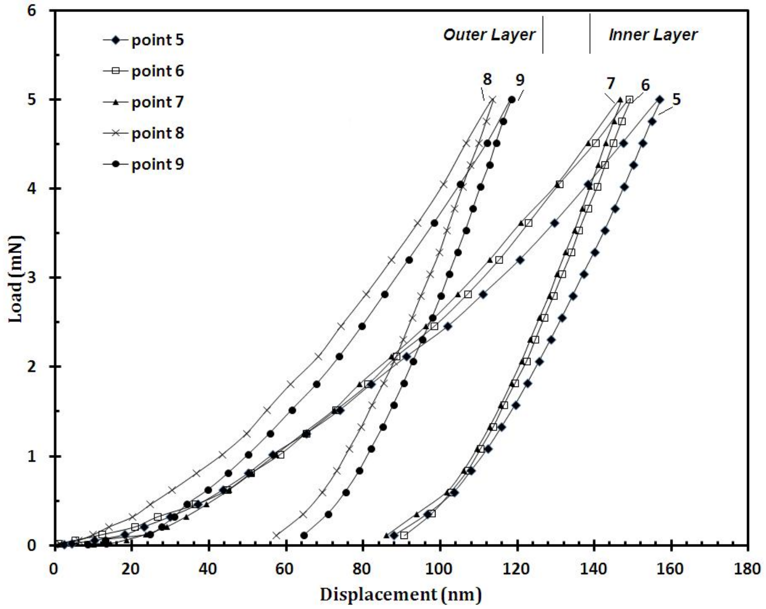

Figure 4.6: The load-displacement curve across the oxide layer with P_{max} = 5 mN.

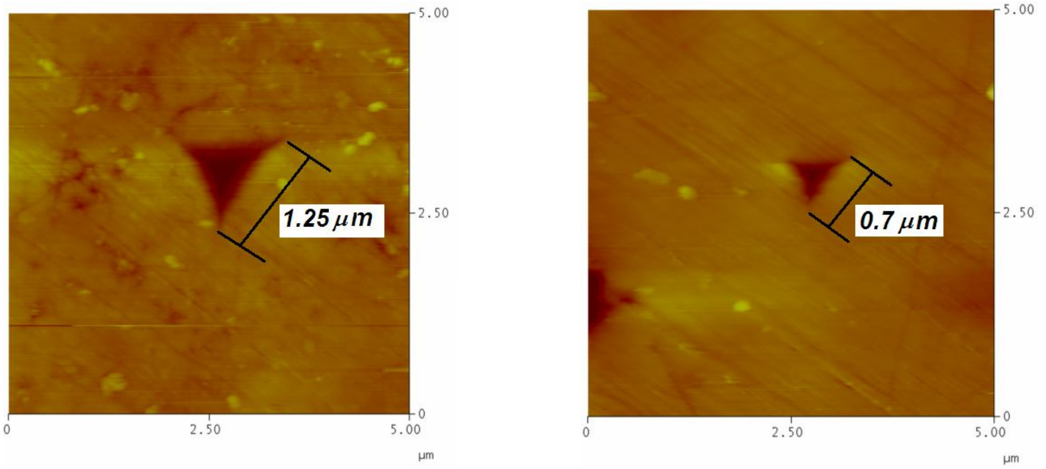

(a) (b)

Figure 4.7: The sizes of the indents in (a) inner sub-layer (b) outer sub-layer from P_{max}= 5 mN nanoindentation.

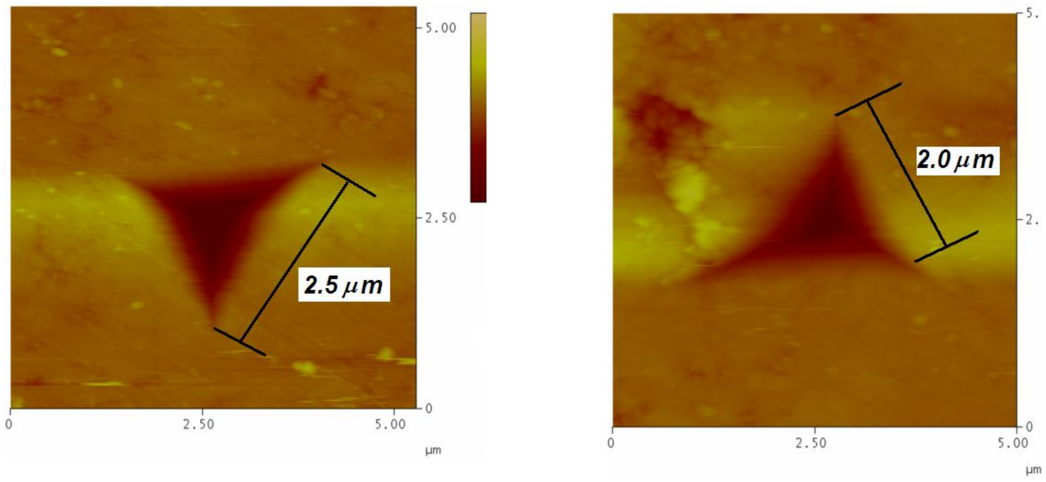

(a) (b)

Figure 4.8: The sizes of the indents in (a) inner sub-layer (b) outer sub-layer from P_{max}= 20 mN nanoindentation.

The inner sub-layer indents under a 20 mN max load are also larger than the outer, i.e. 2.5 µm (Figure 4.8a) and 2 µm (Figure 4.8b). This may be related to the higher porosity and finer grain microstructures of the inner sub-layer. From the TEM analysis, the average grain size of the outer sub-layer was estimated to be 1 µm compared to 0.2 µm for the inner sub-layer.

4.2.3 Development of a nanoindentation model of oxide layers

Since there is no analytical solution to the elastic-plastic indentation problem, Chen *et al.* (2006) proposed a finite element method to investigate the effect of porosity in porous material. Fleck *et al.* (1992) and Chen *et al.* (2006) used the Gurson model to study the effect of porosity on the indentation behaviour of porous solids. The Gurson model simulates the plastic yield of a porous or void containing material using the following yield condition:

$$\frac{3}{2}\frac{S_{ij}S_{ij}}{(\sigma_y^D)^2} + 2f\cosh\left(\frac{3\sigma_m}{2\sigma_y^D}\right) - [1 + f^2] = 0 \qquad (4.1)$$

In Equation (4.1) $\sigma_m = 1/3\sigma_{kk}$ is the hydrostatic pressure, $S_{ij} = \sigma_{ij} - \sigma_m$ is the stress deviator, and σ_y^D is the uni-axial yield stress of the fully dense matrix in the absence of voids. Gurson's approach to simulate the effect of ductile fracture was based on the assumption of continuum mechanics, with a modification of the yield condition and plastic flow rule by the void fracture. When the void volume fraction *f* decreases, the yield stress of the material increases, so where *f* = 0, the yield condition in Eq. (4.1) reduced to the von Mises yield criterion.

In this study the Gurson model (Gurson, 1975) was applied to the specimen and the elastic-plastic model was used to describe the behaviour of the indenter. In the ANSYS FE program, the indenter and the specimen were meshed with SOLID45, as shown in Figure 4.9. Contact elements (CONTA174) were used along the top surface of the bulk oxide (specimen) and target elements (TARGE170) were placed along the bottom surface of the indenter. The Berkovich indenter geometry was modelled as a cone (Bruno et al., 2004) with a vertex angle of 68 degrees. The specimen and the indenter were modelled with 23001 elements and 816 elements respectively.

A prescribed displacement in the y-direction was applied to the bottom surface of the specimen (bulk oxide scales) to control the loading and unloading steps, and at each step the reaction force in the y-direction along the bottom line was measured. The simulated indentations were performed using several displacement steps. The displacement size step during the loading and unloading parts was 2.95 nm.

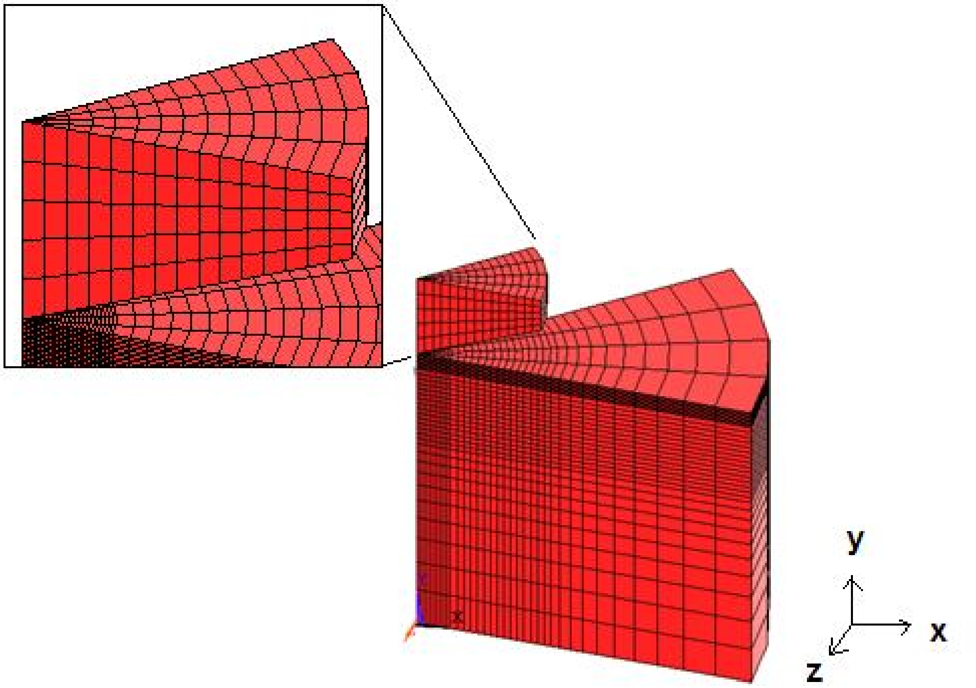

Figure 4.9: Mesh of the sample and indenter in the FE nanoindentation model.

Considerable care was taken while simulating the nanoindentation, for instance Liu *et al.* (2008) reported that the load curve in their simulation was wavy. They claimed this phenomenon is mostly related to the strain rate sensitivity and work hardening in the constitutive model. Hughes *et al.* (1976) explained this problem by punching with triangular and parabolic shaped punches. They also suggested that more sensitive (*i.e.* higher order) impact and release conditions should be applied to avoid taking extremely small steps during the impact and release phases of a contact problem. In the initial process, the simulation also suffered this kind of problem but it was dealt with by changing the load step (increment of depth). Figure 4.10 summarises the trials and errors that occurred in the simulation in order to obtain the ideal loading curve. If the mesh was too small or the load step too large, the simulation could become face distorted, whereas with a large mesh or with too low a load step, the loading curves of load-displacement could become wavy.

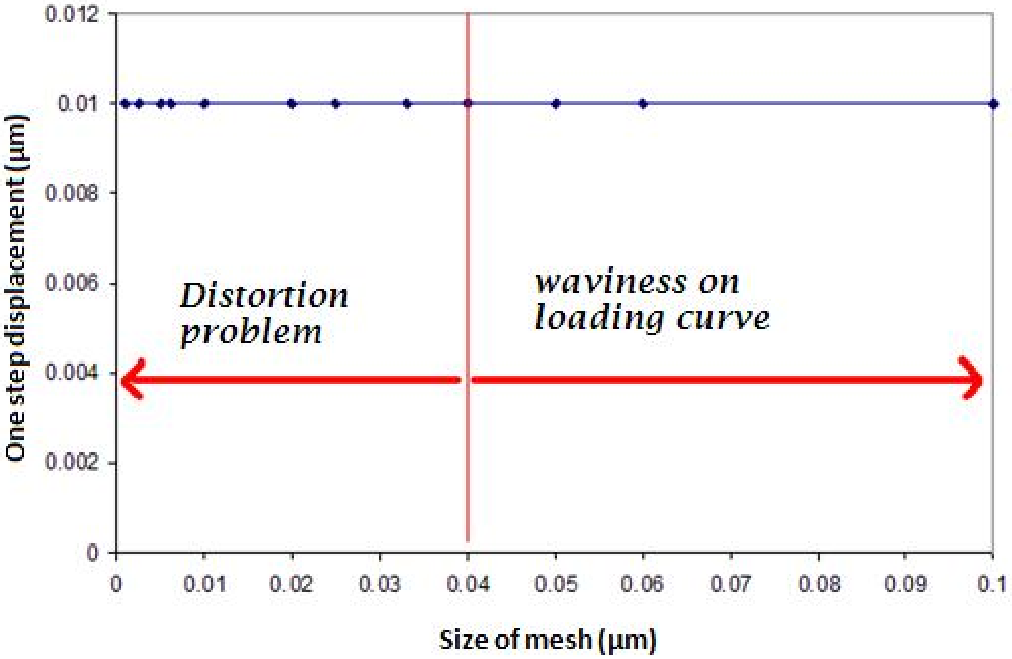

Figure 4.10: The effect of increment (time step) on load-displacement curves.

An example of the loading curve for an ideal and a wavy one is shown in Figure 4.11. The difference between the two loading curves stems from the size of mesh and also is related to the load step. It is obvious here that with the 0.06 μm size mesh the loading curve was affected more than the unloading part and led to waviness. In the simulations, some considerations regarding this problem were taken into account.

Displacement control in the y-direction was applied to the bottom surface of the specimen (bulk oxide scales) to control the loading and unloading steps. At each step the reaction force in the y-direction along the bottom line was measured. The simulated indentations were performed using several displacement steps, the size of which while loading and unloading the parts was 2.95 nm.

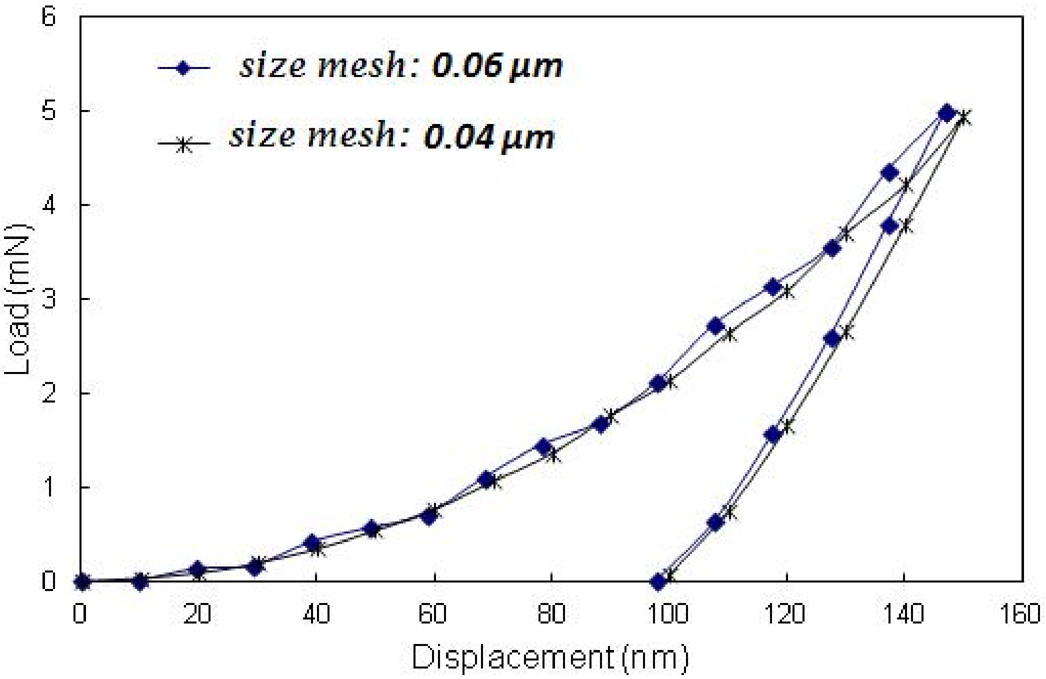

Figure 4.11: The effect of mesh on load-displacement curves.

4.2.4 Validation of the FE model

In order to ensure the reliability of the FE model, the FE simulated load-displacement curve was compared with the nanoindentation measurement from Lichinchi *et al.* (1998) in Figure 4.12. The tested sample was a titanium alloy (TiN) coating on high speed steel (HSS). The sample is a typical sample of a hard film on a softer substrate. The elastic modulus of the TiN sample, the HSS, and the diamond indenter were 427 GPa, 218 GPa, and 1141 GPa respectively. The input Poisson's ratio and yield stress of the TiN sample were 0.25 and 13.5 GPa respectively, and 0.3 and 1.8 GPa for the HSS. The Poisson's ratio and yield stress of the diamond indenter were 0.07 and 35.7 GPa.

The FE derived load-displacement curve agreed reasonably well with the Lichinchi *et al.*(1998) results for both the loading and the unloading parts, but the loading curve showed some deviations from the measured curve, possibly due to differences in the actual and assumed yield strength in the FE model. Other possible reasons for the disparity are the rounding of the tip (Shih *et al.*, 1991) and difference in the actual physical shape of the indenter i.e. Berkovich's indenter was used in the experiment and conical tip in the simulation.

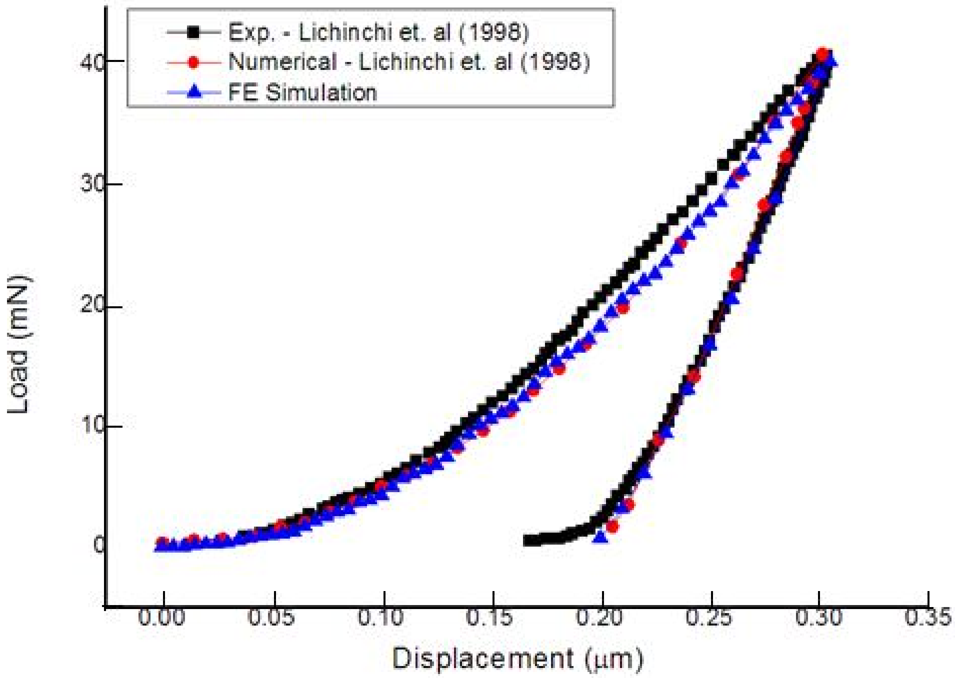

Figure 4.12: Loading-unloading curves: comparison between experimental & numerical data of Lichinchi *et al.* (1998) and the present FE simulation.

4.2.5 Iterative process for simulating the load-displacement curves

As the mechanical properties of the oxide layer were not known, the FE simulation was started with assumed properties. These inputs were then systematically refined until the simulated load and displacement curves matched the measured curves. The correct mechanical properties of the oxide layer were then inferred from this unique set of optimum properties.

The iterative process is described in Figure 4.13. Initially an assumed set of mechanical properties was used in the nanoindentation simulation. The slope of the beginning of the unloading curve (*dP/dh*) is the first feature of the curve compared with the experimental curve. As (*dP/dh*) is related to the elasticity of the material, it is expected to be sensitive to E and υ, hence E was tuned first. The refinement of E serves as a coarse adjustment followed by υ as the fine adjustment.

This refinement process was iterated until the slope criterion Eq. (4.2) was satisfied, such that

$$\frac{\left(\frac{dP}{dh}\right)_{EXP}-\left(\frac{dP}{dh}\right)_{FEM}}{\left(\frac{dP}{dh}\right)_{EXP}} < 1\,\% \tag{4.2}$$

After the slope of the unloading part was matched satisfactorily, the maximum load was then compared. To reach the same depth of indentation, the maximum load applied varied with the yield strength of the oxide σ_y. Hence σ_y was chosen as the next tuned parameter during coarse refinement, followed by porosity for fine tuning. The σ_y search continued until the P_{max} criterion (Eq. 4.3) was satisfied.

$$\frac{P_{max,EXP}-P_{max,FEM}}{P_{max,EXP}} < 1\,\% \tag{4.3}$$

The effects of mechanical properties on the load displacement curve of the oxide layer are demonstrated below. As Figure 4.14 shows, *E* has a significant influence on the slope of the unloading portion, while the other properties σ_y, υ and f had little or almost no influence on the slope, as shown in Figure 4.14b and Figure 4.15. In Figure 4.14a, σ_y, υ and *f* are kept constant in order to observe the dependence of the unloading slope on *E*. The value of *E* was varied from 90 to 110 GPa. It can be seen that the starting slope *dP/dh* of the unloading part of the load displacement curves decrease as *E* decrease. The same trend can also be seen in Figure 4.14b for the υ effect, although with much less sensitivity. As expected, the slope is not sensitive to σ_y and *f* (Figure 4.15). The correlation of *E* to *dP/dh* seems to be monotonical, which means there is a unique *E* that satisfies Eq. (4.2).

Figure 4.15 shows the effect of σ_y and *f* on the load displacement curves. In Figure 4.15a, *E*, υ and f are kept constant in order to observe the effect of σ_y on P_{max}. It is seen that P_{max} decreases monotonically as σ_y decreases, and although *f* has the same effect as σ_y it is to a much less degree.

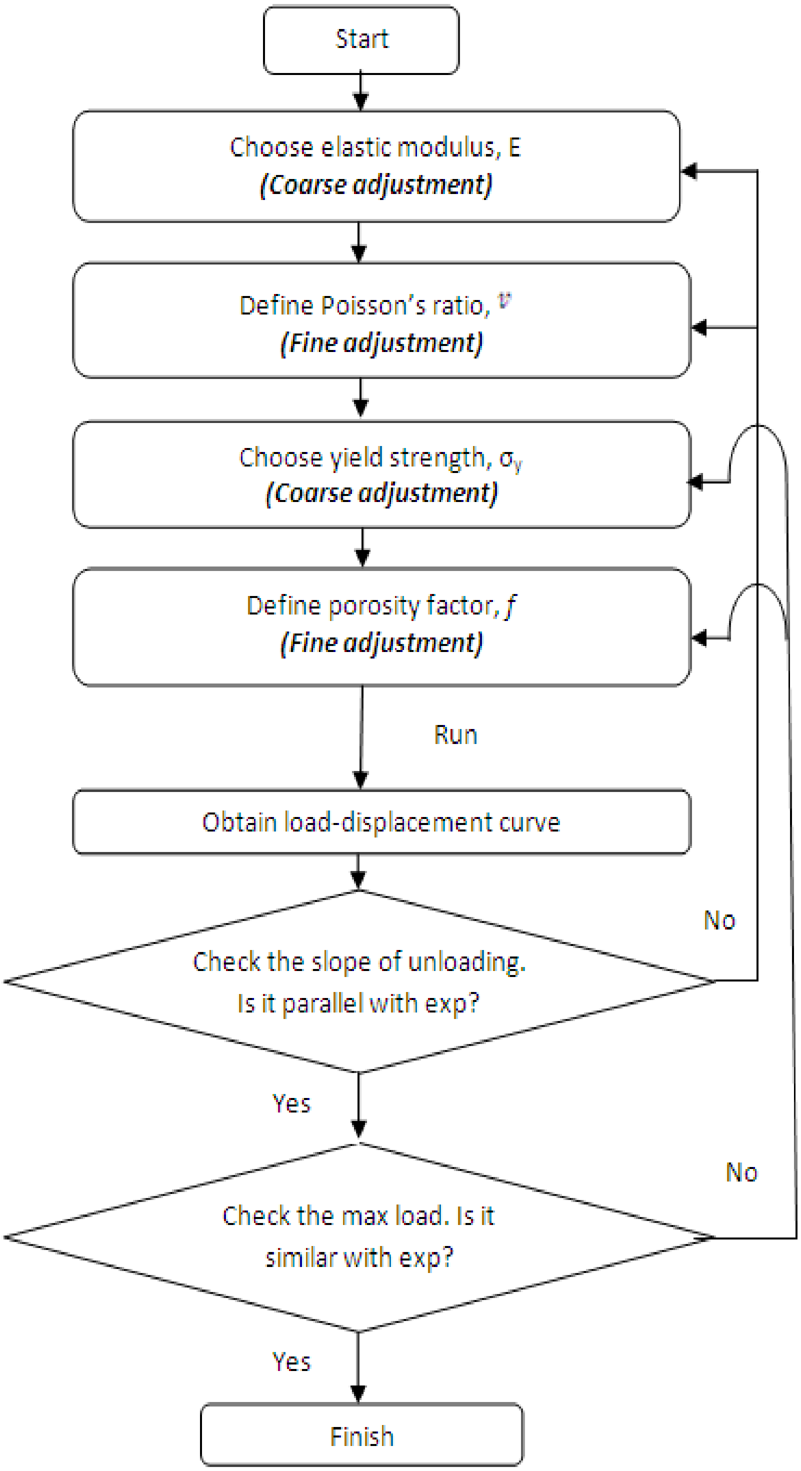

Figure 4.13: Iterative scheme of the FE indentation simulation.

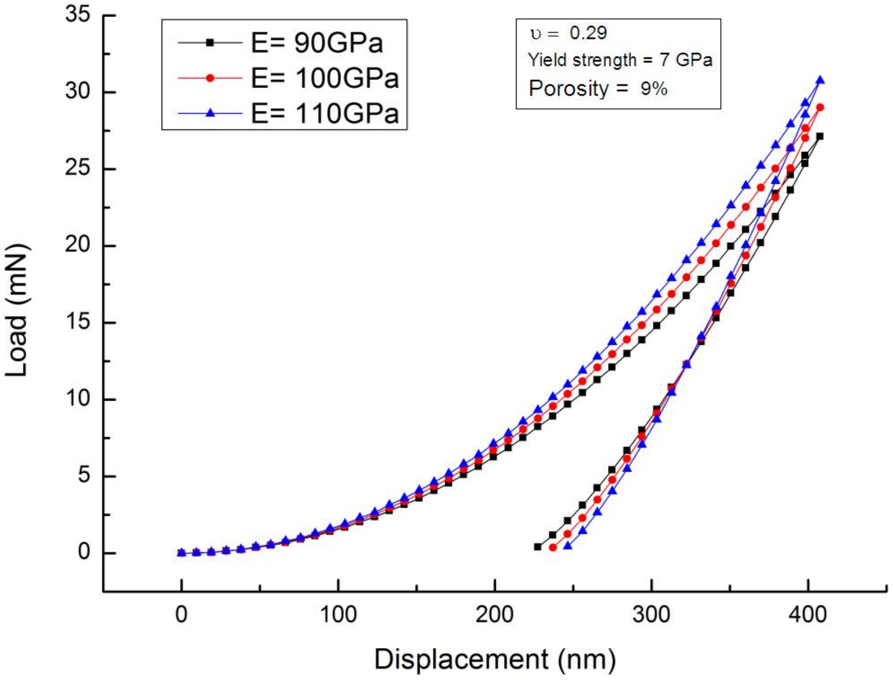

(a)

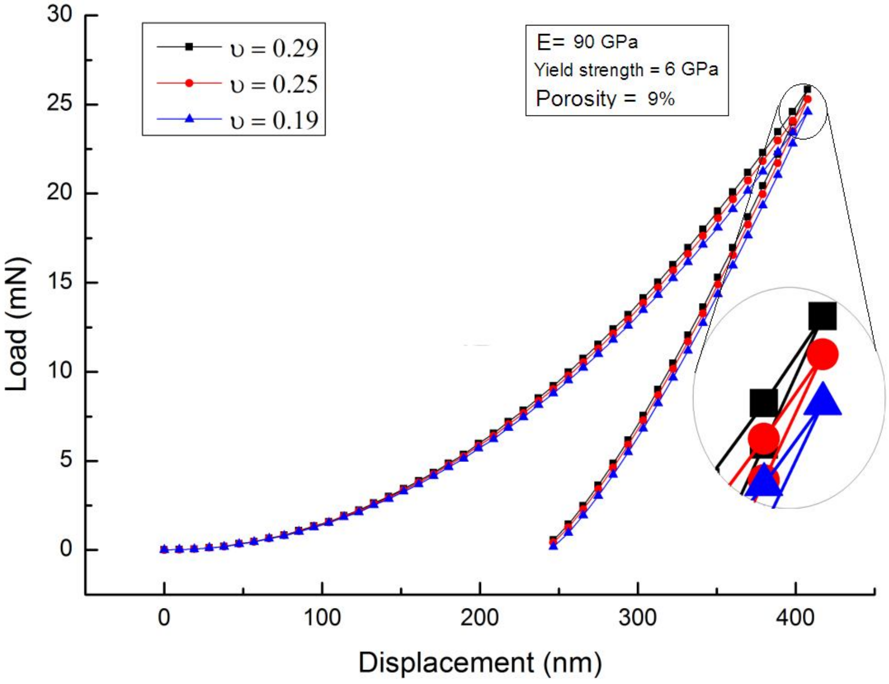

(b)

Figure 4.14: (a) Effect of elastic modulus and (b) Poisson's ratio to load-displacement curves.

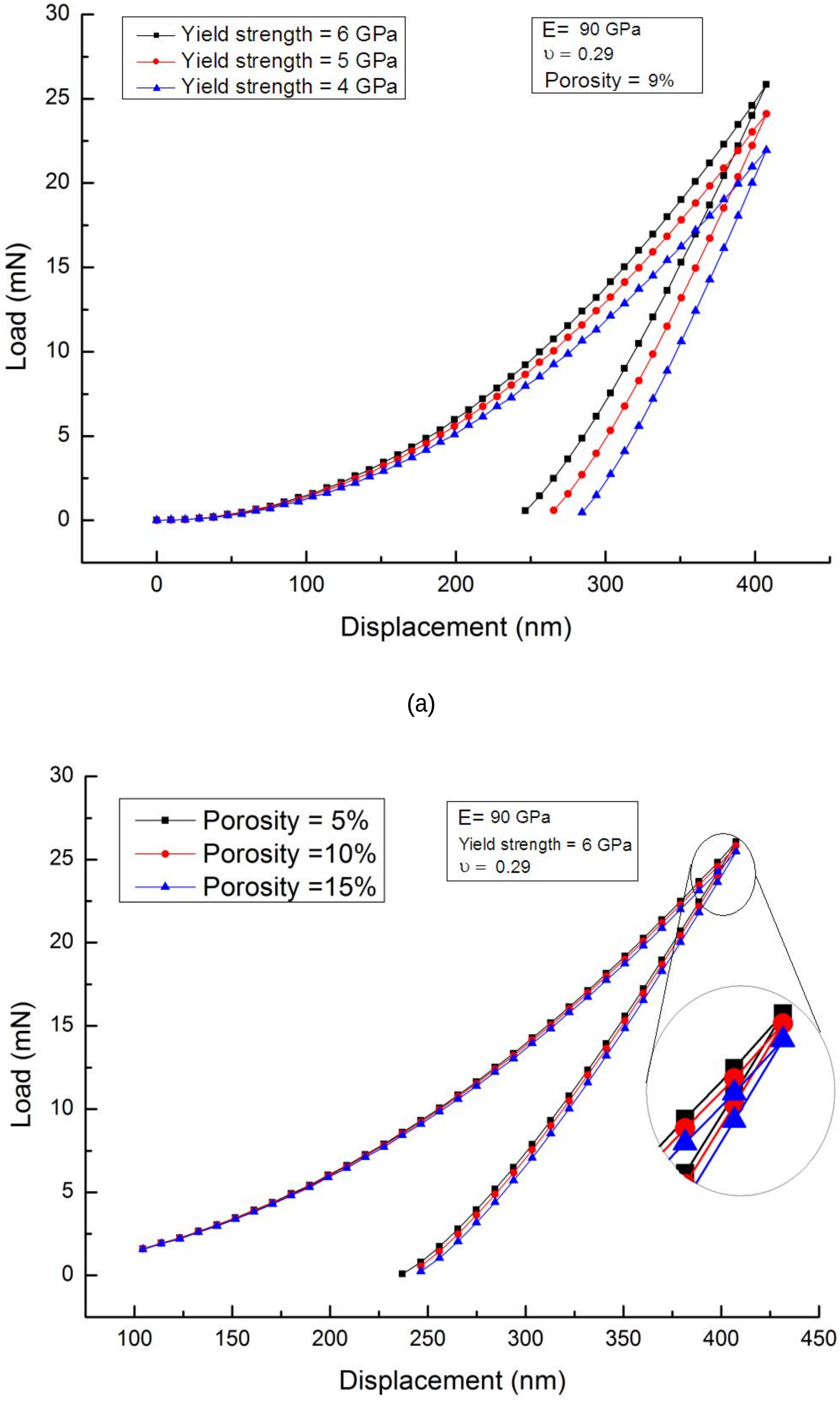

(a)

(b)

Figure 4.15: (a) Effect of yield strength and (b) Porosity to load-displacement curves.

Figure 4.14a and 4.15a show the effect of *E* and σ_y on P_{max}. Hence both can be used as refinement parameters to satisfy the convergence criterion Eq. (4.3). The question is which one is the right one. *E* is known to affect *dP/dh* and P_{max} but σ_y only affects P_{max}, which suggests that matching the slope can be achieved by tuning *E* and υ until the criterion Eq. (4.2) is satisfied. This is then followed by refining σ_y and *f* until Eq. (4.3) has been satisfied. As the second refinement would not affect the slope, the result is a unique set of material values for Young's modulus, Poisson's ratio, porosity, and yield strength.

4.3 Discussion

A combined nanoindentation simulations and experiments to determine the mechanical properties of oxide scale formed on high speed steel based on load-displacement curves was developed. Nanoindentation experiments were carried out on the oxide layers formed on HSS surface first, and then finite element simulations were performed via the iteration to identify the effect of each parameter on the load-displacements. The load-displacements obtained, namely the maximum load and unloading curve, were matched when the correct mechanical properties were applied.

It was found from the experimental works that the oxide layer formed on the HSS sample consisted of two oxide sub-layers. The outer layer was Fe_2O_3 and the inner layer was $(Fe,Cr)_3O_4$. The difference in the maximum depth of penetration between these two sub-layers is significant in that two distinct sub-layers were clearly identified. The indentations were larger in the inner than the outer which may be related to the higher porosity and finer grain microstructure of the inner sub-layer. The residual indent size on the outer oxide layer at 5 mN was around 0.7 μm (Figure 4.7b), while the average grain size of the iron oxide in the outer layer was more than 1 μm (Figure 4.3). Hence, the indentations on this layer are more likely to land on a single grain of oxide, as shown in Figure 4.16a. Another possibility of indentation on the outer layer is on the locations that are very close to these pores (Figure 4.16b). The nanoindentations on these locations will affect the load-displacements obtained, and the measured mechanical properties, which is why the load-displacement curves of the outer sub-layer had a shallower maximum depth of penetration than the inner sub-layer.

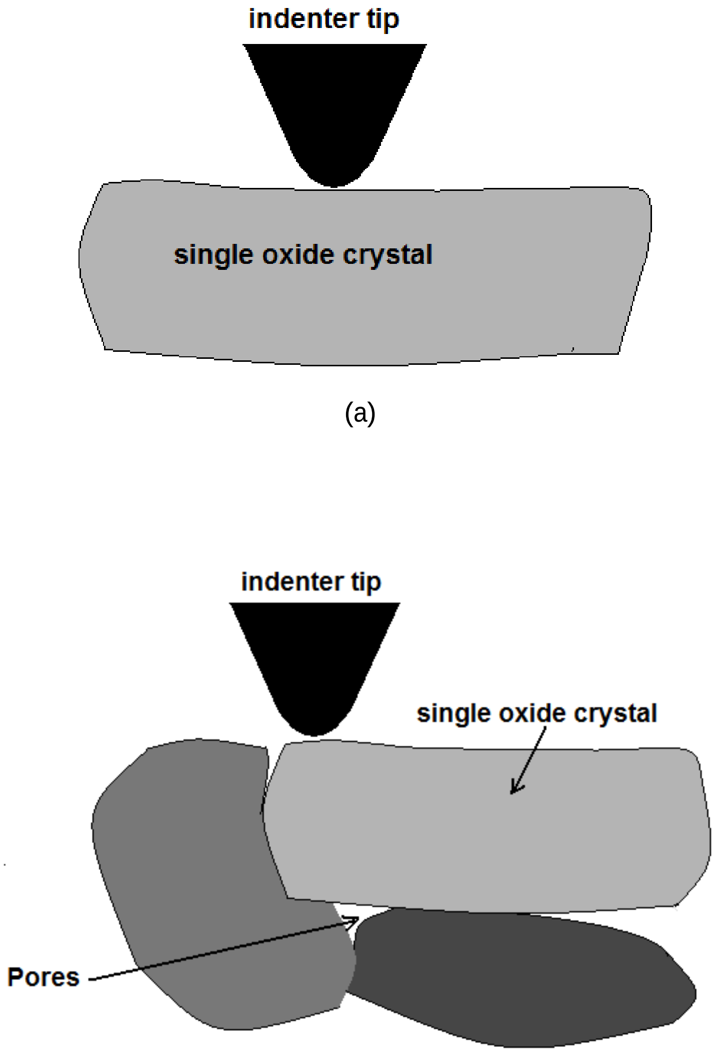

(a)

(b)

Figure 4.16: Schematic illustration of nanoindentation on the outer oxide layer. (a) An indentation on a single oxide crystal and, (b) an indentation at a location close to the pores and the grain boundary.

The residual indent size on the inner oxide layer at 5 mN is approximately 1.25 μm (Figure 4.7a). The load-displacement curves of the inner sub-layer indentations show a deeper maximum depth than the outer sub-layer because this layer was more sensitive to the porosity, grain size, grain boundaries, and binding energies among the oxides. From the TEM image (Figure 4.3), it can be confirmed that the percentage of porosity of the inner sub-layer was higher than the outer sub-layer. Compared to the size of fine-grained oxides (< 200 nm) in the inner oxide layer, the indentations on this layer can be illustrated as shown in Figure 4.17.

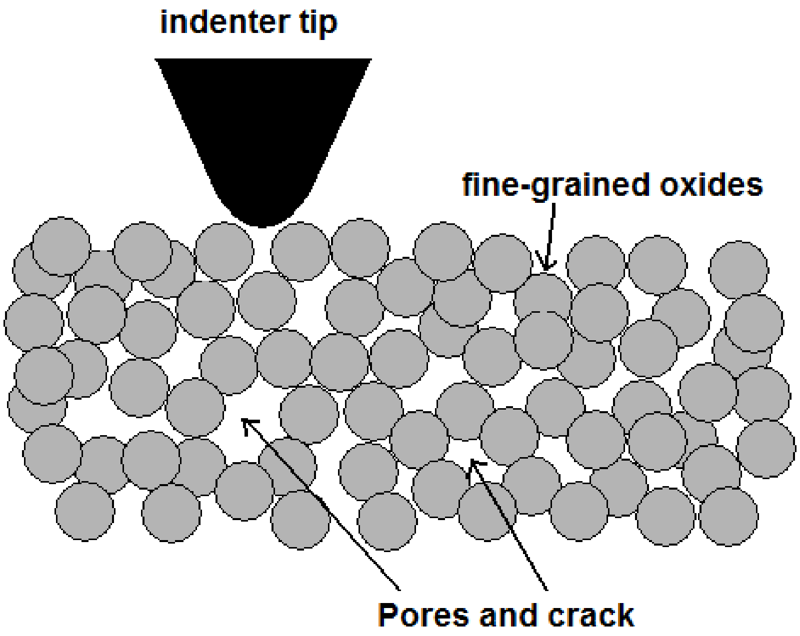

Figure 4.17: Schematic illustration of nanoindentation on the inner oxide layer.

From the iterative approach investigation it was found that *E* has a significant influence on the slope of the unloading portion while other properties σ_y, v and *f* have little or almost no influence on the slope. The result showed that σ_y has a noteworthy influence on P_{max} where P_{max} decreased monotonically as σ_y decreased. Although *f* has the same effect as σ_y, it is to a much less degree. The results from this investigation can be used as a basis to develop a systematic approach to obtain and refine the mechanical properties of the oxide layers. The detailed results of the mechanical properties of oxide layers on high speed steel will be discussed in Chapter 5.

4.4 Conclusions

In this chapter a methodology based on nanoindentation experiments to investigate the mechanical properties of the oxide layer was developed. The nanoindentation load-displacement behaviour of the inner and outer oxide layer with a Berkovich indenter was carefully established an improved method for determining the mechanical properties from the nanoindenation load-displacement curves.

The differences in hardness of the materials are apparent from the large differences in the depth attained at a maximum load. When the depth of indentation of the outer layer is small compared to the inner layer, the contact behaviour is dominated by the hard grains and small pores in the top layer. These different depths of penetration indicate that the outer sub-layer of Fe_2O_3 is generally harder than the inner sub-layer. The result presented using SEM, AFM, and TEM techniques confirmed the hypothesis. The method of analysis described in this chapter can be used to provide a useful computation of simulated load-displacement curves, where the mechanical properties of oxide scale are derived.

From the iterative approaches investigation, *E is* shown to have a significant influence on the slope of the unloading portion while σ_y has an influence on the P_{max}. The other properties, σ_y, υ, and *f* has little or almost no influence on the slope. The results of this investigation can be used as a starting point to determine the mechanical properties of the oxide layers via a systematic refinement approach.

Chapter 5

Characterisation and determination of the mechanical properties of the oxide layer

In the hot rolling process of steel, high speed steel (HSS) work rolls have been widely used because of their excellent mechanical and wear resistance properties at elevated temperatures (>700°C). Under these conditions oxides can rapidly form on the surface of the work rolls by the diffusion of ionic species across the crust (Kim *et al.,* 2003; Molinari *et al.,* 2000; Garza-Montes-de-Oca *et al.,* 2011). The oxide layer can act as protective coating that influences the transfer of heat, and the wear and friction behaviour at the interface between the strip and the roll, and hence prolong the life of the work roll (Garza-Montes-de-Oca and Rainforth, 2009; Garza-Montes-de-Oca *et al.,* 2011; Quinn, 1983).

Because wear on the work roll substrate depends on the wear resistance of the oxide layer, it is important that the mechanical properties of the oxide layer be known accurately. This chapter discusses the mechanical properties of oxide layer that forms on high speed steel work rolls. The mechanical properties of the sub-layers, including elastic modulus, yield strength, Poisson’s ratio and porosity, are inferred from the input parameters to the FE simulations after the simulated load-displacement curves match the experimental curves to within the specified tolerance. At the end of this chapter the interaction correlation between the mechanical properties and nanoindentation parameters, such as the maximum load and loading slope of the load-displacement curves, are established via multiple regression analysis.

One motivation for studying the characteristics and mechanical properties of oxide layer was because the existing knowledge of oxide layer properties is limited, and no studies have ever been carried out on the mechanical properties of oxide layers formed on HSS surfaces, even though the oxide scale plays a significant role in the tribological performance of a work roll in hot rolling. Nicholls and Hall (1994) compared different techniques such as mechanical properties probe, acoustic microscopy, dynamic resonance, and impulse excitation techniques to measure the hardness and elastic modulus of the bulk oxides Al_2O_3 and Cr_2O_3 and compared them with other types of oxides, including FeO, $Fe_2O_3$and Fe_3O_4. However their techniques only measured the mechanical properties of the bulk oxide systems. Nicholls and Hall (1994) reported that data from bulk oxides behaves differently from the oxide layers, for example, there is a significant difference in the values of the mechanical properties between bulk alumina and oxide scales. The discrepancy might be due to the surface interaction of the substrate that influences the characteristics and microstructure of the oxide layer. For this reason the mechanical properties of the layer of oxide formed on HSS surface remain unexplored, and gaining an understanding of this is an important step towards more accurate prediction the wear of hot rolls.

5.1 Finite element simulations

Nanoindentation experiments can only measure some mechanical properties of the oxide layer. One of the parameters that cannot be obtained from the load-displacement analysis is the porosity of the oxide layer. In porous media the load displacement relationship depends on the porosity and grain sizes, which are largely heterogeneous. Moreover, from the measured load-displacement curve, and based on the Oliver-Pharr method (1992), only a reduced elastic modulus ($E/1-\upsilon^2$) can be obtained directly, not the sample elastic modulus E due to the unknown Poisson's ratio value which is porosity dependent. In this work the mechanical properties of the oxide layer and the elastic modulus and hardness were determined using combined nanoindentation experiments with 5 mN and 20 mN maximum loads and finite element (FE) simulations.

The mechanical properties of the oxide sub-layers that cannot be directly measured from the nanoindentation experiments, e.g. the elastic modulus E, the yield strength σ_y, Poisson's ratio υ and the pore fraction f were determined from the FE simulations input parameters. These were optimum parameters that yielded a close agreement between the simulated and measured nanoindentation load-displacement curves. The finite element model used Gurson's model of plasticity for porous material. Information obtained from this chapter will be used to further understand the mechanics of friction and the wear of high speed steel rolls.

5.2 Results

5.2.1 Variation of mechanical properties from the outer to inner sub-layers

Each load-displacement curve from the nanoindentation experiment was simulated from the outer to inner oxide sub-layers (Figure 5.1). Figure 5.2 shows the load displacement curves at points 9 to 5 (*outer to inner sub-layer*) in the oxide layer (please refer to Figure 5.1). Points 8 and 9 (see Figure 5.2a-b) are the load displacement curves in the outer sub-layer while points 7-5 (Figure 5.2c-e) are in the inner sub-layer. At a maximum load of 5 mN the curves show that the maximum indentations in the inner sub-layer were deeper than in the outer sub-layer. This can be explained by the different levels of porosity where the inner sub-layer is more porous than the outer sub-layer and hence is more sensitive to the presence of voids.

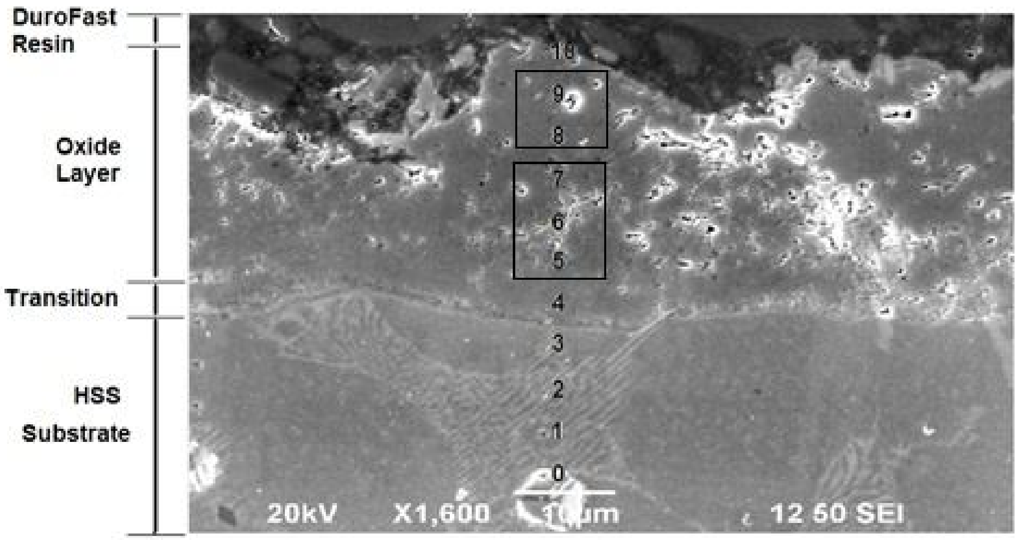

Figure 5.1: Nanoindentation impressions from the outer to inner oxide layer.

Figure 5.3 shows that the grains of the inner layer (0.2 μm) are smaller than the outer sub-layer (1 μm), which means the indentations are more likely to land on a single grain in the outer sub-layer and on multiple grains in the inner sub-layer.

Indentations on multiple grains and higher porosity (*voids*) area are more sensitive to the grain boundaries and result in a lower hardness of the inner sub-layer.

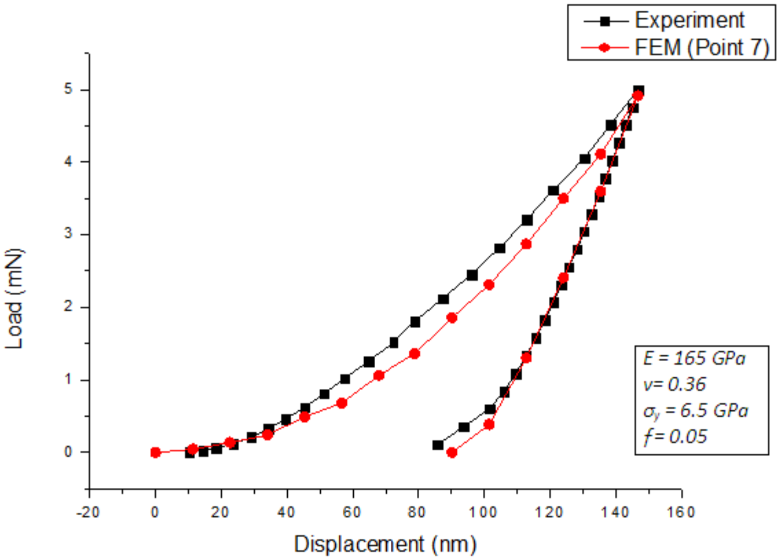

(a)

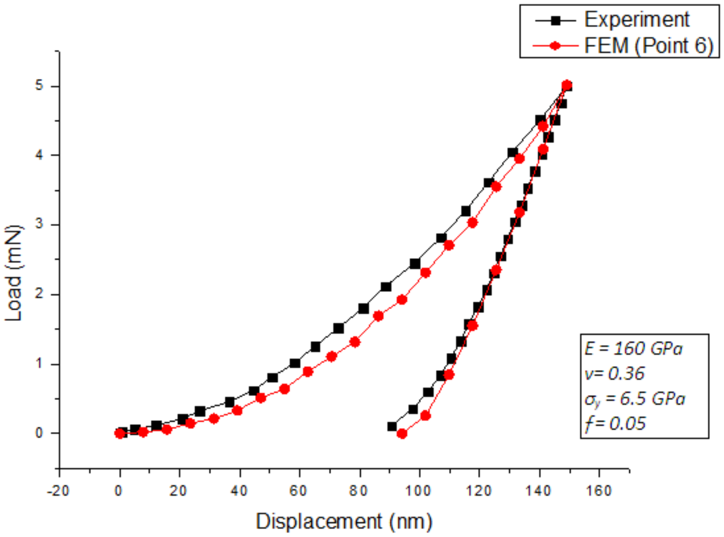

(b)

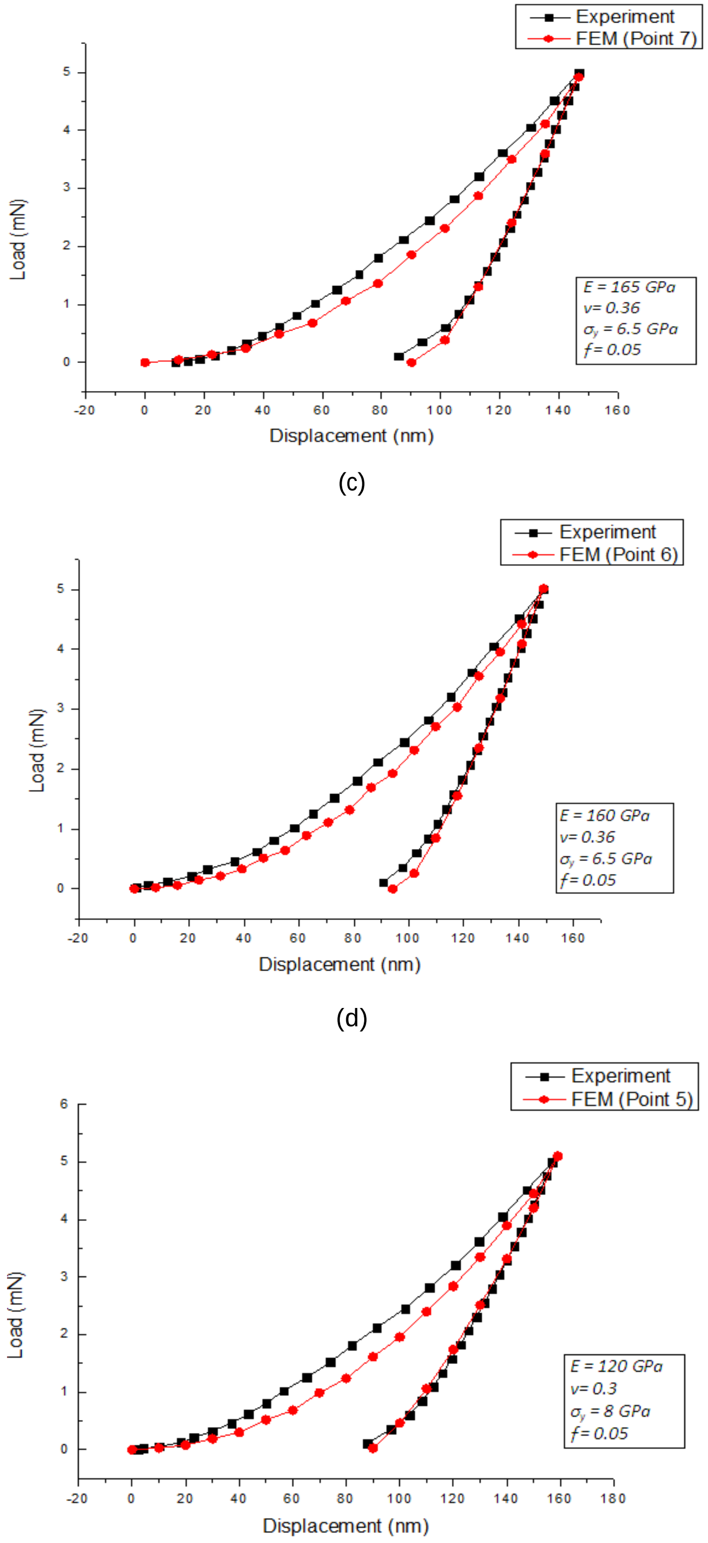

(c)

(d)

(e)

Figure 5.2: Comparison of the measured and simulated load displacement curves: (a) point 9, (b) point 8, (c) point 7, (d) point 6, and (e) point 5.

To validate the FE model, the experimental and FE modelled load-displacement curves were compared. Figure 5.2 shows the load-displacement curves from the experiments and the FE simulations. The experimental load-displacement curves and those obtained from the FE simulations generally match well, particularly in the unloading portion where the elastic modulus *E* was evaluated. The loading curves show a larger deviation than the unloading curves. The difference in the loading region between the experimental curves and the simulated ones can be explained by the different tip radius used (Kopernik and Pietrzyk, 2007) and the most advanced procedure for thin films and nanoindentation testing with dual sharp indenter, using the inverse algorithm and sensitivity analysis (Dao *et al.,* 2001 and Chollacoop *et al*. 2003). According to Kopernik and Pietrzyk (2007), conditions for numerical simulation of nanoindentation test are similar to those in laboratory test, but a geometry simplification is made. In the simulations a perfectly sharp indenter was assumed while in the experiments the tip of the indenter must have been slightly rounded. Therefore the load required to push the indenter is greater in the cases with rounded tips than with the sharp tips used in the simulations.

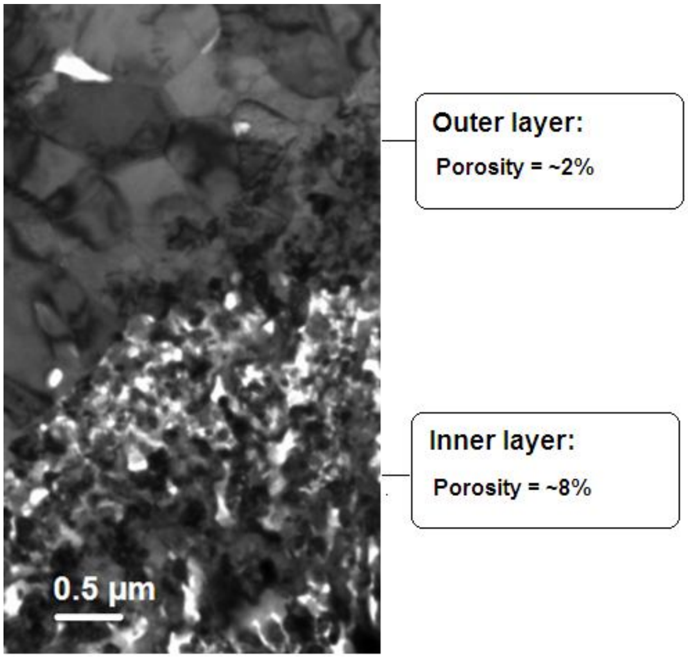

Figure 5.3: The porosity of the oxide layer.

A summary of the mechanical properties extracted from the oxide layer at points 9 to 5 is given in Table 5.1 for the 5 mN maximum load cases. The results in Table 5.1 were measured across the thickness from the outer to inner sub-layers. The hardness *H* and elastic modulus *E* values vary with the depth from the surface. There are large differences in the properties and microstructures of the inner points (5 to 7) and the outer points (8 and 9). It was found that *H* and *E* decreased with depth. The average elastic modulus *E* of the inner sub-layer was approximately 42 % lower than the outer one.

Table 5.1: A summary of the mechanical properties of the oxide layer at different depths for a maximum nanoindentation load test and simulation of 5 mN.

point	max. disp. (μm)	Result (Output)								Location of indent
		Poisson ratio, v	Elastic Modulus, E (GPa)	Dense yield strength, σ_y^D (GPa)	Porous yield strength, σ_y^p (GPa)*	Porosity factor, *f*	Hardness, H (GPa)	Constraint factor, C (H/σ_y)	E/◎$_y$	
9	0.118	0.19	250	15	14.6	0.02	24.4	1.63	16.67	Outer sub-layer
8	0.114	0.29	260	14	13.3	0.02	27.9	1.86	17.33	
7	0.147	0.36	165	6.5	6.12	0.05	15.0	2.31	25.38	Inner Sub-layer
6	0.149	0.36	160	6.5	6.12	0.05	14.3	2.20	24.61	
5	0.157	0.3	120	8	7.53	0.05	13.6	1.70	15	

*Note: The calculation of porous yield strength (σ_y^P) based on Chen *et al.* (2006).

The average *H*, *E*, and σ_y of the outer sub-layer are 26.15 GPa, 255 GPa, and 14.5 GPa respectively. The variation in the yield strength σ_y throughout the layer also decreases with depth. The yield strength σ_y are in the 14-15 GPa range for the outer sub-layer and in the 6.5-8 GPa range for the inner sub-layer. This trend suggested there are differences in the levels of porosity, composition, and microstructure within the oxide layer. To contrast the differences in property, the variations of *H* and *E* across the sub-layer are shown in Figure 5.4. Based on these values, it is clear that the oxide layer developed on HSS surface can be divided into outer and inner sub-layers.

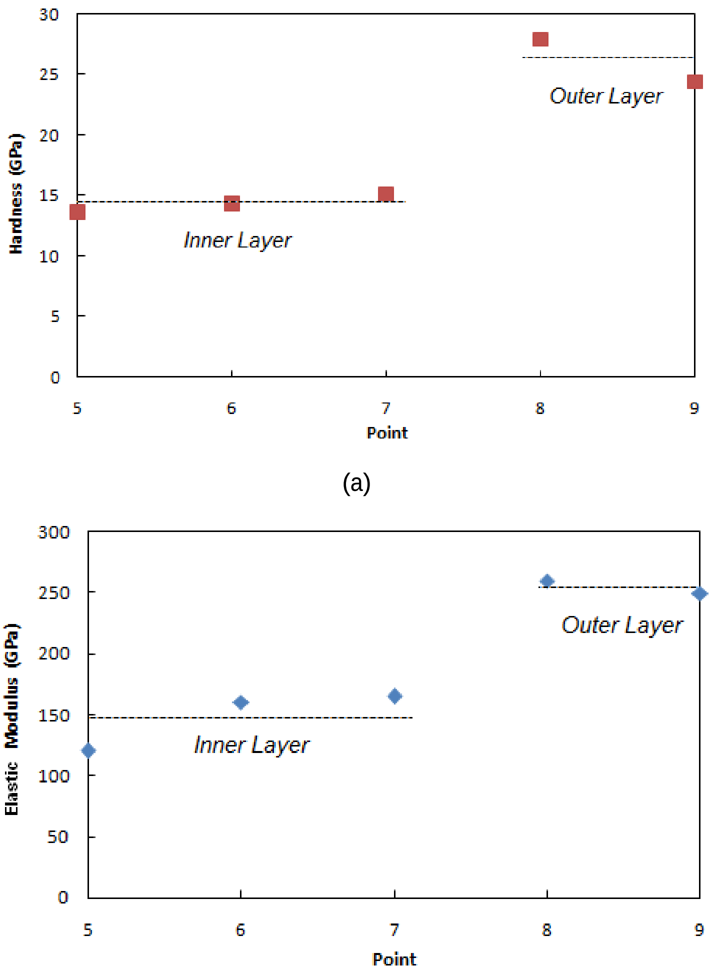

(a)

(b)

Figure 5.4: (a) *H* and (b) *E* based on indent position with 5 mN maximum load.

5.2.2 Mechanical properties of the oxide sub-layers for the outer and inner layers

To ensure that the differences shown in Figure 5.4 are accurate, row (*line*) array indentations at 5 mN (Figure 5.5) and 20 mN (Figure 5.7) were subsequently performed in each sub-layer. Each indentation was separated from the surrounding indents by a distance of 10 μm.

The combined results of the nanoindentation measurements and simulation are shown in Tables 5.1 to 5.3 for a maximum load of 5 mN, and in Table 5.4 to 5.5 for a maximum load of 20 mN. The results in Table 5.1 were measured across the thickness from the inner to outer sub-layers, and in Tables 5.2 to 5.5, from the rows of indentations in the inner and outer sub-layers. In each table, the input parameters of the simulation (all columns except columns 2 and 8) were chosen to match the maximum displacement (column 2) and the hardness *H* (column 8) measured in the nanoindentation experiments.

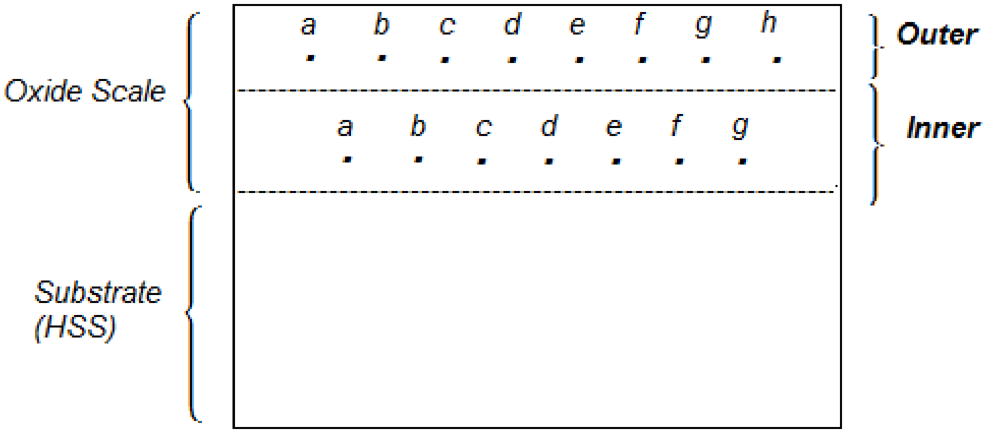

Figure 5.5: Sketches of the indent positions in the outer and the inner sub-layers with 5 mN maximum load.

Table 5.2: Summary of mechanical properties of outer oxide sub-layers with a maximum nanoindentation load of 5 mN.

Point	Max disp. (μm)	Result (Output)							
		Poisson ratio,ν	Elastic Modulus, *E* (GPa)	Dense yield strength, σ_y^D (GPa)	Porous yield strength, σ_y^P (GPa)*	Porosity factor, *f*	Hardness, *H* (GPa)	Constraint factor, *C* (H/σ_y)	E/σ_y
a	0.113	0.29	240	17	16.54	0.02	28.17	1.66	14.12
b	0.118	0.29	240	13	12.65	0.02	24.50	1.88	18.46
c	0.113	0.29	240	17	16.54	0.02	29.59	1.74	14.11
d	0.117	0.29	230	15	14.6	0.02	25.72	1.71	15.33
e	0.133	0.29	200	10	9.73	0.02	19.69	1.97	20
f	0.115	0.29	240	15	14.6	0.02	29.05	1.94	16
g	0.119	0.29	230	13	12.65	0.02	24.41	1.88	17.69
h	0.120	0.29	230	12	11.68	0.02	24.92	2.07	19.17

*Note: The calculation of porous yield strength (σ_y^P) based on Chen *et al.* (2006).

Table 5.3: Summary of mechanical properties of inner oxide sub-layers with a maximum nanoindentation load of 5 mN.

Point	Max disp. (μm)	Result (Output)							
		Poisson ratio,υ	Elastic Modulus, E (GPa)	Dense yield strength, σ_y^D (GPa)	Porous yield strength, σ_y^P (GPa)*	Porosity factor, f	Hardness, H (GPa)	Constraint factor, C (H/σ_y)	E/σ_y
a	0.157	0.30	120	8	7.53	0.05	13.61	1.70	15
b	0.149	0.36	160	6.5	6.12	0.05	14.22	2.19	24.62
c	0.154	0.33	180	5	4.71	0.05	12.88	2.58	36
d	0.181	0.3	120	4	3.76	0.05	9.88	2.47	30
e	0.148	0.36	220	5.5	5.18	0.05	12.53	2.28	40
f	0.207	0.3	90	3	2.82	0.05	7.03	2.34	30
g	0.147	0.36	165	6.5	6.12	0.05	15.05	2.31	25.39

*Note: The calculation of porous yield strength (σ_y^P) based on Chen *et al.* (2006).

A summary of the mechanical properties of the oxide layer extracted from the simulations is shown in Tables 5.2 and 5.3 for the 5 mN load test. The results in Tables 5.2 and 5.3 were measured from the rows of indentations in the outer and inner sub-layers. The values of *E* (200-240 GPa) of the outer sub-layer are higher than the inner sub-layer (90-220 GPa), as shown in Figure 5.6a. The large variation of *E* in the inner sub-layer is probably due to the influence of voids and a non-uniform porosity of the sub-layer. The smaller size grains of the inner sub-layer increase the sensitivity of the indentations to variations in porosity.

The *H* values of the outer sub-layer are approximately two times of the inner values due to differences in the microstructure, porosity, and composition of the sub-layers. The outer sub-layer consists of harder Fe_2O_3 while the inner sub-layer is made up of mostly Fe_3O_4. The *E* results obtained in this study (outer sub-layer = 200-240 GPa; inner sub-layer = 90-220 GPa) are within a similar range as the published data of bulk oxides for Fe_2O_3 and Fe_3O_4 studied by Nicholls and Hall (1994) in the range of 208-220 GPa except that the inner sub-layer shows larger variation of *E*. Nicholls and Hall (1994) obtained the results using mechanical properties microprobe (MPM), scanning acoustics, and techniques based on resonant frequency from measurements on the free surface.

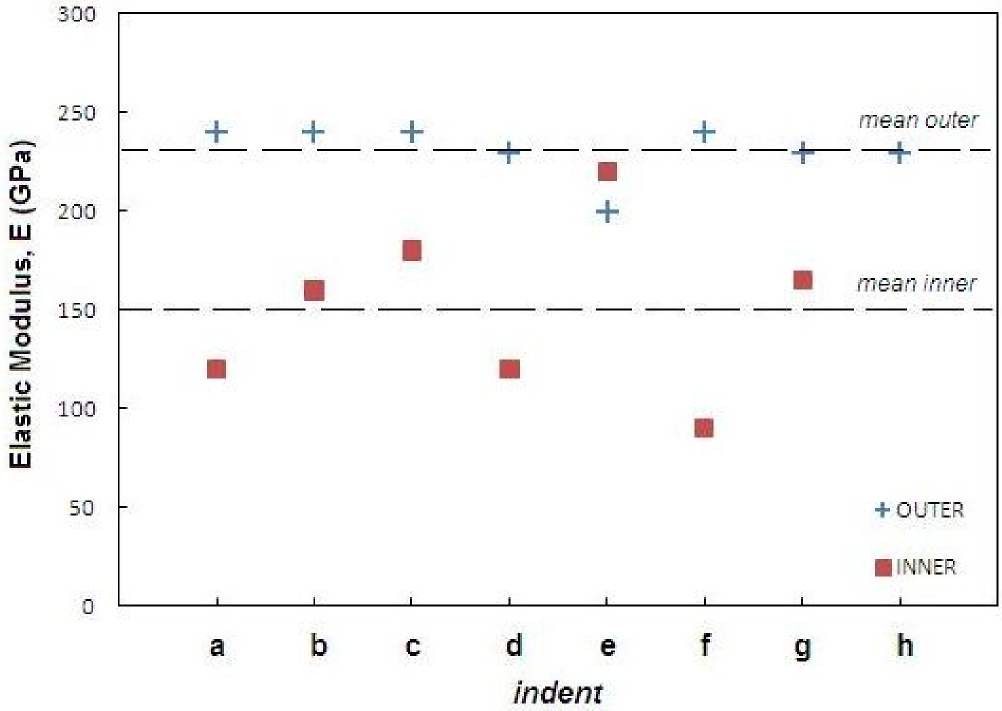

(a)

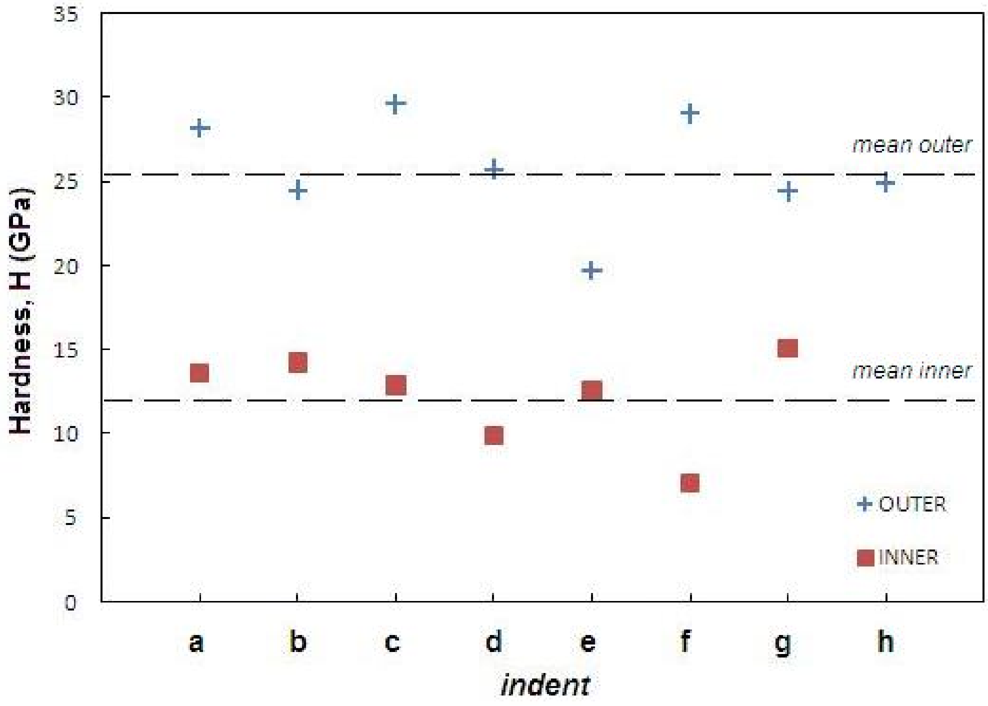

(b)

Figure 5.6: (a) *E* and (b) *H* based on indent position in the outer and inner layers for 5 mN load.

On the basis of the nanoindentation results with 20 mN maximum load, the indent positions in the outer and the inner sub-layers are illustrated in Figure 5.7. Tables 5.4 and 5.5 list *E*, σ_y, υ, and f from 20 mN maximum load experiments on the outer and inner sub-layers. The trend for the 20 mN load is similar to the 5 mN load experiments where the *E* and *H* of the outer sub-layer are higher than the inner ones due to the inner oxide layer being more porous and made up of smaller grains. The porosity of the oxide leads to "deficient" indentation, given the instability of the oxide caused by its porous nature and grade of "compactness". The appearance of the oxide layer in the TEM cross section (Figure 5.3) confirms this finding.

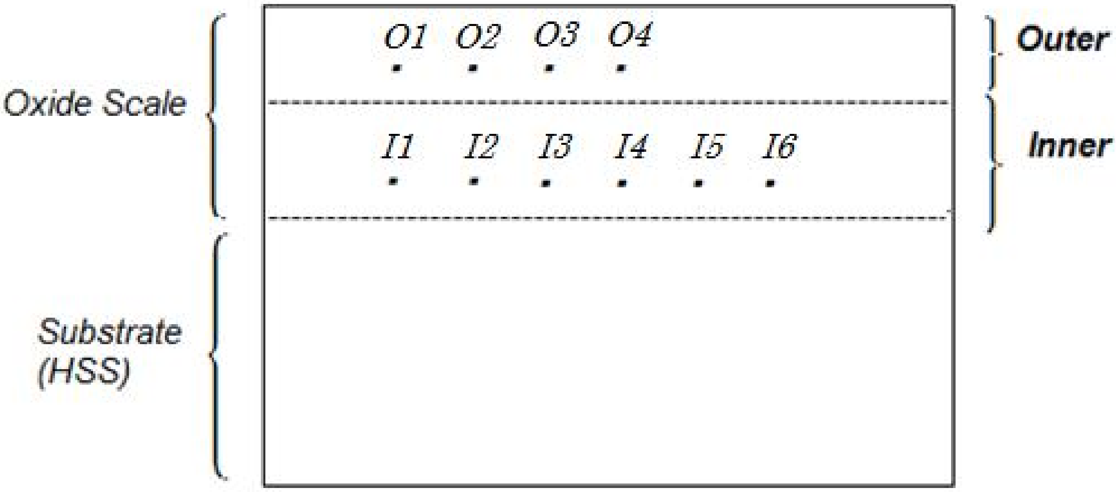

Figure 5.7: Sketches of the indent positions in the outer and the inner layers with 20 mN maximum load.

Figure 5.8 provides a graphical representation of *E* (Figure 5.8a) and *H* (Figure 5.8b) at different indent locations. *E* ranges between 130-245 GPa for the outer layer and 90-110 GPa for the inner layer (Figure 5.8a). The *H* average of the outer layer is about 13 GPa while the inner layer is 10 GPa.

Table 5.4: Summary of mechanical properties of outer oxide sub-layer with a maximum nanoindentation load of 20 mN.

Point	Max disp. (μm)	Result (Output)							
		Poisson ratio, ν	Elastic Modulus, *E* (GPa)	Dense yield strength, σ_y^D (GPa)	Porous yield strength, σ_y^P (GPa)*	Porosity factor, *f*	Hardness, *H* (GPa)	Constraint factor, *C* (H/σ_y)	E/σ_y
O1	0.312	0.19	160	6	5.84	0.02	12.26	2.04	26.67
O2	0.241	0.19	245	14	13.62	0.02	23.54	1.68	17.5
O3	0.313	0.25	180	5	4.71	0.05	11.32	2.26	36
O4	0.394	0.2	130	4.5	4.09	0.08	7.15	1.59	28.9

*Note: The calculation of porous yield strength (σ_y^P) is based on Chen *et al.* (2006). The first letter O in the point identification indicates the outer sub-layer and the number indicates the indent number (Figure 5.8).

Table 5.5: A summary of the mechanical properties of the inner oxide sub-layer with a maximum nanoindentation load of 20 mN.

Point	Max disp. (μm)	Result (Output)							
		Poisson ratio, ν	Elastic Modulus, *E* (GPa)	Dense yield strength, σ_y^D (GPa)	Porous yield strength, σ_y^P(GPa)*	Porosity factor, *f*	Hardness, *H* (GPa)	Constraint factor, *C* (H/σ_y)	E/σ_y
I1	0.338	0.3	100	6	5.64	0.05	11.46	1.91	16.67
I2	0.323	0.3	110	7	6.59	0.05	12.54	1.79	15.71
I3	0.326	0.29	110	7	6.36	0.08	12.23	1.75	15.71
I4	0.351	0.25	100	6	5.33	0.10	9.98	1.66	16.67
I5	0.408	0.29	90	3.5	3.14	0.09	7.09	2.03	25.71
I6	0.415	0.3	90	3.5	3.03	0.12	6.52	1.86	25.71

*Note: The calculation of porous yield strength (σ_y^P) based on Chen *et al.* (2006). The first letter I in the point identification indicates the inner sub-layer and the number indicates the indent number (Figure 5.8).

A comparison of *H* obtained from the 5 mN to the 20 mN maximum load experiments shows that the values from the smaller load are higher in the outer sub-layer. This phenomenon has probably been caused by softening effect arising from an interaction between the Geometrically Necessary Dislocations (GNDs) front and boundaries of the grain. According to Voyiadjis and Peters (2010), GNDs will accumulate during indentation which leads to an expansion of the plastic zone until the boundary of the plastic zone reaches the grain boundary (Figure 5.9).Upon reaching the grain boundary the plastic zone will stop expanding because it is obstructed by the boundary.

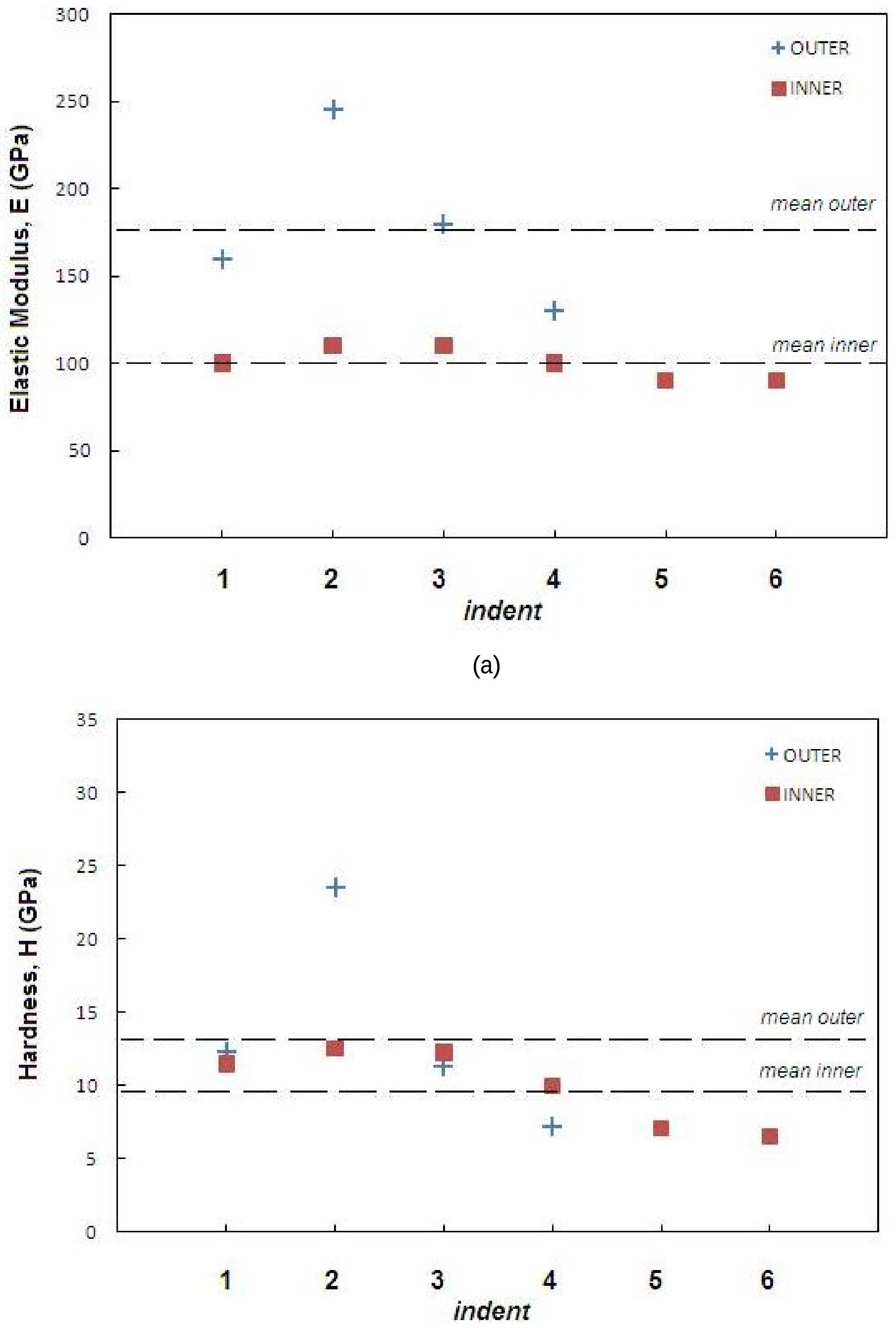

(a)

(b)

Figure 5.8: (a) *E* and (b) *H* based on indent position in the outer and inner sub-layers for 20 mN load.

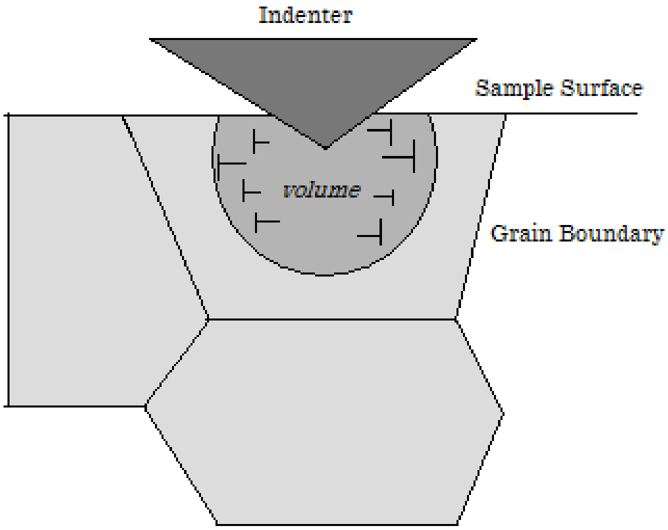

Figure 5.9: The expansion of the plastic zone is obstructed by grain boundary.

The effect of the size of the nanoindentation described above was not observed in the inner sub-layer. The *H* obtained from the 5 mN and 20 mN experiments is similar, as indicated in Figures 5.6b and 5.8b, and also from Tables 5.3 and 5.5. This may be explained from the structure of the oxide in the inner sub-layer which has smaller size grains and higher porosity; hence the indentation was less affected by the expansion of GND but more by the porosity and interactions at the grain boundary.

The relationship between porosity and yield strength can be seen from the results of the simulation, because it is assumed in the simulation that the outer sub-layer *f* range from 2% to 8% (Table 5.2 at 5 mN and Table 5.4 at 20 mN), and the inner *f* range from 5% to 12% (Table 5.3 at 5 mN and Table 5.5 at 20 mN).

The wide range of porosity in the simulation agrees with the values measured by TEM analysis. The measured porosity is shown in Figure 5.3 and the range is from 2% to 8%. The outer sub-layer has a higher yield strength than the inner sub-layer, which may be explained by the thin hematite layer growing first to form the upper sub-layer, followed by thick and porous hematite at the interface between the upper sub-layer and the HSS substrate. Nicholls and Hall (1994) suggested that oxide becomes more porous as it grows thicker. The present results suggest that since the outer sub-layer is less porous it has a lower Poisson's ratio. The Poisson's ratio-porosity dependence was reported by Boccaccini and Boccaccini (1997). They determined the Poisson's ratio and porosity relationship by a number of equations and approaches.

Because the outer oxide sub-layer is only slightly porous, its plastic behaviour is expected to be similar to a dense ductile material. According to Tabor (1985), there is a linear dependence of H/σ_y and E/σ_y bounded by two points (E/σ_y, H/σ_y) = (10, 1.5) and (E/σ_y, H/σ_y) = (100, 3). The property ratios of point 9 are consistent with Tabor's rule where $E/Y \approx 16.67$ and the ratio $H/Y \approx 1.63$ fit the linear dependence rule. The summary of the average mechanical properties obtained by the combined nanoindentation and FEM simulation is given in Table 5.6.

Table 5.6: Summary of mechanical properties of oxide layers on HSS.

Properties	Results				Comments
	5 mN		20 mN		
	Outer Sub-layer	Inner sub-layer	Outer sub-layer	Inner sub-layer	
Elastic modulus, *E*(GPa)	200-240	90-220	130-245	90-110	*E* =219-220 GPa for bulk Fe_2O_3 and *E* =208-210 GPa for bulk Fe_3O_4 (Nicholls and Hall, 1994)
Hardness, *H* (GPa)	26	12	13	10	*H* = 25 GPa for oxide scale formed on Fe_3Al (Tortorelli and Keiser, 1991)
Yield strength, σ_y (GPa)	14	5.5	7	5.5	σ_y = 22GPa for oxide scales on Fe-3wt%Si single crystal (Kramer *et al.*, 1999)
Poisson's ratio, υ	0.29	0.33	0.2	0.29	0.19 for bulk Fe_2O_3 and 0.29 for bulk Fe_3O_4 (Nicholls and Hall, 1994)
Porosity: Measured (%)	2%	8%	2%	8%	
Porosity : Simulation (%)	2%	5%	2-8%	5-12%	

5.2.3 Correlation between the mechanical properties of the oxide layer and the nanoindentation parameters

Due to the large number of controlling mechanical properties variables, it is difficult to accurately predict and investigate the relationship between them, and as a result of these complex interactions it is difficult to establish the relationships that exist between the variables. Thus, multiple correlations can be considered helpful in analysing the mechanical properties as well as determining the significant relationships between the parameters. It is also important to assess the significance and interaction of each variable, and leave out those that are not significant.

Multiple regressions are a statistical technique that enables the correlation between a continuous dependent variable and two or more continuous or discrete independent variables to be determined. It can be used for a variety of purposes, such as analysing experimental, ordinal, or categorical data (Asilturk and Cunkas, 2011).

Regression analysis was used to study correlation based on charting and plotting correlated data. By using a line of best fit and the law of a straight line graph, i.e. $y = mx + c$, values can be obtained from the chart for any extrapolated or interpolated data.

When modelling the mechanical properties of oxide layers on high speed steel work rolls, more than one independent variable exists, and therefore a multiple regression methodology is used. Linear multiple regression analysis (MRA) takes the form of the equation

$$y = b_1x_1 + b_2x_2 + \cdots b_nx_n + c \qquad (5.1)$$

where y is the dependent variable (load, slope), x_i is the independent variable (model inputs, i.e. yield strength (σ_y) and Poisson's ratio (υ), etc.), b_i is the regression coefficient (or slope) of independent variable x_i, and c is the intercept or constant.

With a non-linear MRA, the input variables can be manipulated via functions such as the polynomial, and the log and the inverse to best fit the predictive outputs to the targets. For example, a quadratic polynomial non-linear MRA will take the form of the equation:-

$$y = b_1x_1 + b_2x_2 + b_3x_1^2 + b_4x_2^2 + b_5x_1x_2 \ldots + c \qquad (5.2)$$

A large quantity of computed results is needed to provide general and useful interactive information for the mechanical properties of the oxide layers on high speed steel (HSS) because the maximum load (P_{max}) and slope curve (dP/dh), depend on numerous parameters such as the elastic modulus (*E*), porosity (*f*), yield strength (σ_y) and Poisson's ratio (υ), and the depth of indentation (*d*). Below are the theory and calculation of the correlation parameters.

a) Multiple regressions of non-linear correlation

Consider the multi-dimensional power law equation

$$Y = aX^bZ^c \qquad (5.3)$$

Taking the log of both sides of the power law equations yields

$$\log(Y) = \log(a) + b\log(X) + c\log(Z) \qquad (5.4)$$

Similarly for

$$Y = a{b_1}^{x_1}{b_2}^{x_2}{b_3}^{x_3}{b_4}^{x_4} \qquad (5.5)$$

taking the logarithm to any base of both sides of the power law equation yields

$$\log(Y) = \log(a) + x_1\log(b_1) + x_2\log(b_2) + x_3\log(b_3) + x_4\log(b_4) \qquad (5.6)$$

If *P* = P_{max}; *E* = elastic modulus; σ_y= yield strength; υ = Poisson ratio; *f* = porosity; *d* = indentation depth, *i, j, k, m, n* are coefficients, and a is intercepts (constant) using Eq. (5.5) the dependence of *P* on *E*, σ_y, υ, *f*, and *d* is given

$$P = aE^i\sigma_y^j\upsilon^kf^md^n \qquad (5.7)$$

or

$$\log(P) = \log(a) + i\log(E) + j\log(\sigma_y) + k\log(\upsilon) + m\log(f) + n\log(d) \quad (5.8)$$

Table 5.7 : Regression result for P_{max}.

Regression Statistics	
Multiple R	0.999167464
R Square	0.998335621
Adjusted R Square	0.998209531
Standard Error	0.014737966
Observations	72

ANOVA

	df	*SS*	*MS*	*F*	*Significance F*
Regression	5	8.598907	1.719781	7917.684	3.01E-90
Residual	66	0.014336	0.000217		
Total	71	8.613243			

	Coefficients	*Standard Error*	*t Stat*	*P-value*	*Lower 95%*	*Upper 95%*
Intercept	-5.030921501	0.079586	-63.2137	8.92E-61	-5.18982	-4.87202
Log (*E*)	0.495582878	0.026995	18.35813	1.25E-27	0.441685	0.549481
Log (σ_y)	0.357835269	0.01642	21.79271	7.4E-32	0.325052	0.390619
Log (υ)	0.069652458	0.033922	2.053299	0.04401	0.001925	0.13738
Log (*f*)	-0.027531825	0.008864	-3.10613	0.002793	-0.04523	-0.00983
log (*d*)	1.993197957	0.017267	115.4353	7.1E-78	1.958724	2.027672

This regression analysis was performed to determine how variances in the maximum load and slope of the unloading curve affect the mechanical properties regardless of how those variances were achieved. The regression and standard deviation of both the independent (maximum load, *P* and slope curve, *dP/dh*) and dependent (the elastic modulus, *E*; porosity, *f*; yield strength, σ_y; and Poisson's ratio, υ; and the depth, *d*) variables are shown in Tables 5.7 and 5.8. These tables are given to illustrate the range of values measured. The *R* square (coefficient of determination) in Tables 5.7 and 5.8 represents the contribution of the set of independent variables in describing the variability in the dependent variables.

The result shown in Table 5.7 can be represented in an equation where the independent variables are equivalent to the dependent predictors multiplied by their individual coefficient. Based on the linear regression model, the equation is

$$Y = b_0 + b_1x_1 + b_2x_2 + b_3x_3 + b_4x_4 \quad (5.9)$$

It should be noted that the variables in the Table 5.7 are in the log form. P_{max} was measured as described below, where the coefficient was defined based on Table 5.7. It is important to quantify the maximum load relationships in order to set the design parameters for, and evaluate the outcomes from the load-displacement curves.

i) Calculation for P_{max}

The multiple correlation of P_{max} was computed by noting *P* given by equations (5.7) and (5.8). With P representing the P_{max}, *i,j, k, m, n* are coefficients, we can rewrite Eq.(5.7) and (5.8) as

$$P = aE^i\sigma_y^j v^k f^m d^n \quad (5.10)$$

and

$$\log(P) = \log(a) + i\log(E) + j\log(\sigma_y) + k\log(v) + m\log(f) + + n\log(d) \quad (5.11)$$

Inserting the coefficient expressions (Table 5.7) into Eq. (5.11) again gives,

$$P_{max} = -5.030921501 + 0.495582878(E) + 0.357835269(\sigma_y) + 0.069652458(v) - 0.027531825(f) + 1.993197957(d) \quad (5.12)$$

The intercepts (constant a) in Eq. (5.11) is given by -5.03 (refer Eq. (5.12)). Thus constant parameter is determined using the log equation given by

$$\log(a) = -5.030921501 \quad (5.13)$$

An easy and systematic method of generating a constant now can be achieved. Solving Eq. 5.13 gives

$$a = 9.31\text{E-}6 \tag{5.14}$$

When the coefficient in Eq. (5.10) is evaluated a new set of parameter regressions of P,E, σ_y, υ, f, is defined in terms of P_{max} over the depth of penetration.

$$P = 9.31\frac{E^{0.496}\sigma_y^{0.358}\upsilon^{0.069}d^{1.993}}{f^{0.02753}} \text{ x } 10^{-6} \text{ mN} \tag{5.15}$$

Table 5.8: Regression result for *dP/dh*.

Regression Statistics	
Multiple R	0.810101
R Square	0.656264
Adjusted R Square	0.630223
Standard Error	0.119102
Observations	72

ANOVA

	df	*SS*	*MS*	*F*	*Significance F*
Regression	5	1.787457	0.357491	25.20152	4.068E-14
Residual	66	0.936231	0.014185		
Total	71	2.723688			

	Coefficients	*Standard Error*	*t Stat*	*P-value*	*Lower 95%*	*Upper 95%*
Intercept	-6.66024	0.643158	-10.3555	1.82E-15	-7.944344347	-5.37613
Log (E)	1.427517	0.218157	6.54352	1.04E-08	0.99195167	1.863082
Log (σ_y)	-0.28229	0.132695	-2.12734	0.037133	-0.547220266	-0.01735
Log (υ)	0.097883	0.274136	0.35706	0.722186	-0.449447373	0.645213
Log (*f*)	0.023932	0.07163	0.334101	0.739362	-0.119082714	0.166946
log (*d*)	1.317039	0.139538	9.43854	7.28E-14	1.038441524	1.595636

Table 5.8 presents the results obtained using the multiple regression analysis of *dP/dh.* The compositional measures found to be statistically significant predictors of each mechanical property are presented. Importantly, all four mechanical properties have statistically significant multiple regression models.

The result presented here suggests the coefficient of each dependent variable. These coefficients represent the changes in the dependent variables predicted for a one unit increase in the independent variables. In order to obtain the relationship between these variables in terms of *(dP/dh)*, some calculations were used in the following equations.

ii) Calculation for *dP/dh*:-

Once again non-linear a multiple regressions is defined by Eq. (5.16) and (5.17). This equation shows the relationship of the slope (*dP/dh*) and the dependent variables such as the elastic modulus (*E*), porosity (*f*), yield strength (σ_y); and Poisson's ratio (υ) and the depth (*d*).

$$dP/dh = aE^i\sigma_y^j v^k f^m d^n d \qquad (5.16)$$

and

$$\log(dP/dx) = \log(a) + i\log(E) + j\log(\sigma_y) + k\log(v) + m\log(f) + + n\log(d) \qquad (5.17)$$

The coefficients of *i, j, k, m, n* and the constant a in the Eq. (5.16) and (5.17) were determined by regression analysis. Table 5.8 shows the value of each coefficient via multiple regression analysis. Using the value of intercept, the function of constant is illustrated simply as

$$\log(a) = -6.66024 \qquad (5.18)$$

Thus the constant *a* for the analysis is defined by

$$a = 2.19\text{E-}7 \qquad (5.19)$$

It is easy to verify that the above expression gives the following equation. It is useful to note in this context the following function expression:

$$dP/dh = 2.19\frac{\mathrm{E}^{1.427}\upsilon^{0.098}f^{0.023}\mathrm{d}^{1.317}}{\sigma_y{}^{0.282}} \times 10^{-7} \qquad (5.20)$$

Expression in Eq. (5.20) is valid for determining the relationship between mechanical properties and the unloading slope of load-displacement curves.

Multiple regression statistical analysis was used to simultaneously evaluate the quantitative effects and the functional relationships *P* = f (*E*, σ_y, υ, f, *d*) and *dP/dh* = (*E*,σ_y, υ, f, *d*) by considering the multi-dimensional power law equations. The output of the load-displacement curves by nanoindentation, namely the maximum load (*P*) and slope curve (*dP/dh*), have already been studied in terms of the elastic modulus (*E*), porosity (*f*), yield strength (σ_y) and Poisson's ratio (υ), and the depth (*d*). The values of *dP/dh* were obtained by considering the first three data points of the unloading slope because once all three data points fall around the best fit line, the value of *dP/dh* would be determined.

The coefficients b_1, b_2, b_3, and b_4 are obtained with the least square method. Accordingly the maximum load is given by

$$P = 9.31\,\frac{\mathrm{E}^{0.496}\sigma_{\mathrm{y}}{}^{0.358}\nu^{0.069}\mathrm{d}^{1.993}}{f^{0.02753}} \text{ x } 10^{-6}\ \mathrm{mN} \tag{5.21}$$

From the regression analysis of the tabulated results, the *dP/dh* is given by the following expression

$$\frac{\mathrm{dP}}{\mathrm{dh}} = 2.19\,\frac{\mathrm{E}^{1.427}\nu^{0.098}f^{0.023}\mathrm{d}^{1.317}}{\sigma_{\mathrm{y}}{}^{0.282}} \text{ x } 10^{-7}\ \mathrm{mN/nm} \tag{5.22}$$

where *E* and σ_y are in GPa, and *d* is in nm. It can be said regarding the main effects from equations (5.21), the greatest influence on the maximum load (*P*) of the load-displacement curve is exhibited by the depth of the indentation (*d*), followed by the elastic modulus (*E*), and the yield strength (σ_y). It is reassuring that expressions (5.21) and (5.22) both confirm the relatively weak effect of porosity and Poisson's ratio on the maximum load and slope with *E* as the most significant properties followed by yield strength. The result also shows good correlation (R^2 = 99.9%) between the maximum load (*P*) and the mechanical properties, while R^2 = 81.0% for the slope (*dP/dh*).

In order to validate the performance and the accuracy of the regression analysis, the experimental and FE result were compared. Figure 5.10 shows an example of the load displacement curves from both the experiments and the FE simulations of the outer and inner sub-layers respectively. The experimental load-displacement curves and those obtained from the FE simulations generally match well, particularly in the unloading portion where the elastic modulus *E* has been evaluated.

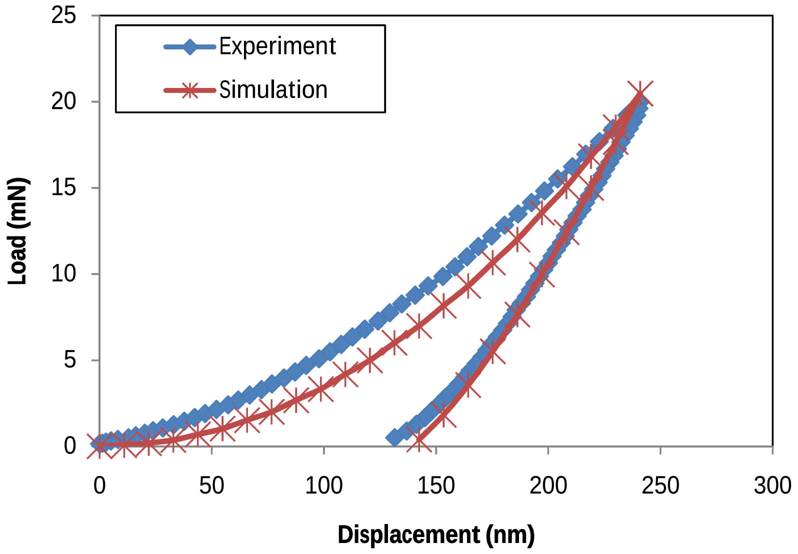

(a)

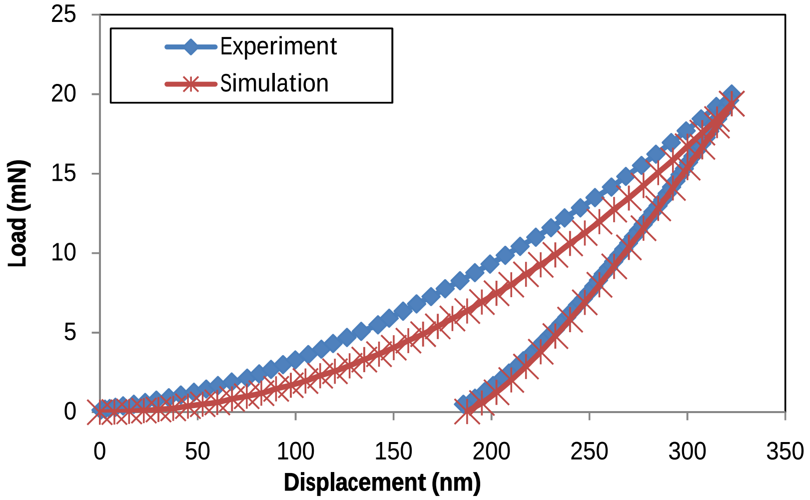

(b)

Figure 5.10: Load-displacement curves for (a) outer and (b) inner sub-layers.

The loading curves show larger deviation than the unloading curves. The difference in the loading region between the experimental curves and the simulated ones can be explained by the different tip radius used (Kopernik and Pietrzyk, 2007) and the most advanced procedure for thin films and nanoindentation testing with dual sharp indenter, using the inverse algorithm and sensitivity analysis (Dao *et al.,* 2001 and Chollacoop *et al*. 2003). According to Kopernik and Pietrzyk (2007), conditions for numerical simulation of nanoindentation test are similar to those in laboratory test, but a geometry simplification is made. In the simulations a perfectly sharp tip has been used while in the experiments, the tip must have been slightly rounded (Figure 5.11). Therefore the force required to push the indenter is greater with rounded tips than the sharp tips used in the simulations.

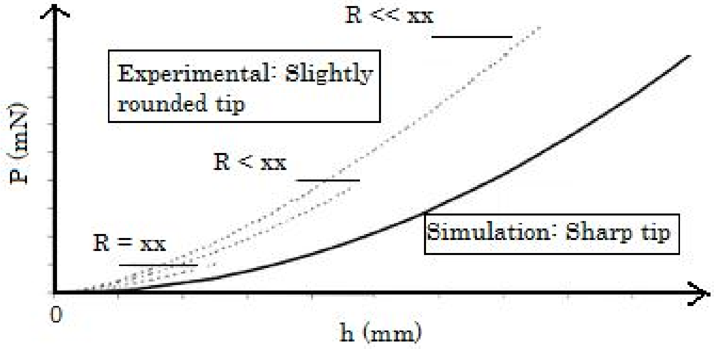

(a)

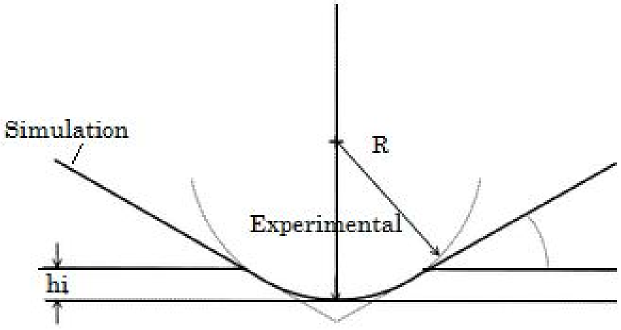

(b)

Figure 5.11: (a) The illustration of load-displacement curves between the sharp tip (simulation) and the slightly rounded tip (experimental) (b) schematic representation of a nanoindentation. Symbol used: R = radius; hi = penetration depth.

5.2.4 The uniqueness of the combination data

The uniqueness of the combination parameters can be proven by these two graphs shown below. Based on the equations (5.21) and (5.22), the maximum load P_{max} and *dP/dh* have been plotted versus displacement depth. In Figure 5.12 the equations have taken into account the related parameters (*E*, σ_y, υ, *f*) that give some effects to the P_{max} and *dP/dh*.

Based on these graphs, we can conclude that there is a unique solution for each P_{max} and *dP/dh* since both graphs increase monotonically. Please note that the combination of parameters is considered as the real parameters once a set of parameters is able to fit both targets, P_{max} (equation 5.21) and *dP/dh* (equation 5.22) of experimental results.

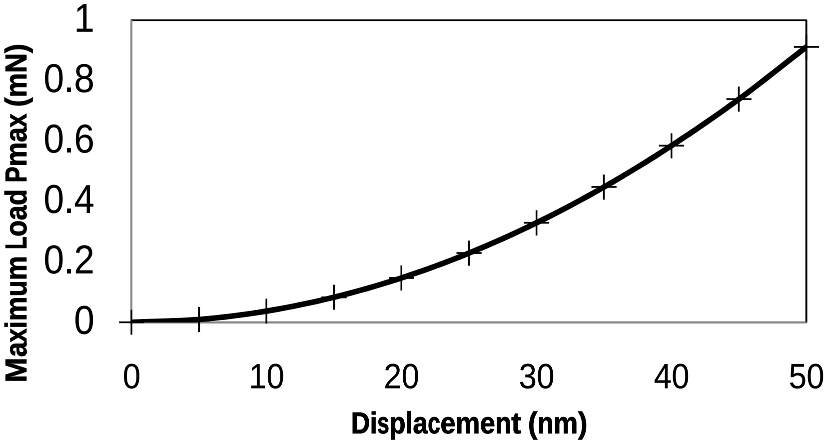

(a)

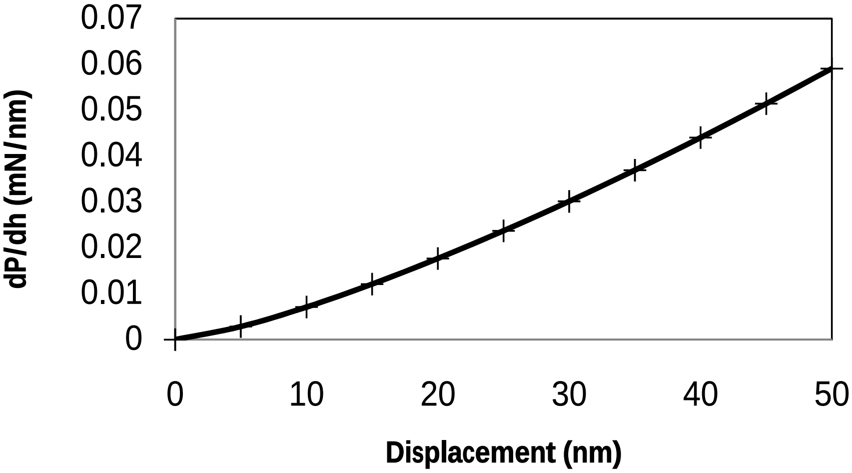

(b)

Figure 5.12: (a) P_{max} and (b) *dP/dh* versus displacement depth.

5.2.5 von Mises stresses of outer and inner sub-layers

Figures 5.13 shows the von Mises stresses of oxide scales on the outer and inner sub-layer respectively. There is no doubt that the greatest von Mises stress is induced on the contact surface. It shows that the von Mises stress of the outer oxide layer is higher than the inner. These phenomena are related to the yield strength of these layers. A von Mises yield criterion is useful for small-strain plasticity like nanoindentation.

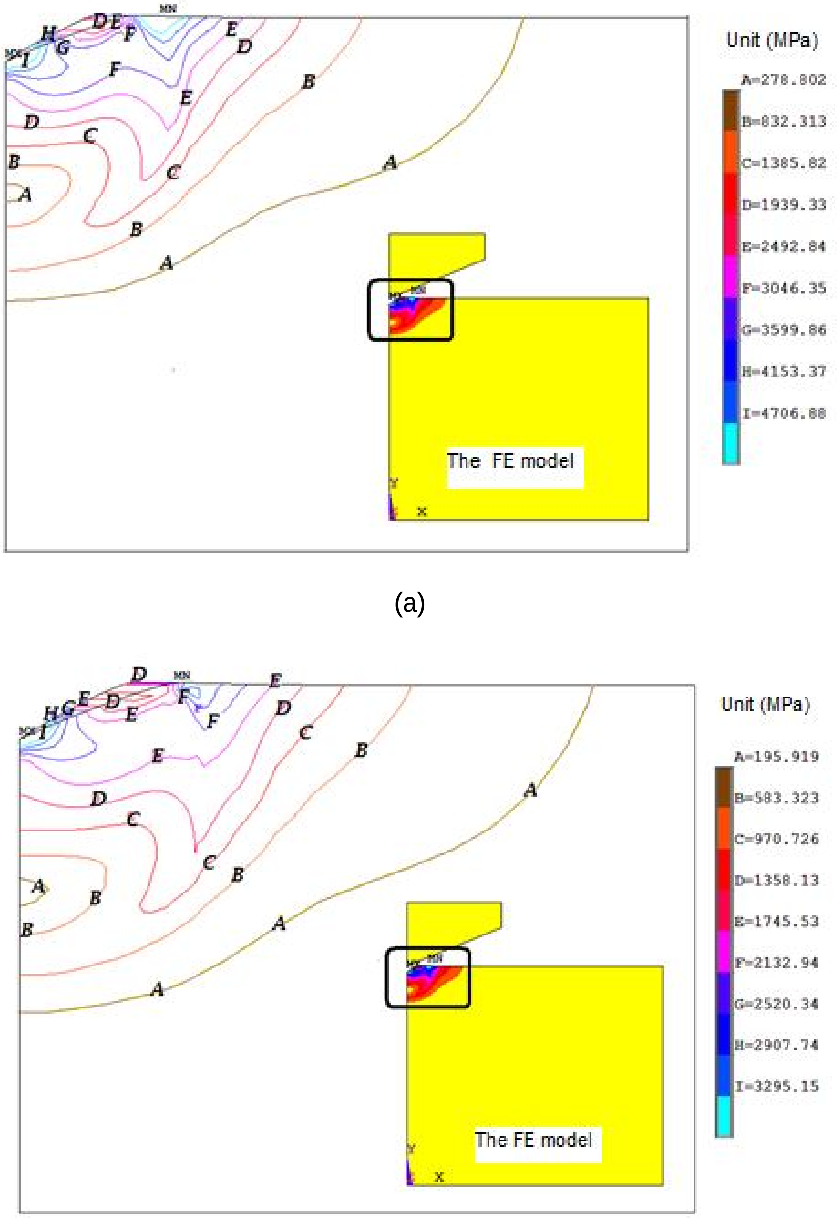

(a)

(b)

Figure 5.13: von Mises stress distribution for a) Outer b) Inner sub-layers.

5.3 Discussion

The nanoindentation experiments performed on the cross section oxide layers formed on the HSS revealed the outer sub-layer are harder than the inner sub-layer. The hardness, *H* and elastic modulus, *E* obtained from the nanoindentation experiments with two different maximum normal loads are consistent with each other. The elastic modulus, *E* of the outer sub-layer (200-240 GPa) are higher than the inner sub-layer (90-220 GPa). The large variation of *E* in the inner sub-layer is probably due to the influence of voids and non-uniform porosity of the sub-layer. The smaller size grains of the inner sub-layer increase the sensitivity of the indentations to variations in porosity.

H values of the outer sub-layer are approximately double that of the inner values. This might be due to the differences in microstructure, porosity, and composition of these sub-layers. The outer sub-layer consists of harder Fe_2O_3 while the inner sub-layer is made up of mostly Fe_3O_4. The trend for the 20 mN load is similar to the 5 mN maximum load experiment where the *E* and *H* of the outer sub-layer are higher than the inner ones. This is due to the inner oxide layer has higher porosity and smaller grains. From the TEM images (Figure 5.3), the higher porosity and the smaller grains sizes of the inner sub-layer are also visible. The porosity of the oxide leads to “deficient” indentation, given the instability of the oxide caused by its porous nature and grade of “compactness”. The information regarding the porosity and grains in this study led to a contribution in explaining the characteristics of inner and outer oxide sub-layers on HSS steel surface.

In this study, a multiple regression was also used to analyse the load-displacement data in order to investigate potential interaction between oxide layer mechanical properties, as well as to explain the increased load and slope of the load-displacement curves associated with depth of indentation. Large data sets from numerous positions of the oxide layer have been analysed, providing a total of 72 data. Parameters such as the elastic modulus (*E*), porosity (*f*), yield strength (σ_y) and Poisson’s ratio, (υ) and the indentation depth (*d*) were analysed to determine their interaction and influence on the maximum load and slope of load-displacement curve. The results of the multiple regression shows that the model proposed is suitable for investigating the interaction between the mechanical properties variables, and also for predicting the mechanical properties at different depths of indentation.

5.4 Conclusions

In this chapter, the mechanical properties of oxide layers formed on high speed steel have been quantified and studied using combined nanoindentation experiments and finite element simulations. The work has revealed variations in the microructure and mechanical properties across the oxide layer.

The findings are summarised below:-

- The layer of oxide on a HSS surface consists of Fe_2O_3 outer sub-layer of oxide and Fe_3O_4 + Cr_3O_4 inner sub-layer of oxide.
- *E* range for the outer and the inner sub-layers of oxide are 200-240 GPa and 90-220 GPa respectively for a load of 5 mN. The large variation of *E* values for the inner oxide sub-layer is probably influenced by the voids and large variation in the porosity of the material. The *E* and *H* for the 20 mN load tests are lower than for 5 mN load. This phenomenon is probably caused by softening which arises from the interaction between geometrically necessary dislocations (GNDs) and grain boundaries. Hence the size of the nanoindentation is more significant in the outer sub-layer.
- The study on yield strength shows that for the 5 mN load test, the inner sub-layer is lower in value than the less porous outer sub-layer. This may be explained by the development of an oxide sub-layer where a thin layer of hematite grows in the top layer first, and then a thick porous layer of hematite at the interface between the upper layer and HSS substrate.

- The less porous outer sub-layer has a lower Poisson’s ratio. This relationship indicates the effect of porosity on the Poisson’s ratio-porosity dependence.

- The outer sub-layer is found to be less porous with *f* = 2-8%, than the inner layer with *f* = 5-12%.

Chapter 6

Study of the wear of the oxide layer using micro scratch experiments and FE simulations

Wear of the work rolls is a phenomenon during industrial hot rolling that can adversely affects the shape of the strip and the performance of a mill, therefore it is important to quantify the wear during the rolling process. Previous experimental works by Colas *et al.* (1999) and Garza-Montes-de-Oca et *al.* (2011) demonstrated the existence of oxide layer on hot rolling roll surface, but their explanation of the behaviour of this oxide is limited, making direct observations of the oxide scale under industrial hot working conditions is difficult. Moreover, exploring the behaviour of the oxide layer during scratch experiments is impossible because of the complex interactions between the indenter, the oxide layer and substrate. For this reason a three dimensional (3D) finite element (FE) simulation of an indenter scratching an oxide layers/high speed steel substrate system was developed in this thesis. This chapter investigates the deformation of the oxide layers when scratched by an asperity using the finite element method with the aim to explain the failure modes and failure mechanisms of the oxide layer on high speed steel (HSS).

6.1 Simulation Methods

In this chapter the ductile and brittle behaviour of the HSS oxide layer were studied using scratch simulation of two-body system, i.e. between asperities and oxide layers. As there is no clear explanation of the behaviour and characteristics of the oxide layer on HSS, either brittle or ductile, selection of the adopted models in the FE simulation are based on the following arguments.

First, the oxide scale layer on HSS can be considered ductile based on the experimental results in Chapter 4. This justification is based on the AFM images and the nanoindentation load-displacement curves. The AFM images show that no cracking occurred and the oxide layer deformed plastically during nanoindentation.

In addition, the mechanical characteristics that were extracted in the previous chapter can be related to the ductile properties. Furthermore, Garza-Montes-de-Oca and Rainforth (2011) reported that hematite buckles and acts as a plastic oxide layer when compressive thermal stresses are applied.

A brittle model was also considered in the current project as a comparison. Krzyzanowski and Rainforth (2010) reported the brittle failure of oxide layers at temperatures below about 800°C. Garza-Montes-de-Oca and Rainforth (2011) claimed that the oxide layers exhibit a wedging behaviour that is normally present in brittle oxide layers, with a strong adhesion to the substrate. In this thesis the Johnson–Holmquist materials model was used to account for the brittle behaviour. This is an established model that has been used by numerous researchers (Wang and Yang, 2008; 2009; Tian *et al.* 2012).

Krzyzanowski and Rainforth (2010) modeled the oxide layer using the MSC/MARC commercial finite element method and combined methods for linking solid continuum models with discrete element methods to simulate multi-scale and multi-phase phenomena. They simulated crack propagation by assuming a brittle behaviour for the oxide layer and mimicked failure of the low carbon steel oxide layer at the low temperature range when the metal interface between the oxide layers was relatively strong and allowed no movement between the metal surface and the oxide layer. The oxide layers were assumed to be adherent when they were within the contact tolerance L_{tol}. However, this model is related to the oxide layers on the strip.

Although the types of oxide layers formed on the strip and the work roll are similar, the mechanical properties of the work roll and the oxide layers on the strip are different (Tang, 2006; Krzyzanowski and Rainforth, 2010). Hirono and Ura (1970) and Steven *et al.* (1971) studied work roll wear and found that magnetite (Fe_3O_4) is harder than the oxide formed on the work roll surface. In fact the work roll and the strip in the strip mills have their own rolling conditions that lead to a different force and friction. As a result, the deformation and wear of the oxide layer formed on the work roll and the strip are distinctive. Since there is lack of studies on the oxide layer formed on the work roll, this study investigated the behaviour of the oxide layer under scratched conditions. Indeed the exact mechanical properties of the oxide layer and the interface integration between the oxide scale and substrate, and the development of the oxide layer during rolling still need to be considered.

The bi-linear model (ductile) and Johnson–Holmquist materials model (brittle) were used to model the oxide layers where the eight-noded brick (oxide layer) and four-noded tetrahedral finite elements (substrate) with large strain and displacement capabilities, were used to discretise the target (Figure 6.1a). In view of their higher accuracy, brick elements were used in the impact region of the oxide layer, while the remaining substrate regions of the target were discretised using tetrahedral elements. The boundary conditions imposed on the above models were as follows: symmetry boundary conditions on the $z = 0$ and $x = 0$ planes, and the fully constrained workpiece bottom surface. The tip was treated as a rigid body and moved vertically and then horizontally into the oxide layer. The tip was kept reasonably low (12 m/min @ 200 μm/milliseconds) and it was assumed, for simplicity, that the temperature of the tip had a negligible influence on the material properties. The oxide layer was assumed to be perfectly bonded with the substrate where the oxide layer metal interface is relatively strong and allows no movement between the metal surface and the oxide layer.

The frictional contact problem of an indenter sliding on the surface of the Fe_3O_4 oxide scale/HSS substrate materials was analysed using Ansys-LSDyna Version 13. In addition, LS-PrePostVer 3.1 was used to export the data. Due to the symmetry of the problem, only one half of the scratch specimen was modelled. After a convergence study, a suitable mesh density around the contact was found where the size of the elements was approximately half the thickness of the oxide layer. The FE model for the specimen, shown in Figure 6.1b, was 600 μm long, 100 μm wide, and 100 μm thick, and that includes 4 μm for the thickness of the oxide layer. These dimensions were determined from numerous analyses to avoid establishing a boundary effect. Symmetric boundary conditions were applied to the central plane of the model. The model only considered one sub-layer due to the large 1:4 ratio of the outer sub-layer and inner sub-layer.

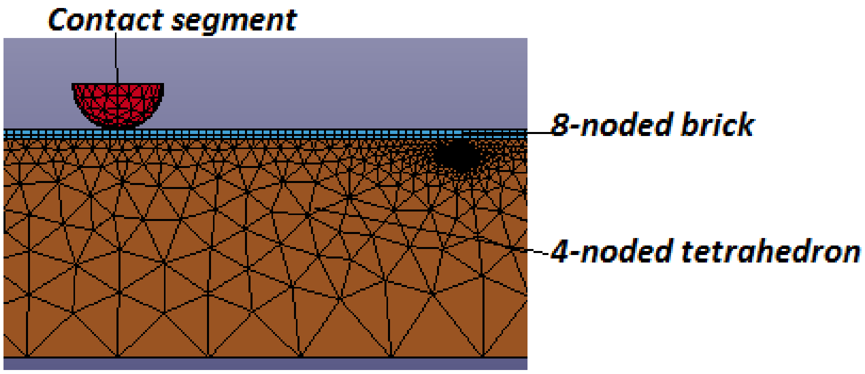

(a)

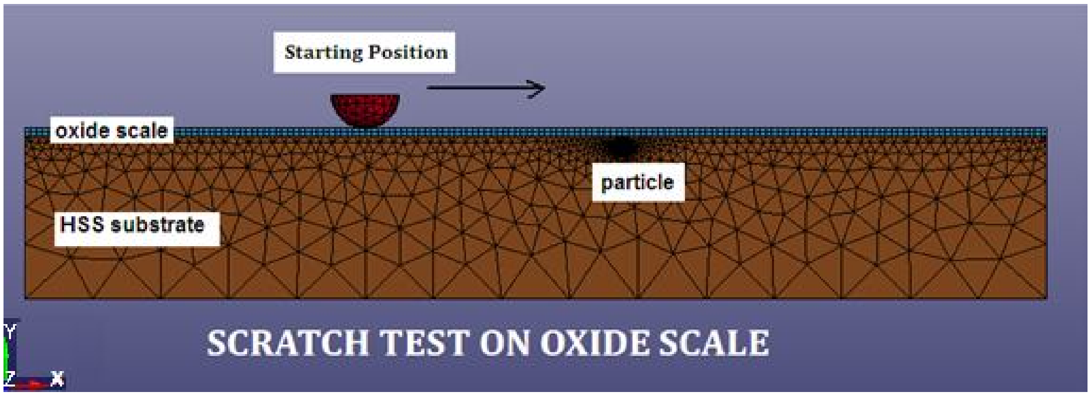

(b)

Figure 6.1: 3D FE model for simulating the scratch test (a) discretised geometry showing contact element (b) geometry and notation used.

6.2 Results

6.2.1 FEM model based on brittle and ductile material behaviour

For the ductile model, the material properties of the oxide layers and substrate were characterised by a bi-linear elastic–plastic model with isotropic hardening. The material deformed elastically when the stress applied was below the yield point (σ_y), but once the stress exceeded σ_y, the material deformed plastically with a strain hardening coefficient α. During plastic deformation the von Mises stress ($\sigma_{von\ Mises}$) is given by

$$\sigma_{von\ Mises} = \sigma_y + E_h \varepsilon_p \qquad (6.1)$$

where σ_y is the yield strength, E_h is the plastic hardening modulus, $E_h = \alpha E$ (*E* is the Young's modulus), and ε_p is the plastic strain. The assumptions and parameters used in the FE modelling are summarised in Table 6.1.

Table 6.1: Assumptions and parameters for FEM–based scratch test modelling for ductile model.

Oxide scale surface	Ideally smooth
Oxide scale/ Substrate interface	Perfectly bonded
Scratch distance (µm)	~200
Indenter tip radius(µm)	20
Oxide scale thickness(µm)	4
Oxide scale material	Fe_3O_4
Oxide scale material properties at room temperature	*E*= 245 GPa, ν= 0.2, σ_y= 7 GPa
Oxide scale material properties at high temperature(600^{o}C)	*E*= 221 GPa, ν= 0.19, σ_y=5 GPa
Substrate material properties	*E*= 210 GPa, ν= 0.3, σ_y= 2 GPa

In order to validate the numerical model, the experimental result of the scratch test was compared with the experimental result of Zhou *et al.* (2008). The test condition in this study was given by a progressive load. The starting load was 0.05 N, the end load was 25 N, the loading rate was 12.48 N/min, the scanning load was 0.05 N, the speed was 0.5 mm/min, and the length was 1 mm. In this study Zhou *et al.* (2008) studied the scratch behaviour of HSS for hot rolls using a Micro-combi tester. Figure 6.2 shows the comparison between the FE validation and Zhou *et al*. (2008) result of the apparent coefficient of friction versus the scratch length. The FE result had a good agreement with Zhou *et al.* (2008) result, but there were discrepancies during the running-in period. This was expected because the effect of local deformation is stronger at the initial stage, but then the coefficient of friction remains constant when the deformation and the pressure distributions are more uniform. The reason why the FE simulation showed the waviness at the initial stage is due to the effect of a rapid change in the contact force at the early operating stage. In this work the average coefficient of friction was calculated from the second stage.

A similar FEM observation was obtained with the previous study by Mezlini *et al.* (2005).

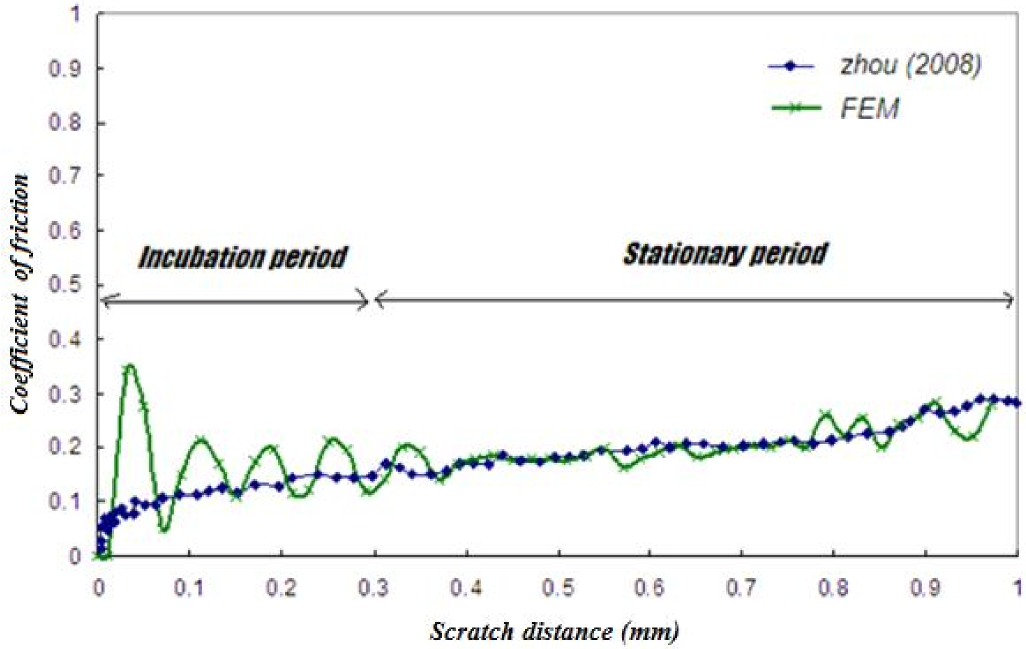

Figure 6.2: Comparison between developed FE model and experimental result of the coefficient of friction by Zhou *et al*. (2008).

For brittle materials the Johnson-Holmquist ceramic constitutive model was used to describe the response of the oxide layers, and because determining the constitutive constants for the oxide layer is complicated and cannot be determined directly, the alumina constants were used to represent the oxide layer. The selection of alumina was based on the load displacement curve and common mechanical properties such as the elastic modulus, hardness, and Poisson's ratio. The properties of several materials are summarised in Table 6.2 which shows that the properties of alumina are the closest to the oxide scale in terms of the ranges that are higher than properties of the oxide layer (> oxide layer). Taking the mechanical properties which are slightly higher was done because of the safety factor during material testing, and because the slope of the loading curves for alumina and the oxide scale is in agreement for the case that is less than 100 mN (Figure 6.3).

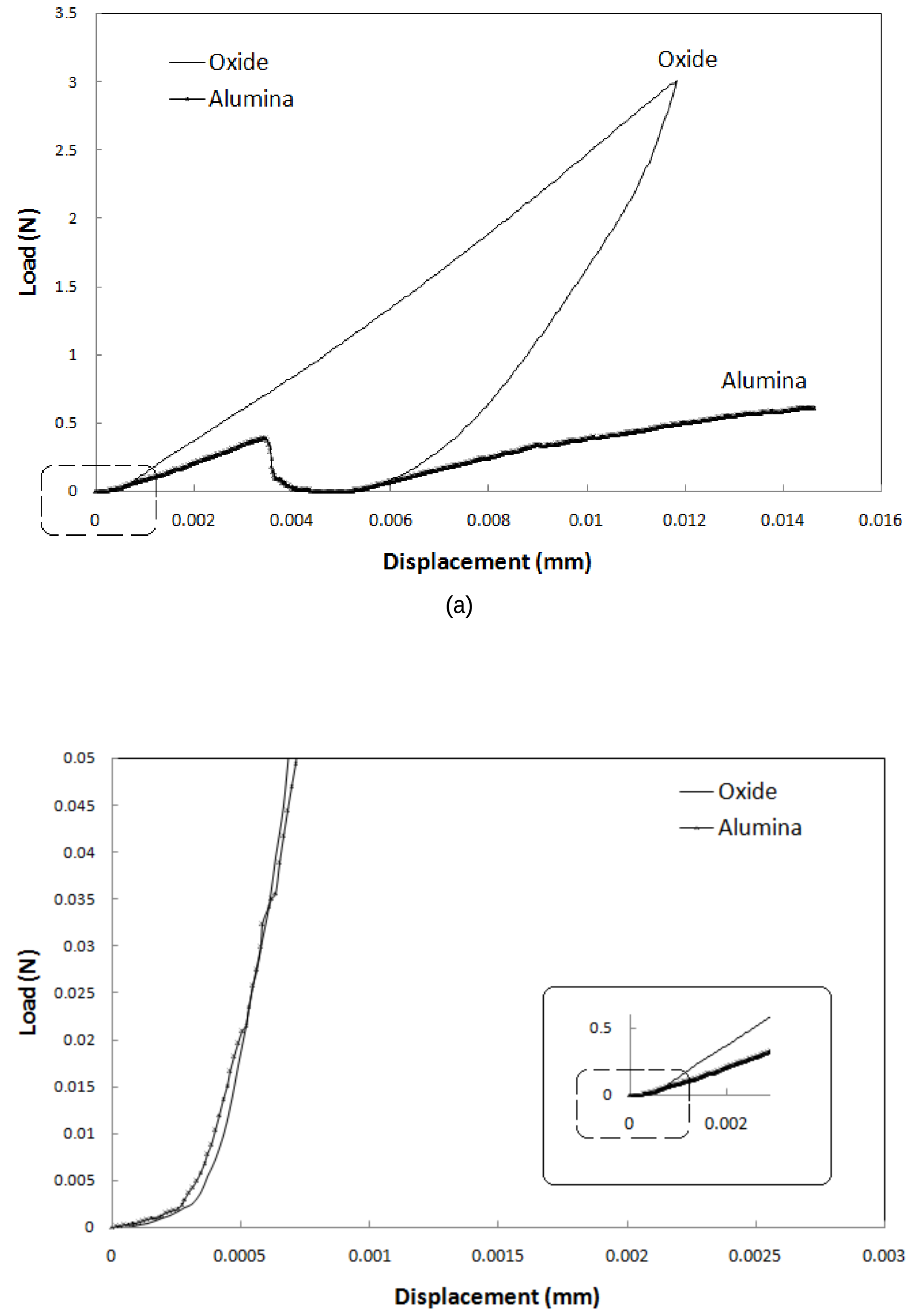

(a)

(b)

Figure 6.3: Comparison of load-displacement curve between alumina and oxide in the range (a) 4 N (b) 0.05 N.

Table 6.2: A list of the mechanical properties of brittle materials.

	Elastic Modulus (GPa)	Hardness (GPa)	Poisson's ratio
Silica	72[d]	10[d]	0.17[d]
Alumina (Al_2O_3)	385[b]	12-20[c]	0.24[b]
Silicon Carbide(SiC)	455[e]	14-26[e]	0.14[e]
Boron Carbide (B_4C)	450[a]	28.4[f]	0.17[f]
Oxide scale (Outer sub-layer)	130-245	13	0.2
Oxide scale (Inner sub-layer)	90-110	10	0.29

[a] Schwetz *et al.*, 1995; [b] Wong *et al.,* 1999; [c] Dutta, 2001; [d] Oliver and Pharr; [e] Milman *et al.,* 1999; [f] Thevenot, 1990.

6.2.2 Scratch on high speed steel samples

The samples of oxidised high speed steel were prepared in the same way as the previous oxidation samples (see Chapter 3). The temperature was set to 700°C because it produced a faster rate of oxidation than at lower temperature. After cooling the oxidised samples were hot mounted in Durofast resin at 150°C under 20 MPa. The samples were then ground with SiC paper, polished, and finished with a 1 μm diamond suspension.

Scratch tests were performed on the oxide using modified UMIS nanoindentation system with a 0.7 μm and 20 μm radius sphero-conical tip indenter. Four different loads, e.g. 100 mN, 200 mN, 300 mN, and 400 mN were used in the scratch tests. The lateral forces were continuously recorded and the coefficient of friction was measured. The ratio of the lateral force to the normal force is the dynamic coefficient of friction.

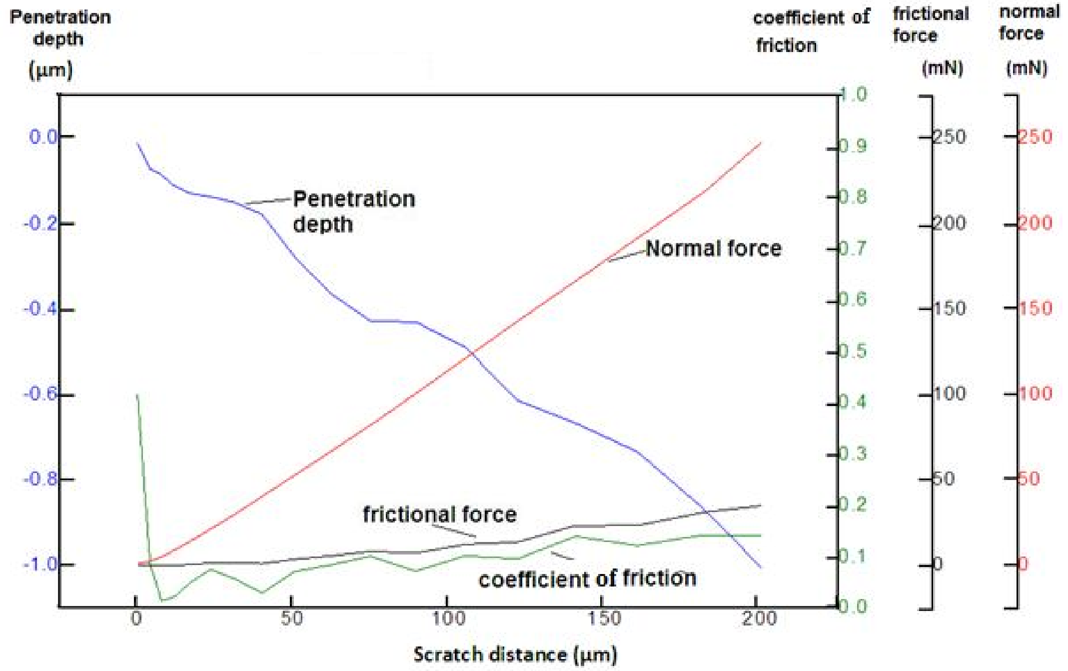

(a)

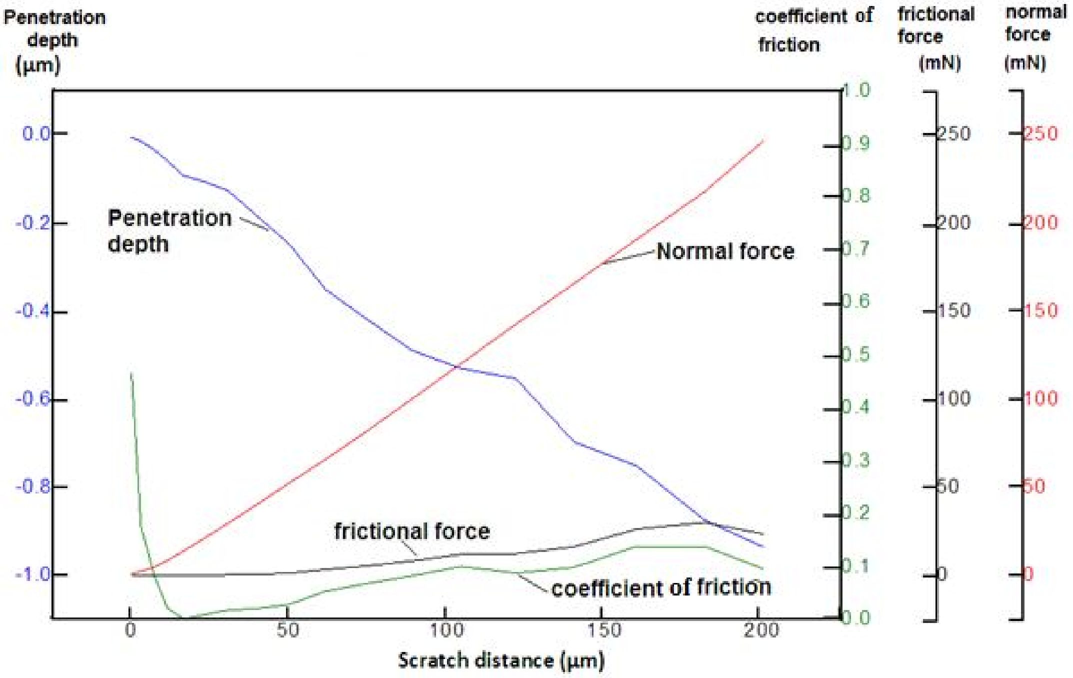

(b)

Figure 6.4: The scratch curves of the HSS (a) case 1-lower scratch (b) case 2-upper scratch.

Before the scratch experiment was conducted on the oxide layers, scratch experiments were carried out on the non-oxidised HSS surface. Figure 6.4 shows the scratch curves of the two samples of HSS. In case 1 (Figure 6.4a), the deepest penetration reached 1 μm, the friction force was 40 mN, and the coefficient of friction was 0.15. In case 2 (Figure 6.4b), the maximum depth of penetration was only 0.9 μm, the friction force was 35 mN, and the coefficient of fiction was 0.1. The trend of the coefficient of friction can be explained by observing the scratch tracks shown in Figure 6.5. Here the coefficient of friction was slightly higher when the scratch was contacted by the carbides. During the scratch experiment the carbides were embedded into the matrix and therefore the different penetration depths are closely related to the carbides.

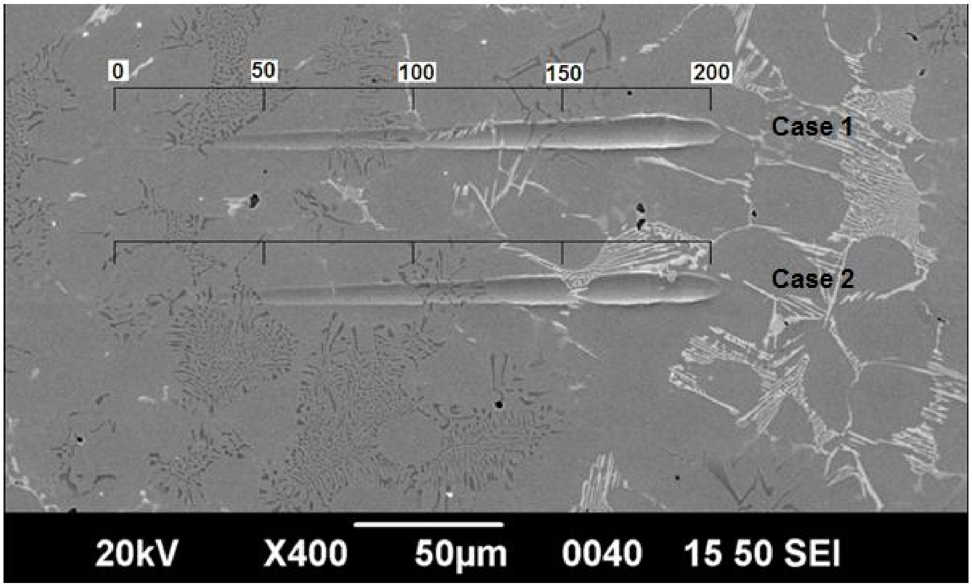

Figure 6.5: The scratch tracks on the HSS sample.

6.2.3 Friction behaviour of oxidised high speed steel grade work roll

6.2.3.1 Effect of the temperatures and thickness of the oxide layers

Garza-Montes-de-Oca and Rainforth (2009) investigated the coefficient of friction as a function of the thickness of the oxide layer on high speed steel. The results of friction of the wet and dry experiments showed an approximately linear increase with temperature (Figure 6.6a). Since the thickness of oxide increased with temperature in a logarithmic relationship, the coefficient of friction appeared to increase almost linearly with the thickness of the oxide (Figure 6.6b).

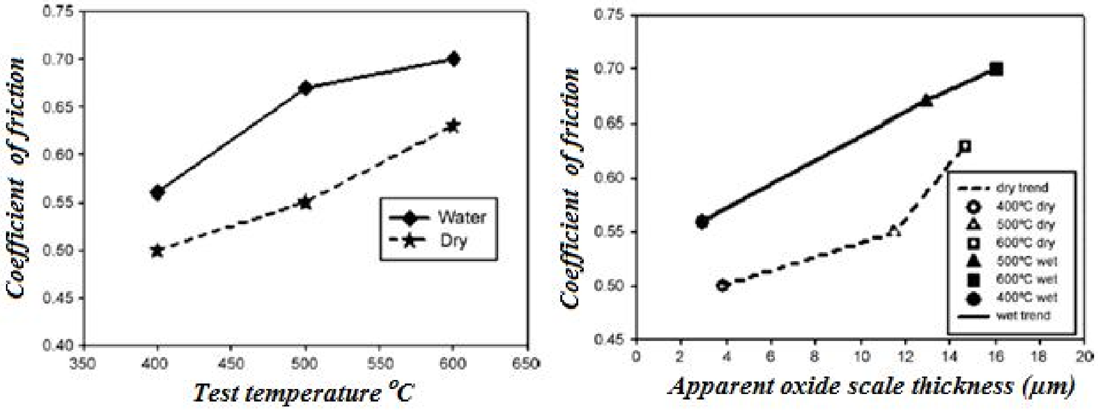

(a) (b)

Figure 6.6: Variation of the coefficient of friction as a function of the (a) temperature; (b) apparent oxide thickness by Garza-Montes-de-Oca and Rainforth (2009).

However, one of the key issues that has not been addressed in the published literature is the role of the second body (asperity) penetration depth in the wear of oxide layers with different thicknesses. In industrial conditions the worn surface is covered by oxide products, and while the temperature causes the thickness of oxide layer to increase, it is clear that the depth of penetration of a single asperity has a major influence on the tribological conditions. Therefore, an investigation on the effect of a single asperity at different depths is significant and practical.

In this case an oxide layer with a consistent thickness was chosen as the model to study the effect of the depth of penetration. A thickness of 4 μm was chosen for two reasons. First, the Krzyzanowski and Rainforth (2010) model which predicted the temperature history in different points of oxide, reported that the temperature of the oxide on the roll surface was between 300-550^{o}C. Based on the Garza-Montes-de-Oca and Rainforth (2009) result described in Figure 6.6, the thickness of the oxide layer where T = 300^{o}C was less than 4 μm, and secondly, based on the thickness of the oxide layer formed on high speed steel as measured by Zhu *et al.* (2010).

Two models were developed using ductile and brittle characteristics in order to simulate the conditions found in a scratch test as closely as possible. The current works specifically look at the influence of the depth of penetration on the wear behaviour and its effect on the coefficient of friction.

6.2.3.2 Effect of the depth of penetration of the scratching asperity

The behavior of asperity scratching on the oxide layer has already been explored using scratch experiments. The significance of this study is due to the existence of abrasive phenomenon during the rolling process. It is important to understand the real size of asperities that can affect the wear of work roll but that is beyond the scope of this thesis. According to Sun (2005), the diameters of the size surface imperfections at 10 and 20 s are close to 1.4 μm. In this case, an asperity can be considered as a particle from oxide scale formed on the strip surface.

Sun (2005), who studied the distribution of asperity using particle analysis, reported that the asperity heights of the oxide scale ranged from 0.06 nm to 800 nm after 10 s of oxidation time and from 0.045 to 1000 nm for 20 s. The mean particle diameters at 10 and 20 s are close to 1.4 μm. The size of the asperity in this simulation was determined based on the literature data because it did not focus on the validation of the real size of the asperities.

In the present work a 0.7 μm tip (diameter = 1.4 μm) was used in the scratch simulation to mimic the asperity sliding on oxide layer grown on work roll surface. In order to investigate the effect of tip size on the depth of penetration a 20 μm tip was used as a comparison (Figure 6.7). The result shows that the depth of penetration by the 0.7 μm tip was at least twice as deep as with the 20 μm tip, and can actually penetrate the substrate in the real case of work rolls. In order to avoid the additional effect of the substrate during scratching, the 20 μm tip was applied in the following investigation on the behaviour of the oxide layer. Moreover, the behaviour of the scratch test would have been easier to investigate using numerical modelling if the larger tip was used.

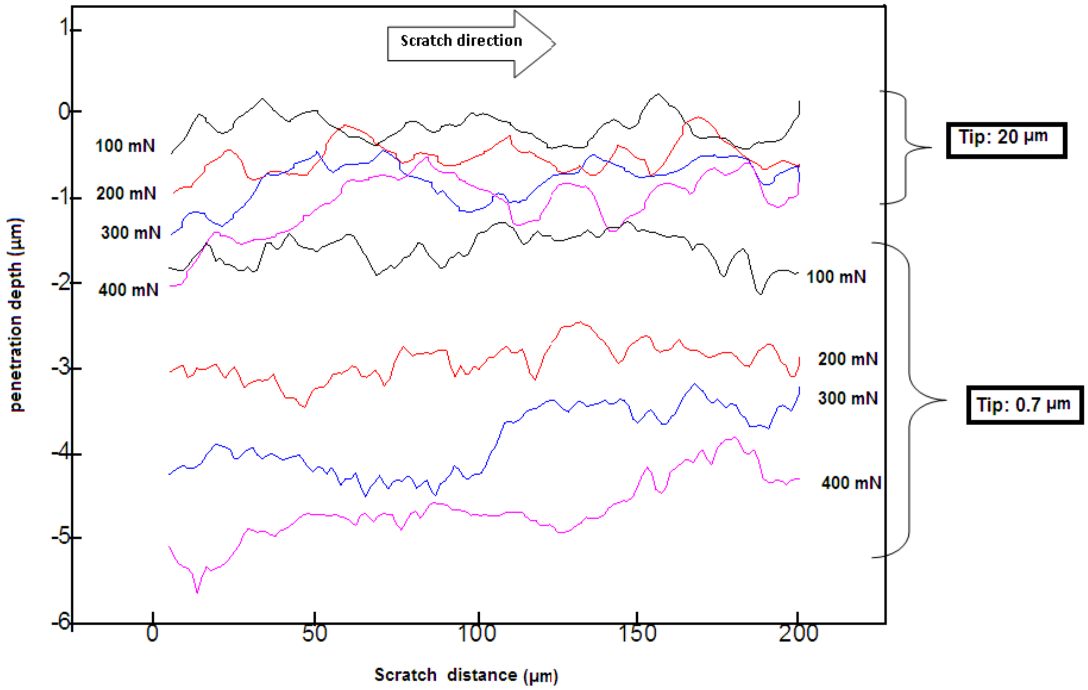

Figure 6.7: Variation of penetration depth of different tips for scratch test.

The results of the evolution of the coefficient of friction by the 20 µm tip for a load of 100 mN, 200 mN, 300mN, and 400 mN are shown in Figure 6.8. Periodic changes in the coefficient of friction are clearly visible. This mode mimicked the wear testing of the material very well, and can therefore provide some insight into the wear behaviour of the material during scratching. With an increased load the magnitude of fluctuations in the coefficient of friction also increased because of the increased severity of the fractured regions on the oxide layer.

The average coefficient of friction as a function of the depth of the scratch is given by Figure 6.9. The coefficient of friction increased in an approximately linear function with the depth of scratch due to saturation in ploughing of the oxide layer during scratching. As the indenter moves over the oxide layer, ploughing occurs during scratching and the ridges are formed on the sides of the track. When the scratching load is increased, deeper ploughing occurs due to increased load support and the indenter is pushed further into the material. As ploughing increases the friction there is a subsequent increase in the coefficient of friction, and the increased load also led to the formation of fractured surfaces consisting of micro-cavities.

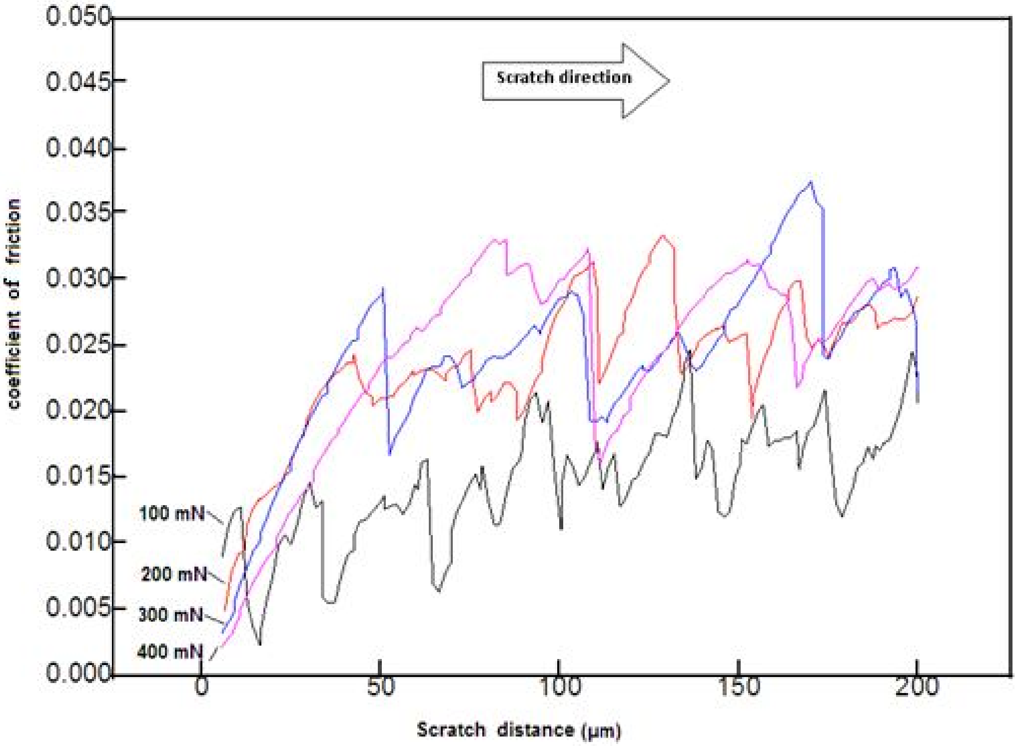

Figure 6.8: Evolution of the coefficient of friction of a 20 µm tip.

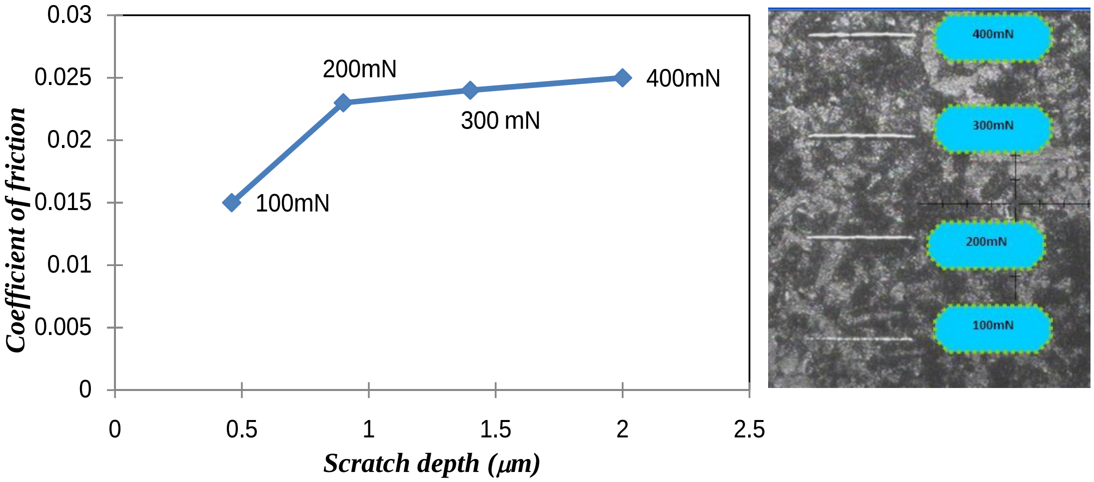

(a) (b)

Figure 6.9: (a) Variation of average coefficient of friction of a 20 µm tip as a function of the scratch depth (b) the scratch tracks at four different loads.

6.2.3.3 Predicted coefficient of friction at room and high temperatures

The simulation results obtained from the scratch experiments were plotted to show coefficient of friction versus the depth of penetration. Figure 6.10 shows the variation in the coefficient of friction as a function of depth of scratch of 2 μm, 3.2 μm, and 4 μm for the ductile and brittle model. The testing range between 2 - 4 μm of the penetration depth was selected based on the roughness of oxide scale on the strip that affects the work roll, which is around 1.44-3.13 μm, as reported by Sun (2005). The coefficient of friction increases in an approximately linear function with the depth of scratch for both conditions, but is significantly higher under brittle conditions because of the method of failure and energy associated with the scratching process. The detachment component is dominated by the brittle model while the damage due to deformation occurred with the ductile model. This situation can be related to the association of energy where the energy from the brittle model is highly distributed and leads to a higher coefficient of friction. In the brittle model, some of the energy goes into the creation of new surfaces (wear) while in the ductile model some is used to deform the materials.

The coefficients of friction of the oxide scale for the ductile model at room temperature are slightly lower than at high temperature due to the mechanical properties where the hardness and *E* are higher at room temperatures which lead to better scratch resistance and lower coefficient of friction. This finding is consistent with the trend of the coefficients of friction reported by Garza-Montes-de-Oca and Rainforth (2009) in Figure 6.6.

The results of comparing the coefficient of friction at a scratch depth of 2 μm with the experimental (Figure 6.9) and measured coefficients of friction (Figure 6.10), show that the measured coefficient of friction is marginally higher than experimental result at around 0.05 μm. This trend was probably due to the wide range of mechanical properties of oxide layers that lead to a discrepancy in the coefficient of friction. However, the coefficients of friction predicted by both models are consistent with the experimental works in terms of the increased trend where the coefficients of friction are correlated with the depth of penetration, as shown in Figure 6.9.

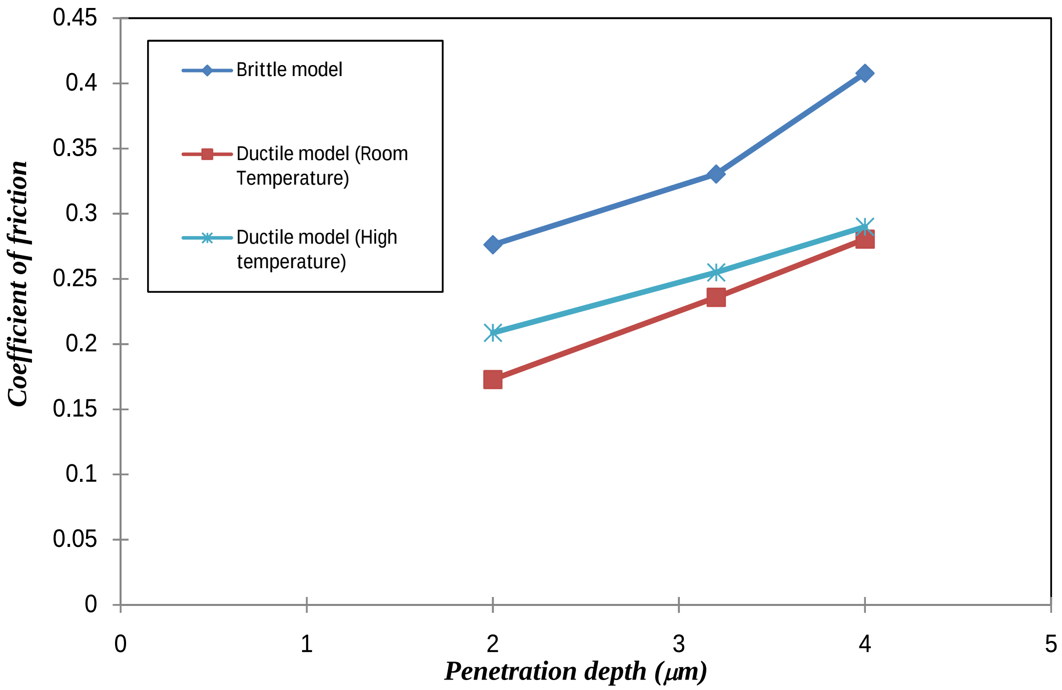

Figure 6.10: The variation of coefficient of friction as a function of scratch depth.

The prediction model in this study considered a set of mechanical properties based on brittle and ductile models. There are many challenges in developing an accurate numerical friction test and analytical friction models. The accuracy of the established model is helped by the attribution of the contact conditions and the materials that influence the friction force as pointed out by Blau (2001) who suggested a number of possible variables for use in the predictive model.

6.2.4 Effect of depth on the deformation of oxide layer using ductile model

In order to gain a better understanding of the scratch behaviour during the scratch experiments, an FE simulation was used. To simplify the modelling the scratch processes were simulated with constant applied depth mode. Figure 6.11 shows the examples of von Mises stress contours in the Fe_3O_4 oxide scale/HSS substrate system. It shows that plastic deformations occur near the tip of the indenter in the top layer (stress level of 7 GPa) and propagate to the substrate.

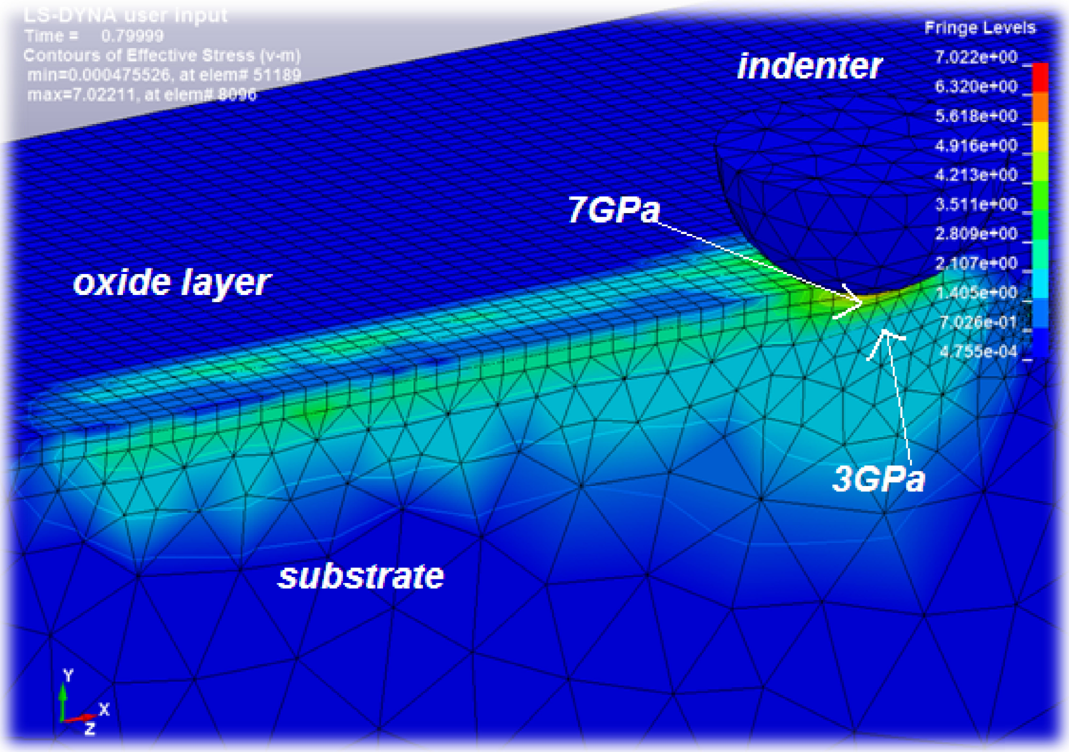

Figure 6.11: 3-D stress contours during scratch process after unloading step.

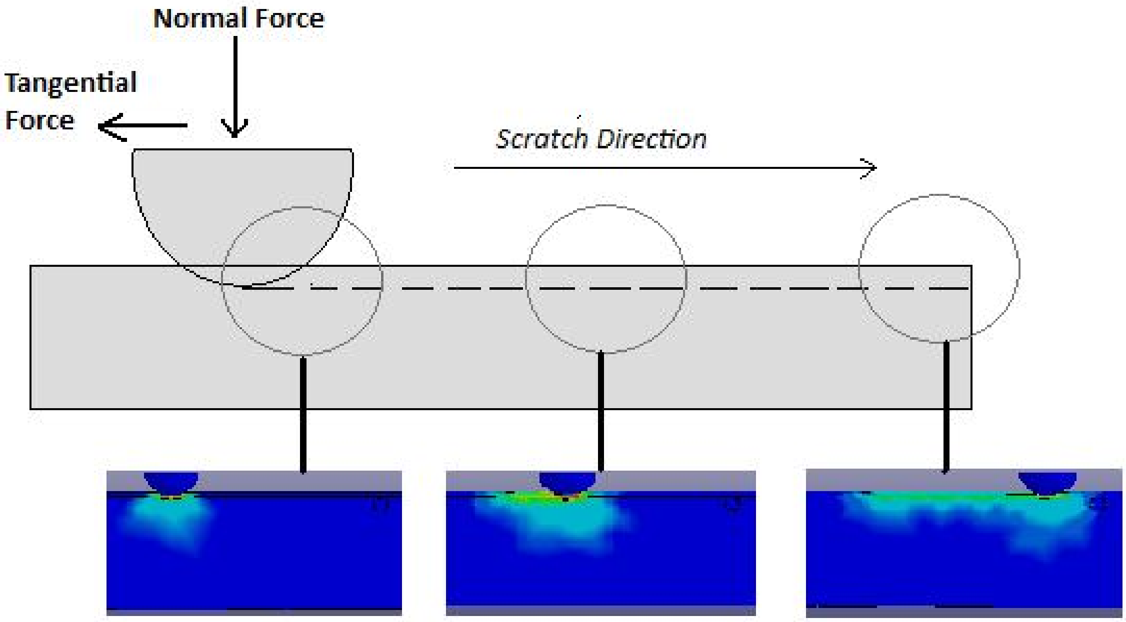

Figure 6.12: Deformation behavior during ductile regime nano-machining.

To further understand the results of the scratch simulation, the progressive stress field and deformation of the oxide layers at three stages are explained as illustrated in Figure 6.12. Three locations were considered, after indentation, at approximately half of the total scratch length, and at the final stage of scratch process. Detailed descriptions of these three locations are described below for three different depths of penetration, 4 μm, 3.2 μm, and 2 μm. The progressive stress fields are shown in Figure 6.13 for a 4 μm depth of penetration and in Figure 6.14 and 6.15 for 3.2 μm and 2 μm depths of penetration, respectively.

Figures 6.13 to 6.15 (a) show the step of indentation into the oxide scale where there was no sliding movement, but only a normal load applied by the indenter. At a small depth of indentation plastic deformations occur around the tip of the indenter, which propagate vertically and laterally as a round shape. As the depth of penetration increases the plastic deformation propagates further under the surface and at the substrates. Plastic deformation also propagates vertically and laterally in the oxide layer and the substrate.

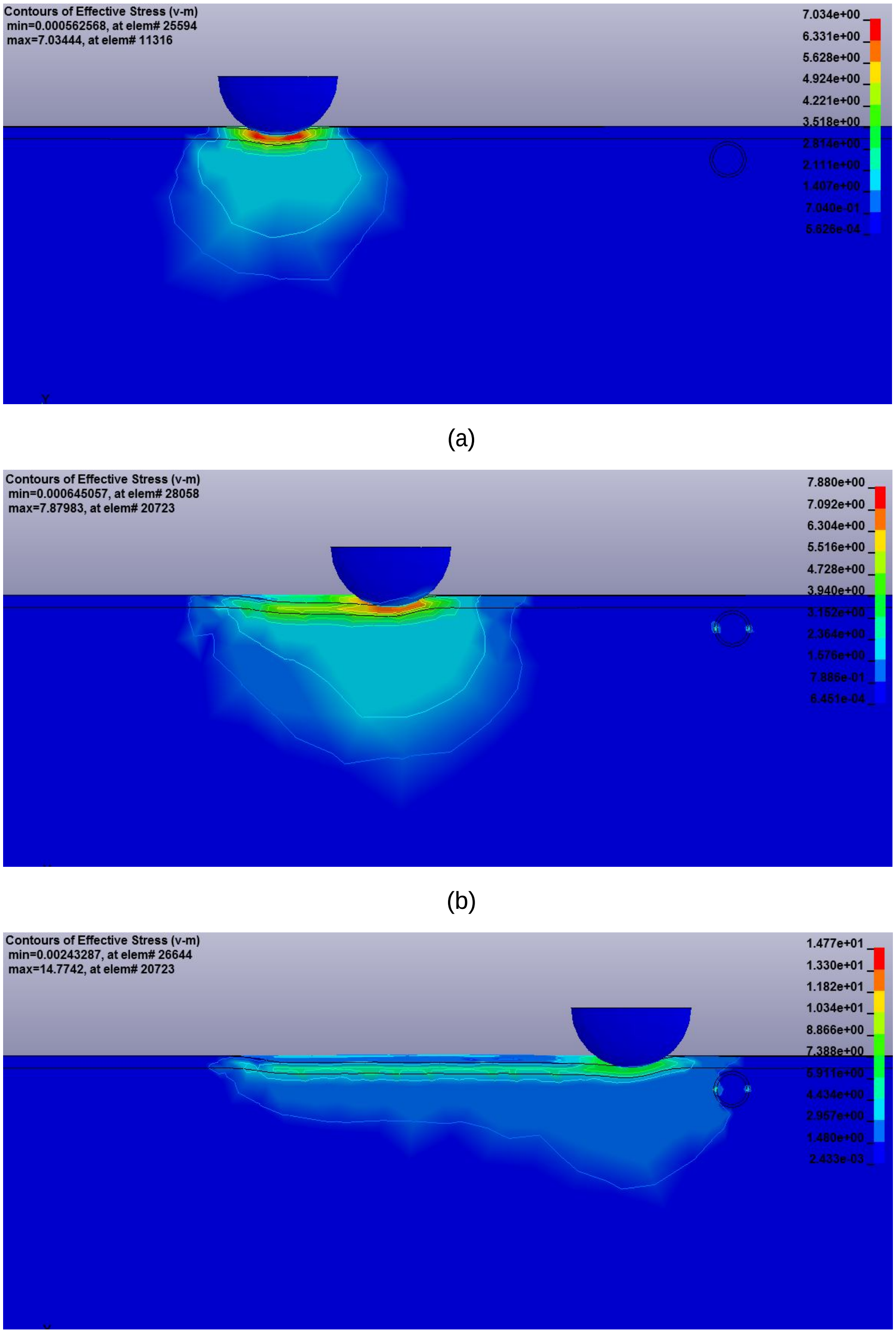

(a)

(b)

(c)

Figure 6.13: Development of a plastic zone in the scratch process (transverse section view): (a) loading process at 4 μm depth of penetration, (b) during scratch process (c) final stages.

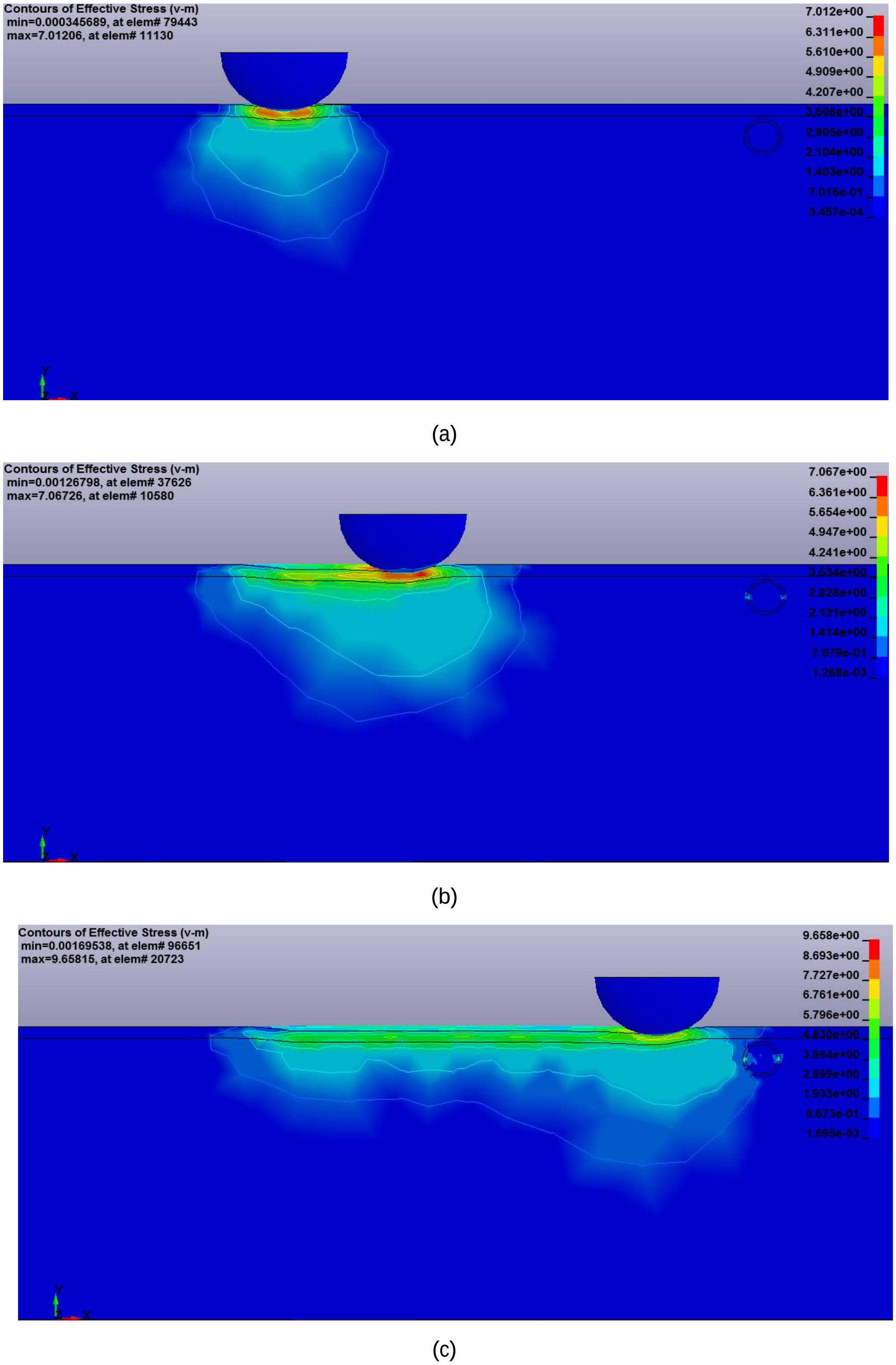

Figure 6.14: Development of plastic zone in the scratch process (transverse section view): (a) loading process 3.2 μm depth of penetration, (b) during scratch process (c) final stages.

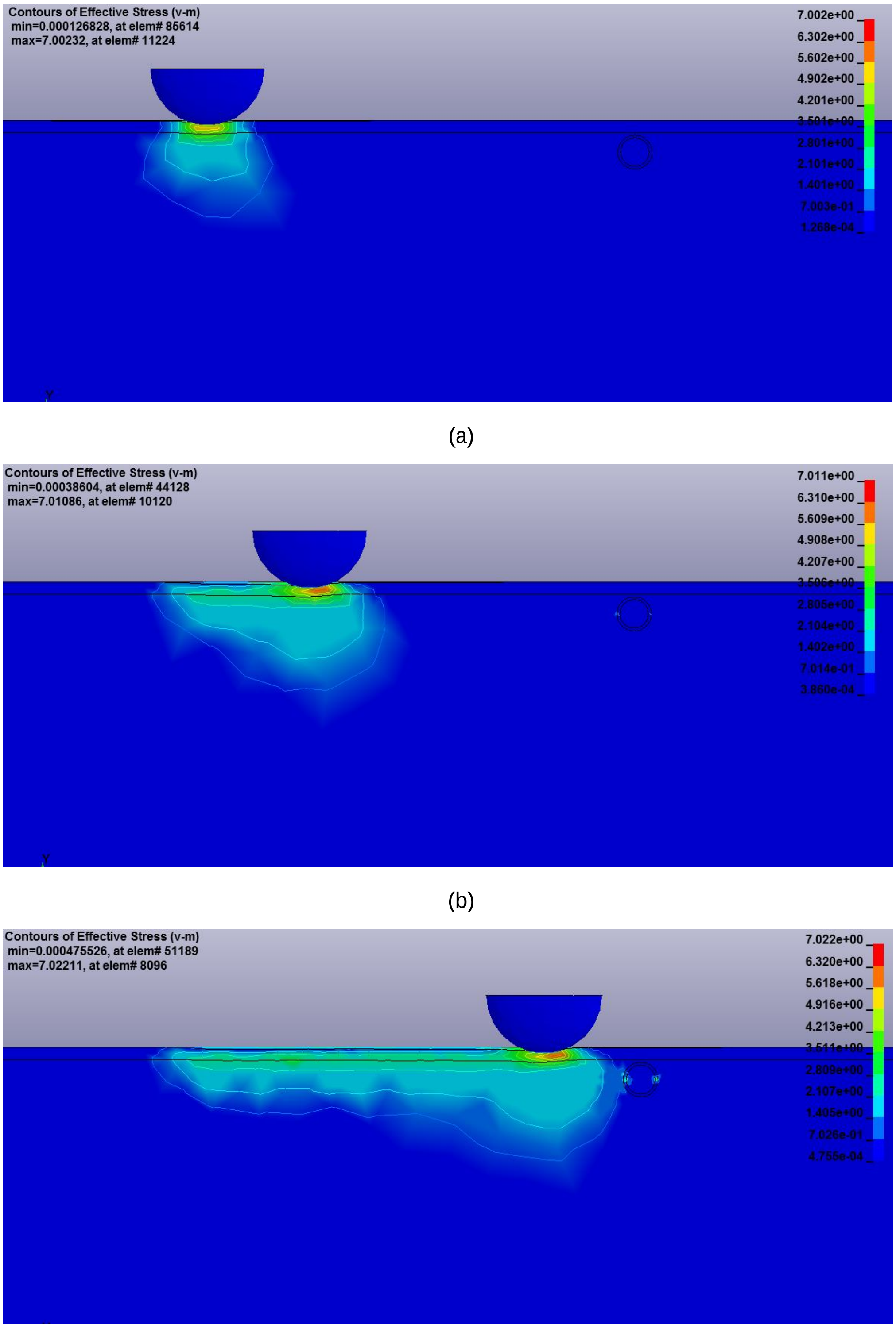

(a)

(b)

(c)

Figure 6.15: Development of plastic zone in the scratch process (transverse section view): (a) loading process at 2 μm depth of penetration, (b) during scratch process (c) final stages.

Figures 6.13 to 6.15 (b) show the middle stage of the scratching process (100 μm) where indenter slides on the surface under an applied normal depth and the material is ploughed. As the stylus moves the plastic deformation zone moves in the same direction and the plastic deformation zone has moved from the centre of the indenter towards the leading edge of the indenter, as shown in Figures 6.13 to 6.15 (c).

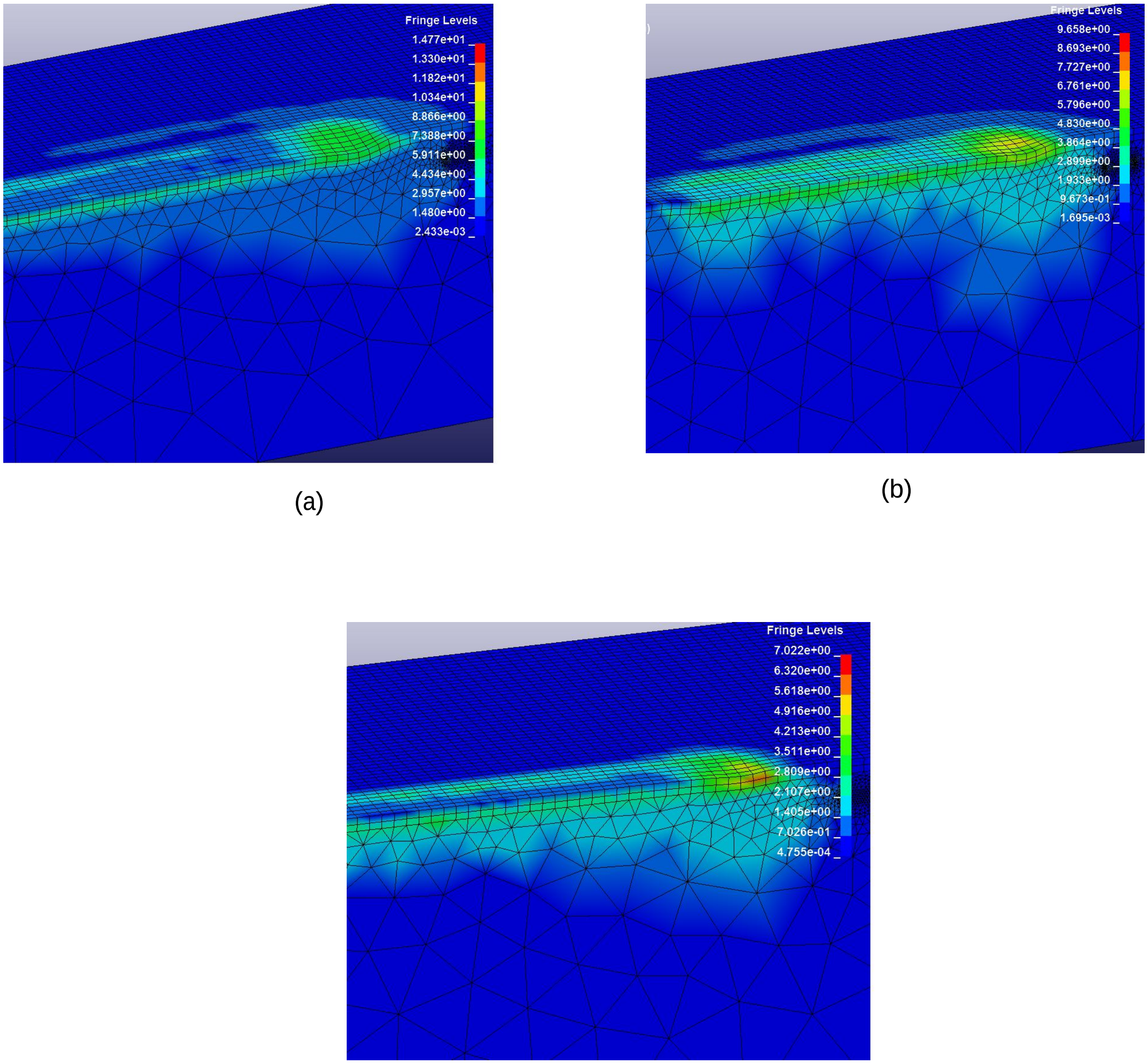

(a)

(b)

(c)

Figure 6.16: Stress field map showing von Mises stress on the oxide scale after scratch test. Sliding direction is from left to right and stress field at three different depths (a) 4 μm; (b) 3.2 μm; (c) 2 μm.

In order to observe how the depth of scratching deforms the oxide layer, three scratch simulations were performed at three different depths, 4 μm, 3.2 μm, and 2 μm. The displacement controlled model was used to simulate the stress field when the same diamond tip slides over the oxide. The variations in compression and the tensional stress field at the final stage of the scratch for three different depths are shown in Figure 6.16(a) to (c). The compression and tensional stress field under the tip at 4 μm (Figure 6.16a) and 3.2 μm (Figure 6.16b) are around 14 GPa and 9 GPa respectively. The maximum von Mises for both cases is significantly higher than the yield stress of the oxide layer (σ_y = 7 GPa) so that high plastic deformation occurs. Meanwhile, the maximum von Mises at 2 μm is about 7 GPa. The maximum stress correlates with the scratch penetration where the maximum stress increases with the increases in the depth of penetration. This is because the maximum tensile strength and shear strength that reacted on the scratched surface – the main cause of the deformation – increased with the increased penetration of the tip.

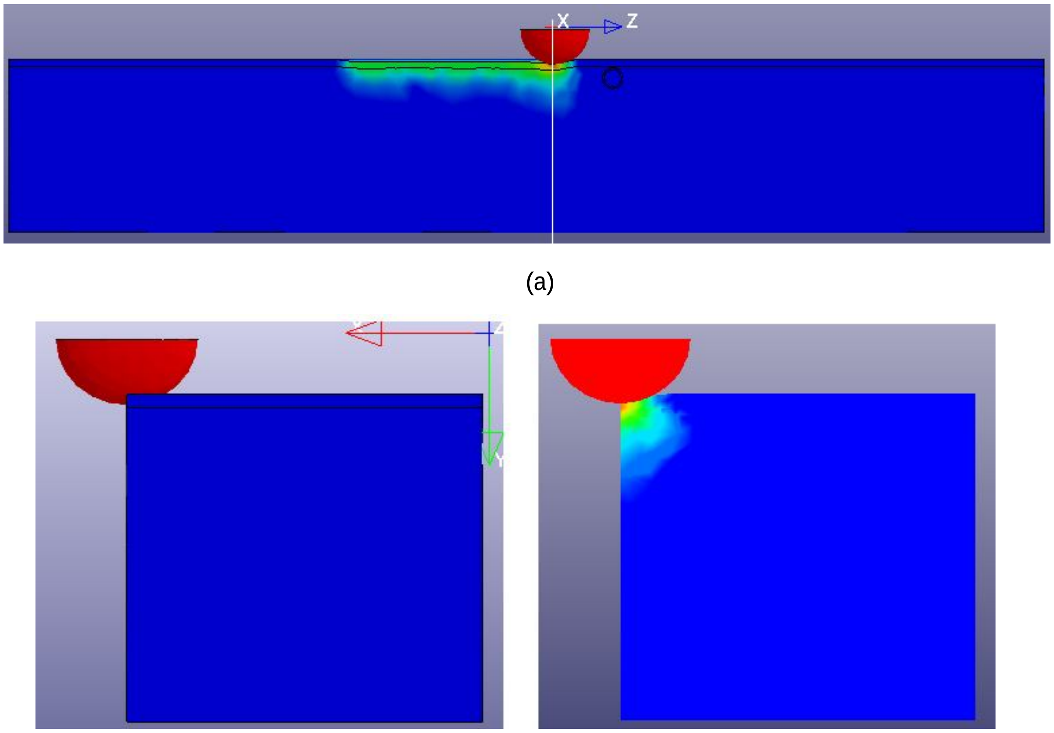

(a)

(b) (c)

Figure 6.17: The scratch test (a) the location of cutting plane (b) the side view (z-axes) before cutting (c) the cross section (z-axes) at the cutting plane.

For a more precise observation, the pile-up at the final stage (200 μm) was identified, as illustrated in Figure 6.17. The pile-ups that developed after the scratching tests at three different depths (4 μm, 3.2 μm and 2 μm) were investigated.

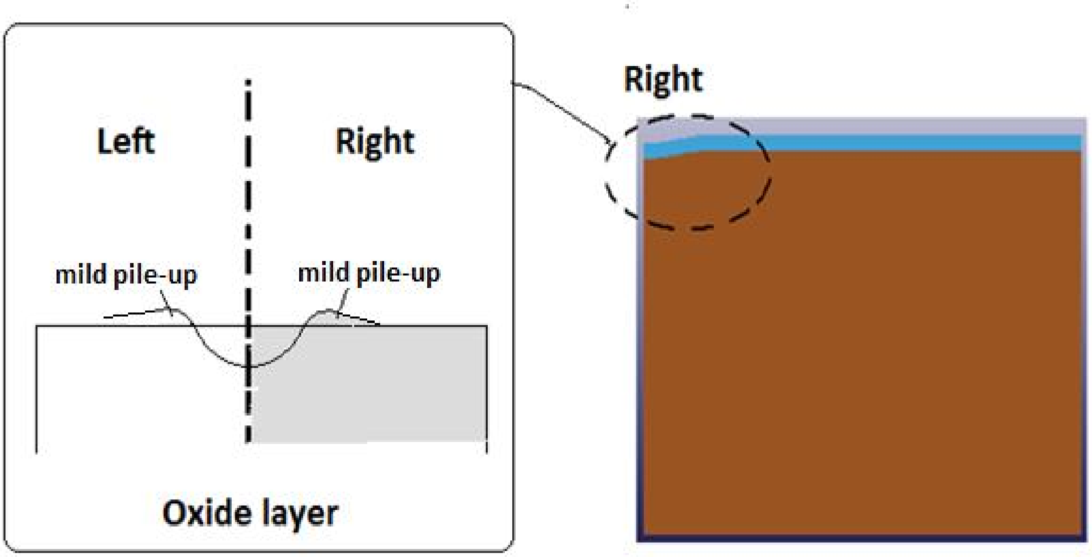

(a) (b)

Figure 6.18: The pile-up (a) the illustration of the pile-up (b) the region of pile-up.

A pile-up is generated because most of the plastic deformation occurred near the tip of the diamond, and markedly occur for non-strain hardening materials with a large value of *E/Y* (Youn and Kang, 2004). A half mild pile-up phenomenon occurred in the side of the model (Figure 6.18). The cross sections of the post-profile displacement obtained by the scratch simulation tests are shown in Figure 6.19. This figure shows a very clean cross section and low pile-up that was due to the plastic zone being typically contained within the boundary of the circle of contact and the elastic deformation that accommodates the volume of indentation spreading further away from the indenter (Youn and Kang, 2004). Therefore, sink-in is more likely to occur in this case. All three cases (4 μm, 3.2 μm and 2 μm) have elastic recovery of around 0.4-0.7 μm.

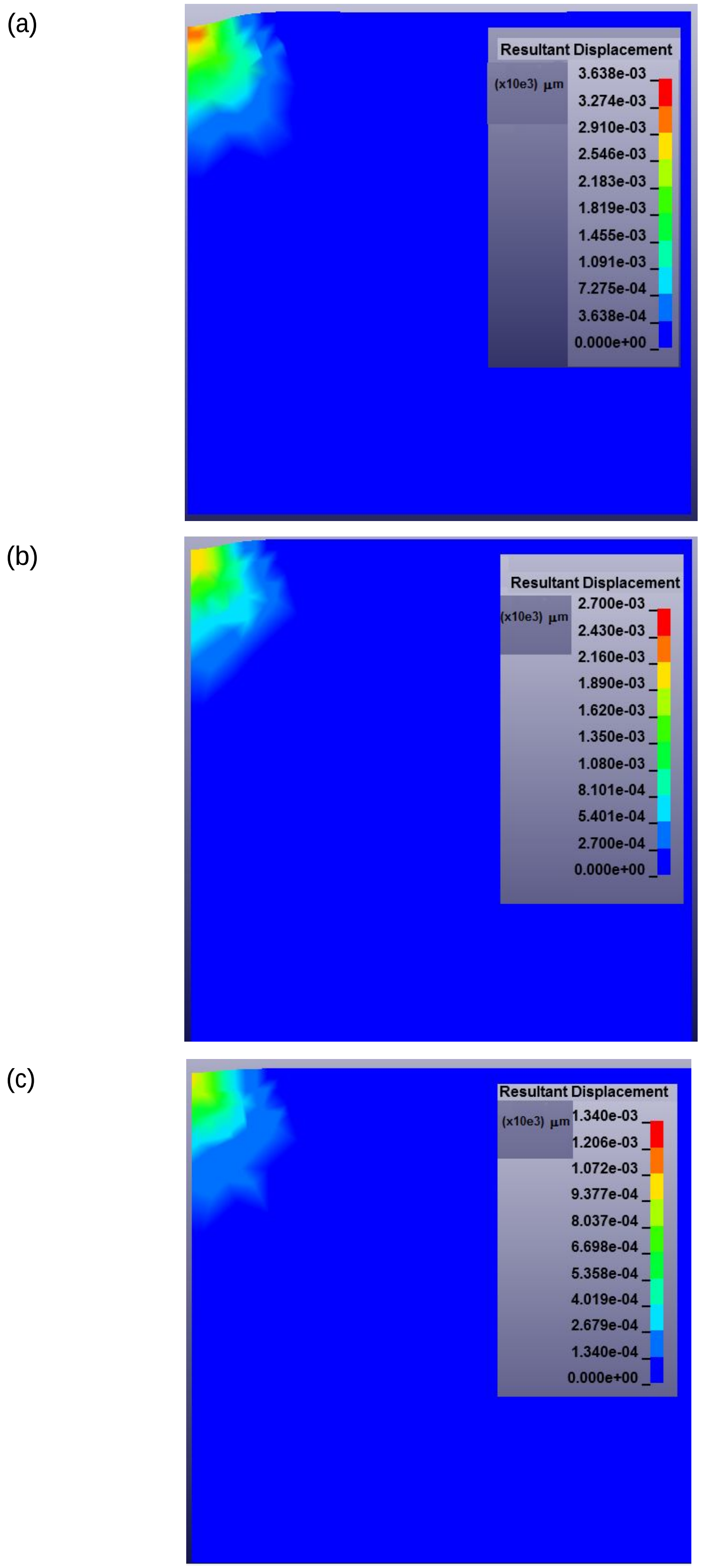

Figure 6.19: The displacement at the cross section for (a) 4 µm; (b) 3.2 µm; (c) 2 µm depth.

Based on the pile-ups, the wears for three different cases were estimated using a profilometric study. The cross section study is often used to calculate the real wear area, A_w (Kato *et al.*, 1992), which also measures the difference between the grove area and the area at both sides (Figure 6.20).

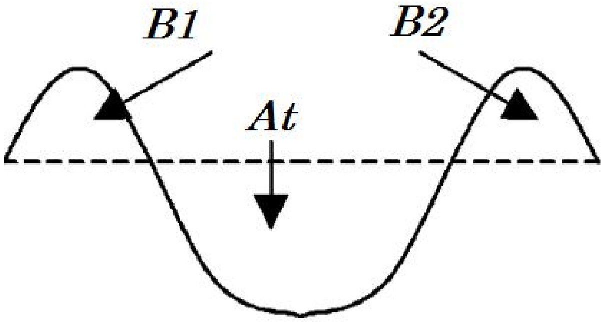

Figure 6.20: Definition of the degree of wear.

In this calculation the real wear area can be defined as

$$A_w = At - (B1 + B2) \tag{6.2}$$

where *At* is the groove area and *B1* and *B2* are the ridge area. Thus, the real wear volume can be written as

$$V_w = A_w \times L \tag{6.3}$$

and where *L* is the length of the scratch. Based on the result of the simulation the real wear volume for *L* = 200 μm at three different depths was estimated. The side ridges were very mild due to the creation of a frontal pile up that represents the ploughing mechanism. The trend of real wear volume is shown in Figure 6.21. As expected, the scratching at 4 μm provided the highest wear volume of 4140 μm^3 followed by scratching at 3.2 μm (2290 μm^3) and 2 μm (564 μm^3). This scenario was due to the correlation between the wear and contact load (given by different depths of penetration). In other words the wear depends on the capability of the slider tip to penetrate into the oxide layer during sliding. The higher penetration means that more materials are removed.

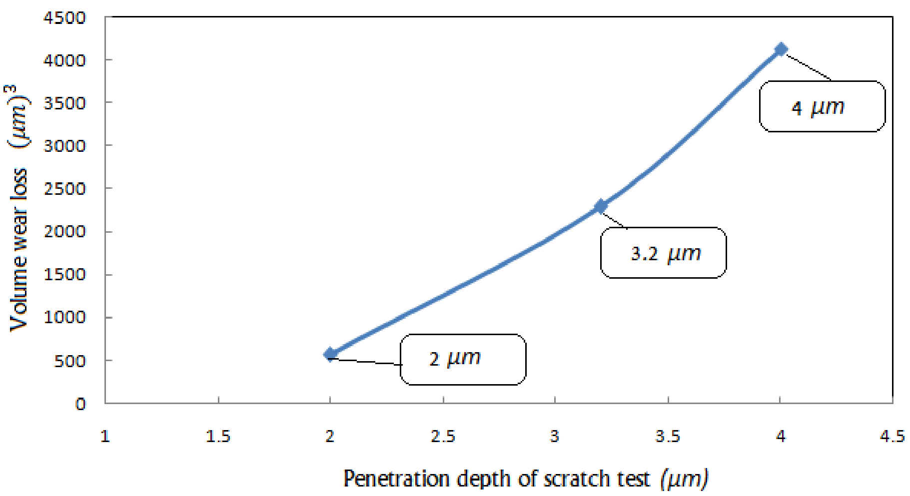

Figure 6.21: An estimation of the real wear volume for three different scratching depths.

6.2.5 Effect of depth on the damage of oxide layer using the brittle model

As the influences caused by the ductile model have previously been discussed, especially in terms of deformation and stress concentration, other aspects concerning the detachment of the oxide layer that affects the failure of the oxide layer is discussed here using the brittle model. Some conflicting opinions still exist in literature regarding the characteristics of the oxide layers. Based on Garza-Montes-de-Oca *et al.* (2011) findings, a different failure mechanism has been observed in the magnetite layer as expressed by the formation of cracks on the surfaces which reflect brittle characteristics. Therefore, in this section the oxide layer is assumed to be the brittle oxide layer.

The Johnson-Holmquist constitutive model (JH-2) was used to simulate the brittle behaviour of oxide layer. The JH-2 constitutive model was implemented in LS-Dyna as a material 110 (*MAT_JOHNSON_HOLMQUIST_CERAMICS). Initially the material was considered to be elastic, with the stress state described by the elastic material properties and the equation of state. Under compressive loading, damage began to accumulate within the material when the deviator stress exceeded a critical value. Thus, the current material strength was determined by the current material damage. The current increment in damage can be determined as the current increment in plastic strain (ε_p) per plastic strain to fracture (ε_f) under a constant load:

$$\Delta D = \frac{\Delta \varepsilon_p}{\Delta \varepsilon_f} \tag{6.4}$$

The detachment of oxide scale was modelled based on the loss of elastic energy. Under a dynamic loading, the equation of state for the brittle material can be defined by the hydrostatic pressure expression (Wang and Yang, 2008; 2009; Tian *et al.* 2012).

$$P = K_1\mu + K_2\mu^2 + K_3\mu^3 \tag{6.5}$$

where $\mu = \rho/\rho_0 - 1$, and ρ_0, ρ are the initial and final densities, respectively. K_1, K_2 , and K_3 are constants determined from the tool impact (slider tip). There is an increase in pressure when damage begins, and once it begins the loss of elastic energy is converted into hydrostatic potential energy, and as a result the materials become detached from the substrate (target).

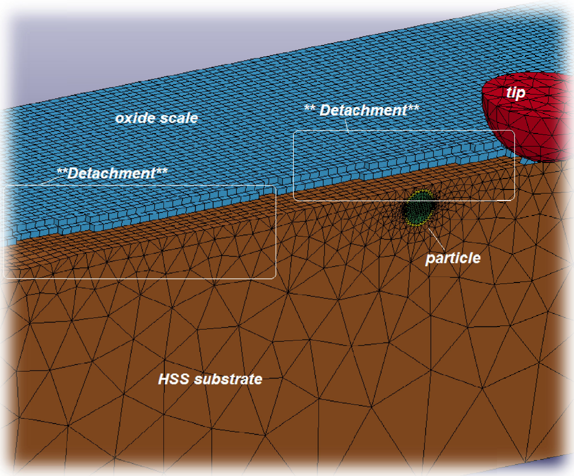

Figure 6.22: Detachment of oxide scale (spallation) by brittle model.

Figure 6.22 shows the example of failure damage by the detachment of oxide scale from the HSS substrate. The formation and breaking-up of the oxide films influence the wear behaviour. At small indentation depths the oxide layer detaches from around the tip of the indenter and propagates along the scratch tracks.

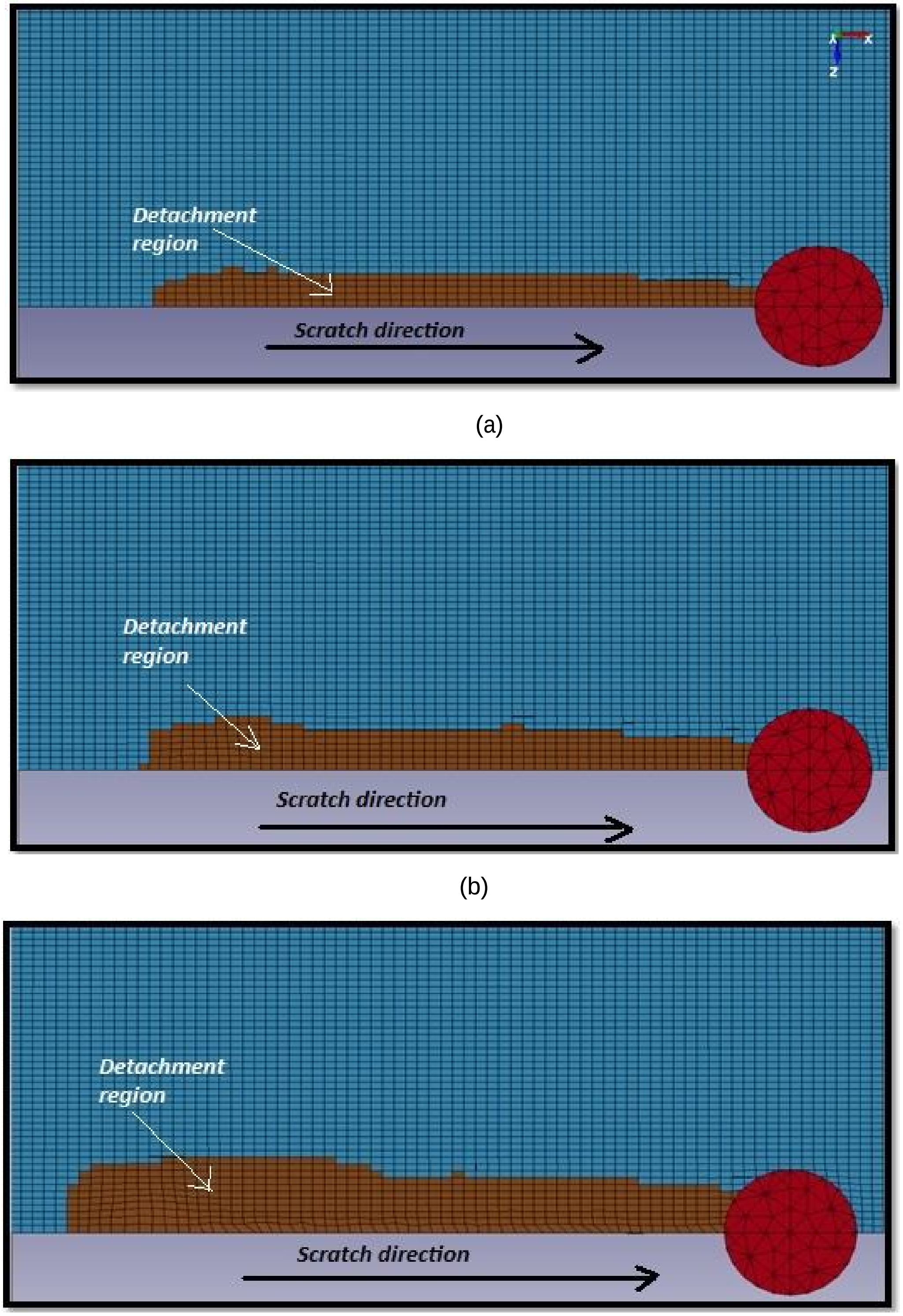

(a)

(b)

(c)

Figure 6.23: The top view of the detachment of oxide layer for different depth (a) 2 μm; (b) 3.2 μm and (c) 4 μm. The brown color of meshes represents the detachment area.

This simulation gives a fundamental understanding of scratch detachment by the brittle material model. Whilst most of the literature on the behavior of oxide scale formed on HSS work roll has centred on experimental investigations, numerical modelling efforts are limited.

Regarding the damage, it begins when the stress of the intact material exceeds the material strength at the current pressure. This leads to an increment of plastic strain and corresponding damage. The resulting contours of damage (detachment) are shown in Figure 6.23 at three different penetration depths. The brown meshes represent the detachment area for the oxide layers. It can readily be seen that the detachment generated by the tip, as shown in Figure 6.23, increases the detachment region with the depth of penetration which in turn increases the contact pressure between the tip and oxide layer.

For a quantitative measurement the loss of volume based on the detachment region were measured. Figure 6.24 shows the loss of volume at different depths based on the simulation results. The loss of volume increases as the depth of scratch increases. The loss of volume at a 4 μm depth of penetration was around 3500 μm^3 while the loss of volume at 2 μm depth of penetration was only 2000 μm^3. To explain this, the wear mechanisms and the coefficient of friction are correlated. For low scratching depth (2 μm), coefficient of friction between the tip and the oxide layer is lower, which reduces the loss of volume.

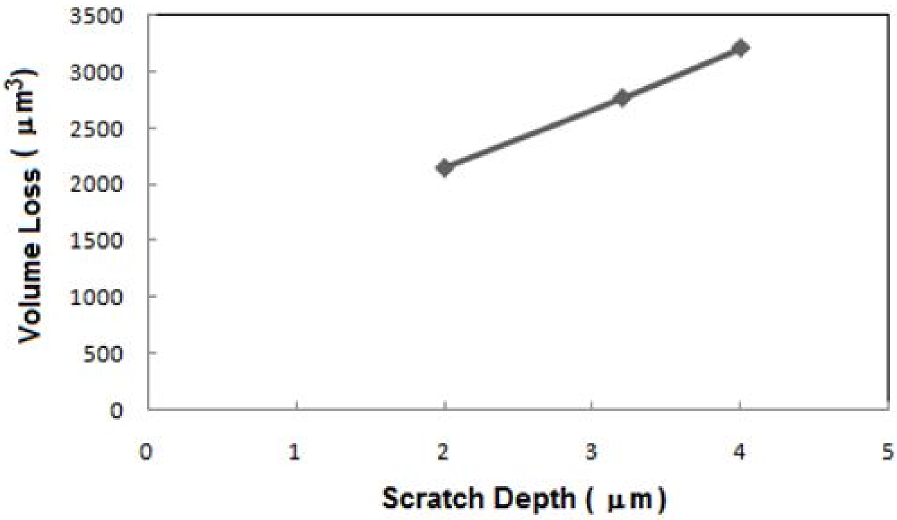

Figure 6.24: The volume loss at the different penetration depth.

In addition, the distribution of damage can also be related to the adhesive component between the oxide layer and substrate. If the scratch depth is shallow, detachment will not occur due to the existence of an adhesive component at the interface. For deep scratches (3.2 and 4 μm), the detachment component dominates due to the higher coefficient of friction between the tip and the oxide layer. For comparison, Figure 6.25 shows the track of the scratch test on the oxide layer at 2 μm. Although not compared directly here, the experimental tests demonstrate similar results in terms of damage evolution and spall.

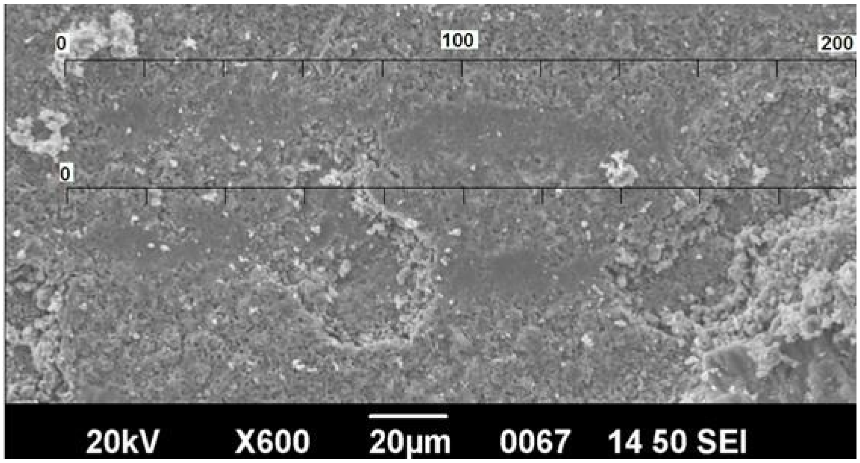

Figure 6.25: The scratch test on the oxide layer at 2 μm depth.

6.2.6 Prediction of hot work rolls wear

In the present work the result from the simulation was applied to predict wear in the work roll in actual rolling conditions. It has been reported that at least 182 wear equations have been published (Tahir, 2003). However most models are empirical and only a few influential parameters are taken into account (Meng, 1994). Tahir (2003) proposed a prediction wear model (Figure 6.26) and this model was tested on work rolls such as HSS, HiCr, and IC and can be used as a general prediction model for hot finishing mills. In this prediction model the wear was measured in terms of the depth of wear onthe work roll. By using this prediction model and the data in this chapter, the wear of the work rolls was calculated. An example of the wear prediction associated with HSS-rolls is presented below.

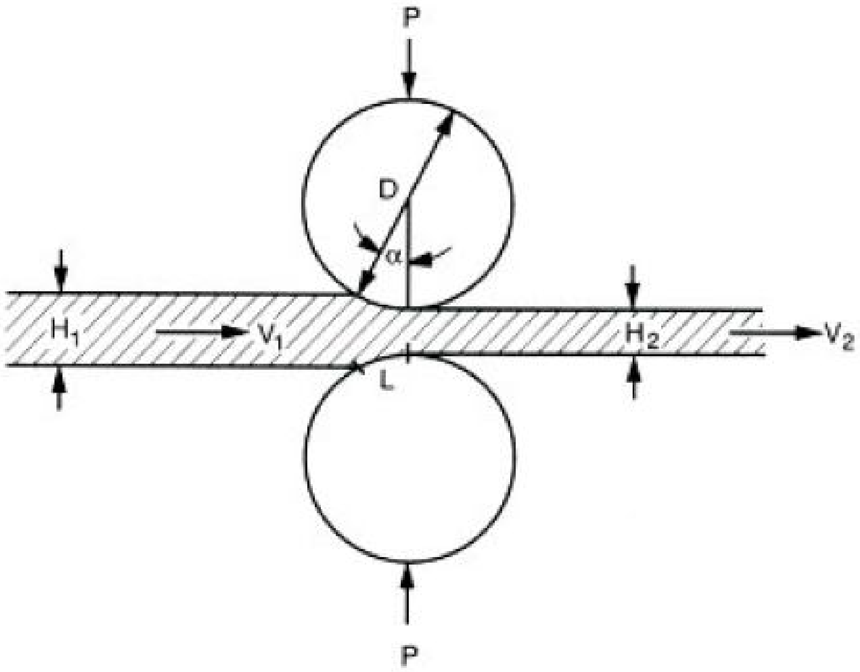

Figure 6.26: Prediction wear model.

These variables are shown in the rolling schedule and can be measured as follows:

Strip reduction, $\frac{\Delta H}{H_1} = \frac{H_1 - H_2}{H_1}$ (6.6)

Bite angle, $\cos \alpha = 1 - \frac{\Delta H}{D}$ (6.7)

Contact length between the strip and work roll,

$$L = \frac{\alpha}{360} \cdot \pi \cdot D \tag{6.8}$$

Average specific load on strip in the gap,

$$p = \frac{P}{L \cdot B} \tag{6.9}$$

Depth of work rolls wear,

$$\delta(x) = \sum_j a_i \times \left(\frac{L_i}{D_i}\right) \times \left(\frac{P_i}{B_i}\right) \qquad (6.10)$$

where δ is the depth of work roll wear, a is the wear factor, *L* is the length of rolled strip, *D* is the roll diameter, *P* is rolling load, *B* is the width of strip, H_1 is the thickness of the strip before, and H_2 is thickness of the strip after rolling.

Referring to the results of the simulation shows that the depths of penetration of the scratch tests were 4 μm, 3.2 μm, and 2μm. The total length of the scratch tests was 200 μm, the strip is 455 μm wide, the diameter of the roll is 165.6 mm, and the rolling load was 400 mN. Assuming that the depth of penetration of the oxide layer on simulation, $\delta(x)$ is 2 μm, the wear factor of the simulation can be expressed using Eq. (6.10). Inserting coefficient expression into Eq. (6.10) again gives,

$$2e\text{-}3 \text{ mm} = a_i \text{ x } \left(\frac{200e-3\ mm}{165.6mm}\right) \text{ x } \left(\frac{400e-3N}{455e-3mm}\right) \qquad (6.11)$$

Thus, the wear factor of the simulation test can be written as

Wear factor, a_i = 1.885e-4 mm^2/N (6.12)

The bite angle can now be determined from Eq. (6.7), as shown below. Consider the thickness of H_1 is 12 mm and H_2 = 1.5 mm, the cos α is given by

$$\text{Cos } \alpha = 1 - \frac{12mm-1.5mm}{165.6mm} \qquad (6.13)$$

Consequently α is 20.51°. Then the contact length between strip and work roll can be determined using Eq. (6.8). By adding α in (Eq. 6.8), the contact length is given as

$$L = \frac{20.51}{360} \cdot \pi \cdot 165.6mm \qquad (6.14)$$

Now, using Eq. (6.14), the contact length can be measured where L = 29.64 mm. The final step is to determine the load per width using Eq. (6.9). By inserting the average specific load on the strip, p = 100 N/mm^2 in Eq. (6.9), and the value of load per width can be written as

$$\frac{P}{B} = p \cdot L = 100\text{N/mm}^2 \times 29.64\text{mm} \qquad (6.15)$$

Solving for Eq. (6.15), we get the load per width = 2964 N/mm.

By using the calculated parameter based on the FE simulation, the predicted wear of the work roll at the contact length can be measured using Eq. (6.10) as below:-

$$\delta(x) = 1.885\text{e-}4\text{mm}^2/\text{N} \times \frac{29.64mm}{165.6mm} \times 2964\text{N/mm} = 0.10\text{ mm} \qquad (6.16)$$

Examples of the calculations of predicted work roll wear using the scratch data are presented above. According to this result, the work roll wear is 0.1 mm. Compared to Tahir's (2003) finding where he reported that the roll wear of HSS work roll is 0.02-0.03 mm and the HiCr work roll is 0.09-0.12 mm. The reason for higher wear in the simulation based model was probably due to the use of lubrication in the industrial work-roll by Tahir (2003).

6.3 Discussion

The simulations of the stress fields in the surface of the loaded oxide scale illustrate the complexity of the loading and stress conditions in the surface when it is exposed to a sliding action. Two basic wear factors/material removals have been proposed to explain the scratch behaviour, 1) coefficient of friction, and 2) material characteristics and concentration of bulk plasticity.

The effect of coefficient of friction is well illustrated in Figures 6.9 and 6.10. The coefficient of friction increased in an approximately linear function with scratch depth. In the ductile model the friction force pulls the oxide scale and causes tensional stresses in the oxide scale in a sliding direction behind the contact. Friction force also results in a pushing the oxide scale in front of the sliding tip. This behaviour causes deformation on a fairly plastic oxide in the HSS work roll.

Meanwhile, friction in the brittle model friction tends to wedge the oxide layer from the substrate in the HSS work roll, which also shows strong adhesion between brittle material and substrate. In the brittle model, some of the energy goes into the creation of new surfaces (wear) while in the ductile model some is used in deforming the materials.

The oxide layer that forms on HSS tended to be classified as ductile rather than brittle because the coefficients of friction predicted by the ductile model were closer with experimental result than the brittle model. In fact, there was no cracking during nanoindentation on the oxide scales so the oxide layer could be considered as having ductile behaviour. At this stage, it is believed that the oxide scale formed on the high speed steel behaved as ductile within the oxide thickness range < 4 μm after considering the coefficient of friction as well as the failure of the oxide layer.

The effect of the material characteristics is well illustrated in Figures 6.13 to 6.15 because in this study they are related to the role of classic ploughing wear. This result also confirms the earlier observations by Garza-Montes-de-Oca *et al.* (2011) where the characteristics of the oxide layer on HSS might act as fairly plastic when compressive thermal stress is applied. The roll wear was also measured in terms of the depth of work roll wear using the prediction model. By using this prediction model and the data in this chapter, the wear of the work rolls was calculated. The work roll wear of oxide layers formed on HSS was slightly higher (0.1 mm) than the HSS work roll (0.02-0.03 mm), probably due to the lubrication factor used in the industrial work roll.

6.4 Conclusions

A three-dimensional (3D) finite element (FE) simulation of an indenter scratching on oxide layers and high speed steel substrate system has been presented. The finite element result can be used to explain the failure modes and mechanisms of oxide layer on high speed steel (HSS). The friction and wear behaviour observed in the current study are related to the role of oxide detachment, as well as the classical ploughing wear mechanism. Two basic factors that explained the scratch behaviour were described in terms of, 1) coefficient of friction and, 2) the material characteristics and concentration of bulk plasticity.

The coefficient of friction increases in an approximately linear function with the depth of scratch. By considering the mechanical property based arguments for the brittle and ductile models, the coefficient of friction increases with the depth of scratch under both conditions, but is significantly higher for the brittle conditions compared to the ductile model. This is because in the brittle model some of the energy goes into the creation of new surfaces (wear) while in the ductile model some is used in deforming the materials. The reasons why the simulated coefficients of friction are higher than experimental ones are due to many attributions which contributed to the measured friction force such as the mechanical property based arguments (shear properties of the solids and of the substances between the surfaces), fluid dynamics approaches, considerations of electrostatic forces between surface atoms, and chemical compatibility arguments. Therefore, the results of the simulation may only be compared qualitatively with the experiments.

Regarding the characteristics of oxide scale formed on HSS, the oxide layer tends to be classified as ductile rather than brittle, a justification based on three reasons: a) the predicted coefficients of friction by ductile model are closer to the experimental result than the brittle model, and b) no cracking occurred during nanoindentation on the oxide scales. As a result the characteristic of the oxide layer can be assumed to be ductile. Finally, c) the material characteristics observed in this study are related to earlier observations by Garza-Montes-de-Oca *et al.* (2011). In summary, it is believed that the oxide scale formed on high speed steel behaves as ductile within the oxide thickness range < 4μm after considering the coefficient of friction and the failure behaviour of the oxide layer.

Chapter 7

FE study of the effect of carbide particles on the behaviour of the oxide layer

7.1 Introduction

The existence of carbides in HSS material can influence the contact friction and wear of the oxide layer. Because carbides are much harder than the matrix they contribute to the mechanical strength, load bearing capacity, and wear resistance (Park *et al.,* 1999; Badisch and Mitterer, 2003). There are many carbides factors that are related to variations in the wear resistance such as the content of carbon and chromium, and the fraction, size, and distribution of carbide, etc. Kang *et al.* (2001) found that the wear resistance of high speed steel rolls increases with the increase of the total fraction of carbide because of increased carbon content. The authors also indicated that the wear resistance of HSS work roll improves with a smaller amount of chromium because it results in the formation of a number of very hard MC carbides. Rodenburg and Rainforth (2007) found that carbide size distribution is a major controlling factor in the mild oxidational wear of high speed steel. A reduction in the size of carbide for a constant volume fraction lowers the matrix being exposed to contact damage by decreasing the mean distance between the carbides.

Since oxidation on HSS work roll leads to the formation of an oxide layer, the influence and the role of carbide formed on HSS may be changed after oxidation because the oxide layer covers not only the matrix but also the carbides. In-situ observations indicate that the oxide layer nucleates at the carbides/matrix interfaces and then spreads outward to cover the carbides, followed by a continuous growth over the whole surface (Zhu *et al.,* 2011). Since the wear of a high speed steel work roll is influenced by the oxide layers (Molinari *et al*., 2000), an investigation into the role of carbides in the wear process becomes significant.

Carbide precipitates in high speed steel due to the high vanadium content of these alloys (Boccalini and Sinatora, 2002). HSS work rolls consist of complex multicomponent alloys. The main alloying elements in HSS are carbon, vanadium, chromium, tungsten, and molybdenum. The typical microstructure of HSS consists of primary carbides (10-20%) distributed in a matrix of tempered martensite and fine secondary carbides formed from the high concentration of strong carbide forming elements such as V, W, and Mo. Boccalini and Sinatora (2002) reported that an increasing amount of vanadium causes the formation of MC eutectic with an intercellular network of M_2C or M_7C_3 carbides that have a tendency to micro-spalling and subsequent falling off. As the oxidation behaviour of carbides affects the homogeneity of the oxidised surface of work rolls, this has an important influence on wear, and therefore it is instructive to investigate the effect that carbide particles have on the behaviour of the oxide layer.

In this chapter the interaction between the carbide and the asperity by an abrasive mechanism is investigated. The abrasive factor in the hot strip mill is given by asperities where the oxide layers of strips act as multiple asperities and abrade the oxide layers of the work rolls. In a previous work we analysed the wear of the oxide layer using a micro-scratch. In order to work out how carbide affects the behaviour of the oxide layer, a 3D FE model was established to analyse the deformation of the oxide layers and the indenter-carbide particle interactions during a scratch process. The 3D FE model was able to show the interaction between the indenter and the carbide particle reinforcements of these following scenarios: particles above, along, and below the scratch path. The development of stress and strain fields in the oxides and high speed steel substrate was analysed and physical phenomena such as removal materials, particle de-bonding, and material displacement were explored. The model developed here represents an incremental advancement of the scratching FE models that explain the failure modes and mechanisms of the oxide layer on high speed steel (HSS).

7.2 Simulation methods

7.2.1 Cases studied

In the present investigation the interaction between the scratch tip and particle was categorised into 3 scenarios: particle above the scratching path, particle along the scratching path, and particle below the scratching path. All three cases were chosen based on the three different possibilities of particle location which (Figure 7.1) are:-

a. on oxide free surface

b. on oxide-substrate interface

c. below oxide-substrate interface (in the substrate)

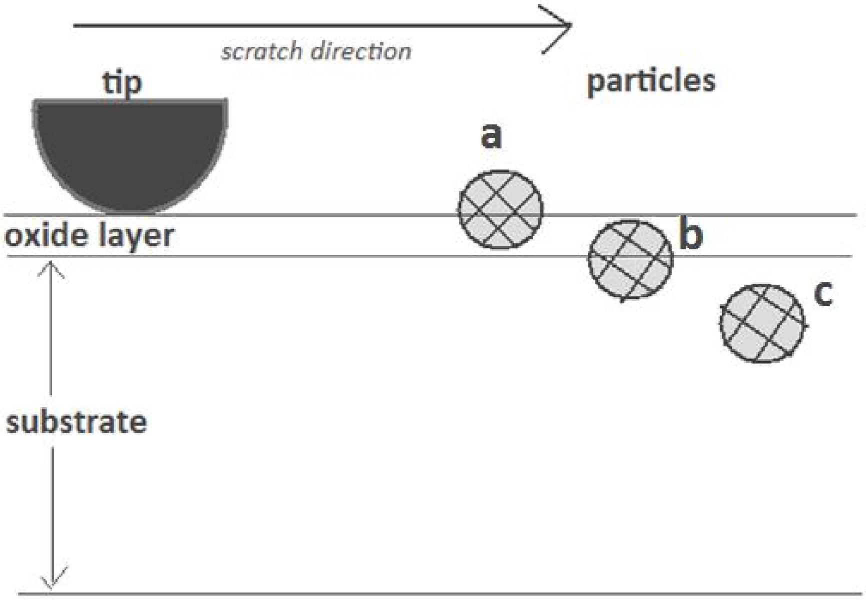

Figure 7.1: Particle locations with the respect to the oxide layer: (a) particle on oxide free surface; (b) particle on oxide-substrate interface (c) particle below oxide-substrate interface (in the substrate).

Since in the real case of HSS the carbide particles are only precipitated in the oxide-substrate interface (case b), or in the substrate (case c), as reported by Boccalini and Sinatora (2002) and Zhu (2012), these two cases were analysed in section 7.3.1 and 7.3.2 respectively. The distribution of carbides particles in the HSS substrate and oxide layer was shown in Figure 7.2. For case, (a) which is particle located on oxide free surface, the simulation is explained in section 7.3.3. Although the location of the carbide is not real, this simulation can be modelled as debris in a real case.

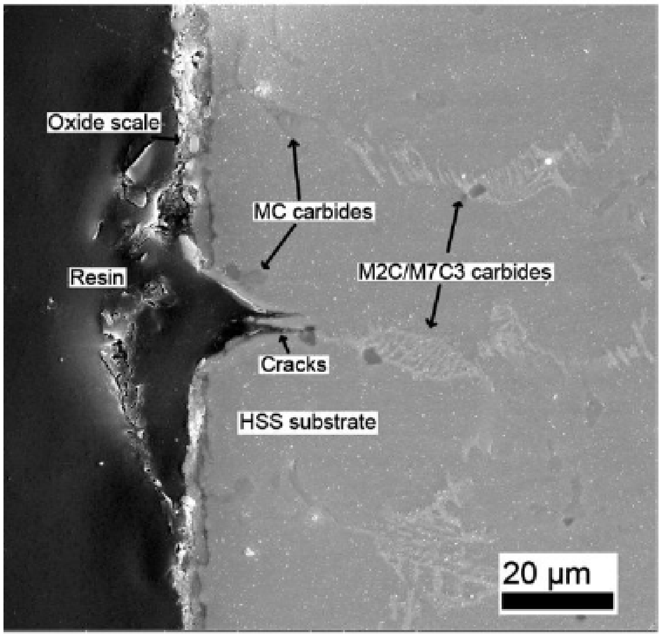

Figure 7.2: The distribution of carbides in HSS substrate and oxide layer (Zhu, 2012)

Two cases of temperature occurred during the scratching tests: low temperature (room temperature) and high temperature (600°C). The model only considered one sub-layer due to the large 1:4 ratio of the outer sub-layer and inner layer sub-layer. During the scratch test a particle will probably go into the chip, some will be de-bonded and fractured, and the remainder will probably remain on the HSS substrate.

7.2.2 FE modelling

A three dimensional finite element model was constructed using the explicit finite element method. In accordance with practice the particle was assumed to have a diameter 10 µm. This is an agreement with the size of primary M_6C and MC carbide particles reported by Vardavoulis (1994) where the particles vary between 2 and 10 µm. The assumptions and parameters used in the FE modelling are summarised in Table 7.1.

Table 7.1: Assumptions and parameters for FEM of scratch test.

Scratch depth (μm)		3.2
Outer radius zone (μm)		5.1
Inner radius particle (μm)		5
Centre point of particle (um):	*a*	(x, y= 40, 4)
Centre point of particle (um):	*b*	(x, y= 40, 2.8)
Centre point of particle (um):	*c*	(x, y= 40, -3.2)
Centre point of particle (um):	*d*	(x, y= 40, -6.2)
Centre point of particle (um):	*e*	(x, y= 40, 4)

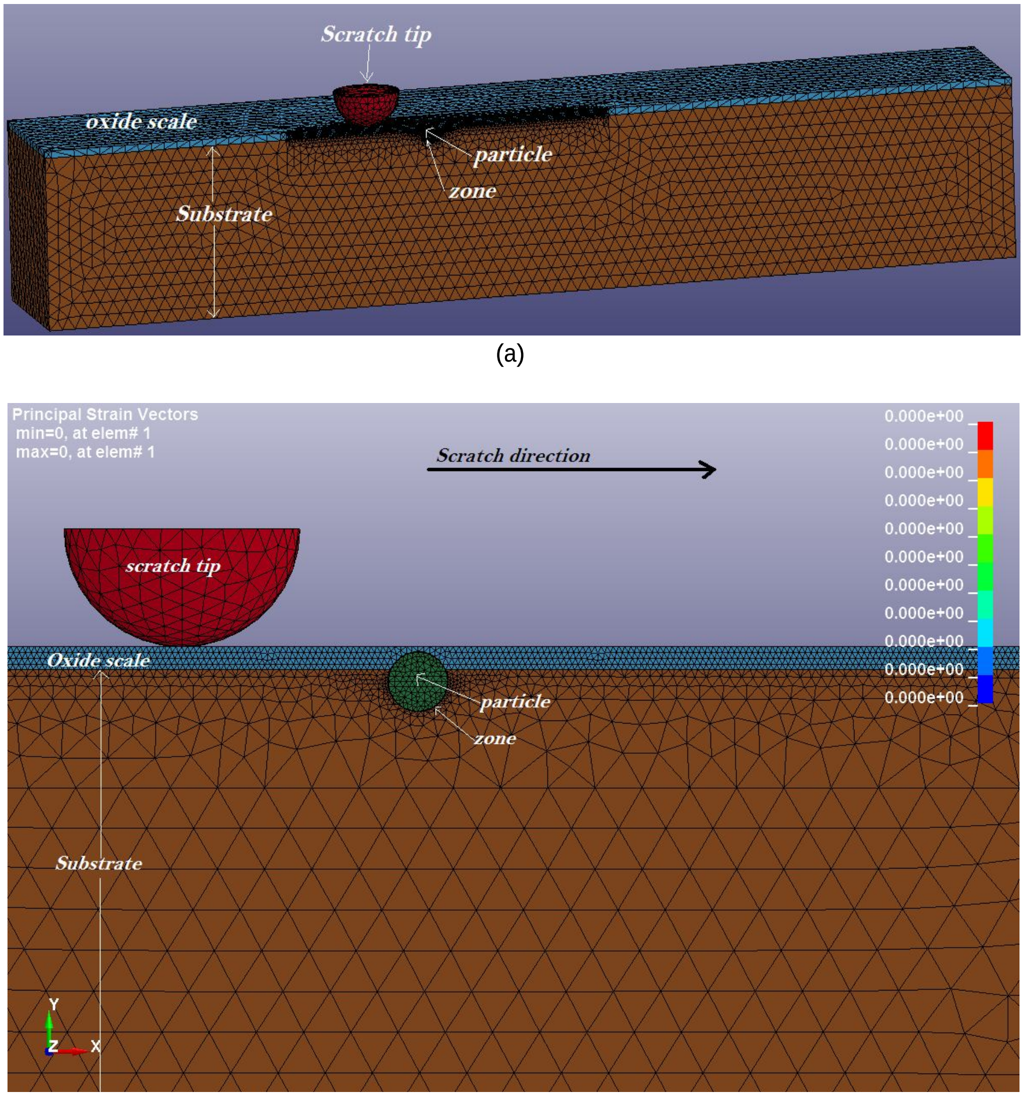

(a)

(b)

Figure 7.3: 3D FE model for simulating the scratch test; (a) overall model (b) details around the original location.

A three dimensional finite element model was constructed using the explicit finite element software package ANSYS/LS-DYNA version 13. The geometry of the scratch is shown in Figure 7.3 (a). The particle was assumed to be perfectly bonded, which is similar to the work reported by Pramanik *et al.* (2007). In this case the interface nodes of the matrix and particle were tied together by an interface zone. Since the interface zone is very hard and brittle and hence similar to the particles, the interface was considered to be an extension of the particle. The indenter was treated as a rigid body and moved horizontally in the oxide scale. The substrate was fully fixed on its bottom surface to eliminate rigid body motion.

The oxide scale material was a Fe_3O_4 reinforced with a carbide particle that was surrounded by an interface zone. The substrate is high speed steel (HSS). A plastic kinematic material and associative flow rule were used for the interface zone respectively. The strain rate was accounted for by using the Cowper-Symonds model which scaled the yield stress by a strain rate dependent factor and the equation to calculate yields stress in plastic kinematic material model is given below:-

$$\sigma_y = \left[1 + \left(\frac{\dot{\varepsilon}}{C}\right)^{\frac{1}{P}}\right](\sigma_o + \beta E_p \varepsilon_p^{eff}) \qquad (7.1)$$

$$E_p = \frac{E_{tan}E}{E - E_{tan}}\pi r^2 \qquad (7.2)$$

where σ_y is the yield stress, σ_o is the initial yield stress, $\dot{\varepsilon}$ is the strain rates, C and P are the Cowper-Symonds strain rate parameters, ε_{eff} is the effective plastic strain, β is the hardening parameter, and E_p is the plastic hardening modulus, E_{tan}, is the tangent modulus, and E is the modulus of elasticity. The material properties of the oxide layer were based on the experimental results from Zamri *et al.* (2012). The two sets of mechanical properties which correspond to room temperature and high temperature were applied to the model.

Table 7.2: Assumptions and parameters for FEM–based scratch test modelling for ductile model

Oxide scale surface	Smooth
Oxide scale/ Substrate interface	Perfectly bonded
Scratch distance (µm)	~200
Indenter tip radius(µm)	20
Oxide scale thickness(µm)	4
Oxide scale material	Fe_3O_4
Oxide scale material properties at room temperature	E = 245 GPa, υ= 0.2, σ_y= 7 GPa
Oxide scale material properties at high temperature (600^{o}C)	E = 221 GPa, υ= 0.19, σ_y= 5 GPa
Substrate material properties	E = 210 GPa, υ = 0.3, σ_y= 2 GPa
Particle properties	E = 345.1 GPa, υ = 0.3

A failure separation criterion available in ANSYS/LS-DYNA for this material model was used in the simulation. According to this criterion, failure separation occurs when the strain energy release rate is exceeded a critical value. During the scratch test, a cohesive zone surrounding the particle will probably go into the chip, some will be de-bonded and fractured and the rest will probably remain on the HSS substrate. In the present investigation, the interaction between the scratch tip and particle was investigated following 2 scenarios: particle on oxide-substrate interface, and particle in the substrate. The consideration of the particle in both positions was based on the actual carbides where they are embedded into the oxide layer and substrate. The model of the oxide layers in this chapter was considered to be a ductile model based on the results in the previous chapter (Chapter 6). In this finding the behaviour of the oxide layers was confirmed to be ductile, which corresponds to their failure characteristic. The assumptions and parameters used in the FE modelling are summarised in Table 7.2. The model has considered one sub-layer only due to the large 1:4 ratio of the outer sub-layer and inner sub-layer.

7.3 Results

7.3.1 Evolution strain field

The behaviour of the oxide layer and carbide particle was investigated in terms of the strain field contour. Strain is a description of deformation in terms of relative displacement, but it also becomes an indicator to identify the failure of the element when the strain is greater 1.

The plastic strain contour has clearly increased as the scratch tip moves into the oxide layer during nanoindentation. A high distribution of the plastic strain contour occurred at the interface zone of the particle when the scratch tip and the particle came into contact. Plastic deformation occurred as the oxide layer material entered into the deformation zone. Contact interaction between the scratch tip and particles caused the particles to de-bond.

There are two ways particle can de-bond, either partially or completely. De-bonding leads to particle failure during scratching. The partial de-bonding of the interface zone may cause the particles to become embedded into the oxide layer while the complete de-bonded zone may cause the particles to be removed from the oxide layer. Thus, the evolutions of strain at room temperature and high temperature leading to particle de-bonding are explained in the following section. Two cases were considered, (i) particle on oxide substrate interface, and (ii) particle below oxide-substrate interface (in the substrate). The FE model was validated in the previous chapter by comparing the FE result with Zhou *et al.* (2008), so that the FE model with a particle in this chapter can be assumed to be reliable.

7.3.1.1 Particle on oxide substrate interface

The evolution of strain fields during scratching for a particle located on the oxide-substrate interface was analysed in 3 stages; after nanoindentation, during tip-particle contact, and post tip-particle contact (Figure 7.4). Initially the tip indents on the oxide layer and substrate (stage 1 in Figure 7.4), then interacts with the particle at the scratching edge (stage 2 in Figure 7.4), and then continues to move until the scratching process ends (stage 3 in Figure 7.4).

Figure 7.5 shows the simulation at room temperature strain field result while Figure 7.6 is the result from simulation at high temperature (600^{o}C) for the three consecutive stages of the scratching process. The strain contours after nanoindentations are shown in Figures 7.5a and 7.6a. The compressive and tensile strains are perpendicular to the scratch tip during nanoindentation into the oxide layer and substrate.

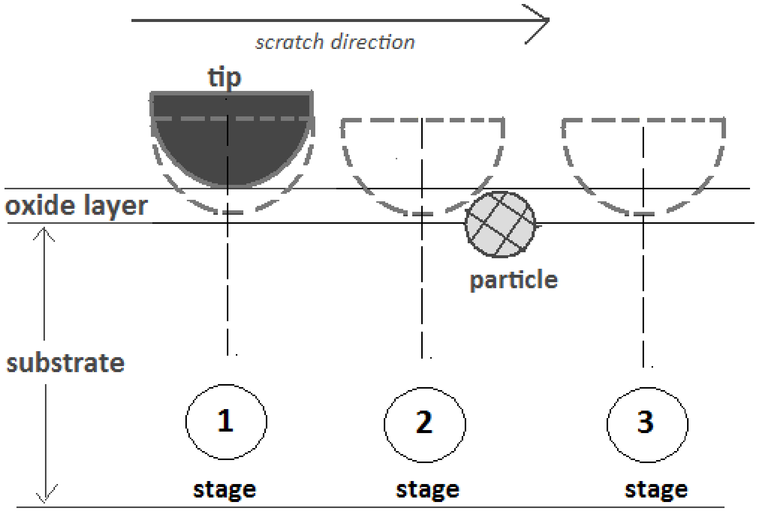

Figure 7.4: Particle locations on oxide-substrate interface (Case b).

As can be seen from Figures 7.5a and 7.6a, the maximum strain is up to 0.02, after which it then slides into the oxide scale layer causing a high plastic strain in the surrounding oxide and substrate (stage 2). As scratching progresses the particle is partially de-bonded after the tip and the particle interact at the edge of the scratching (Figure 7.5b and 7.6b). Both cases (low and high temperature) showed the maximum strain contour beyond the strain limit which were 1.025 (Figure 7.5b) and 1.07 (Figure 7.5b) respectively.

Since the maximum strain was slightly higher than the strain limit (strain limit = 1), the fragment of the interface zone was not too significant so as a result, the movement of the particle was not too obvious. This situation might be related to the attack angle between the scratch tip and particle. As the tip moved further (stage 3), the particle moved slightly forward (Figure 7.5c and 7.6c).

The movement of slider lead to the particle appearing at the surface due to fracture at the bonding interface between the particle and oxide layer. At this stage the contours section had the higher strain of 1.05 compared to stage 2 at room temperature, as shown in Figure 7.5c. This condition might be due to particles on the lower part of cutting edge becoming de-bonded, leading to an increase in the strain.

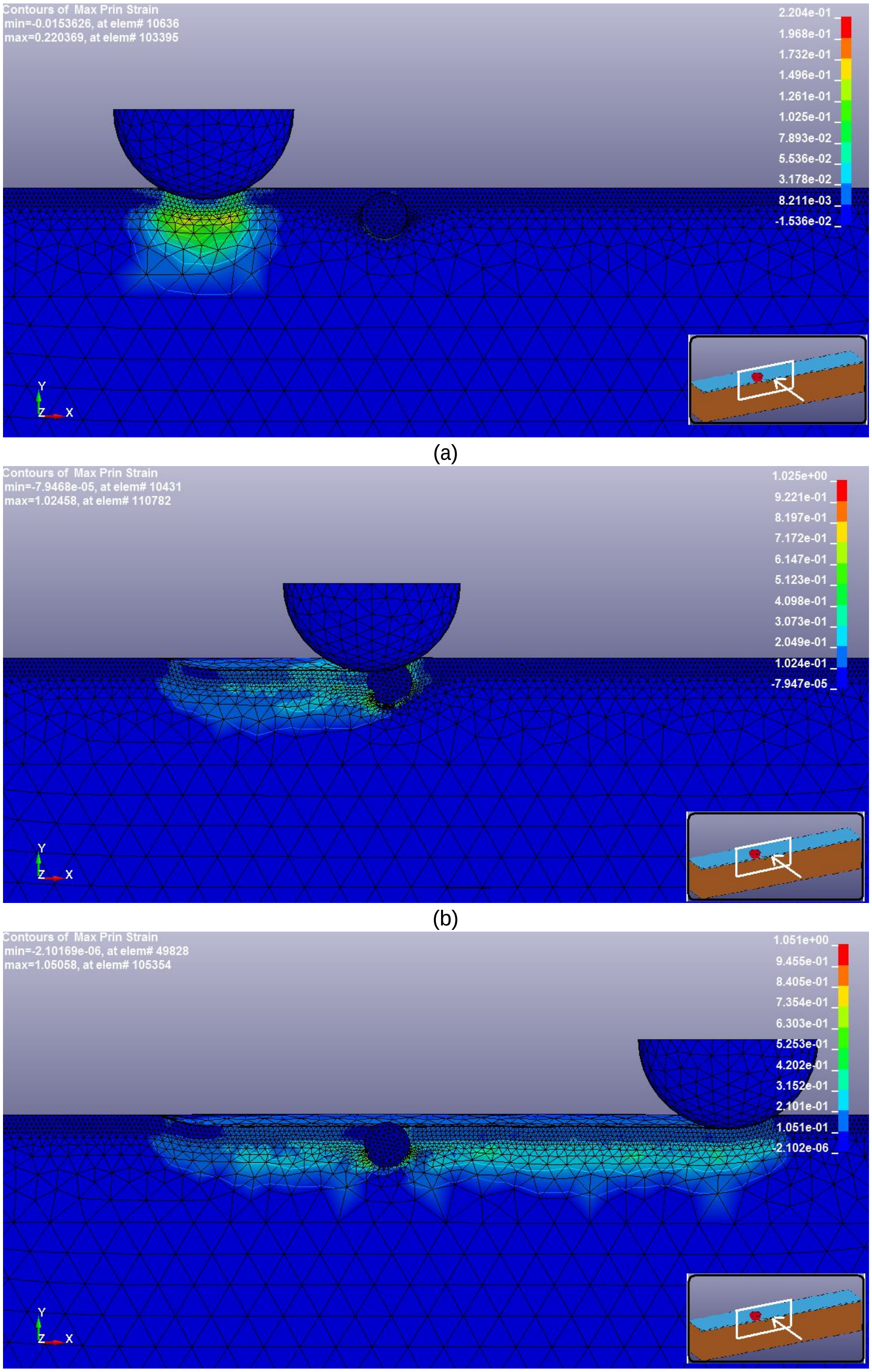

(a)

(b)

(c)

Figure 7.5: The strain field of the particle on oxide substrate interface at room temperature (a) before scratching (b) during scratching. (c) after scratching.

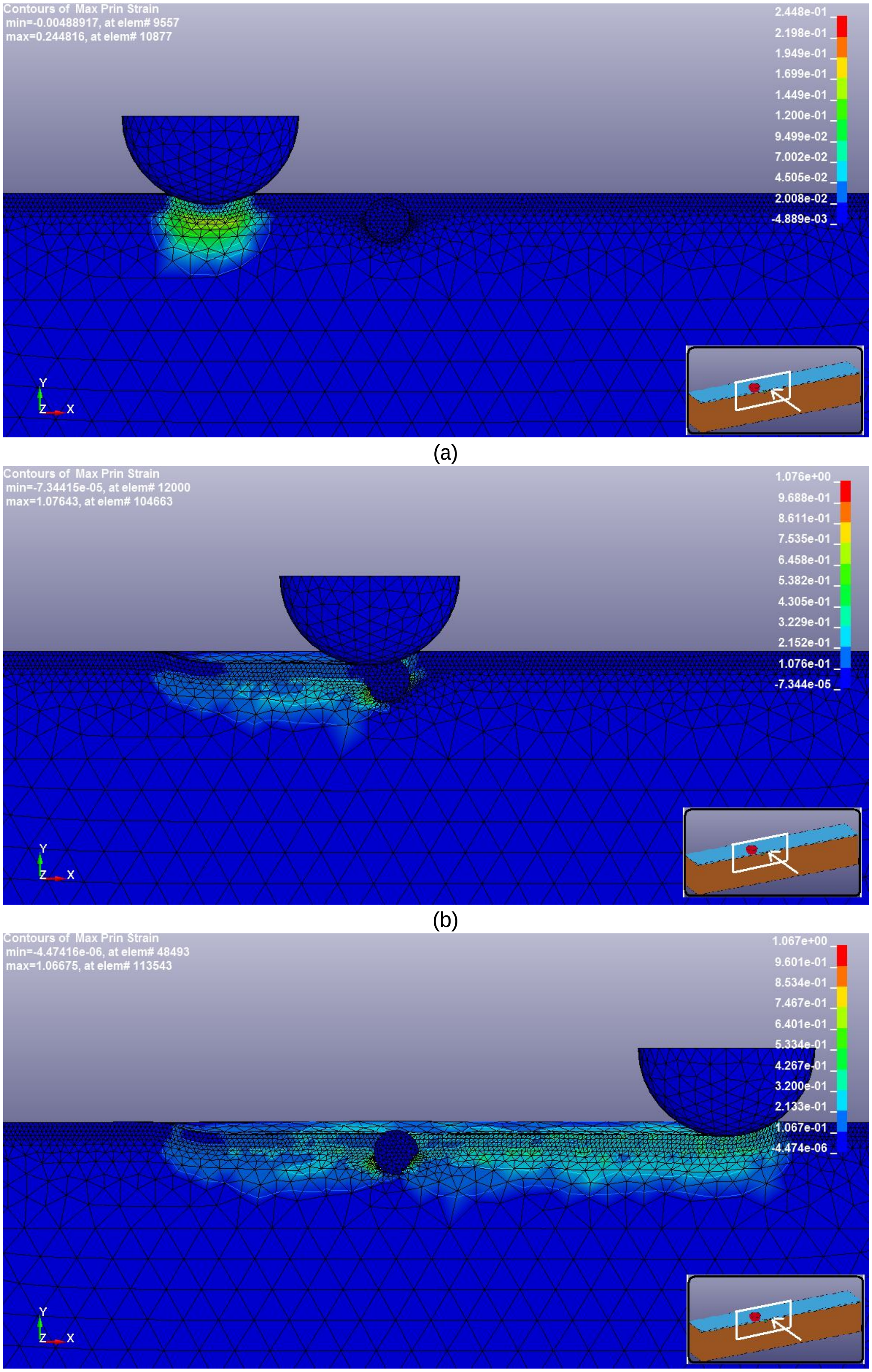

Figure 7.6: The strain field of the particle on oxide substrate interface at high temperature (a) before scratching (b) during scratching (c) after scratching.

Comparing the strain obtained from room temperature (Figure 7.5) and high temperature (Figure 7.6), maximum strain at high temperature was higher than at a low temperature. This situation was probably influenced by the mechanical properties of the oxide layer and carbide. The lower elastic modulus and yield strength of oxide scale at high temperature influenced the higher strain result of oxide scale and particles. If the material has a high elastic modulus, it takes higher load for the shape to deform. In other words, the high potential for abrasive wear is given by the oxide layer formed on high speed steel at high temperature.

7.3.1.2 Particle below the oxide-substrate interface (in the substrate)

The orientation between the tip and the particle was categorised under this case if the particle is situated below the oxide-substrate interface (Figure 7.7). Figures 7.8 and 7.9 depict the strain contours in the oxide scale and in the substrate at room temperature and high temperature respectively. The strain contours below the scratching edge, when the tip moved further into the oxide layer are shown Figures 7.8a and 7.9a. The maximum strain during nanoindentation in both cases was around 0.2.

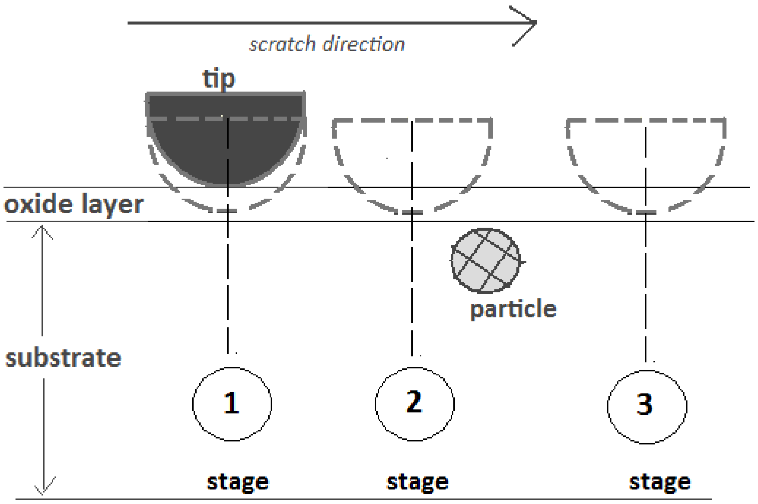

Figure 7.7: Particle locations below oxide-substrate interface (Case c).

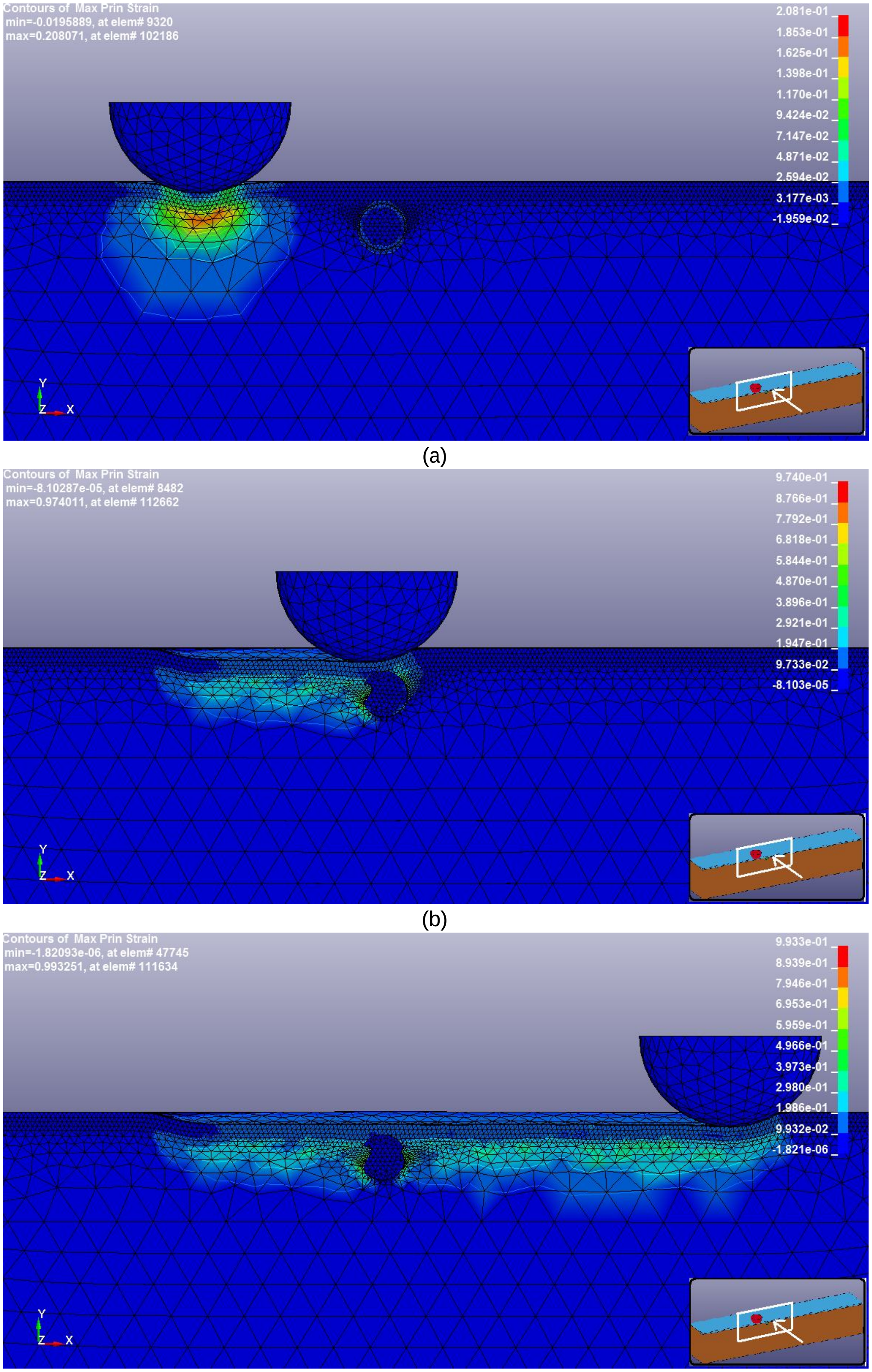
(a)
(b)
(c)

Figure 7.8: The strain field of the particle below oxide-substrate interface (in the substrate) at room temperature (a) before scratching (b) during scratching(c) after scratching.

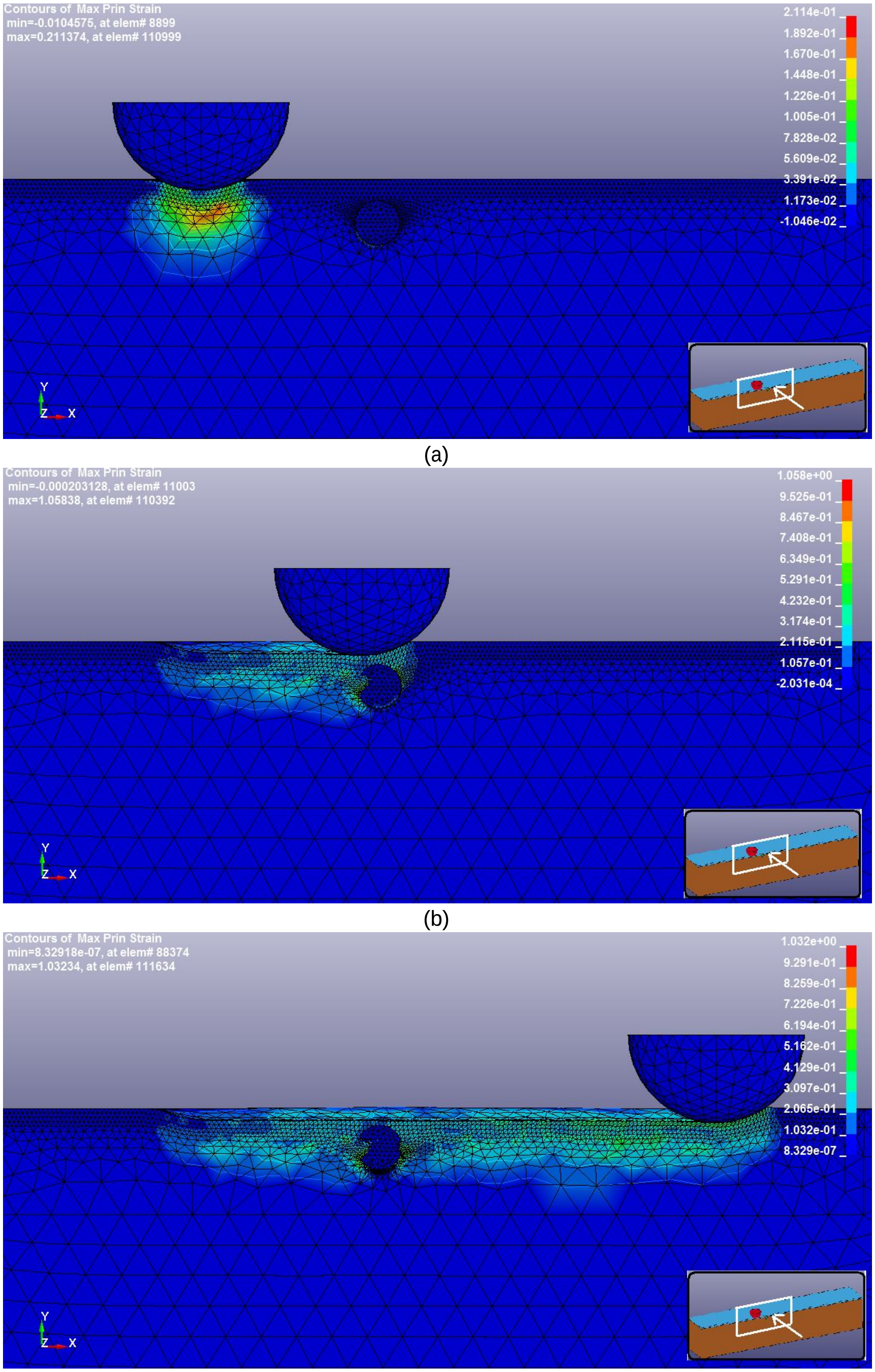

(a)

(b)

(c)

Figure 7.9: The strain field of the particle below oxide-substrate interface (in the substrate) at high temperature (a) before scratching (b) during scratching (c) after scratching.

With further advancement of the tip in the x-direction, the tip would pass the particle without any interaction between the tip and the interface zone of the particle (Figure 7.8b and 7.9b). The interface zone of the particle does not experience any plastic deformation due to scratching in the substrate if the particle is located well below the edge of the scratching, but particles situated immediately below the scratching edge are subjected to plastic deformation when the tip passes over them. Although tip-particle interaction does not happen, the tip movement causes a significant change in strain in the particle and surrounding oxide layer (Figure 7.8b and Figure 7.9b). As a result, the strain increased up to 0.97 and 1.05 at room temperature and high temperature respectively. After leaving the particle region, the strain contours increased slightly up to 0.99 for the room temperature case.

Table 7.3: The summary of maximum strain of particles.

	Maximum strain at the stage 2	
	Particle on oxide substrate interface	*Particle below oxide-substrate interface (inside the substrate)*
Room temperature	1.025	0.97
High temperature	1.076	1.058

These experiments revealed two positions of the particle which caused them to become embedded into the oxide layer and HSS substrate. The summary of the results is given in Table 7.3 and Figure 7.10. At high temperatures the mechanical properties such as the elastic modulus and yield strength were lower than that of the room temperature case. As a result the strain at high temperature was higher than that at room temperature. This situation was probably due to the lower yield strength at high temperature being more sensitive to failure. Based on these findings it can be concluded that the high temperature of the work roll would probably increase wear because the increased temperature leads to an increase in the strain, which means there is a high possibility of particle movement to remove and eventually produce delamination of the layer.

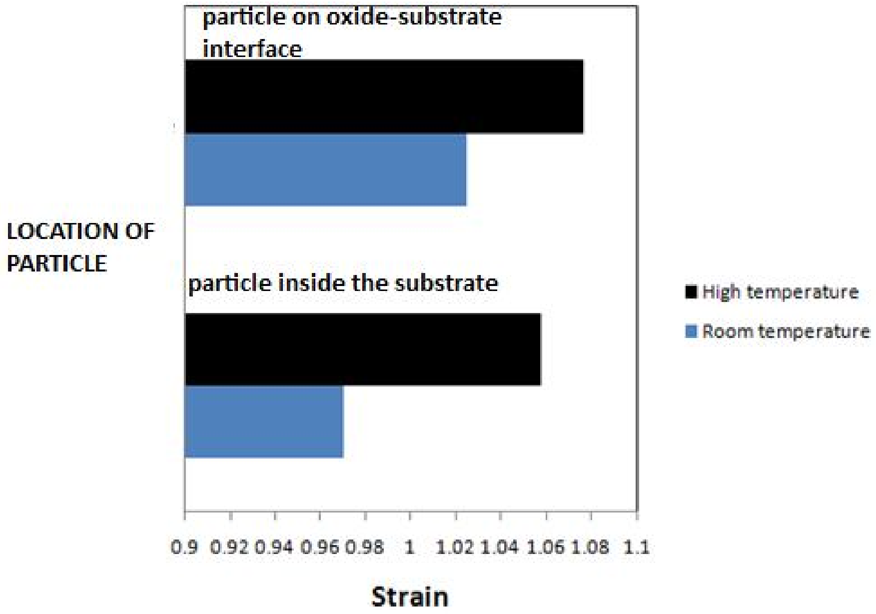

Figure 7.10: The strain value of the oxide layer and particle at stage 2.

7.3.2 Development of the stress field

The evolution of a stress field in the oxide layer and particles during scratching is now considered.

7.3.2.1 Particle on oxide substrate interface

The von Mises stress distribution during nanoindentation at room temperature is given by Figure 7.11a where the maximum stress at this stage was around 7 GPa. As the scratch tip advanced the stress distribution has initiated fracture in the particle and de-bonding at the interface (Figure 7.11b).

Due to the attack angle from the tip, this type of scenario leads the particles to move down into the substrate. The maximum von Mises stress when tip-particle interaction occurs was slightly higher than 7.4 GPa, and since the von Mises at oxide scale exceeded the yield of the oxide layer (σ_y = 7 GPa), it can be assumed that the oxide layer may experience failure. If the metallic oxide layer/zone cohesion is not strong enough the particle can be rapidly detached after the oxide breaks up into debris. If this happens the wear rates of both sliding bodies has probably increased because the detached hard particles can function as third body abrasives.

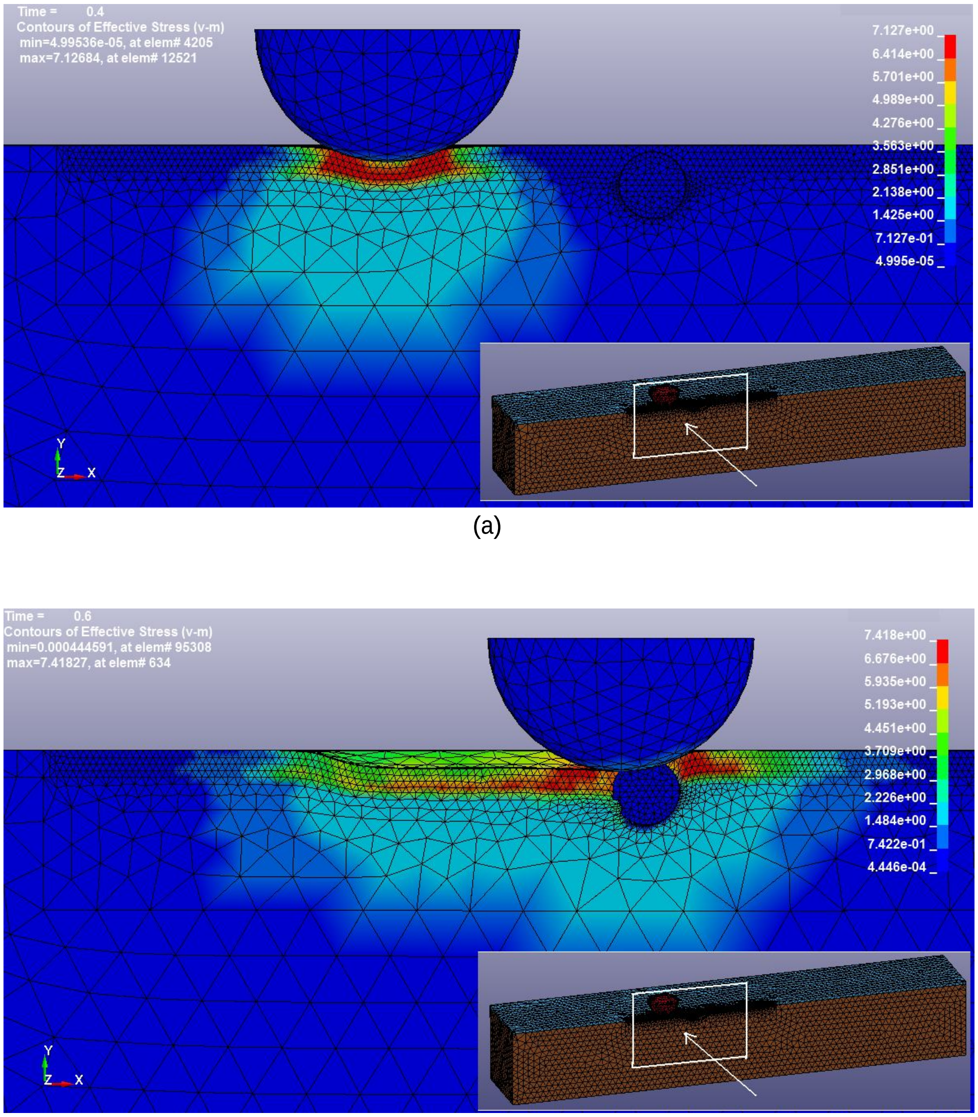

(a)

(b)

Figure 7.11: The von Mises stress on the oxide layer and particle at room temperature during (a) nanoindentation (b) scratch test.

In a comparison between at room temperature (Figure 7.11) and high temperature (Figure 7.12), the von Mises stress at high temperature is lower than at room temperature. This situation is contributed to by the yield strength of the oxide layer since the yield strength at room temperature is σ_y = 7 GPa and σ_y= 5 GPa at high temperature. Both scratch test conditions showed that the von Mises stress exceeded the yield strength of the oxide layer.

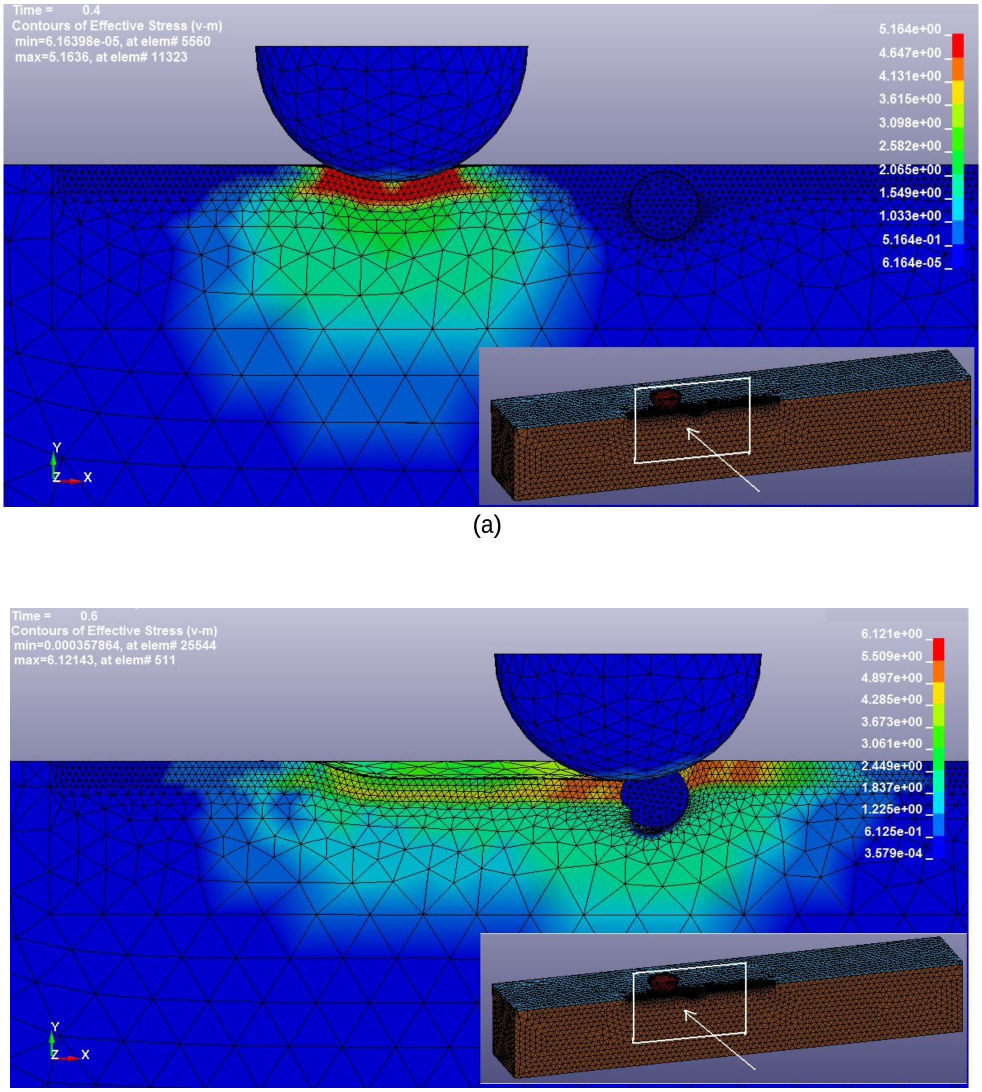

(a)

(b)

Figure 7.12: The von Mises stress on the oxide layer and particle at high temperature during (a) nanoindentation (b) scratch test.

7.3.2.2 Particle below the oxide-substrate interface (in the substrate)

A typical orientation of particles for the case at room temperature and high temperature is shown in Figures 7.13 and 7.14 respectively. There is a high compressive stress field perpendicular to the tip face through the particle and in the oxide layer, and as the tip moved, the oxide layer between the scratching edge and particle was under compressive stress. While the scratch tip would pass the particle without any interaction between the tip and the interface zone of particle, the compressive stress may initiate a zone particle fracture. The oxide layer situated immediately below the scratching edge was subjected to plastic deformation when the tip passed over them. As a result, the von Mises around the oxide layer increased and the magnitudes of stress also increased.

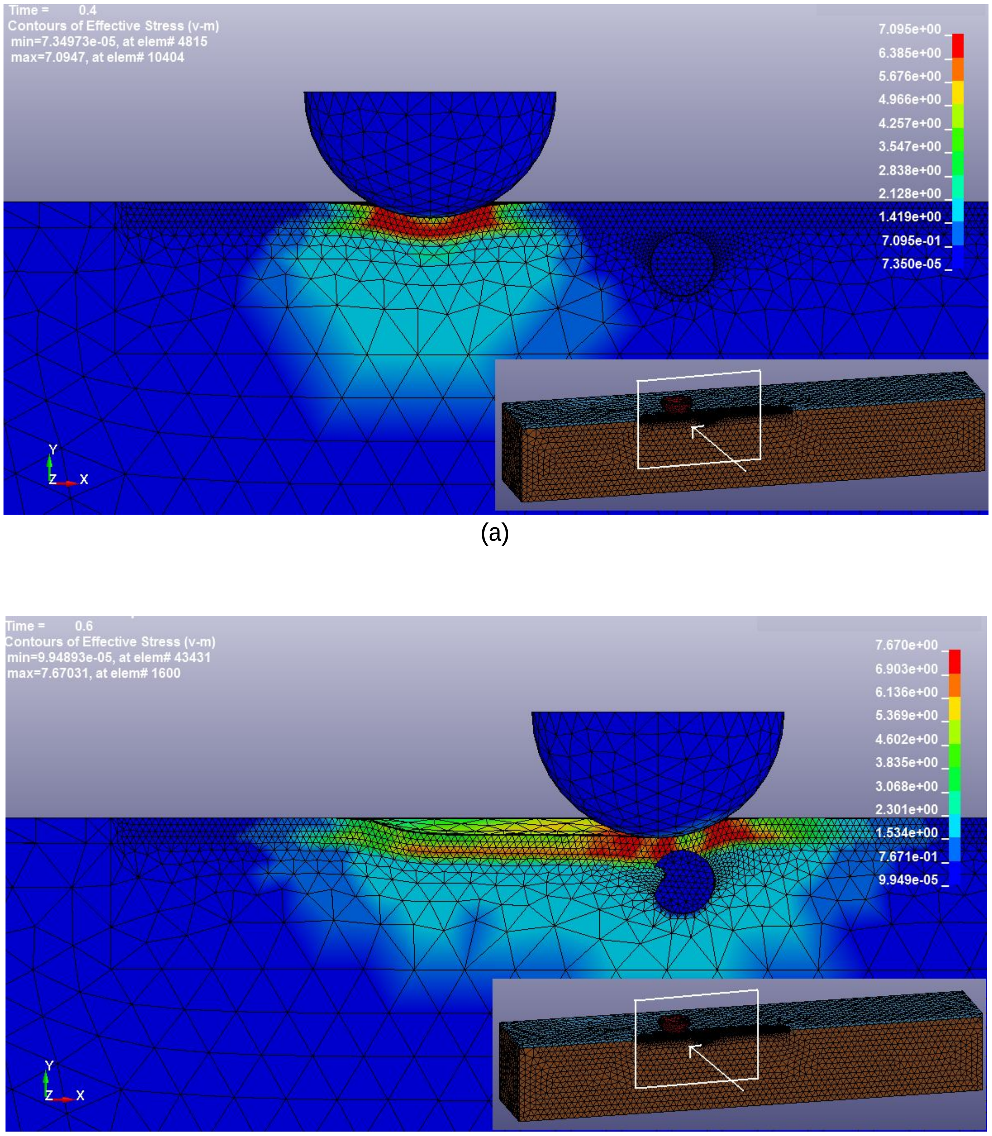

(a)

(b)

Figure 7.13: The von Mises stress on the oxide layer and particle at room temperature during (a) nanoindentation (b) scratch test.

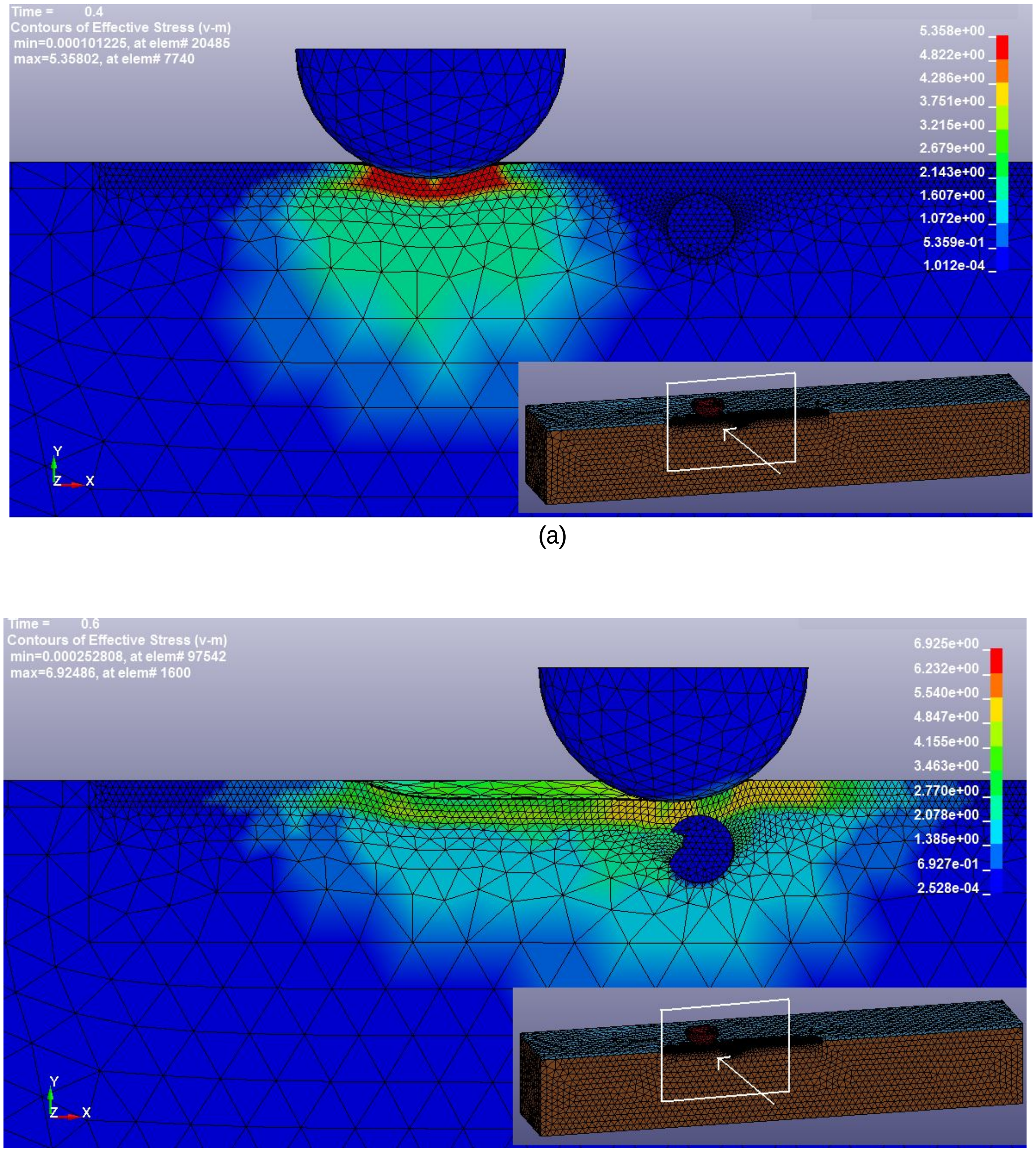

(a)

(b)

Figure 7.14: The von Mises stress on the oxide layer and particle at high temperature during (a) nanoindentation (b) scratch test.

Figures 7.13b and 7.14b show that the maximum von Mises at room temperature and high temperature are almost σ = 7.7 GPa and σ = 6.9 GPa respectively. The value of von Mises for both cases exceeded the yield strength. This clearly means that the oxide layers had deformed and changed into plastic deformation. In this case the particle did not resist deformation so the von Mises for the particle in the substrate was higher than the particle on the oxide-substrate interface. This may lead to a high abrasion wear of the counter-body (strip). Direct tip-particle interactions do not happen when the particles are well below the scratching path, but the tip movement caused a significant change of stress in the particles and the stress/strain surrounding the oxide layer. The degree of plastic deformation of the particles depends on their positions.

7.3.3 Particle movement and abrasive wear

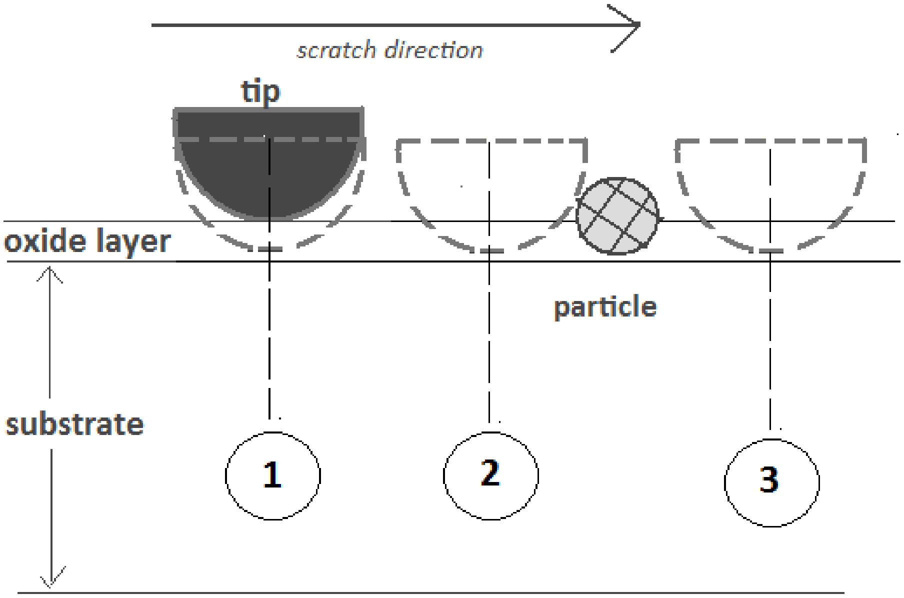

Figure 7.15: Case (a) Particle locations on oxide free surface.

The positions of the carbide particles were found to play an important role on the degree of plastic deformation. A significant movement of a particle would happen if its position was on the oxide free surface (Figure 7.15). However, this position is not an actual position of carbide in the oxide layer formed on high speed steel, which means this simulation probably represented the debris attached to the oxide layer, and since this simulation was not real, only the von Mises at room temperature was calculated.

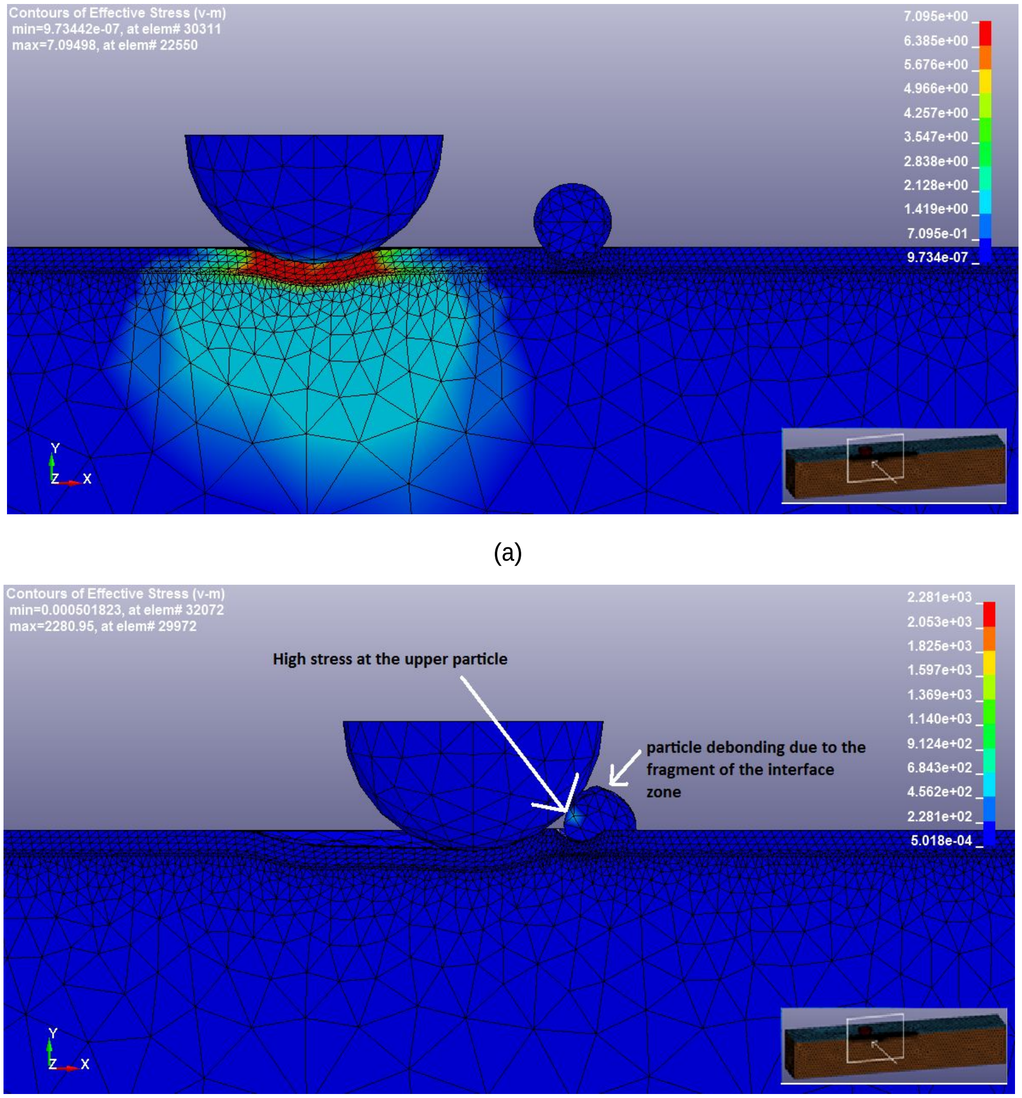

(a)

(b)

Figure 7.16: The von Mises stress on the oxide layer and particle at room temperature during (a) nanoindentation (b) scratch test.

This simulation can be used as additional knowledge. The von Mises stress in the oxide layer is presented in Figure 7.16. At first, the interface zone of the particle did not experience any strain plasticity, but due the scratch tip moving into the oxide layer, the stress has reasonably increased (Figure 7.16b). As the rake face of the tip approached the particle interface zone became highly stressed, and as the tip advance further, the particle partially de-bonded and became embedded into the oxide layer. The stress at this stage was over 200 GPa which caused the interface zone of the particle to fragment dramatically due to the material having reached its limiting stress value. As a result the corresponding element would be deleted (Figure 7.16b). This may lead a high abrasion wear of the counter-body (strip).

7.4 Discussion

It was found from the finite element simulations that particle position plays an important role in the abrasive wear of oxide scale because de-bonded particles can contribute to the abrasive wear process in hot strip mills. The two types of particle positions that chosen were based on the position of carbide which formed on the high speed steel and oxide layer (Boccalini and Sinatora, 2002; Zhu, 2012).

Based on this simulation, the particle on oxide-substrate interface and particle in the substrate de-bonded partially which caused the particles to move into the substrate. The results showed that the von Mises stress of the oxide layer at both room temperature and high temperature are higher than the yield strength of the oxide layer, which mean that the oxide layer reaches plastic deformation.

The results of strain/stress at room temperature are significantly higher than at high temperature, probably due to the difference in the mechanical properties such as the elastic modulus and yield strength of the oxide layer between both cases. The higher elastic modulus and yield strength lead to hardening effect of the oxide layer.

Particles on an oxide free surface became highly de-bonded during interaction between the tip and the particle, so in this case the particle actually represents the debris in the actual case. The way particles are either embedded into or removed from the oxide layer probably depends on the angle of attack of the tip. Yan and Zhang (1994) and Zhang *et al.* (1995) who studied a metal matrix composite MMCs by scratching tests observed pull out of the reinforcement particle and formation of cavities on the scratched surface.

Under normal work roll operations the abrasive factor in the hot strip mill is given by asperities, where the oxide layers of strips acting as multiple asperities abrade the oxide layers of the work rolls. On the other hand, knowledge about a carbide particle is also important to understand its influences on the abrasive wear. This chapter describes a comprehensive modelling method of the behaviour of the oxide layer and particles. The particle was 10 μm in diameter. In this analysis the tip is considered to be a rigid body, while the oxide layer, the substrate, and the particle must be modelled as a deformable body in order to obtain the necessary deformation formation of the abrasion mechanism.

7.5 Conclusions

The behaviour of particles and the oxide layer on a high speed steel surface undergoing scratching presents a variety of abrasive phenomena, so a finite element analysis using a physically based oxide scale model is a crucial aspect of this approach. The analysis was used to interpret the wear of the oxide layer formed on the work roll and it also gives a basis for engineering applications. The model of oxide layers was treated as a ductile model due to the results in the previous chapter (Chapter 6) where the behaviour of oxide layers was confirmed as a ductile that corresponds to their failure characteristics. In general, the existence of particles in the oxide layer would increase the wear rate due to the de-bonded particles that contributed to the abrasive factor in the hot strip mills. For example, particles on the oxide-substrate interface have partially de-bonded, which lead to movement of particles.

A comparison of the strain at different temperatures showed that the strain at high temperature (600^{o}C) offered an increase in strain compared to the low temperature case. This increase in temperature can be so significant if it can exceed the transition temperature range, making the interface weaker and giving a high possibility of particle movement. In the FE modelling approach discussed here the tip acted as an asperity that contributes to abrasive wear, whereas in real cases, the abrasive factor in a hot strip mill results from multiple asperities from the oxide layers of strips. The possibility of abrasion by multiple asperities on the oxide layers of the work rolls is probably higher because of the potential effect of deterioration.

The following conclusions can be drawn based on a finite element modelling of the abrasion mechanism during scratching on the oxide layer formed on HSS work roll, and the physical characteristics of the oxide layer and the particles:-

- The magnitude and distribution of stresses and strains in the oxide layer and interaction of particles with the tip are the main reason for particle de-bonding during scratching.

- The strain at high temperature is higher than at room temperature which leads to a higher sensitivity to failure. Increasing the strain means high probability of particle movement that produces delamination of the layer.

- The strains for particles on the oxide-substrate interface at both temperatures are higher than the particle in the substrate. The interaction between the tip and the particle significantly influences the strains.

- The von Mises stress at room temperature is significantly higher than that at high temperature, probably due to the influence of the difference in mechanical properties such as the elastic modulus and yield strength of the oxide layer between both cases. The yield strength at room temperature is σ_y= 7 GPa and at the high temperature it was σ_y = 5 GPa.

Chapter 8

Conclusions and recommendations for future work

8.1 Conclusions

Detailed conclusions have been described in Chapter 4, 5, 6, and 7. The general conclusions are outlined below.

8.1.1 Development of combined FE simulations and nanoindentation experiments for characterising the oxide layers

- The XRD pattern and SEM-EDS analysis indicated that two types of oxide sub-layers formed on the HSS surface, namely Fe_2O_3 and $(Fe,Cr)_3O_4$ in the outer and inner sub-layers respectively.

- The difference in the maximum depth of penetration between these two sub-layers is significant in that two distinct sub-layers can be clearly identified.

- Based on the TEM images, the porosity of the inner and outer sub-layers can be estimated from the fractional area of the pores. The porosity of the outer sub-layer is approximately 2% while the inner sub-layer is around 8%.

- A model for the FE nanoindentation of oxide scale has been developed based on the contact non-linearity and the non-linear material properties where the load-displacement curves have been determined.

- The iterative process of finite element to determine the mechanical properties of the oxide layer has been introduced, and the effects of each mechanical property on the load-displacement curves have been discussed.

- *E* has a significant influence on the slope of the unloading portion. The other properties σ_y, *v* and *f* have little or a very small influence on the slope, while σ_y has a significant influence on P_{max}. P_{max} decreases monotonically as σ_y decreases, and although *f* has the same effect as σ_y it is to a much less degree.

8.1.2 Characterisation and determination of the mechanical properties of the oxide layer

- The *E* range for the outer and inner sub-layers of oxide is 200-240 GPa and 90-220 GPa respectively, for a load of 5 mN. The large variation of *E* values for the inner oxide sub-layer is probably influenced by the voids and large variation in the porosity of the material. The *E* and *H* for the 20 mN load tests are lower than for a load of 5 mN. This phenomenon was probably caused by hardening/softening arising from the interaction between geometrically necessary dislocations (GNDs) and grain boundaries. Hence the size of the nanoindentation is more significant in the outer sub-layer.

- The study on yield strength showed that for the 5 mN load test, the inner sub-layer is lower in value than the less porous outer sub-layer. This may be explained by the development of a sub-layer of oxide where a thin layer of hematite grows in the top layer first, and then a thick porous layer of hematite grows at the interface between the upper layer and HSS substrate.

- The less porous outer sub-layer has a lower Poisson's ratio. This relationship indicates the effect of porosity on the Poisson's ratio-porosity dependence.

- A multiple regression analysis was conducted on the computed results to obtain the functional relationships *P* = f (E,σ,ν,f,d) and *dP/dh* = (E,σ,ν,f,d) by considering the multi-dimensional power law equations. The greatest influence on the maximum load (*P*) of the load-displacement curve was shown by the depth of indentation (*d*), followed by the elastic modulus (*E*), and the yield strength (σ). It was reassuring that both confirmed the relatively weak effect of porosity and Poisson's ratio on the maximum load and slope.

8.1.3 Study of the wear of the oxide layer using micro scratch experiments and FE simulations

- For a ductile model the indenter slides are on the surface under the applied normal depth. As the stylus is moving the plastic deformation zone moves in the same direction but the plastic deformation zone is no longer located in the centre of the indenter tip region; rather, it moves towards the leading edge of the indenter. The ploughing of the material and a tangential force is due this ploughing action.

- With an increasing depth of penetration the plastic deformation propagates further below the surface into the substrates. Plastic deformation also propagates vertically and laterally in the oxide layer and in the substrate.

- For the brittle model, the wear damage by the oxide scale detaching was shown from the HSS substrate. The formation and breaking-up of the oxide film would influence the wear behaviour. At a small indentation depth (3.2 μm), detachment of the oxide layer occurs around the indenter tip region and then propagates along the scratch tracks.

- Coefficient of friction increases with the depth of scratch for the brittle and the ductile models, but is significantly higher under brittle conditions than the ductile model. This occurs because some of the energy in the brittle model goes into the creation of new surfaces (wear) while in ductile model and some of the energy is used to deform the materials.

8.1.4 FE study of the effect of the presence of carbide particle on the behaviour of the oxide layer

- The magnitude and distribution of stresses/strains in the oxide layer and interaction of the particle with the tip are the main reason for particles de-bonding during scratching.

- The stress/strain at room at room temperature was significantly higher than at high temperature, probably due to the influence of the difference in the mechanical properties of the oxide layer between both cases, such as the elastic modulus and yield strength.

8.2 Recommendations for future work

- The combined technique developed in the current work has proved to be effective when the mechanical properties of the oxide layers formed on high speed steel (HSS) can be identified. Since various carbides exist in the oxide layers, the mechanical properties of different carbides should be investigated in order to gain a better understanding of the oxidation of these high speed steel series.

- Nanoindentation has successfully revealed the mechanical properties of the oxide scale formed on the surface of a HSS sample, but more nanoindentation tests are needed to investigate how the thin oxide scale influences the surface properties of high speed steel.

- Work rolls are actually subjected to thermal cycling during hot rolling at low temperature, but a higher temperature leads to very different oxidation kinetics and oxidation behaviour because the rolls are sensitive to temperature. Scratch simulation at high temperature will be carried out in order to simulate a thermal condition that is closer to hot rolling.

References

A

Abbaspour, M., & Saboonchi, A. (2008). Work roll thermal expansion control in hot strip mill. *Applied Mathematical Modelling*, *32*(12), 2652-2669.

Asiltürk, İ., & Çunkaş, M. (2011). Modeling and prediction of surface roughness in turning operations using artificial neural network and multiple regression method. *Expert Systems with Applications*, *38*(5), 5826-5832.

B

Badisch, E., & Mitterer, C. (2003). Abrasive wear of high speed steels: Influence of abrasive particles and primary carbides on wear resistance. *Tribology international*, *36*(10), 765-770.

Bai, M., Kato, K., Umehara, N., & Miyake, Y. (2000). Nanoindentation and FEM study of the effect of internal stress on micro/nano mechanical property of thin CN_x films. *Thin Solid Films*, *377*, 138-147.

Ben-Tkaya, M., Zahouani, H., Mezlini, S., Kapsa, P., Zidi, M., & Dogui, A. (2007). The effect of damage in the numerical simulation of a scratch test. *Wear*, *263*(7), 1533-1539.

Berns, H., Fischer, A., & Kleff, J. (1991) Design and construction of a new scratch tester for elevated temperatures. *Proc. Int. Conf. on Wear of Materials, Orlando, FL , American Society for Mechanical Engineers*, 661–665.

Bhattacharya, A. K., & Nix, W. D. (1991). Finite element analysis of cone indentation. *International Journal of Solids and Structures*, *27*(8), 1047-1058.

Birks, N., Meier, G. H., & Pettit, F. S. (2006). *Introduction to the high temperature oxidation of metals*. Cambridge University Press.

Blau, P. J. (2001). Experimental aspects of friction research on the macroscale. In *Fundamentals of Tribology and Bridging the Gap Between the Macro-and Micro/Nanoscales*. Springer Netherlands.

Boccaccini, D. N., & Boccaccini, A. R. (1997). Effect of pore shape on the ultrasonic velocity--porosity correlation in sintered materials. *Journal of materials science letters*, *16*(8), 623-625.

Boccalini, J. M., & Sinatora, A. (2002). Microstructure and wear resistance of high speed steels for rolling mill rolls. In *Proceedings of 6th International Tooling Conference,* 509-524.

Bruno, P., Cicala, G., Losacco, A. M., & Decuzzi, P. (2004). Mechanical properties of PECVD hydrogenated amorphous carbon coatings via nanoindentation and nanoscratching techniques. *Surface and Coatings Technology*, *180*, 259-264.

Bucaille, J. L., Felder, E., & Hochstetter, G. (2001). Mechanical analysis of the scratch test on elastic and perfectly plastic materials with the three-dimensional finite element modeling. *Wear*, *249*(5), 422-432.

C

Cai, X., & Bangert, H. (1995). Hardness measurements of thin films-determining the critical ratio of depth to thickness using FEM. *Thin Solid Films*, *264*(1), 59-71.

Chen, X., Xiang, Y., & Vlassak, J. J. (2006). Novel technique for measuring the mechanical properties of porous materials by nanoindentation. *Journal of materials research*, *21*(3), 715-724.

Chollacoop, N. (2003). *Mechanical Properties at the Microscopic and Nanoscopic Size Scales: Computational Modeling and Experiments* (Doctoral dissertation, Massachusetts Institute of Technology).

Colas, R., Ramírez, J., Sandoval, I., Morales, J. C., & Leduc, L. A. (1999). Damage in hot rolling work rolls. *Wear*, *230*(1), 56-60.

D

Da Silva, W. M., & De Mello, J. D. B. (2009). Using parallel scratches to simulate abrasive wear. *Wear*, *267*(11), 1987-1997.

Dai, W. S., Ma, M., & Chen, J. H. (2007). The thermal fatigue behavior and cracking characteristics of hot-rolling material. *Materials Science and Engineering: A*, *448*(1), 25-32.

Dao, M., Chollacoop, N., Van Vliet, K. J., Venkatesh, T. A. and Suresh, S. (2001). Computational modeling of the forward and reverse problems in instrumented sharp indentation. *Acta Mater.* 49 (19), 3899–3918.

De Carvalho, M. A., Xavier, R. R., Da Silva Pontes Filho, C., Morone, C., Boccallini Jr, M., & Sinatora, A. (2002). Microstructure, mechanical properties and wear resistance of high speed steel rolls for ho rolling mills. *Iron & steelmaker*, *29*(1), 27-32.

Doerner, M. F., & Nix, W. D. (1986). A method for interpreting the data from depth-sensing indentation instruments. *J. Mater. Res*, *1*(4), 601-609.

Dutta, A. K., Narasaiah, N., Chattopadhyaya, A. B., & Ray, K. K. (2001). The load dependence of hardness in alumina–silver composites. *Ceramics international*, *27*(4), 407-413.

E

Earles, S.W.E. & Hayler, G.M. (1972) Wear characteristics of some metals in relation to surface temperature, *Wear*, 20, 51–57.

Echsler, H., Ito, S., & Schütze, M. (2003). Mechanical properties of oxide scales on mild steel at 800 to 1000 C. *Oxidation of metals*, *60* (3-4), 241-269.

El-Rakayby, A. M., & Mills, B. (1986). The role of primary carbides in the wear of high speed steels. *Wear*, *112*(3), 327-340.

Erickson, L. C., & Hogmark, S. (1993). Analysis of banded hot rolling rolls.*Wear*, *165*(2), 231-235.

F

Fang, L., Cen, Q., Sun, K., Liu, W., Zhang, X., & Huang, Z. (2005). FEM computation of groove ridge and Monte Carlo simulation in two-body abrasive wear. *Wear*, *258*(1), 265-274.

Fang, L., Liu, W., Du, D., Zhang, X., & Xue, Q. (2004). Predicting three-body abrasive wear using Monte Carlo methods. *Wear*, *256*(7), 685-694.

Fink, M. (1930).Wear oxidation, a new component of wear. *Trans Am Soc Steel Treating*, 18, 1026–1034.

Fleck, N. A., Otoyo, H., & Needleman, A. (1992). Indentation of porous solids. *International journal of solids and structures*, *29*(13), 1613-1636.

G

Garza-Montes-de-Oca, N. F., & Rainforth, W. M. (2009). Wear mechanisms experienced by a work roll grade high speed steel under different environmental conditions. *Wear*, *267*(1), 441-448.

Garza-Montes-de-Oca, N. F., Colás, R., & Rainforth, W. M. (2011). On the damage of a work roll grade high speed steel by thermal cycling. *Engineering Failure Analysis*, *18*(6), 1576-1583.

Garza-Montes-de-Oca, N. F., Colás, R., & Rainforth, W. M. (2011). High temperature oxidation of a work roll grade high speed steel. *Oxidation of metals*, *76*(5-6), 451-468.

Garza-Montes-de-Oca, N. F., Colás, R., & Rainforth, W. M. (2011). Failure Modes of the Oxide Scale Formed on a Work Roll Grade High Speed Steel.*Oxidation of metals*, *76*(3-4), 149-160.

Ginzburg, V. B. (1989). *Steel-rolling technology: theory and practice*. Marcel Dekker, Inc.

Goto, K., & Mase, T. (1991). Friction and Wear Properties of Graphite Cast Iron for Hot Working Rolls. *Tetsu-to-Hagane(Journal of the Iron and Steel Institute of Japan)*, *77*(1), 107-114.

Graf, M., & Kawalla, R. (2012). Scale Behaviour and Deformation Properties of Oxide Scale during Hot Rolling of Steel. *Key Engineering Materials*, *504*, 199-204.

Grigoroudis, K., & Stephenson, D. J. (1997). Modelling low stress abrasive wear. *Wear*, *213*(1), 103-111.

Guo, R. M. (1998). Development of an optimal crown/shape level-2 control model for rolling mills with multiple control devices. *Control Systems Technology, IEEE Transactions on*, *6*(2), 172-179.

Gurson, A. L. (1975). Continuum theory of ductile rupture by void nucleation and growth. Part I. Yield criteria and flow rules for porous ductile media. *J. Engrg. Mater. Technol*, 99, 2–15.

H

Hanlon, D. N., & Rainforth, W. M. (2003). The rolling sliding wear response of conventionally processed and spray formed high speed steel at ambient and elevated temperature. *Wear*, *255*(7), 956-966.

Harewood, F. J., & McHugh, P. E. (2007). Comparison of the implicit and explicit finite element methods using crystal plasticity. *Computational Materials Science*, *39*(2), 481-494.

Higginson, R. L., Roebuck, B., & Palmiere, E. J. (2002). Texture development in oxide scales on steel substrates. *Scripta materialia*, *47*(5), 337-342.

Hirano, F., & Ura, A. (1970). Effect of difference in hardness of rubbing surfaces on abrasive wear. *Tribology in iron and steel works iron and steel inst, London, 1970, 163-167*.

Hosemann, P., Swadener, J. G., Welch, J., & Li, N. (2008). Nano-indentation measurement of oxide layers formed in LBE on F/M steels. *Journal of nuclear materials*, *377*(1), 201-205.

Hughes, T. J., Taylor, R. L., Sackman, J. L., Curnier, A., & Kanoknukulchai, W. (1976). A finite element method for a class of contact-impact problems.*Computer Methods in Applied Mechanics and Engineering*, *8*(3), 249-276.

Hwang, K. C., Lee, S., & Lee, H. C. (1998). Effects of alloying elements on microstructure and fracture properties of cast high speed steel rolls: Part I: microstructural analysis. *Materials Science and Engineering: A*, *254*(1), 282-295.

J

Jiang, P., He, X. L., Li, X. X., Yu, L. G., & Wang, H. M. (2000). Wear resistance of a laser surface alloyed Ti–6Al–4V alloy. *Surface and Coatings Technology*, *130*(1), 24-28.

John, S., Sikdar, S., Mukhopadhyay, A., & Pandit, A. (2006). Roll wear prediction model for finishing stands of hot strip mill. *Ironmaking & steelmaking*, *33*(2), 169-175.

Joos, O., Boher, C., Vergne, C., Gaspard, C., Nylen, T., & Rezai-Aria, F. (2007). Assessment of oxide scales influence on wear damage of HSM work rolls. *Wear*, *263*(1), 198-206.

K

Kang, Y. J., Oh, J. C., Lee, H. C., & Lee, S. (2001). Effects of carbon and chromium additions on the wear resistance and surface roughness of cast high-speed steel rolls. *Metallurgical and Materials Transactions A*, *32*(10), 2515-2525.

Kato, K. (1997). Abrasive wear of metals. *Tribology International*, *30*(5), 333-338.

Kato, O., Yamamoto, H., Ataka, M., & Nakajima, K. (1992). Mechanisms of surface deterioration of roll for hot strip rolling. *ISIJ international*, *32*(11), 1216-1220.

Kim, H. H., Lim, J. W., & Lee, J. J. (2003). Oxidation behavior of high-speed steels in dry and wet atmospheres. *ISIJ international*, *43*(12), 1983-1988.

Knapp, J. A., Follstaedt, D. M., Myers, S. M., Barbour, J. C., & Friedmann, T. A. (1999). Finite-element modeling of nanoindentation. *Journal of Applied Physics*, *85*(3), 1460-1474.

Kopernik, M., & Pietrzyk, M. (2007). 2D numerical simulation of elasto-plastic deformation of thin hard coating systems in deep nanoindentation test with sharp indenter. *Archives of Metallurgy and Materials*, *52*(2), 299.

Kramer, D., Huang, H., Kriese, M., Robach, J., Nelson, J., Wright, A., ... & Gerberich, W. W. (1998). Yield strength predictions from the plastic zone around nanocontacts. *Acta Materialia*, *47*(1), 333-343.

Krzyzanowski, M., & Beynon, J. H. (2006). Modelling the behaviour of oxide scale in hot rolling. *ISIJ international*, *46*(11), 1533-1547.

Krzyzanowski, M., & Rainforth, W. M. (2010). Oxide scale modelling in hot rolling: assumptions, numerical techniques and examples of prediction.*Ironmaking & Steelmaking*, *37*(4), 276-282.

L

Lee, G. Y., Dharan, C. K. H., & Ritchie, R. O. (2002). A physically-based abrasive wear model for composite materials. *Wear*, *252*(3), 322-331.

Li, C. S., Xu, J. Z., He, X. M., Liu, X. H., & Wang, G. D. (2001). Formation and control of strip scale pores in hot rolling. *Journal of Materials Processing Technology*, *116*(2), 201-204.

Li, J., & Beres, W. (2006). Three-dimensional finite element modelling of the scratch test for a TiN coated titanium alloy substrate. *Wear*, *260*(11), 1232-1242.

Lichinchi, M., Lenardi, C., Haupt, J., & Vitali, R. (1998). Simulation of Berkovich nanoindentation experiments on thin films using finite element method. *Thin Solid Films*, *312*(1), 240-248.

Liu, Y., Varghese, S., Ma, J., Yoshino, M., Lu, H., & Komanduri, R. (2008). Orientation effects in nanoindentation of single crystal copper. *International Journal of Plasticity*, *24*(11), 1990-2015.

Lundberg, S. E. (1993). Evaluation of deterioration mechanisms and roll life of different roll materials. *Steel research*, *64*(12), 597-603.

M

Magnee, A., Gaspard, C., & Gabriel, M. (1980). Wear Behavior of Steels for Hot Working Rolling-Mill Rolls. *C. R. M. Metall. Rep.*, (57), 25-39.

Matsuda, U., Sakamoto, K., Sugimoto, Y., Goto, K., Hino T., & Unno, M. (1991) Basic characteristic of roll material in hot rolling. *CAMP-ISIJ*, (4), 438.

Meng, H. C. (1994). Wear modeling: evaluation and categorization of wear models. *PhD Thesis,* The University of Michigan.

Mercado-Solis, R. D., Talamantes-Silva, J., Beynon, J. H., & Hernandez-Rodriguez, M. A. L. (2007). Modelling surface thermal damage to hot mill rolls.*Wear*, *263*(7), 1560-1567.

Mezlini, S., Zidi, M., Arfa, H., Ben-Tkaya, M., & Kapsa, P. (2005). Experimental, numerical and analytical studies of abrasive wear: correlation between wear mechanisms and friction coefficient. *Comptes Rendus Mecanique*, *333*(11), 830-837.

Milman, Y. V., Chugunova, S. I., Goncharova, I. V., Chudoba, T., Lojkowski, W., & Gooch, W. (1999). Temperature dependence of hardness in silicon–carbide ceramics with different porosity. *International Journal of Refractory Metals and Hard Materials*, *17*(5), 361-368.

Molinari, A., Straffelini, G., Tomasi, A., Biggi, A., & Corbo, G. (2000). Oxidation behaviour of ledeburitic steels for hot rolls. *Materials Science and Engineering: A*, *280*(2), 255-262.

Molinari, A., Pellizzari, M., Tremea, A., Biggi, A., & Corbo, G. (2005). Effect of matrix microhardness on thermal fatigue behaviour of spincast high speed steels for hot rolls. *Materials science and technology*, *21*(3), 352-356.

N

Nakagawa, M., Asano, A., Fukushima, M., & Hoshi, A. (1982). Effect of maintenance on backup roll life. *Iron Steel Eng.*, *59*(8), 23-27.

Nicholls, J. R., & Hall, D. J. (1994). Hardness and modulus measurements on oxide scales. *Materials at high temperatures*, *12*(2-3), 141-150.

Noels, L., Stainier, L., & Ponthot, J. P. (2004). Combined implicit/explicit time-integration algorithms for the numerical simulation of sheet metal forming.*Journal of computational and applied mathematics*, *168*(1), 331-339.

O

Ohnuki, A., Hasuka, K., Nakajima, K., & Kawanami, T. (1984). Deterioration of Work Rolls in Hot Strip Rolling. *J. Jpn. Soc. Technol. Plast.*, *25*(285), 936-941.

Oliver, W. C., & Pharr, G. M. (1992). Improved technique for determining hardness and elastic modulus using load and displacement sensing indentation experiments. *Journal of materials research*, *7*(6), 1564-1583.

P

Panich, N., & Sun, Y. (2006). Mechanical characterization of nanostructured TiB_2 coatings using microscratch techniques. *Tribology international*, *39*(2), 138-145.

Park, J. W., Lee, H. C., & Lee, S. (1999). Composition, microstructure, hardness, and wear properties of high-speed steel rolls. *Metallurgical and Materials Transactions A*, *30*(2), 399-409.

Pelletier, H., Krier, J., Cornet, A., & Mille, P. (2000). Limits of using bilinear stress–strain curve for finite element modeling of nanoindentation response on bulk materials. *Thin Solid Films*, *379*(1), 147-155.

Pellizzari, M., Molinari, A., & Straffelini, G. (2005). Tribological behaviour of hot rolling rolls. *Wear*, *259*(7), 1281-1289.

Pellizzari, M., Cescato, D., & De Flora, M. G. (2009). Hot friction and wear behaviour of high speed steel and high chromium iron for rolls. *Wear*, *267*(1), 467-475.

Pramanik, A., Zhang, L. C., & Arsecularatne, J. A. (2007). An FEM investigation into the behavior of metal matrix composites: Tool–particle interaction during orthogonal cutting. *International Journal of Machine Tools and Manufacture*, *47*(10), 1497-1506.

Q

Quinn, T. F. J. (1983). Review of oxidational wear: Part I: The origins of oxidational wear. *Tribology International*, *16*(5), 257-271.

R

Rao, C. S., & Reddy, C. E. (2009). Finite element modeling of nanoindentation to extract load-displacement characteristics of bulk materials and thin films.*Indian Journal Of Pure & Applied Physics*, *47*(1), 54.

Reddy, J. N. (2004). *Nonlinear finite element analysis*. Oxford University Press.

Rodenburg, C., & Rainforth, W. M. (2007). A quantitative analysis of the influence of carbides size distributions on wear behaviour of high-speed steel in dry rolling/sliding contact. *Acta materialia*, *55*(7), 2443-2454.

S

Sauvú, R. G., & Morandin, G. D. (2004). Simulation of contact in finite deformation problems–algorithm. *International Journal of Mechanics and Materials in Design*, *1*(3), 287-316.

Schroeder, K. H. (2004). FAQs about hot strip mill work roll surface (wear, oxidation, firecracks, sticking and fiction). *Association for Iron and Steel Technology. AIST Process Metallurgy, Product Quality and Applications Proceedings*, 349-360.

Schwetz, K. A., Sigl, L. S., Greim, J., & Knoch, H. (1995). Wear of boron carbide ceramics by abrasive waterjets. *Wear*, *181*, 148-155.

Shetty, R., Keni, L., Pai, R., & Kamath, V. (2008). Experimental and analytical study on chip formation mechanism in machining of DRACs. *ARPN Journal of Engineering and Applied Sciences*, *3*(5), 27-32.

Shih, C. W., Yang, M., & Li, J. C. M. (1991). Effect of tip radius on nanoindentation. *Journal of Materials Research(USA)*, *6*(12), 2623-2628.

Spuzic, S., Strafford, K. N., Subramanian, C., & Savage, G. (1994). Wear of hot rolling mill rolls: an overview. *Wear*, *176*(2), 261-271.

Stevens, P. G., Ivens, K. P., & Harper, P. (1971). Increasing work-roll life by improved roll-cooling practice. *J Iron Steel Inst*, *209*(1), 1-11.

Stott, F. H. (1998). The role of oxidation in the wear of alloys. *Tribology International*, *31*(1), 61-71.

Suarez, L., Houbaert, Y., Eynde, X. V., & Colás, R. (2009). High temperature deformation of oxide scale. *Corrosion Science*, *51*(2), 309-315.

Suárez, L., Rodríguez-Calvillo, P., Houbaert, Y., Garza-Montes-de-Oca, N. F., & Colás, R. (2011). Analysis of Deformed Oxide Layers Grown on Steel. Oxidation of Metals, 75(5-6), 281-295.

Sun, J. S., Lee, K. H., & Lee, H. P. (2000). Comparison of implicit and explicit finite element methods for dynamic problems. *Journal of Materials Processing Technology*, *105*(1), 110-118.

Sun, W. (2005). A study on the characteristics of oxide scale in hot rolling of steel. *PhD Thesis,* University of Wollongong.

Sun, Y., Bell, T., & Zheng, S. (1995). Finite element analysis of the critical ratio of coating thickness to indentation depth for coating property measurements by nanoindentation. Thin Solid Films, 258(1), 198-204.

T

Tabor, D. (1986). Indentation hardness and its measurement: some cautionary comments. *Microindentation techniques in materials science and engineering, ASTM STP*, *889*, 129-159.

Tahir, M. (2003). Some aspects on lubrication and roll wear in rolling mills. *PhD Thesis,* KTH Sweden.

Tang, K. C., Faulkner, A., Schwarzer, N., Arnell, R. D., & Richter, F. (1997). Comparison between an elastic-perfectly plastic finite element model and a purely elastic analytical model for a spherical indenter on a layered substrate. *Thin Solid Films*, *300*(1), 177-188.

Tang, J., Tieu, A. K., & Jiang, Z. Y. (2006). Modelling of oxide scale surface roughness in hot metal forming. *Journal of materials processing technology*,*177*(1), 126-129.

Tang, J. (2006). A study of oxide scale deformation and surface roughness transformation in hot strip rolling. *PhD Thesis,* University of Wollongong.

Thévenot, F. (1990). Boron carbide—a comprehensive review. *Journal of the European Ceramic Society*, *6*(4), 205-225.

Tian, X. L., Mao, Y. T., Wang, J. Q., Li, F. Q., & Zhang, B. G. (2012). Finite Element Simulation of Axial Creep-Feed Grinding Engineering Ceramics Based on ANSYS/LS-DYNA. *Advanced Materials Research*, *472*, 927-931.

Torres, M., & Colás, R. (2000). A model for heat conduction through the oxide layer of steel during hot rolling. *Journal of Materials Processing Technology*, *105*(3), 258-263.

Tortorelli, P. F., & Keiser, J. R. (1991). The use of depth-sensing submicron indentation testing to characterize the mechanical behavior of thin oxide scales. Scripta metallurgica et materialia, 25(10), 2339-2344.

V

Vardavoulias, M. (1994). The role of hard second phases in the mild oxidational wear mechanism of high-speed steel-based materials. *Wear*, *173*(1), 105-114.

Vergne, C., Boher, C., Levaillant, C., & Gras, R. (2001). Analysis of the friction and wear behavior of hot work tool scale: application to the hot rolling process.*Wear*, *250*(1), 322-333.

Vergne, C., Boher, C., Gras, R., & Levaillant, C. (2006). Influence of oxides on friction in hot rolling: Experimental investigations and tribological modelling.*Wear*, *260* (9), 957-975.

Voyiadjis, G. Z., & Peters, R. (2010). Size effects in nanoindentation: an experimental and analytical study. *Acta mechanica*, *211*(1-2), 131-153.

W

Wang, X. D., Yang, Q., He, A. R., & Wang, R. Z. (2007). Comprehensive contour prediction model of work roll used in online strip shape control model during hot rolling. *Ironmaking & steelmaking*, *34*(4), 303-311.

Wang, Y. F., & Yang, Z. G. (2008). Finite element model of erosive wear on ductile and brittle materials. *Wear*, *265*(5), 871-878.

Wang, Y. F., & Yang, Z. G. (2009). A coupled finite element and meshfree analysis of erosive wear. *Tribology International*, *42*(2), 373-377.

Wong, C. W., Gupta, M., & Lu, L. (1999). Effect of variation in physical properties of the metallic matrix on the microstructural characteristics and the ageing behaviour of Al-Cu/SiC metal matrix composites. *Journal of materials science*, *34*(7), 1681-1689.

Wriggers, P. (1996). Finite element methods for contact problems with friction.*Tribology International*, *29*(8), 651-658.

X

Xia, J., Li, C. X., Dong, H., & Bell, T. (2006). Nanoindentation and nanoscratch properties of a thermal oxidation treated γ-TiAl based alloy. *Surface and Coatings Technology*, *200*(16), 4755-4762.

Y

Yan, C., & Zhang, L. (1994). Single-point scratching of 6061 Al alloy reinforced by different ceramic particles. *Applied Composite Materials*, *1*(6), 431-447.

Yang, D. Y., Jung, D. W., Song, I. S., Yoo, D. J., & Lee, J. H. (1995). Comparative investigation into implicit, explicit, and iterative implicit/explicit schemes for the simulation of sheet-metal forming processes. *Journal of materials processing technology*, *50*(1), 39-53.

Youn, S.W., & Kang, C.G. (2004). A study of nanoscratch experiments of the silicon and borosilicate in air. *Materials Science and Engineering A*, 384(1), 275-283.

Z

Zamri, W. F. H., Kosasih, P. B., Tieu, A. K., Zhu, Q., & Zhu, H. (2012). Variations in the microstructure and mechanical properties of the oxide layer on high speed steel hot rolling work rolls. *Journal of Materials Processing Technology, 212(12),* 2597–2608.

Zhang, Z. F., Zhang, L. C., & Mai, Y. W. (1995). Particle effects on friction and wear of aluminium matrix composites. *Journal of Materials Science*, *30*(23), 5999-6004.

Zhou, L., Sun, D., Liu, C., Li, C., & Yao, L. (2008). Scratch behavior of high speed steels for hot rolls. *Journal of University of Science and Technology Beijing, Mineral, Metallurgy, Material*, *15*(4), 402-406.

Zhu, Q., Zhu, H. T., Tieu, A. K., Reid, M., & Zhang, L. C. (2010). In-situ investigation of oxidation behaviour in high-speed steel roll material under dry and humid atmospheres. *Corrosion Science*, *52*(8), 2707-2715.

Zhu, Q., Zhu, H. T., Tieu, A. K., & Kong, C. (2011). Three dimensional microstructure study of oxide scale formed on a high-speed steel by means of SEM, FIB and TEM. *Corrosion Science*, *53*(11), 3603-3611.

Zhu, Q. (2012). A study of oxidation and wear on high speed steel roll material. *PhD thesis*, University of Wollongong.

Appendix

There are several potential factors such as the type of contact formulation, time step, element size, etc., that must take into account in order to obtain an accurate and reliable result. A brief introduction of the theory and formulation related to FEM simulation will be discussed in the following sub-sections.

9.1. Non-linearities Finite Element Analysis and Governing Equations

In solid mechanics, structural non-linearities can be classified as geometric non-linearity, material non-linearity, and contact or boundary non-linearity (Figure 9.1), while geometric non-linearity results from large strains and/or large rotations. Material non-linearity stems from a non-linear relationship between the kinetic and kinematic variables such as the stress-strain relationships, heat flux-temperature gradient relationships, and so on (Reddy, 2004).

The presence of contact conditions also leads to a non-linear structural analysis because the extent of the contact region and the contact stress are not known a priori. Analysing nanoindentation can be very complex because of two principal and strongly non-linear phenomena such as material non-linearity (elastic-plastic deformation of indented materials) and contact non-linearity (frictional contact between the indenter and materials).

Structural Nonlinearities

Geometric Nonlinearity

Material Nonlinearity

Contact/Boundary Nonlinearity

Figure 9.1: Classification of structural non-linearity.

In the finite element method the governing equations related to large deformations are non-linear with respect to displacements and velocities. The solution to the non-linear governing equations can be achieved with an incremental approach. The incremental form of governing equations can be written as

$$K(u)\Delta u = \Delta P \tag{9.1}$$

where Δu and ΔP represent the unknown incremental displacement vector and the known incremental applied load vector, respectively. The solution is constructed by taking a series of linear steps in the appropriate direction in order to closely approximate the exact solution. Depending on the nature of the non-linearity, the magnitude of each step and its direction may involve several iterations.

9.2 Small Deformation Theory of Elasticity and Plasticity

Materials for which the constitutive behaviour is only a function of the current state of deformation are known as *elastic.* Meanwhile, the material is called *hyperelastic* when the work done by the stresses during deformation depend only on the initial state and current configuration. A strain energy density function U_o (E_{ij}) such that

$$S_{ij} = \frac{\partial U_0}{\partial E_{ij}} \tag{9.2}$$

where S_{ij} and E_{ij} are the components of the second Piola-Kirchhoff stress tensor and Green-Lagrange starin tensor, respectively. A non-linearly elastic material has the following features: (a) U_o is a non-linear function of strains, (b) all of the deformation is recoverable when the loads causing the deformation are removed, and (c) there is no loss of energy (i.e. loading and unloading is along the same stress-strain path (Figure 9.2).

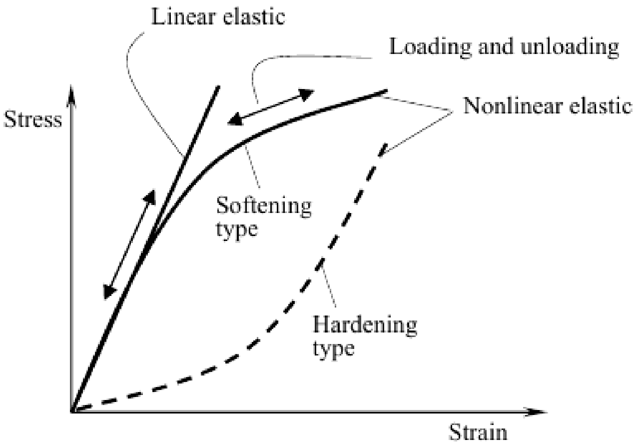

Figure 9.2: A nonlinear elastic stress-strain curve (Reddy, 2004).

Plasticity refers to non-recoverable deformation and non-unique stress paths in contrast to non-linear elasticity, where the entire load-deflection path is unique and the strains are recovered when the load is removed. Plastic behaviour is characterised by irreversible stress paths and the development of permanent deformation (i.e. non-recoverable), known as yielding (or plastic flow). Unloading part of the curve determines whether it is elastic or plastic (Figure 9.3); the elastic material follows the same path in loading and unloading, while the plastic material shows a history dependent path unloading.

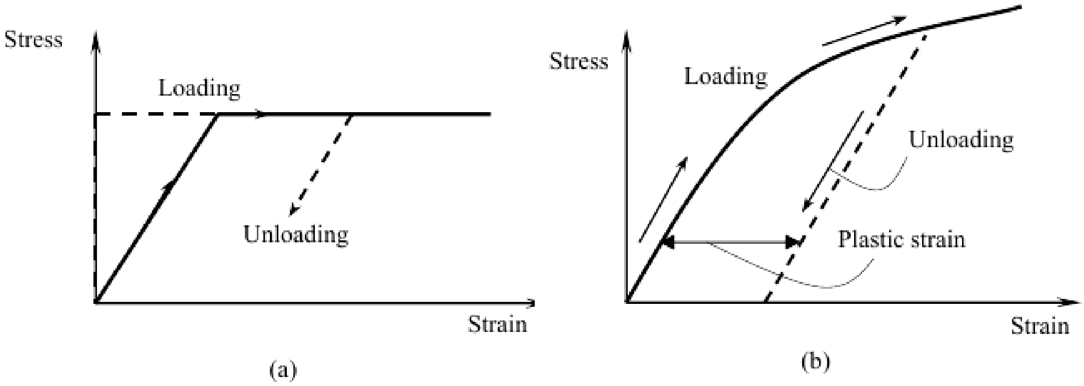

Figure 9.3: Stress-strain behavior of (a) ideal plasticity, and (b) strain-hardening plasticity (Reddy, 2004).

9.3 Nanoindentation Contact Theory

Large scale non-linear simulation poses a number of challenging issues that involve arbitrary contact (Wriggers, 1996). Understanding the contact behaviour at material interfaces is very importantwhen modellingnanoindentation and scratch in order to provide realistic predictions. According to previous research (Wriggers, 1996; Hughes *et al*., 1976), two different approaches were used in the literature to model mechanical behaviour in the contact area. By focusing on the contact condition imposed in a normal direction, two types of contact were categorised: the non-penetration condition as geometrical constraints, and constitutive laws for the micro-mechanical approach within the contact area. The concept of both contacts relies on the condition at the interface which is, *c* is a material surface with respect to both bodies.

For case 1 we refer to it as the impenetrability condition where the primary kinematic axiom of a contact problem is that configurations b^1 and b^2 of B^1 and B^2 (Figure 9.4), respectively, do not penetrate each other, i.e

$$b1 \cap b2 = 0 \qquad (9.3)$$

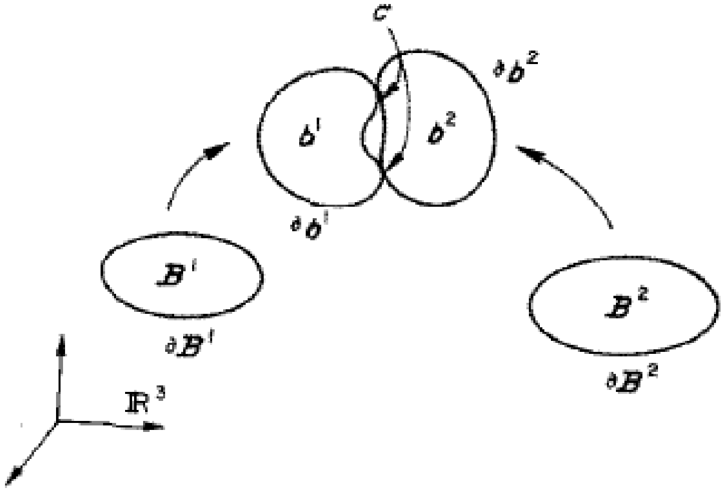

Figure 9.4: Contact condition (Hughes *et al*., 1976).

However, the nanoindentaion simulation would concentrate on case 2 (constitutive laws for the micromechanical approach) because the indentation test has undergone a contact condition in this category. In this case the material points on the boundaries of B^1 and B^2 may coalesce during the motion of the bodies. Thus we say B^1 and B^2 are in contact if $\delta b1 \cap \delta b^2 \neq 0$, and we define the contact surface c by

$$c = \delta b1 \cap \delta b^2 \qquad (9.4)$$

Based on this discussion on the general contact principle, the type of nanoindentation which is related to micromechanical approach has been explained. This clarification of the type of contact in nanoindentation is important to further understand the theory/formulae that explained the contact characteristics. The explanation regarding the relationship between the general principle of contact and nanoindenatation will be discussed in the following section (9.4and 9.5) in detail.

9.4 Contact geometry

This section describes a relationship that is needed to formulate the geometrical contact conditions. When two bodies undergo a large deformation we assume they come into contact (Figure 9.5).

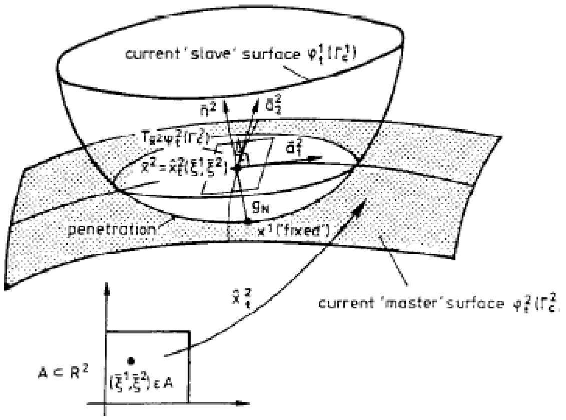

Figure 9.5: Contact geometry and geometrical approach (Wriggers, 1996).

Let B^γ, γ=1,2, denote the two bodies on interest. We donate ϕ_t^1 (Γ_c^1) as the current slave surface which penetrates in the case of contact into the current master surface ϕ_t^2 (Γ_c^2).

We parameterise the master surface Γ_c^2 in its reference and current configuration by the natural parameters ξ_1, ξ_2. As the first relevant function for the contact geometry we define a *penetration function* on the current slave surface ϕ_t^1 (Γ_c^1) by setting :-

$g_{N+} = \| x^1 - x_t^2 (\xi^1, \xi^2) \|$ for $[x^1 - x_t^2 (\xi^1, \xi^2)] \cdot n^2 < 0$; (9.5)

or 0 otherwise

Here $\xi = (\xi^1, \xi^2)$ is the minimiser of the distance function for a given slave point x^1.

$d^1(\xi^1, \xi^2) \| x^1 - x_t^2 (\xi^1, \xi^2) \| \rightarrow MIN$ (9.6)

The penetration function contains two items of information:-

(1) g_{N+} serves as a local contact check , i.e we set: contact $g_N > 0$

(2) g_{N+} enters for $g_{N+} > 0$ as a local kinematical variable the constitutive function for the contact pressure.

We note $g^L{}_{N+} = [x^1 - x_t^2 (\xi^1, \xi^2)] \cdot n^2 \geq 0$ represents the classical non-penetration condition for finite deformation. Based on the above explanation, the existing knowledge of the penetration and relative slip in the contact area in terms of its mathematical formulation has been described to better understand the theory of contact formulation in nanoindenation.

9.5 Contact algorithm

Based on numerous publications dealing with the modelling contact, Sauvu and Morandin (2004) summarised the contact algorithms into 6 categories; that is the automatic contact surface generation, global search phase, local search phase, enforcement of interface contact conditions, interface friction model, and erosion.

Sauvu and Morandin (2004) also suggested that in the *enforcement of the contact conditions*, the numerical algorithms usually used one of the following methods: Lagrange multiplier method, penalty method, constraint method or distributed parameter method.

From the Sauvu and Morandin (2004) explanation it seems that the contact algorithms and numerical algorithms are related to each other. Meanwhile, Wriggers (1996) comprehensively explained the method/ technique that should be used when dealing with contact problems. However, Wriggers (1996) did not elaborate on the type of contact algorithm when discussing the contact problems in finite element method; but Wriggers (1996) suggested to apply a combination of the penalty and the Lagrangian multiplier techniques, called the *augmented Lagrangian method*, when the constitutive interface laws (penetration case) are used. According to Wriggers (1996) review, this approach avoids the common problem of ill-conditioning. On this basis the nanoindentation has been performed using augmented Lagrangian method in Ansys software to simulate the nanoindentation test.

The Ansys software offered 4 possible approaches when dealing with the nanoindentation test; they are pure penalty, augmented Lagrange, MPC, and normal Lagrange. However, an augmented Lagrange approach only showed a good result in terms of convergence. The reason for this trend would probably relate to the theory of contact formulation and the algorithms discussed above. In addition, an augmented Lagrangian algorithm has combined the merits of both the penalty and Lagrange multiplier so that this algorithm is appropriate for the nanoindentation test. Moreover, this algorithm is only related to penetration case where the constitutive interface laws are applied.

9.6 Implicit vs Explicit

Two types of computational simulation were used in this project, the nanoindentation test and scratch test. The question is which method is appropriate for these simulations, either implicit or explicit. The Ansys classic offers the implicit method while the Ansys-Lsdyna uses the explicit method. The obvious differences between these methods are how the contact surfaces are represented, how contact penetration is interpreted, and what advance features and limitations exist in the different algorithms. In implicit Ansys, segments of contacting bodies (example: CONTA 174 or TARGET 170) must be defined, but explicit Ansys-Lsdyna will automatically create the segment from specified nodal components, etc. In explicit Ansys-Lsydna, the load (input displacement) should be applied to the component (part) while there is more flexible way to applied load in Ansys (nodes, areas, volume).

In this study, the implicit Ansys has been applied for the nanoindentation test because of the quasi-static nature of the nanoindentation problem. In addition, most of the numerical studies on nanoindentation have applied static analyses based on an implicit method using various numerical codes such as Ansys (Tang *et al*., 1997; Bai *et al.,* 2000; Pelletier *et al.,* 2000), ABAQUS/Standard (Lichinchi *et al.,* 1998; Sun *et al.,* 1995; Bhattacharya and Nix, 1991; Shih *et al.,* 1991; Knapp *et al.,* 1999) and MARC (Cai and Bangert, 1995). The implicit has been used due to the reliability that was established fairly well via a comparison with the experimental results. The explicit method was not used as extensively in nanoindentation problems because it is time consuming. Knapp *et al.* (1999) reported that both methods resulted in the same computational methods, whilst the explicit method took about 24 times longer time for a 2D problem.

On the other hand explicit Ansys-LsDyna was used for the scratch test because implicit Ansys has limitations in terms of large displacement. Unlike an implicit static analysis, an explicit dynamic analysis must have all the loads applied as a function of time. There is a unique procedure for applying loads in an explicit dynamic analysis using two array parameters. One array is for the time values and the other array is for the loading condition. Because of the time dependence, many standard ANSYS loading commands (e.g., F and SF) are not valid in Ansys-LsDyna.

Understanding the advantages and disadvantages of these algorithms is very important for choosing the right algorithm for a particular problem. In general, the implicit method based on direct solver is effective for quasi-static non-linear problems while the explicit method is based on a dynamic solution for linear dynamic problems.

A comparison of implicit and explicit methods in non-linear problems was reported by Sun *et al.* (2000), Noels *et al.* (2004), Harewood and McHugh (2007). In the implicit FE method (Ansys), a solution requires iteration for each time increment (time step) until a convergence criterion has been satisfied. In the explicit FE method however, the solver equation can be solved directly without iteration. An implicit procedure means that the state at t + Δt is determined based on information at time t + Δt while the explicit method solves for t + Δt based on information at time t.

The implicit procedure uses an automatic increment strategy based on a full Newton iterative solution method:

$$\Delta u^{(i+1)} = \Delta u^{(i)} + K_t^{-1}.(F^{(i)} - I^{(i)}) \qquad (9.7)$$

where K_t is the current tangent stiffness matrix, F the applied load vector, I the internal force vector, and Δu is the increment of displacement.

The explicit procedure available in Ansys-LsDyna is based on the implementation of an explicit integration rule. The explicit procedure has been implemented in the scratch simulation in Chapter 6 and 7 since it is suitable for analysing high speed dynamic events (Yang *et al*., 1995). In the explicit method the acceleration, velocities, and displacements are calculated first without taking the contact conditions into consideration. The equation of motion for the body is integrated using an explicit central difference integration rule:

$$u^{(i+1)} = u^{(i)} + \Delta t^{(i+1)}\dot{u}^{(i+1)}, \qquad (9.8)$$

$$\dot{u}^{(i+\frac{1}{2})} = \dot{u}^{(i-\frac{1}{2})} + \frac{1}{2}(\Delta t^{(i+1)} + \Delta t^{(i)})\ddot{u}^{(i)} \qquad (9.9)$$

where $\dot{u}$ is the velocity, $\ddot{u}$ the acceleration , and I and i-1/2, i+1/2 refer to the increment number and mid-increment numbers.

$$\ddot{u}^{(i)} = M^{-1} \cdot (F^{(i)} - I^{(i)}) \tag{9.10}$$

where M is the mass matrix, F is the applied load vector, and I is the internal force vector.

9.7 Consideration of the time step

Consideration of the time step parameter is an important aspect during simulations because it is related to the quality of loading curve. Liu *et al.* (2008) reported that the waviness trend of the load curve in their simulation (Figure 9.6). They claimed this phenomenon is due to mostly related to strain rate sensitivity and work hardening in the constitutive model. In the initial process of simulation it also suffered this kind of problem, and dealt with it by changing the time step. An improvement has been done in the current project to deal with waviness of the unloading part.

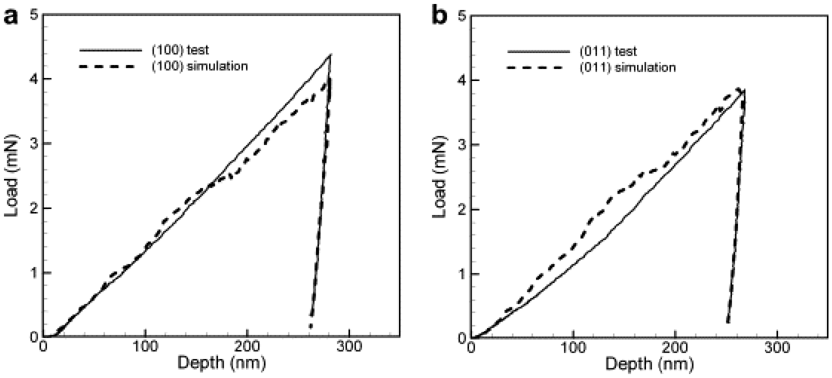

(100) surface

(011) surface

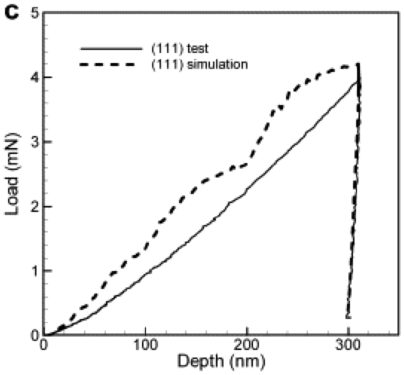

(111) surface

Figure 9.6: Comparison of load-displacement curve between simulation and experimental (Liu *et al.*, 2008).

With regards to the waviness of load-displacement curves, Hughes *et al.* (1976) explained this problem by punching with triangular and parabolic shaped punches. In these findings both curves of the total contact force (Figure 9.7) varied linearly or quadratically. They also claimed that this result was due to displacement impact conditions because the indenter used velocity which caused displacement to vary linearly over the time step. In this paper Hughes *et al.* (1976) suggested that more sensitive (i.e. higher-order) impact and release conditions were needed to avoid taking extremely small steps during the impact and release phases of a contact problem. Therefore, in this project a consideration regarding the time step was done to overcome this problem.

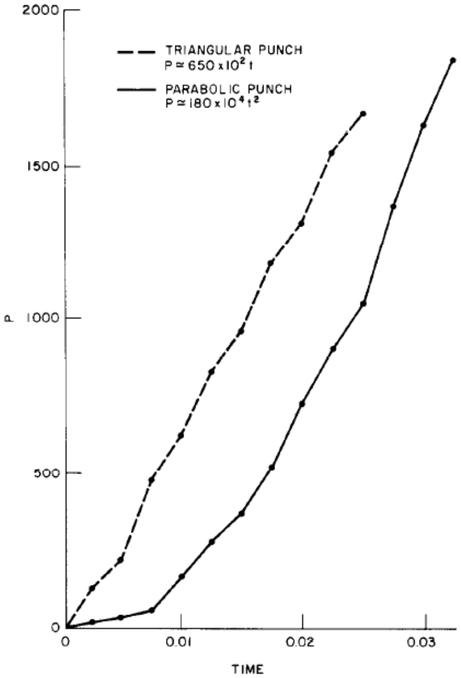

Figure 9.7: Total contact force vs time for rigid punch problem (Hughes *et al.*, 1976)